University of New Mexico
UNM Digital Repository

Chemistry ETDs

Electronic Theses and Dissertations

7-2-2011

Spectroscopic and electronic structure studies of metalloenzyme active sites

Joseph Sempombe

Follow this and additional works at: https://digitalrepository.unm.edu/chem_etds

Recommended Citation

Sempombe, Joseph. "Spectroscopic and electronic structure studies of metalloenzyme active sites." (2011).
https://digitalrepository.unm.edu/chem_etds/19

This Dissertation is brought to you for free and open access by the Electronic Theses and Dissertations at UNM Digital Repository. It has been accepted for inclusion in Chemistry ETDs by an authorized administrator of UNM Digital Repository. For more information, please contact disc@unm.edu.

JOSEPH SEMPOMBE
Candidate

CHEMISTRY AND CHEMICAL BIOLOGY
Department

This dissertation is approved, and it is acceptable in quality and form for publication:

Approved by the Dissertation Committee:

, Chairperson

SPECTROSCOPIC AND ELECTRONIC STRUCTURE STUDIES OF METALLOENZYME ACTIVE SITES

BY

JOSEPH SEMPOMBE

B.Sc., Education (Hons), University of Dar Es Salaam, 1999
M.Sc., Chemistry, University of Dar Es Salaam, 2002

DISSERTATION

Submitted in Partial Fulfillment of the
Requirements for the Degree of

Doctor of Philosophy
Chemistry

The University of New Mexico
Albuquerque, New Mexico

May, 2011

DEDICATION

To My Wife and Two Sons

&

To Mom and Dad

ACKNOWLEDGEMENTS

I would like to thank the Almighty God for giving me health and strength throughout my study in the USA and be able to accomplish this work. Many thanks to the Department of Chemistry and Chemical Biology for a scholarship award at the University of New Mexico. Special thanks to Prof. Martin L. Kirk (my advisor) for his moral and financial support of my well being, supply of research materials and guidance during the whole period of my research, and we both have made this work a success. I would like also to thank our collaborators, Prof. Dehua Pei (from Ohio State University) and Prof. Changjian Feng (from College of Pharmacy, UNM) for providing us with LuxS and iNOS enzymes to study and ultimately contribute our research findings to the body of Chemistry knowledge and to the public. To my wife, Matilda and my two sons, Kelvin and Joseph, thank you for your huge sacrifices, support, encouragement and prayers as I pursued my carrier. I also thank my Mom and Dad for their prayers, encouragement to me and support to my family back home in Tanzania during my absence. I sincerely appreciate their overwhelmingly support. My friends, relatives, sisters and brothers also contributed a lot through their prayers during this journey, I thank them for that. To the Kirk research group: Dr. Sushilla Z. Knottonbelt, Dr. Nick Rubie, Dr. J. Yang, Dr. Tony, Dr. Abebe, Meita, Regina, Diana, Ben, Dominic and Chao, thank you for your academic advices and making a research work in our lab convenient and enjoyable. God bless you all.

SPECTROSCOPIC AND ELECTRONIC STRUCTURE STUDIES OF METALLOENZYME ACTIVE SITES

BY

JOSEPH SEMPOMBE

ABSTRACT OF DISSERTATION

Submitted in Partial Fulfillment of the
Requirements for the Degree of

Doctor of Philosophy
Chemistry

The University of New Mexico
Albuquerque, New Mexico

May, 2011

SPECTROSCOPIC AND ELECTRONIC STRUCTURE STUDIES OF METALLOENZYME ACTIVE SITES

BY

JOSEPH SEMPOMBE

B.Sc., Education (Hons), University of Dar Es Salaam, 1999
M.Sc., Chemistry, University of Dar Es Salaam, 2002
Ph.D., Chemistry, University of New Mexico, 2011

ABSTRACT

This work reports on the electronic and geometric structural studies of xanthine oxidoreductase (XO), S-ribosylhomocysteinase (LuxS) and inducible nitric oxide synthase (iNOS) active sites resulting from the joint applications of electronic absorption, electron paramagnetic resonance and magnetic circular dichroism spectroscopic methods.

XO catalyzes formal oxygen atom insertion into a substrate C-H bond, but differs from monooxygenase enzymes in that the inserted oxygen atom derives from metal activated water and reducing equivalents are generated rather than consumed. Studies on aldehyde “inhibited” XO (a paramagnetic form observed during XO catalysis), analyzed in terms of the relationships between the g-, ^{95,97}Mo hyperfine, and the ^{13}C hyperfine tensors have provided structural insights into the nature of substrate/product bound at the Mo active site. The results

indicate that aldehyde “inhibited” is a tetrahedral analogue of the calculated transition state in XO catalytic mechanism.

S-ribocylhomocysteinase (LuxS) catalyzes the non-redox cleavage of a stable thioether bond, a difficult reaction from chemist’s perspective. This metalloenzyme plays a key role in quorum sensing which makes its investigation an attractive target for inhibition and development of novel antibacterial agents. This study utilized Co(II)-d^7 substituted tetrahedral LuxS. Thus, analysis for g-, ^{59}Co hyperfine and zfs (D and E) tensors of wild-type, mutants (C84A and C84D) and relevant small molecule analogues, (PATH)CoBr and (PATH)CoNCS have provided a detailed description of LuxS active site. The results indicate that the LuxS active site is a distorted tetrahedral with approximate C_{3V} geometry and the catalytic reaction begins by the substrate displacing water.

The iNOS catalyzes the oxidation of L-arginine to a signaling molecule, NO and L-citrulline with NADPH and O_2 as cosubstrates. The emerging evidence suggests that the production of NO is facilitated by the interdomain electron transfer from the FMN to the catalytic heme site. This work reports a comparative spectroscopic study of wild-type and mutant proteins of a human iNOS bidomain oxygenase/FMN construct. The results indicate notable effects of mutations in the adjacent FMN domain on the heme structure suggesting that the conserved surface residues in the FMN domain (E546 and E603) play key roles in facilitating a productive alignment of the FMN and heme domains in iNOS.

Table of Contents

List of Figures……………………………………………………………………..xiii

List of Tables…………………………………………………………………...xxxix

Chapter 1. Spectroscopic Methodologies………………………………......…1

1.1 Introduction……………………………………………………......…....1

1.1.1 Spectroscopy and Mechanisms of Metalloenzymes……………..….1

1.1.2 Spectroscopic Methodologies…………………………..….……….2

1.1.2.1 Electronic Absorption Spectroscopy (EA)…..…..….…2

1.1.2.2 Electron Paramagnetic Resonance Spectroscopy (EPR)………………………………………….....…....8

1.1.2.3 Magnetic Circular Dichroism Spectroscopy (MCD)..24

Chapter 2. Spectroscopic and Electronic Structure Studies Probing the Reaction Coordinate of Xanthine Oxidase………………………35

2.1 **Introduction ………………………………………………………………..35**

2.1.1 Xanthine Oxidase Family…………………………………………..35

2.1.2 The Crystal Structures of Xanthine Oxidase Family Enzymes.….38

2.1.3 The Active Site of Xanthine Oxidase……………………………..…41

2.1.4 The Reductive Half Reaction of Xanthine Oxidase……………….42

2.1.4.1 Hydride Transfer Mechanism ………………………..42

2.1.4.2 Proton Transfer Mechanism………………………….46

2.1.5 XO “Inhibited”………………………………..……………………47

2.2 Statement of the Research Problem……………………………………49

2.3 Hypothesis……………………………………………………………………49

2.4 Materials and Methods……………………………………………………50

2.5 Results and Analysis………………………………………………………52

2.5.1 Reduction of Mammalian XO and Bacterial XDH Enzymes by Substrates…………………………………………………………52

2.5.2 Inhibited Signals and ^{95,97}Mo Hyperfine Analysis…………………..54

2.5.3 Structural Insights of the "Inhibited" Species……………………….64

2.5.4 Molecular Orbital Description of XO/XDH Derived "Inhibited" Structure…………………………………………………………..75

2.5.4.1 Ligand Field Splitting and Nature of the β-LUMO.....75

2.5.4.2 The Magnitude and Orientations of the Hyperfine Tensors for ^{95,97}Mo, ^{13}C, ^{1}H, ^{17}O and ^{33}S of the "Inhibited" Structure…………………………………...78

2.6 Discussion…………………………..…………………………………..83

2.6.1 The Structure of XO/XDH "Inhibited" Signal Giving Species.……..83

2.6.2 The Stability and Oxygen Dependence of XO/XDH "Inhibited" Species………………………………………………………………87

2.6.3 Mechanistic Insights for the Generation of XO "Inhibited" Species and Relationship to CODH…………………………………………93

2.6.4 Relationship between "Inhibited" and the Calculated Transition State in XO Catalytic Mechanism...…...104

2.7 Conclusion…………………………………………………………………107

Chapter 3. Ground and Excited State Spectroscopy of LuxS……………109

3.1 Introduction…………………………………………………………………109

3.1.1 S-Ribosylhomocysteinase (LuxS)…………………………………109

3.1.2 The Proposed Catalytic Mechanism……………………….………113

3.2 Statement of the Research Problem…………………………..………..117

3.3 Hypothesis………..……………………………………………………….117

3.4 Materials and Methods…………………………………………………….118

3.5 Results and Analysis………………………………………………………120

3.5.1 Ligand Field Transitions in Tetrahedral Co(II)……………………120

3.5.2 Observed Ligand Field Transitions in LuxS, C84A and C84D…..126

3.5.3 Determination of Spin Hamiltonian and the Zero Field Splitting Parameters Using VTVH-MCD………..…………………………...131

3.5.4 Determination of Spin Hamiltonian Parameters by EPR Spectroscopy……………………………………………………….....135

3.5.5 Theoretical Calculations of Electronic Structure of LuxS Active Site………………………………………………………………….....141

3.5.5.1 Density Functional Theory on LuxS-C84A and LuxS-C84D……………………………………………………141

3.5.5.2 Angular Overlap Model (AOM) Applied to Wt-luxS, LuxS-C84A and LuxS-C84D……………..……………………150

3.5.6 Spectroscopy and Computational Study of the LuxS Model Compounds (PATH)CoBr and (PATH)CoNCS……………………157

3.5.6.1 (PATH)CoBr and (PATH)CoNCS and Their Observed Transitions……………………………………………...157

3.5.6.2 Determination of Spin Hamiltonian and the Zero Field Splitting Parameters by VTVH-MCD…..……………..161

3.5.6.3 Determination of Spin Hamiltonian Parameters by EPR Spectroscopy…………………………………………165

3.5.6.4 Density Functional Theory (DFT) Calculations……….167

3.5.6.5 Angular Overlap Model (AOM)………………………….175

3.6 Discussion and Conclusion……………………………………………178

3.6.1 LuxS Active Site Geometry and Mechanistic Implications……….178

Chapter 4. Mutations in the FMN Domain Modulate MCD Spectra of the Heme Site in the Oxygenase Domain of Inducible Nitric Oxide Synthase……………………………………………………………187

4.1 Introduction……………………………………………………………187

4.1.1 Nitric Oxide Synthase (NOS), Isoforms and Cofactors………….187

4.1.2 The Proposed Catalytic Mechanism…………………………….191

4.2 Statement of the Research Problem…………………………………197

4.3 Hypothesis……………………….……………………………………198

4.4 Materials and Methods………………………………………………198

4.5 Results and Analysis…………………………………………………199

4.5.1 Perturbations of MCD Spectra from Mutations in the FMN Domain (Wt-iNOSoxyFMN vs. E546N and E603N)………………….……199

4.5.2 L-arginine Perturbation on the MCD Spectra of the iNOSoxyFMN, E546N, E603N and iNOS Oxygenase Domain……………………..201

4.5.3 Perturbations of VTVH-MCD Spectra From Mutations in the FMN Domain (Wt-iNOSoxyFMN vs. E546N-iNOS oxyFMN)…………206

4.5.4 L-arginine Perturbations on the VTVH-MCD of iNOSoxyFMN, E564N, E603N…………………………..………………………….209

4.5.5 L-arginine Perturbations on the EPR spectra of Wt-iNOSoxyFMN and E564N Mutant.……………………………………….………...212

4.6 Discussion……………………………………………………..………..219

4.6.1 L-arginine Perturbations on Wt-iNOS oxyFMN and E546N-iNOS oxyFMN……………………………………………………………..…219

4.6.2 L-arginine Perturbations on Wt-iNOS oxyFMN and E546N-iNOS oxyFMN Cyanide Complexes…………………………………….220

4.6.3 Nature of Interdomain FMN - Heme Interactions with L-arginine Binding……………………………………………………..………224

4.7 Conclusion…………………………………………………………..…..227

References……………………………………………………………..……..228

List of Figures

Figure 1.1: A summary of the ligand field and charge transfer transitions observed in a tetrahedral complex…..…………………………….…….....4

Figure 1.2: Increasing Zeeman splitting with increasing magnetic field for S = ½ system for fixed input microwave frequency (hυ)………..…….……..9

Figure 1.3: The “magic pentagon” for evaluating n of equations (1.18) and (1.19) which is the number on the line linking the orbitals which mix by spin-orbit coupling………...………………………………………….....……15

Figure 1.4: Energy level spacing showing spin systems for $S = \frac{3}{2}$ and $S = \frac{5}{2}$ which have $D > 0$. However, for systems with $D < 0$, the spin microstates $\pm m_s$ are reversed……………………..…………………....21

Figure 1.5: Splitting of the ground state energy levels for Co(II)-d^7 in a magnetic field ($D > h\upsilon$)………..…………………………………………………...24

Figure 1.6: The origin of A term MCD intensity. The absorption of circularly polarized light is based on a transition from an orbitally non-degenerate ground state to an orbitally degenerate excited state within a magnetic field applied parallel to the axis of light propagation. However, when the field is zero (H = 0), the RCP and LCP light absorptions cancel each other resulting to no absorption. In the presence of an applied magnetic field (H ≠ 0), A derivative-shaped A term (right-top in Figure 1.8) is observed due to the Zeeman splitting of states and the associated energy separation of bands absorbing

RCP and LCP light based on the $m_J = \pm 1$ selection rule……………………………………………………………..…………..26

Figure 1.7: The origin of B term MCD intensity mechanism. The splitting of the negative and positive Gaussian shaped MCD signals is determined by the energy separation of the RCP and LCP light absorption bands that arise within the applied field due to field induced mixing of states via a magnetic dipole transition moment……….……………….……..28

Figure 1.8: The origin of C term MCD intensity mechanism. The C term MCD signal arises due to a transition from an orbitally degenerate ground state to an orbitally non-degenerate excited state within a magnetic field applied parallel to the axis of light propagation ………..……….30

Figure 2.1: A (Top) represents the XDH dimmer isolated from bovine milk with the cofactors labeled (The structure was downloaded from PDB 1FO4. B (bottom) represents the geometrical structures of cofactors in xanthine oxidase family. Electrons flow from Moco via FeSI and FeSII to the FAD where the oxidative half reaction takes place. The FAD is on the surface of the protein whereas the Moco is buried deep in the protein………………………………………………..……………..….39

Figure 2.2: Schematic representation of the homologies that exist in xanthine oxidase family. The aldehyde oxidoreductase from *D. gigas* does not have an FAD domain. In the *R. capsulatus* xanthine dehydrogenase the iron–sulfur and flavin-binding portions of the protein constitute one subunit (XdhA), and the molybdenum-binding portion a second

(XdhB). In the *O. carboxydovorans* CO dehydrogenase, the iron–sulfur centers are together in one subunit (CoxS), the flavin in a second (CoxM) and the molybdenum in a third (CoxL)……………………………………………………….……………40

Figure 2.3: Represents the active site for bovine xanthine oxidase downloaded from the PDB file with a code 1FIQ, (in parentheses is the numbering convention for the *R. capsulatus* XDH): The structure on the left (in the box) represents the orientation for the substrate channel. (i) Represents the active site for Moco, (ii) is the oxidized form at oxidation state of (VI) at the metal center and (iii) is the reduced form at an oxidation state of (IV) at the metal center……………………....41

Figure 2.4: The charge transfer complex (band at 650 nm) formed between dithionite reduced xanthine oxidase with violapterine isolated from the aerobic reaction of lumazine and xanthine oxidase. The solid line (─) in blue represents oxidized enzyme at its resting state, the dashed line (-·-) in red represents the spectrum of the violapterin and dithionite reduced enzyme with a charge transfer band at 650 nm. The dotted line (…) represents the re-oxidized enzyme from the dithionite reduced XO. Note that, the charge transfer band at 650 nm decays quickly upon exposure of the enzyme to oxygen................44

Figure 2.5: Proposed structures for xanthine oxidase “inhibited”………………..48

Figure 2.6: Reaction of oxidized XO/XDH with acetaldehyde…………………..…53

Figure 2.7: Anaerobic reaction of oxidized XO/XDH with formaldehyde………..53

Figure 2.8: Anaerobic reaction of oxidized XO/XDH with 2-pyridinecarboxaldehyde………...53

Figure 2.9: Anaerobic reaction of oxidized XO/XDH with 3-pyridinecarboxaldehyde……………………………………………54

Figure 2.10: Electron paramagnetic resonance (EPR) signals for various aldehydes at 9.41 GHz during reaction with xanthine oxidase (0.07 mM) in 50 mM Bicine/NaOH buffer, pH 8.2. The aldehydes used for spectra (a), (b), (c) and (d) are respectively formaldehyde (0.20 M), 2-pyridinecarboxaldehyde (0.03 M), 3-pyridinecarboxaldehyde (0.03 M) and acetaldehyde (0.50 M). Their incubation times with xanthine oxidase are 6, 0.5, 1.5 and 0.12 hours respectively. The black spectra (upper) represent data whereas the red spectra (below) are their corresponding simulations..…..55

Figure 2.11: Electron paramagnetic resonance (EPR) signals for various aldehydes at 9.42 GHz during reaction with XDH (0.07mM) in 50 mM Bicine/NaOH buffer, pH 8.2. The aldehydes used for spectra (a), (b) and (c) are respectively formaldehyde (0.20 M), 2-pyridinecarboxaldehyde (0.03M) and 3-pyridinecarboxaldehyde (0.03 M). Their incubation times with xanthine oxidase are 0.25, 0.50 and 0.17 hours respectively. The black spectra (upper) represent data whereas the red spectra (below) are their corresponding simulations……………………………………………………….…56

Figure 2.12: Electron paramagnetic resonance (EPR) signals at 9.41GHz during reaction of xanthine oxidase (0.07 mM) with formaldehyde (0.20 M) in 50 mM Bicine/NaOH buffer, pH 8.2. At intervals, samples were bubbled with oxygen in the EPR tubes and frozen for EPR measurement. Reaction times for (1), (2) and (3) were 1, 3 and 6 hours respectively. Spectrum (4) represents a ‘rapid type’ signal which is the difference spectrum obtained from subtracting (1) from (3). The insert in (2) shows the proton splitting at g_x at lower concentrations of the “inhibited” species……………………….….....60

Figure 2.13: Electron paramagnetic resonance (EPR) signal at ≈ 9.4 GHz during reaction of 0.07 mM XO (top) and 0.07 mM XDH (bottom) with ^{13}C-labeled formaldehyde (0.20 M) in 50 mM Bicine/NaOH buffer pH 8.2 and its corresponding simulation. The reaction mixture was bubbled with oxygen in an EPR tube for 15 minutes and then frozen for EPR measurement. The black spectrum (upper) is the data whereas the red spectrum (below) is the simulation in each set…..………………61

Figure 2.14: Electron paramagnetic resonance (EPR) signals at 9.41GHz during reactions of 0.07 mM wild type xanthine dehydrogenase from *R. capsulatus* (black spectrum - below) and 0.07 mM of E232A-xanthine dehydrogenase (red spectrum – upper) with 3-pyridinecarboxaldehyde (0.03 M) in 50 mM Bicine/NaOH buffer, pH 8.2. Note; the E232A-XDH (red spectrum) is relatively shifted to higher field compared with the wild type XDH (black spectrum)……62

Figure 2.15: Electron paramagnetic resonance (EPR) signal at 9.439 GHz during reaction of E232A-xanthine dehydrogenase (0.07 mM) with 3-pyridinecarboxaldehyde (0.03 M) in 50 mM Bicine/NaOH buffer pH 8.2 and its corresponding simulation. The reaction mixture was incubated in an open EPR tube for 10 minutes and then frozen for EPR measurement. The black spectrum (upper) is the data whereas the red spectrum (below) is the simulation……………………………63

Figure 2.16: Proposed xanthine oxidase structures and their spin density maps (R = H). The numbers between the atoms are Mayer bond orders. Notice, Structure (i) has its spin density localized on molybdenum whereas structures (ii) and (iii) are identical and have their spin densities mostly localized on the aldehydic carbon. Secondly, there is no Mo-C bond order calculated in all the proposed structures……..66

Figure 2.17: The energy level diagram for the proposed "inhibited" structure (i) showing the presence of unpaired electron in the Mo-d_{xy} orbital (SOMO). ……………….……………………………………………….67

Figure 2.18: The energy level diagram for the proposed "inhibited" structures (ii) and (iii) showing the presence of unpaired electron in the carbon $2p_z$ orbital (SOMO)…………………………..…..…….…..……………..70

Figure 2.19: Comparison of the theoretical formaldehyde (R = H) "inhibited" EPR spectra of the proposed xanthine oxidase structures with the observed formaldehyde generated xanthine dehydrogenase "inhibited" spectrum. Notice; structure (i) is in a very good agreement with the observed EPR spectrum whereas structures (ii) and (iii) (organic radicals) are identical and do not agree with the experimental spectrum. The little rhombicity for structures (ii) and (iii) indicates reduction of metal character and increase in ligand character. The splitting at g_x is due to a formaldehyde proton (R = H)…………………………………………………………………….72

Figure 2.20: Comparison of the theoretical with the observed “inhibited” spectra for (a) ^{13}C-formaldehyde (b) 3-pyridinecarboxaldehyde, (c) 2-pyridinecarboxaldehyde and (d) acetaldehyde generated XO/XDH. (a’), (b’), (c’) and (d’) are their corresponding theoretical spectra respectively……………………………………………………………..74

Figure 2.21: calculated ligand field molecular orbital energies for formaldehyde, 3-pyridinecarboxaldehyde and 2-pyridinecarboxaldehyde XO/XDH “inhibited” structures. The molecular orbital energies have been normalized to Mo-d_{xy} orbital (LUMO)……………………………..……75

Figure 2.22: Schematic representation of the top view (Z coming out of the plane) of the molecular frame (X Y Z) relative to the laboratory frames for g (g_x g_y g_z) and A (A_x A_y A_z) tensors as drawn from the orientation matrices in ORCA output files. The g-tensor is highly rotated from the symmetry axes (X Y Z) of the “inhibited” complex compared to the A-tensor. Using the ZXZ convention, the largest value of the A- tensor is rotated 4.75^0 away from Z direction (Mo=O) whereas the largest value of the g-tensor (g_z) that has the smallest Δg shift is rotated 137^0 from Z-direction (Mo=O……………………….79

Figure 2.23: Schematic representation of the side view of the molecular frame (X Y Z) relative to the laboratory frames for g (g_x g_y g_z) and A (A_x A_y A_z) tensors as drawn from the orientation matrices in ORCA output files……………………………...……..……….………………….80

Figure 2.24: Part of ORCA output files showing the orientation of the g-tensor (in a box) and the largest component of the hyperfine tensors relative to the molecular frame for ^{95,97}Mo, ^{13}C, ^{1}H, ^{17}O and ^{33}S isotopes. The numbers circled in blue on the **A (Tot)** and in the **orientation** matrix represent the largest hyperfine component and its orientation coordinate respectively. When the hyperfine tensor is perfectly oriented along either X or Y or Z coordinated then its value is a unit…………………………………………………………………...81

Figure 2.25: Overlap population density of states (OPDOS) plot showing the magnitude and nature of anti-bonding between Mo and C atoms. This overlap is indicated by the solid line in blue and is the strongest interaction in the β-LUMO……………………………………...……….85

Figure 2.26: Schematic representation of the side view (left) and top view (right) showing the orientation of the ^{13}C hyperfine tensor (A_x, A_y, A_z) relative to molecular frame (X, Y, Z) drawn from the orientation matrices in ORCA output files. The largest ^{13}C hyperfine tensor component A_z lies along the XY plane and interacts in the anti-bonding fashion with the Mo-d_{xy} orbital……………………………..…...86

Figure 2.27: Electronic absorption spectra representing anaerobic incubation of 3-pyridinecarboxaldehyde with xanthine dehydrogenase (XDH) from *R. capsulatus*. The inserts are the corresponding EPR spectra obtained for XDH + 3-pyridinecarboxaldehyde at anaerobic conditions (black: —···—) and then adding oxygen to XDH + 3-pyridinecarboxaldehyde kept at anaerobic conditions that immediately forms the “inhibited” spectrum (blue: —). The band at 620 nm (shown by an arrow) has been confirmed to represent the absorption for a flavin semiquinone (The black (—···—) EPR spectrum)……………………………………………………………87

Figure 2.28: Electronic absorption spectra representing anaerobic incubation of 3-pyridinecarboxaldehyde with xanthine dehydrogenase (XDH) from *R. capsulatus* in and without the presence of 1mM dithionite. The insert is the corresponding EPR spectrum obtained for XDH + 3-pyridinecarboxaldehyde at anaerobic conditions with and without 1mM dithionite which are represented by red (—) and black (—···—) spectra respectively……………………..………………………….91

Figure 2.29: EPR pH dependent studies for 3-pyridinecarboxaldehyde generated xanthine dehydrogenase “inhibited” from *R. capsulatus*. The EPR intensity increases from pH 8 to pH 12. Notice; from pH 9 to pH 10, there is a dramatic increase in intensity. However, pH 8 and pH 9 are close in signal intensities and on the other hand pH 10 and pH 12 are close with higher intensities than pH 8 and pH 9………..92

Figure 2.30: Low temperature EPR spectra for anaerobic incubation of XDH with 3-pyridinecarboxaldehyde at 9.436 GHz and 40K. Solid black spectrum is the data whereas the dashed red spectrum is the simulation. The g-values for $FADH^{\bullet}$ derived from EPR simulation are $g_x = g_y = g_z = 2.0170$. The g-values for FeSI and FeSII were adapted from Leimkuhler et al, 2003 which are $g_x = g_y = 1.9217$, $g_z = 2.0222$ for FeSI and $g_x = 1.8964$, $g_y = 1.9711$, $g_z = 2.0730$ for FeSII. These (g-values for FeSI and FeSII) were obtained from a reduction of XDH by sodium dithionite at anaerobic conditions…..……………………….95

Figure 2.31: EPR spectra showing the presence and absence of the 2Fe-2S clusters and $FADH^{\bullet}$ obtained upon exposure to oxygen at different times. The **INITIA**L spectra (7 minutes incubation) contain all spin states for the three cofactors whereas the **FINAL** spectra (further 5 minutes incubation) contain only the molybdenum cofactor after further oxygenation of the sample……..……..……………….……….98

Figure 2.32: 1.09Å crystal structure of n-butylisocyanide “inhibited” CODH. The molybdenum center is at the oxidation state of (IV). Notice, both XO (schemes 2.7 and 2.8) and CODH “inhibited” form Mo-S-C and Mo-O-C bonds, however, substrate C in XO “inhibited” complex is tetrahedral whereas in CODH is a trigonal planar……………..……102

Figure 2.33: The reaction profile for formaldehyde substrate as a function of C-H bond distance……………………………………………………………….106

Figure 2.34: Mulliken charge distributions along formaldehyde pathway at the **IM**, **TS** and **P**…………………………………………………………...107

Figure 3.1: A stereo representation of the luxS dimmer showing the two active sites with Fe^{2+} coordinated to His-54, His-57, Cys-126 and a H_2O/OH^- in *Bacillus subtilis* luxS. On the right hand side is a stereo representation of the van der Waals surface of the luxS dimmer showing the substrate channel. The protein was downloaded from the protein data bank (PDB) 1J6X…………………………………...109

Figure 3.2: A magnified stereo representation of the of the van der Waals surface of the luxS dimmer showing the substrate channel with Fe^{2+} at the active site coordinated to His-54, His-57, Cys-126 and a H_2O/OH^- in *Bacillus subtilis* luxS. The position of Cys-84 is also shown (4.86 Å from Fe^{2+} metal center). On the right hand side is the opposite end of the channel. The protein was downloaded from the protein data bank (PDB) 1J6X...113

Figure 3.3: A magnified stereo representation of the of the van der Waals surface of the luxS dimmer showing the substrate channel with Fe^{2+} at the active site coordinated to His-54, His-57, Cys-126 and a H_2O/OH^- in *Bacillus subtilis* luxS. The positions of Arg-39 and Glu-57 are shown. Arg-39 is located at 4.04 Å from Cys-84 and Glu-57 is located at 4.67 from Fe^{2+} metal center……………………………114

Figure 3.4: Simplified Tanabe sugano diagram showing the energy differences between terms of the three spin allowed ligand field transitions occurring in tetrahedral d^7 Co^{2+} complex……………………………121

Figure 3.5: Splitting diagram for tetrahedral Co^{2+} complex – ground state configuration……………………………………………………………123

Figure 3.6: Splitting of the T_d terms with both distortions (C_{2v}, C_{3v}) and spin orbit coupling (SOC) followed by splitting of each multiplet due to magnetic field (H) for Co^{2+}, d^7. The higher excited states, $^4T_1$ (F) and $^4T_1$ (P) also split in the same way as $^4T_2$ (F) upon application of the magnetic field (H) though not shown. The splitting of the ground state term due to both low symmetry and spin orbit coupling (SOC) results into zero field splitting zfs which can be probed by EPR spectroscopy and VTVH-MCD. Transitions to higher excited states $^4T_2$ (F), $^4T_1$ (F) and $^4T_1$ (P) can be probed by electronic absorption (EA) and magnetic circular dichroism (MCD)…………………………………………….125

Figure 3.7: MCD and electronic absorption (EA) spectra overlays for wt-luxS……………………………………………………………..……128

Figure 3.8: MCD and electronic absorption (EA) spectra overlays for luxS-C84A…………………………………………………………………..129

Figure 3.9: MCD and electronic absorption (EA) spectra overlays for luxS-C84D..…130

Figure 3.10: VT-MCD for wt-luxS, C84A and C84D collected at 5, 10 and 20K. The MCD intensities for all bands increase with decreasing temperature which is a characteristic of C-term behavior..............131

Figure 3.11: MCD magnetization curves of the luxS-C84A construct at 357, 650 and 1364 nm. Spectral simulation has been achieved with $g_x = 2.300$, $g_y = 2.300$, $g_z = 1.800$, $S = 1.5$, $D = -10\ cm^{-1}$, $E/D = 0.095\ cm^{-1}$; polarizations are: xy = 1.000, xz = yz = 0.900 at 430 nm, xy = 1.000, xz = 0.000, yz = 0.400 at 1364 nm, and xy = 0.600, xz = 0.700, yz = 1.000 at 357 nm..133

Figure 3.12: MCD magnetization curves of the luxS-C84D construct at 580, 638 and 1354 nm. Spectral simulation has been achieved with $g_x = 2.180$, $g_y = 2.180$, $g_z = 2.115$, $S = 1.5$, $D = 8\ cm^{-1}$, $E/D = 0.045\ cm^{-1}$; polarizations are: xy = xz = 0.000, yz = 1.000 at 638 nm, xy = 1.000, xz = 0.900, yz = 0.000 at 1354 nm, and xy = xz = 1.000, yz = 1.000 at 580 nm..134

Figure 3.13: EPR spectral overlays for the wt, C84A and C84D-luxS at 4K and 20 dB...135

Figure 3.14: Temperature dependent EPR spectral data (——) and simulations (.........) overlays for C84A and C84D mutants collected and simulated at 4, 8 and 20K...136

Figure 3.15: Full width EPR spectral overlays for the wt, C84A and C84D-luxS at 4K and 20 dB. The derivative shaped signal at 12000G represents the absorption for the paramagnetic oxygen. The insert represents the signal for the empty cavity at 4K which interferes with the sample signals (visible between 2000 and 4000G in sample spectra)…….137

Figure 3.16: Energy levels as a function of magnetic field for the three canonical orientations of the field relative to the principal zfs axis calculated for C84A, using the same set of EPR spin Hamiltonian parameters. Observed EPR transitions are marked with red bars. However, there are four transitions in H//X and H//Y, two originating from m_s = ±1/2 Kramers doublet and two from m_s = ±3/2 Kramers doublet……….139

Figure 3.17: Energy levels as a function of magnetic field for the three canonical orientations of the field relative to the principal zfs axis calculated for C84D, using the same set of EPR spin Hamiltonian parameters. Observed EPR transitions are marked with red bars. However, there are two transitions for H//X and H//Y both originating from m_s = ±1/2 Kramers doublet and two transitions for H//Z, one originating from m_s = ±1/2 and the other from m_s = ±3/2 Kramers doublets..................140

Figure 3.18: Electronic absorption spectra overlays for wt, C84A and C84D showing the splitting of the $^4T_1$(F) and $^4T_1$ (P) states……………….142

Figure 3.19: Selected bond distances (Å) and bond angles (degrees) of the computational models C84A and C84D which have been partially optimized by freezing the first coordination sphere with *B. subtillis* wt-luxS crystal structure values. The Co-OH/H2O bond lengths were allowed to optimize. However, the crystal structure value for Co-

OH/H2O bond length is 1.93 Å. The crystal structure values have been downloaded from the protein data bank (PDB 1IE0)..……….143

Figure 3.20: Experimental electronic absorption (top) and theoretical absorption simulated spectra (bottom) from TD-DFT computed transitional energies and oscillator strengths for C84D and C84A mutants......144

Figure 3.21: C84A TD-DFT calculated absorption spectrum from 40 excited states depicted by bars. Excited states 5 and 6 constitute to band 1 whereas excited states 7 and 8 constitute to band 2. Excited states 14 and 17 are the two components of the pseudo A term in the MCD for S → Co charge transfer transitions mixed with LLCT…...…….145

Figure 3.22: C84D TD-DFT calculated absorption spectrum from 40 excited states depicted by bars. Excited states 5 and 6 constitute to band 1 whereas excited states 7 and 8 constitute to band 2. Excited states 10 and 11 are the two components of the pseudo A term in the MCD for S → Co charge transfer transitions……………………….…….146

Figure 3.23: Electron density difference maps (EDDMs) for C84A where dark red represents loss of electron density and green represents gain of electron density…………………………………………………..147

Figure 3.24: Electron density difference maps (EDDMs) for C84D where dark red represents loss of electron density and green represents gain of electron density…………………………………………………..148

Figure 3.25: Electron density difference maps (EDDMs) for S → Co charge transfer transitions of C84A and C84D. Dark red represents loss of electron density and green represents gain of electron density.….149

Figure 3.26: S → Co charge transfer transitions for C84A and C84D. The two transitions, excited states 14 and 17 for C84A occur at 31677 and 32637 cm^{-1} whereas for C84D these transitions (excited states 10 and 11) occur at 28432 and 29213 cm^{-1}……………….……….….150

Figure 3.27: Explanation of metal-ligand interactions in a tetrahedral Co(II) – d^7 by AOM………………….……………..…………………………..151

Figure 3.28: MCD, electronic absorption (EA) and AOMX overlays for wt-luxS……………………………………………………………………154

Figure 3.29: MCD, electronic absorption (EA) and AOMX overlays for C84A…………………………………………………………………....155

Figure 3.30: MCD, electronic absorption (EA) and AOMX overlays for C84D………………………………………………………………….156

Figure 3.31: MCD and electronic absorption (EA) spectra overlays for (PATH)CoBr. The insert represents the enlarged NIR ligand field absorption bands depicting the splitting pattern for $^4A_2$ (F) → $^4T_1$ (F)……………………………………………………………………..159

Figure 3.32: MCD and electronic absorption (EA) spectra overlays for (PATH)CoNCS. The insert represents the enlarged NIR ligand field absorption bands depicting the splitting pattern for $^4A_2$ (F) → $^4T_1$ (F).

The shoulder at 10600 cm^{-1} in the MCD spectrum could be originating from the spin forbidden doublet transition ^{2}E…………..…160

Figure 3.33: VT-MCD for (PATH)CoBr collected at 5, 10 and 20K. Bands 672, 627 and 422 nm were used for collection of VTVH-MCD magnetization data. The MCD intensities for all bands increase with decreasing temperature, a characteristic of C-term behavior…..…161

Figure 3.34: VT-MCD for (PATH)CoNCS collected at 5, 10 and 20K. Bands 672, 600 and 428 nm were used for collection of VTVH-MCD magnetization data. The MCD intensities for all bands increase with decreasing temperature, a characteristic of C-term behavior...…...162

Figure 3.35: MCD magnetization curves of the (PATH)CoBr model compound at 422, 627 and 672 nm. Spectral simulation has been achieved with g_x = 2.380, g_y = 2.030, g_z = 2.025, S = 1.5, D = -12 cm^{-1}, E/D = 0.05 cm^{-1}; polarizations are: xy = 1.000, xz = yz = 0.700 at 422 nm, xy = 1.000, xz = yz = 0.100 at 627 nm, and xy = 1.000, xz = yz = 0.700 at 672 nm………………………………………………………………..…..163

Figure 3.36: MCD magnetization curves of the (PATH)CoNCS model compound at 428, 600 and 672 nm. Spectral simulation has been achieved with g_x = 2.300, g_y = 1.900, g_z = 1.980, S = 1.5, D = -12 cm^{-1}, E/D = 0.085 cm^{-1}; polarizations are: xy = 1.000, xz = 0.500, yz = 1.000 at 428 nm, xy = 1.000, xz = yz = 0.000 at 600 nm, and xy = 1.000, xz = 0.700, yz = 1.000 at 672 nm……………………………………………………..…..164

Figure 3.37: (PATH)CoBr EPR spectral data (———) and simulation (.........) overlay collected and simulated at 15K and 20dB. The parameters used for this simulation are exactly the same as those used for VTVH-MCD simulation. Notice, the resolved hyperfine structure at g_z resonance position due to I = 7/2 for ^{59}Co…...............................166

Figure 3.38: (PATH)CoNCS EPR spectral data (———) and simulation (.........) overlay collected and simulated at 15K and 20dB. The parameters used for this simulation are exactly the same as those used for VTVH-MCD simulation. Features at g_z resonance position could be from hyperfine coupling due to I = 7/2 of ^{59}Co and possibly the impurity from the empty cavity……………………………….........167

Figure 3.39: Experimental electronic absorption (top) and theoretical absorption simulated spectra (bottom) from TD-DFT computed transitional energies and oscillator strengths for (PATH) CoBr and (PATH)CoNCS………………………………………………….......168

Figure 3.40: TD-DFT calculated absorption spectrum for (PATH)CoBr from 40 excited states depicted by bars. Excited states 5 and 6 constitute band 1 whereas excited states 8, 9 and 10 constitute band 2. Excited states 15 and 18 are the two components of the pseudo A term in the MCD for S → Co charge transfer transitions……………………......169

Figure 3.41: Electron density difference maps (EDDMs) for (PATH)CoBr where dark red represents loss of electron density and green represents gain of electron density………………………………….….………….170

Figure 3.42: TD-DFT calculated absorption spectrum for (PATH)CoNCS from 40 excited states depicted by bars. Excited states 5 and 6 constitute band 1 whereas excited states 7 - 12 constitute band 2. All EDDMs for excited states 7 – 12 are almost identical displaying a LLCT. Excited states 14 and 18 are the two components of the pseudo A term in the MCD for S → Co charge transfer transitions. Excited state 17 also contains a one electron transition for S → Co charge transfer but with a smaller molecular orbital coefficient than excited state 14…………………………………………………………………………...171

Figure 3.43: Electron density difference maps (EDDMs) for (PATH)CoBr where dark red represents loss of electron density and green represents gain of electron density……………………………………..……..…..172

Figure 3.44: S → Co charge transfer transitions for (PATH)CoBr and (PATH)CoNCS. The two transitions for (PATH)CoBr occur at 26615 and 29030 cm^{-1} whereas transitions for (PATH)CoNCS occur at 23846 and 26563 cm^{-1}………………………………………………..173

Figure 3.45: Electron density difference maps (EDDMs) for S → Co charge transfer transitions of (PATH)CoBr and (PATH)CoNCS where dark red represents loss of electron density and green represents gain of electron density……………………………………………………..…174

Figure 3.46: Selected bond distances (Å) and bond angles (degrees) for (PATH)CoBr and (PATH)CoNCS adapted from Chang and co-workers……………………………………………………….……..…175

Figure 3.47: MCD, electronic absorption (EA) and AOMX overlays for (PATH)CoBr…………..……………………………………………….…..177

Figure 3.48: MCD, electronic absorption (EA) and AOMX overlays for (PATH)CoNCS………………..……………………………………..….178

Figure 3.49: Spin density maps for C84A, C84D and the model compounds ((PATH)CoBr and (PATH)CoNCS).……...…………………………179

Figure 3.50: Electrostatic interactions at the active sites of wt-luxS, C84D, C84A and analysis of the S → Co charge transfer transition. Water is stabilized in wt-luxS and C84D whereas a hydroxide is stabilized in C84A……………………………………………...………………..183

Figure 3.51: Molecular orbital energy level diagram for mutants and model compounds...…………………………………………………………..….185

Figure 4.1: Stereo view of iNOS oxygenase dimmer showing two domains which are Heme (red) and tetrahydrobiopterin (green). L-arginine (cyan), the substrate is also shown to be bound close to the heme domain. The structure was downloaded from protein data bank (PDB) 1NOD……………………………………………………………………187

Figure 4.2: stereo view of the nNOS reductase dimmer showing different domains of iNOS reductase which are NADP domain (white), FAD domain (cyan) and FMN domain (orange). The structure was downloaded from protein data bank (PDB) 1TLL…………………..….188

Figure 4.3: Redox cofactors in NOS enzymes; NADP, FAD and FMN constitute the reductase domain whereas H_4B and heme constitute the oxygenase domain……………………………………………………189

Figure 4.4: Domain structure of human nNOS, eNOS and iNOS showing Oxygenase, reductase and PDZ domains denoted by solid boxes and the amino acid residue number at the start/end in each isoform. The cysteine residue ligating the heme and the CaM-binding site is indicated for each isoform, myristoylation (Myr) and palmitoylation (Palm) sites on eNOS are shown, together with the location of the zinc-ligating cysteines. The auto inhibitory loop within the FMN regions of nNOS and eNOS are also shown. Grey bars indicate the dimmer interface in the oxygenase domain………………………......190

Figure 4.5: Electron flow in NOS enzymes. Here electrons are delivered to the heme domain for NO production from FMN domain by mechanisms that are not well understood...195

Figure 4.6: Representation of a tethered shuttle model: FMN-binding domain shuttles between the FAD domain and heme-containing oxygenase domain. Top: input state; bottom; putative output state. The two tethers correspond to the hinge region between the FMN and FAD domains, and the CaM-binding linker between the FMN and oxygenase domains. CaM binding unlocks the input state, thereby enabling the FMN domain to shuttle between the two enzyme states…………………………………………..…………………………196

Figure 4.7: a, b and c are VT-MCD spectra recorded at 5, 10, 20K and 7T for the heme site in the as-isolated human iNOS oxyFMN construct whereas d represents an MCD overlay of wt-iNOS oxyFMN and mutants without L-arginine recorded at 5K and 7T…….………....200

Figure 4.8: a, b and c are VT-MCD spectra recorded at 5, 10, 20K and 7T for the heme site in the as-isolated human iNOS oxyFMN construct with L-arginine whereas d represents an MCD overlay of wt-iNOS oxyFMN and mutants with added L-arginine recorded at 5K and 7T…....…201

Figure 4.9: MCD overlays for wt-iNOS oxyFMN, wt-iNOS oxygenase and mutants without and with added L-arginine MCD spectra. The overlays were recorded at 5K and 7T……..………………………...202

Figure 4.10: VT-MCD spectra recorded at 5, 10, 20K and 7T for the heme site of the cyanide treated wt iNOS oxyFMN and mutant constructs with and without L-arginine……….……………………………………….….……203

Figure 4.11: MCD overlays for wt-iNOS oxyFMN and E546N mutant cyano adducts without and with added L-arginine MCD spectra overlays recorded at 5K and 7T…….………………………………………...…205

Figure 4.12: MCD magnetization curves of the as isolated wt human iNOS oxyFMN construct at 406, 420 and 444 nm without L-Arginine. Spectral simulation has been achieved with $g_x = 2.003$, $g_y = 1.949$, $g_z = 2.015$, $S = 2.5$, $D=20\ cm^{-1}$, $E/D = 0.08\ cm^{-1}$, $Ax = Ay = Az = 0\ cm^{-1}$, $Lx = 90$, $Ly = 40$, $Lz = 50$; polarizations are: $xy = 1.000$, $xz = 0.000$, yz = -0.100 at 420 nm; xy = 1.000, xz = -0.010, yz = -0.08 at 406 nm, and xy = 1.000, xz = -0.030, yz = -0.040 at 444 nm……..…………207

Figure 4.13: MCD magnetization curves of the as isolated E546N-iNOS oxyFMN construct at 414, 430 and 458 nm without L-Arginine. Spectral simulation has been achieved with g_x = 2.6740, g_y = 2.3048, g_z = 1.8540, S = 0.5, Ax = Ay = Az = 0 cm^{-1}, Lx = 60, Ly = 15, Lz = 110; polarizations are: xz at 430 nm; xz at 414 nm, and xy at 458 nm...208

Figure 4.14: MCD magnetization curves of the as isolated wt human iNOS oxyFMN construct at 408, 424 and 444 nm with added L-Arginine. Spectral simulation has been achieved with g_x = 2.020, g_y = 1.949, g_z = 2.024, S = 2.5, D = 20 cm^{-1}, E/D = 0.08 cm^{-1}, Ax = Ay = Az = 0 cm^{-1}, Lx = 90, Ly = 40, Lz = 50; polarizations are: xy = 1.000, xz = -0.010, yz = -0.100 at 424 nm; xy = 1.000, xz = 0.019, yz = 0.100 at 408 nm, and xy = 1.000, xz = 0.140, yz = -0.130 at 444 nm..……..210

Figure 4.15: MCD magnetization curves of the as isolated E546N-iNOS oxyFMN construct at 414, 430 and 458 nm with added L-Arginine. Spectral simulation has been achieved with g_x = 2.030, g_y = 1.949, g_z = 2.030, S = 2.5, D = 18 cm^{-1}, E/D = 0.08 cm^{-1}, Ax = Ay = Az = 0 cm^{-1}, Lx = 90, Ly = 40, Lz = 50; polarizations are: xy = 1.000, xz = 0.000, yz = -0.100 at 430 nm, xy = 1.000, xz = -0.012, yz = -0.050 at 414 nm, and xy = 1.000, xz = -0.010, yz = -0.040 at 458 nm……………………..211

Figure 4.16: MCD magnetization curves of the as isolated E603N-iNOS oxyFMN construct at 408, 430 and 456 nm with added L-Arginine. Spectral simulation has been achieved with $g_x = 2.0030$, $g_y = 1.9600$, $g_z = 2.0092$, S = 2.5, D = 22 cm^{-1}, E/D = 0.08 cm^{-1}, Ax = Ay = Az = 0 cm^{-1}; polarizations are: xy = 1.000, xz = -0.008, yz = -0.090 at 430 nm; xy = 1.000, xz = -0.010, yz = -0.080 at 408 nm, and xy = 1.000, xz = -0.020, yz = -0.050 at 456 nm……………………….……………212

Figure 4.17: EPR spectra collected at 20K for wt-iNOS oxyFMN (top) and E546N mutant (bottom) without L-arginine showing a mixture of low and high spin states. Notice the relative ratios of low and high spin states for the wt and mutant...…..213

Figure 4.18: EPR spectra collected at 20K for wt-iNOS oxyFMN (top) and E546N mutant (bottom) with added L-arginine showing ratios of low and high spin states present. Notice the wt is predominantly a high spin heme whereas the mutant still has both low and high spin states…………………………………………………………………214

Figure 4.19: Data and simulation EPR spectra overlays for wt human iNOS oxyFMN construct with added L-Arginine. Spectral simulation has been achieved with $g_x = 2.020$, $g_y = 1.949$, $g_z = 2.024$, S = 2.5, D = 20 cm^{-1}, E/D = 0.08 cm^{-1}, Ax = Ay = Az = 0 cm^{-1}, Lx = 90, Ly = 40, Lz = 50. These values are the same ones used for the VTVH-MCD simulation for wt construct with added L-arginine (Figure 4.17)…..216

Figure 4.20: EPR spectra overlays for cyanide treated wt human iNOS oxyFMN and E546N mutant construct with and without L-arginine (top). Bottom; EPR overlays between wt construct in normal buffer and in deuterated buffer. Notice, the asymmetrical splitting at g2 position disappears in deuterated buffer……….……………………………….217

Figure 4.21: Data and simulation EPR spectra overlays for cyano-wt human iNOS oxyFMN construct and cyano- E546N mutant with and without added L-Arginine. Notice; g values for the mutant are slightly higher than the wt construct………………………………………………..……218

Figure 4.22: calculated ligand field molecular orbital energies for L-arginine, CN^- and CN^- .L-arginine bound at the Fe^{3+} heme site for iNOS. The ligand field splitting energies are 12340 cm^{-1} for L-arginine, 50249 cm^{-1} for CN^{-1} and 52910 cm^{-1} CN^- .L-arginine. The molecular orbital energies have been normalized to LUMO+2 which is the first unoccupied metal orbital…………………………………………………………….222

Figure 4.23: Optimized geometries for computational model compounds of L-arginine (high spin), CN^{-1}.L-arginine (low spin), CN^{-1} (low spin) and bound at the Fe^{3+} heme site. Note; L-arginine does not bind directly to the Fe^{3+} heme site……………………………………………….223

Figure 4.24: Calculated spin densities for L-arginine (high spin), CN^{-1}.L-arginine (low spin) and CN^{-1} (low spin) and bound at the Fe^{3+} heme site. Notice; the spin density for low spin CN^{-1} and CN^{-1}.L-arginine bound is in the d_{yz} type orbital……………………………………………….223

Figure 4.25: Represent selected positively charged surface residues at the back face of heme in a human eNOS oxygenase domain (left, downloaded from PDB; 3NOS), and negatively charged surface residues near the

FMN edge in a rat nNOS reductase construct (downloaded from PDB; 1TLL). GLU 762 in nNOS corresponds to GLU 546 in iNOS whereas GLU 819 in nNOS corresponds to GLU 603. The charged surface residues are conserved in NOS isoforms…..……………..…225

Figure 4.26: Electrostatic interactions between the FMN (blue, negative) and heme (red, positive) domains guide the CaM-induced docking, resulting in formation of the IET-competent FMN/heme complex (output state). The FAD and NADPH cofactors are omitted for clarity...……..226

Figure 4.27: Schematic diagram of the truncated bidomain oxyFMN construct of human iNOS (left). Charge neutralization mutation at E546 or E603 of the FMN domain diminishes the L-Arg perturbation of the heme MCD spectrum, presumably by disrupting proper alignment of the FMN and heme domains (right)……..……………….....……………..227

List of Tables

Table 1.1: Allowed and forbidden transitions……………………………………..7

Table 2.1: Amino acids for substrate recognition………………...……………42

Table 2.2: EPR Parameters for XO Inhibited (bovine)…………….…………57

Table 2.3: EPR Parameters for XDH Inhibited (*R. capsulatus*)……….….…58

Table 2.4: EPR Parameters for E232A-XDH Inhibited (*R. capsulatus*)…..……58

Table 2.5: Comparison between “inhibited” proposed structures (i) and (iv).…65

Table 2.6: Theoretical spin Hamiltonian parameters for “inhibited” species (S-configuration)……………………………………………………………..68

Table 2.7: Theoretical spin Hamiltonian parameters for “inhibited” species (R-configuration)……………………………………………………………..68

Table 2.8: Formaldehyde “inhibited” present data vs. reported………..……69

Table 2.9: Theoretical EPR parameters for Mo(V) proposed “inhibited” structures……………………………………………………………...71

Table 2.10: Mo d_{xy} (β – LUMO) composition for the “inhibited” species………..77

Table 2.11: Spin density composition for the “inhibited” species………………..77

Table 2.12: Calculated Mayers C-S bond order for various XO substrates……..90

Table 3.1: Character table for tetrahedral symmetry (T_d)…………...………124

Table 3.2: Energy states and observed transitions for wt, C84A and C84D....128

Table 3.3: Observed vs. AOMX-calculated d-d transitions for wt, C84A and C84D ……………………………………………………………………152

Table 3.4: Observed transitions for the (PATH)CoBr and (PATH)CoNCS…...159

Table 3.5: Observed vs. AOMX-calculated d-d transitions for (PATH)CoBr and (PATH)CoNCS……………..……………………….…………………….....176

Table 4.1: NOS isoforms homology…………………..………………………………..191

Chapter 1

Spectroscopic Methodologies

1.1 Introduction

1.1.1 Spectroscopy and Mechanisms of Metalloenzymes

A metalloenzyme catalytic mechanism is a step by step sequence of elementary reactions by which an overall chemical transformation of a substrate into a product occurs. This transformation occurs at the active site (a region where substrates bind and undergo chemical transformations to products) of a metalloenzyme yielding intermediates and transition states depicting which bonds are broken and which are formed to give product(s). However, understanding or formulating a particular reaction mechanism requires the proper knowledge of the electronic and geometrical structures of the reactants (metalloenzymes active sites and substrates), intermediates, transition states and products, particularly the chemical changes occurring at transition metal centers that are involved in redox chemistry. Spectroscopic methods such as electronic absorption (EA) coupled with electron paramagnetic resonance (EPR) and magnetic circular dichroism (MCD) have been proven to be very powerful in developing a comprehensive electronic structure description of metalloenzymes active sites and the results have given a detailed insight to the reactions they catalyze [1-11]. In particular, electron paramagnetic resonance (EPR) spectroscopy is unique in its ability to selectively probe the electronic structure of paramagnetic molecules including those involving transition metal ions [12-19]. On the other hand, MCD and EA provide the same set of electronic information but with MCD being a much higher resolution technique than EA. However, MCD in combination with the variable temperature variable field (VTVH-MCD) provide a detailed description of the d orbitals (ligand field and zero-field splitting parameters) which contains information on the geometric and electronic structure of metalloenzymes active sites [20-23]. Altogether, these methodologies were intensively applied in probing the active sites of metalloenzymes, xanthine oxidase (XO), S-ribocylhomocysteinase (luxS) and inducible nitric oxide synthase (iNOS). The results have been used either to establish new reaction mechanisms or evaluate the previously proposed catalytic mechanisms. In particular, the results have given new and detailed information in terms of substrate reactivity pathway for XO, the nature of the catalytic geometry at the active site of luxS and the nature of interdomain electron transfer between FMN and catalytic heme site of iNOS. Below is the theoretical description of these spectroscopic methods used for the investigation and analysis of this work.

1.1.2 Spectroscopic Methodologies

1.1.2.1 Electronic Absorption Spectroscopy

This technique refers to the absorption of the electromagnetic radiation by the sample which is recorded as a function of the wavelength. The relationship between the absorption of electromagnetic radiation to the properties of the material through which this radiation is traveling is expressed by Beer's law (equation 1.1) [24-26].

$$A = \log_{10}\left(\frac{I_0}{I}\right) = \varepsilon c l \text{ ....(1.1)}$$

Where A is the absorbance, I_0 is the intensity of the incident light, I is the intensity of the transmitted light, ε is the molar extinction coefficient at the wavelength of the investigation, c is the molar concentration of the sample and l is the pathlength in centimeters. Equation 1.1 is the basis formula for the majority of applications of spectrophotometry. However, the absorbance A is increased if the pathlength l is increased because the longer the pathlength the greater the reduction in the intensity of light. The absorbance also increases if the concentration c is increased. The molar extinction coefficient ε measured in $M^{-1}cm^{-1}$ is an intrinsic property of the species which measures how strongly a chemical species absorbs light at a given wavelength. This parameter is unique for a particular compound at a particular wavelength.

However, as the sample absorbs energy in form of photons from the radiating source electrons are excited to a higher energy level. The energy level from which the electron is coming from is called the ground state (occupied energy level) and the higher level to which it is going is called the excited state (unoccupied or partially occupied energy level) and this migration is called an electronic transition. However, electronic transitions in metal complexes can either be from an orbital to an orbital within the same molecule (intramolecular charge transfer) or involving an electron from an orbital in one molecule to an orbital in another molecule which is referred to as intermolecular charge transfer.

In transitional metal complexes encountered in metalloenzymes, Intramolecular charge transfer transitions are generally ligand field or d-d transitions, ligand to metal charge transfer transitions (LMCT) and metal to ligand charge transfer transitions (MLCT) [1] summarized in Figure 1.1.

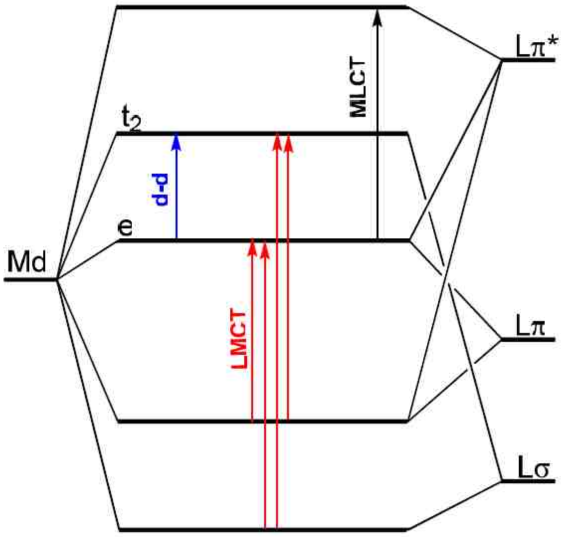

Figure 1.1: A summary of the ligand field and charge transfer transitions observed in a tetrahedral complex.

Charge transfer transitions from the ligand to metal (LMCT) are observed in complexes where the metal is at a high oxidation state and the ligands contain lone pairs of electrons whereas the metal to ligand charge transfer transitions (MLCT) are observed in complexes having ligands with low lying π* orbitals like CN^-, CO and aromatic ligands [27]. Charge transfer transitions are generally more intense than the ligand field or d-d transitions. In general, the intensity of a transition (distributed over a band with a finite width) is given by the dimensionless quantity, oscillator strength $f_{\psi_e\psi_g}$ in equation (1.2), where ε is the molar absorptivity and $\bar{\nu}$ is the frequency in wavenumbers.

$$f_{\psi_e\psi_g} = 4.32\,x\,10^{-9}\int \varepsilon(\bar{\nu})d\,\bar{\nu} \;\ldots\ldots\ldots\ldots\ldots\ldots\ldots\ldots\ldots\ldots\ldots\ldots\ldots\ldots\ldots\ldots\ldots(1.2)$$

However, the intensity of a transition given by oscillator strength $f_{\psi_e\psi_g}$ in equation 1.2 above, is proportional to the square of the transition dipole moment which measures the strength of coupling between the excited state and the ground state wavefunctions [27,28]. This relationship is given by equation (1.4) referred to as the transition moment integral.

$$\mu_{eg} = \langle \psi_e | \mu | \psi_g \rangle \;\ldots\ldots\ldots\ldots\ldots\ldots\ldots\ldots\ldots\ldots\ldots\ldots\ldots\ldots\ldots\ldots\ldots\ldots\ldots\ldots(1.3)$$

$$f_{\psi_e\psi_g} = \frac{2m_e}{\hbar^2}\left(E_{\psi_e} - E_{\psi_g}\right)\left|\langle \psi_e | \mu | \psi_g \rangle\right|^2 \;\ldots\ldots\ldots\ldots\ldots\ldots\ldots\ldots\ldots\ldots\ldots\ldots\ldots\ldots\ldots\ldots (1.4)$$

Where equation (1.3) is the expression for the transition dipole moment, ψ_e is the excited state wavefunction and ψ_g is the ground state wave function, m_e is the mass of an electron, $\hbar$ is the reduced Planck constant, E_{ψ_e} and E_{ψ_g} are the excited and ground states wavefunction energies respectively, μ is the electric dipole moment operator which transforms as x, y and z. If the symmetry of a transition dipole moment integral (equation 1.3) spans the totally symmetric representation of the point group to which the molecule belongs then its value is nonzero (that is, an integral is nonzero if the direct product of the integrand contains a totally symmetric representation, A_1) and the transition is allowed and if the integral is zero (does not equal or contain A_1), the transition is forbidden [24-26]. However, in order to have an allowed transition at least one of the following integrals (1.5) to (1.7) must be non-zero.

$$\mu_{eg} = \langle \psi_e | \mu_x | \psi_g \rangle \quad \text{.....(1.5)}$$

$$\mu_{eg} = \langle \psi_e | \mu_y | \psi_g \rangle \quad \text{.....(1.6)}$$

$$\mu_{eg} = \langle \psi_e | \mu_z | \psi_g \rangle \quad \text{.....(1.7)}$$

If all of the above integrals are zero, then the transition is forbidden. Spin-orbit and vibronic coupling may introduce some allowedness to these forbidden transitions.

1.1.3.1 Selection Rules

There are two selection rules governing transitions between electronic energy levels in transitional metal complexes;

1. The orbital rule (laporte), $\Delta l = \pm 1$.

If the molecule has the center of symmetry (g for gerade or u for ungerade), electronic transitions conserving either symmetry or asymmetry with respect to an inversion center are forbidden. That is $g \rightarrow g$ or $u \rightarrow u$ are forbidden, whereas $g \rightarrow u$ or $u \rightarrow g$ are allowed. d and s orbitals are g whereas p orbitals are u. However, ligand field transitions in a strict O_h symmetry are forbidden and are therefore weak. In contrast, tetrahedral complexes lack the center of symmetry and therefore the electronic transitions become allowed.

2. The spin rule, $\Delta S = 0$.

Transitions between states of different multiplicity are spin-forbidden. Therefore, allowed transitions must involve the promotion of electrons without a change in their spins. Thus singlets to triplets or triplets to singlets transitions are forbidden or very weakly allowed.

These rules can relax due to vibronic (the interaction between electronic and vibrational modes) and spin orbit coupling as well as low symmetry mixing of states leading to complicated spectra. When the molecule vibrates, the center of symmetry is removed. Ligands around the central metal ion can also disrupt or lower its perfect symmetry and the laporte selection rule is not applied rigorously leading to allowedness of forbidden transitions. However, laporte and spin forbidden bands are more intense in transition metal complexes of metalloproteins due to larger spin orbit coupling and low symmetry distortions which result into mixing of the states. In general forbidden transitions are much weaker than the allowed transitions (see Table 1.1) [27].

Table 1.1: Allowed and forbidden transitions.

Band type	ε ($M^{-1}cm^{-1}$)
Spin forbidden	< 1
Laporte forbidden	100 – 200

Larporte allowed	Ca. 500
Symmetry allowed	1000 - 50000

1.1.2.4 Electron Paramagnetic Resonance Spectroscopy (EPR)

Electron paramagnetic resonance (EPR) spectroscopy is one of the most important experimental techniques of studying compounds containing unpaired electrons which include organic radicals, inorganic radicals and triplet states. EPR has been used to investigate kinetics, mechanisms and structures of paramagnetic species. Typical applications encompass biological systems, paramagnetic defects in extended solids, transition metal complexes, or simple organic radicals (e.g., in zeolites) [29]. The theory of EPR spectroscopy is well explained elsewhere [24,26,30-35]. In EPR spectroscopy, a fixed radiation of microwave frequency (υ) (≈ 9 GHz for X-band and 35 GHz for Q-band) is absorbed by molecules, ions, or atoms possessing electrons with unpaired spins (EPR samples can be single crystals, solutions, powders and frozen solutions). The total spin is then perturbed by the application of an external magnetic field H that produces a Zeeman splitting equal to $g\beta H$. When the scanning magnetic field results in a Zeeman splitting equal to the fixed microwave energy, absorption occurs (Equation 1.8 and Figure 1.2).

$$g\beta H = h\upsilon \ldots\ldots\ldots\ldots\ldots\ldots\ldots\ldots\ldots\ldots\ldots\ldots\ldots\ldots\ldots\ldots\ldots\ldots \text{(1.8)}$$

In equation 1.8 above, g is the quantity of experimental and theoretical interest called the g-value (or g-tensor or g-factor) (for a free electron, g has the value

2.0023193) that characterizes the position of a resonance signal, β is a constant called the Bohr magneton equal to 4.67 x 10^{-5} cm^{-1}/gauss, H is the applied magnetic field, h is the planck's constant (6.626 x 10^{-34} Js^{-1}); hυ = 0.30 cm^{-1} for X-band and 1.16 cm^{-1} for Q-band. For S = ½ spin system, the magnetic components are m_s = +1/2 and m_s = -1/2.

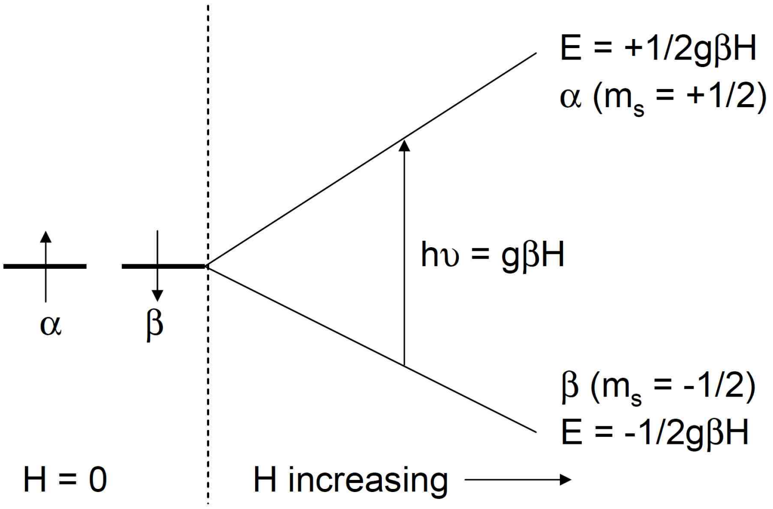

Figure 1.2: Increasing Zeeman splitting with increasing magnetic field for S = ½ system for fixed input microwave frequency (hυ).

In the presence of an external magnetic field, the electron's magnetic moment aligns itself either parallel (m_s = -1/2) or anti-parallel (m_s = +1/2) to the field, each alignment having its specific energy. The parallel alignment corresponds to the lower energy state and the anti-parallel alignment to the higher energy state and these two are separated by gβH (Figure 1.2).

The g-tensor. The knowledge of the g-tensor can give information about a paramagnetic center's electronic structure. This parameter is characteristic of the sample and is something to be determined experimentally [31]. When the paramagnetic species exhibits anisotropy, the spatial dependence of the g-tensor is represented by a 3x3 matrix referred to as a g-matrix. It is normally represented by three diagonal principle values, g_x, g_y and g_z of the general coordinate system, (x, y, z) or $g_\perp$ and $g_\parallel$ in which the off-diagonal terms of the g-matrix are zero.

$$g = \begin{vmatrix} g_x & 0 & 0 \\ 0 & g_y & 0 \\ 0 & 0 & g_z \end{vmatrix} \text{ or } g = \begin{vmatrix} g_\perp & 0 & 0 \\ 0 & g_\perp & 0 \\ 0 & 0 & g_\parallel \end{vmatrix} \ldots\ldots\ldots\ldots\ldots\ldots\ldots\ldots\ldots\ldots\ldots\ldots\ldots\ldots\ldots\ldots(1.9)$$

For spherical or cubic symmetries, the paramagnetic center under consideration results into isotropic spectra ($g_x = g_y = g_z$). For paramagnetic centers with lower symmetry (as it is the case in these investigations for Mo, Co and Fe in xanthine oxidase, luxS and iNOS enzymes respectively), anisotropic effects in g-values are manifested in the frozen solutions spectra ($g_x = g_y \neq g_z$ for axial distortions and $g_x \neq g_y \neq g_z$ for rhombic distortions). However, for these lower symmetry systems, the solution spectra appear as isotropic because the anisotropic effects are averaged to zero because of the rapid rotation of the molecules. All these have general forms of the Zeeman spin Hamiltonian in the magnetic field as given by equations (1.10), (1.11) and (1.12) for cubic, axial and rhombic symmetries respectively if only the g-tensor is the contribution to the total Hamiltonian.

$$H_z = \beta H . g . \overrightarrow{S} \quad \ldots\ldots (1.10)$$

$$H_z = g_{\parallel} \beta H_z \overrightarrow{S_z} + g_{\perp} \beta (H_x \overrightarrow{S_x} + H_y \overrightarrow{S_y}) \quad \ldots\ldots (1.11)$$

$$H_z = \beta (g_x H_x \overrightarrow{S_x} + g_y H_y \overrightarrow{S_y} + g_z H_z \overrightarrow{S_z}) \quad \ldots\ldots (1.12)$$

In general, experimentally determined g values commonly deviate from g for a free electron (g_e) primarily due to coupling of the spin angular momentum and orbital angular momentum termed as spin-orbit coupling. This effect is much greater in many transition metal ion complexes than in organic free radicals. The spin orbital angular momentum is oriented with the field H whereas the orbital angular momentum which is associated with the electrons moving in the molecular orbitals is locked to the molecular wavefunction. For spherical symmetry (an isolated atom) when the orbital and spin angular momenta are good quantum numbers, the magnetic moment of the atom is given by the ground state expectation value of the magnetic moment operator;

$$\overrightarrow{\mu} = -\beta (\psi_g \left| \overrightarrow{L} + g_e \overrightarrow{S} \right| \psi_g) \quad \ldots\ldots (1.13)$$

where β is the Bohr magneton and g_e ≈ 2, the electronic g-factor. However, molecules that have odd number of electrons which include transition metals such as Mo(V), tetrahedral-Co(II) and Fe(III) that have unpaired d or f electrons have a permanent magnetic moment. In the presence of a magnetic field, the degenerate ground state splits according to the Zeeman Hamiltonian;

$$H_z = \overrightarrow{\mu} . \overrightarrow{H} \quad \ldots\ldots (1.14)$$

Combining equations (1.13) and (1.14) gives a Zeeman operator which is a function of the total orbital angular momentum operator $\vec{L}$ and the total spin angular momentum operator $\vec{S}$ (equation 1.15) both operating on the ground state wavefunction (ψ_g).

$$H_Z = \beta H \langle \psi_g | \vec{L} + g_e \vec{S} | \psi_g \rangle \text{ .... (1.15)}$$

However, if the ground state of the molecule has no orbital angular momentum associated with it, field induced mixing in of an excited state that does have orbital angular momentum can lead to g anisotropy via spin-orbit operator $\lambda \vec{L}.\vec{S}$. The Hamiltonian for the system with spin-orbit coupling in a magnetic field is given by;

$$H = \beta H \langle \psi_g | \vec{L} + g_e \vec{S} | \psi_g \rangle + \lambda \vec{L}.\vec{S} \text{ .... (1.16)}$$

Where the first term is the Zeeman Hamiltonian, the second term is the spin orbit coupling term (λ is the spin orbit coupling constant for a particular shell in a particular atom = ± $\xi/2S$; $\lambda = +\xi/2S$ for a shell that is less than half-filled whereas $\lambda = -\xi/2S$ for a shell that is more than half filled, S is the spin system of the transition metal ion and the symbol ξ represents the one electron spin-orbit coupling and is dependent upon the effective nuclear charge and the average distance of the electron from the nucleus (equation 1.17)) [26,30,31].

$$\xi = \frac{Z_{eff} e^2}{2m^2c^2.\langle r^3 \rangle} \text{……………………………………………………….(1.17)}$$

Consider the spin-orbit coupling operator $\lambda \vec{L}.\vec{S}$. Since the electron spin of the ground state and the excited state must be the same, then, the two states will mix via spin-orbit coupling if the integral;

$$I = \int \psi_{ground} \vec{L}.\psi_{excited}\, d\mathrm{T} \neq 0 \text{ (or } I = \langle \psi_{ground} | \vec{L} | \psi_{excited} \rangle \neq 0 \text{)………….(1.18)}$$

However, in group theory, the operator $\vec{L}(= \vec{L}_x + \vec{L}_y + \vec{L}_z)$ possesses the symmetry properties of rotations about the three Cartesian axes. If its irreducible representation is $\Gamma_{R_{x,y,z}}$, then equation (1.18) may be written as;

$$I = \Gamma_{\psi_{ground}}.\Gamma_{R_{x,y,z}}.\Gamma_{\psi excited} \text{……………………………………………….(1.19)}$$

The integral I is non zero only if the direct product $\Gamma_{\psi_{ground}}.\Gamma_{R_{x,y,z}}.\Gamma_{\psi excited}$ includes Γ_{A_1}, a totally symmetric representation of the group to which the molecule belongs.

The amount of orbital mixing for a single electron in a non-degenerate d orbital (S = ½) along any direction, x, y or z depends on both the spin-orbit coupling constant ξ and the energy gap $\Delta = E(0) - E(n)$ between the ground state and the "mixed in" excited state arising from the first order perturbation theory, equations (1.20);

$$|+\rangle = |0, \alpha\rangle + \sum_n \frac{\langle n | \xi \vec{L}.\vec{S} \,|\, 0, \alpha \rangle}{E(0) - E(n)} |n\rangle \text{ and } |-\rangle = |0, \beta\rangle + \sum_n \frac{\langle n | \xi \vec{L}.\vec{S} \,|\, 0, \beta \rangle}{E(0) - E(n)} |n\rangle \text{……… (1.20)}$$

Where 0 indicates the ground state whereas α and β designate m_s = +1/2 and -1/2 and n is the number of the excited states [30]. These wavefunctions are then used to calculate the matrix elements of the Zeeman Hamiltonian in equation ((1.16), the first term) and then compared with the corresponding matrix elements of the spin Hamiltonian, $H_s = \beta H.g.\vec{S}$ for evaluation of the principle components of the effective g-tensor. When the shell is more than half filled (that is, $\lambda = -\xi/2S$), the spin-orbit coupling effects result into g-values > g_e (equation 1.21) whereas g-values < g_e (equation 1.22) results from spin-orbit coupling effects on the shell which is less than half filled ($\lambda = +\xi/2S$).

$$g = g_e + n.\xi/\Delta \quad \text{………………………………………………………} \ (1.21)$$

$$g = g_e - n.\xi/\Delta \quad \text{………………………………………………………} (1.22)$$

Where n is the orbital mixing number that depends on which of the d orbitals mix according to the magic pentagon (Figure 1.3).

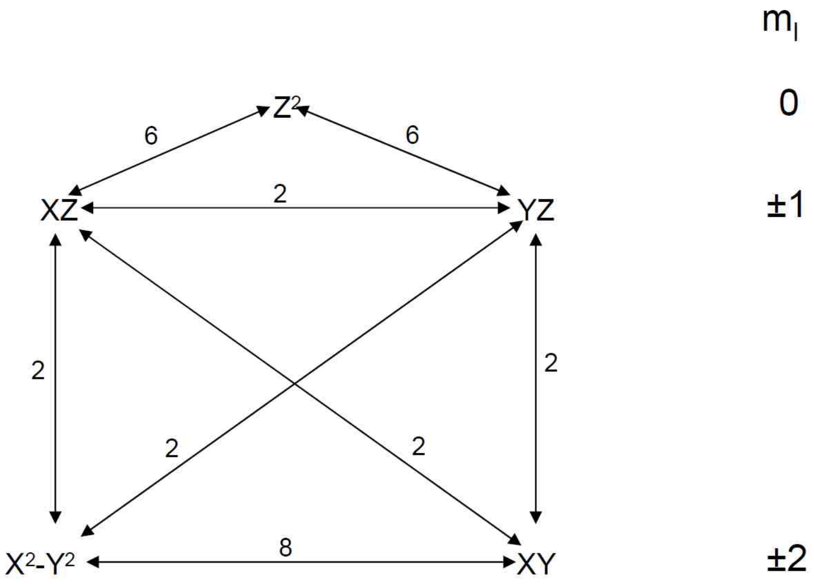

Figure 1.3: The “magic pentagon” for evaluating n of equations (1.18) and (1.19) which is the number on the line linking the orbitals which mix by spin-orbit coupling.

The mixing of the ground state with other excited state orbitals by means of spin-orbit coupling depends on the orientation of the molecule with respect to the applied magnetic field H. However, different g-values are observed in different directions in frozen solutions EPR spectra. However, the above treatment is from a perturbation assumption (first order perturbation theory) and is valid only when $n\xi/\Delta$ is small compared to the diagonal Zeeman elements. However, a term proportional to $\xi^2/\Delta E^2$ is added when second order perturbation theory is pertinent.

When an electron is residing in a d_{xy} ground state orbital, only electron circulation into a $d_{x^2-y^2}$ orbital would give orbital angular momentum along the z-axis, thus the quantity g_z (equation 1.23) has contributions only from d_{xy} and $d_{x^2-y^2}$. The "magic pentagon" connects these two orbitals by n equal to 8;

$$g_z = g_e + \frac{8\xi}{E_{xy} - E_{x^2-y^2}} \quad \text{……………………………………………(1.23)}$$

g_x and g_y have non zero matrix elements only when ground state $|0\rangle$ and the excited state $|n\rangle$ differ by $\Delta m_l = 1$ which gives;

$$g_x = g_e + \frac{2\xi}{E_{xy} - E_{xz}} \quad \text{……………………………………………(1.24)}$$

$$g_y = g_e + \frac{2\xi}{E_{xy} - E_{yz}} \quad \text{……………..…………………………………..(1.25)}$$

The formulae in equations (1.23) to (1.25) tell us what orbitals permit electron circulations about the respective axes; that is $d_{x^2-y^2}$ and d_{xy} about z, d_{xy} and d_{xz} about x and d_{xy} and d_{yz} about y [12,26].

For transitional metal complexes that have delocalized systems, the above treatment which considered only the free ion and then took account of spin-orbit coupling is inadequate. However, the effects of covalent bonding in these delocalized complexes have been taken into account and the g-tensor contribution analyzed within the framework of crystal field by taking into account the spin-orbit coupling as;

$$g_{\alpha\beta} = g_e \delta_{\alpha\beta} + \frac{2\lambda \langle d_0 | l_\alpha | d_n \rangle \langle d_n | l_\beta | d_0 \rangle}{E(0) - E(n)} \text{……………………………}(1.26)$$

Where d_0 is the singly occupied orbital in the ground state configuration, as determined by the crystal field whereas d_n is one of the other d-orbitals which may be empty or full in the ground configuration. Evaluation of the matrix elements in equation (1.26) has been shown to give rise to a simple numerical factor, $a_{\alpha\beta}$ and reduces equation (1.26) to

$$g_{\alpha\beta} = g_e \delta_{\alpha\beta} + \frac{2\lambda a_{\alpha\beta}}{\Delta_{0,n}} \text{……………………………………..………}(1.27)$$

However, one can use the value of $\Delta_{0,n}$ observed in the electronic absorption spectrum of the transition metal ion in the "assumed" crystal field and the observed values of the elements of the g-tensor to compute the value of λ and then compare this value with the value obtained from the spectrum of the free ion [31].

Hyperfine tensor Describe the magnetic interactions of electrons and the nucleus characterized by the hyperfine coupling constant A measured in MHz or cm^{-1}. For one magnetic nucleus, the Hamiltonian for the hyperfine interaction can be written as

$$H_{hf} = I.A.\vec{S} \text{………………………………………………………….}(1.28)$$

The A-tensor is centered from g-tensor, however, for any molecule with an axis of trigonal or higher symmetry, the A-tensor can as well be written in diagonal form as

$$A = \begin{vmatrix} A_\perp & 0 & 0 \\ 0 & A_\perp & 0 \\ 0 & 0 & A_\parallel \end{vmatrix} \quad \ldots\ldots\ldots\ldots\ldots\ldots\ldots\ldots\ldots\ldots\ldots\ldots\ldots\ldots\ldots\ldots\ldots\ldots\ldots\ldots(1.29)$$

And the Hamiltonian as;

$$H_{hf} = A_\parallel \vec{S}_z I_z + A_\perp(\vec{S}_x I_x + \vec{S}_y I_y) \ldots\ldots\ldots\ldots\ldots\ldots\ldots\ldots\ldots\ldots\ldots\ldots\ldots\ldots\ldots(1.30)$$

The 3x3 hyperfine tensor can be separated into its isotropic (A_{iso}) and anisotropic (A_{dip}) components (equation 1.31).

$$A = \begin{vmatrix} A_\perp & 0 & 0 \\ 0 & A_\perp & 0 \\ 0 & 0 & A_\parallel \end{vmatrix} = \begin{vmatrix} A_{iso} & 0 & 0 \\ 0 & A_{iso} & 0 \\ 0 & 0 & A_{iso} \end{vmatrix} + \begin{vmatrix} -A_{dip} & 0 & 0 \\ 0 & -A_{dip} & 0 \\ 0 & 0 & +2A_{dip} \end{vmatrix} \ldots\ldots (1.31)$$

The isotropic part (A_{iso}) which is also called the Fermi contact term reflects the spin density at the magnetic nucleus to which only the s electrons significantly contribute. The anisotropic part or dipolar (A_{dip}), that occurs for p, d electrons, yields additional information about the local environment of the paramagnetic center. The hyperfine structure for A_{iso} if it is the only contribution is given by;

$$A_{iso} = \frac{8\pi}{3h} g_e \beta\, g_N \beta_N |\psi(0)|^2 \ldots\ldots\ldots\ldots\ldots\ldots\ldots\ldots\ldots\ldots\ldots\ldots\ldots\ldots\ldots\ldots(1.32)$$

Here β is the Bohr magneton, β_N is the nuclear magneton, g_N is the g value of the nucleus and $|\psi(0)|^2$ is the spin density at the nucleus expressed in units of cm^{-3} or $a.u^{-3}$. On the other hand, the hyperfine structure for A_{dip} [26] as the only contribution to the ligand hyperfine interaction is given by;

$$A_{dip} = \frac{g_e g_N \beta\beta_N}{a^3} \quad \ldots\ldots(1.33)$$

Here, a is the metal ligand distance derived by considering metal-ligand distance is large compared to the metal nucleus-electron distance. However, if the tensor axes are mutually parallel and one axis on each are coincident, we have;

$$A_{dip} \| = \frac{2g_N \beta\beta_N g_\|}{a^3} \quad \ldots\ldots(1.34)$$

$$A_{dip} \perp = -\frac{g_N \beta\beta_N g_\perp}{a^3} \quad \ldots\ldots(1.35)$$

However, experimentally, A_{iso} may be obtained from solution EPR measurements or calculated from the average of anisotropic hyperfine tensor observed in frozen EPR measurements. From A_{iso} and the observed A_{aniso}, the A_{dip} can be computed. The p or d and s character of the orbital on the ligand with which the unpaired electron is interacting may give information about the hybridization of the ligand orbital.

Generally, the hyperfine tensor is controlled by the nature of the ground state wave function. In contrast, the g-tensor reflects also energies and character of the excited states. Both of these are sensitive to the local metal coordination [32].

However, if only the g- and A-tensors contribute to the total Hamiltonian, then the Hamiltonian for the axial symmetry that comprises the Zeeman and the hyperfine is given by;

$$H = g_{\parallel}\beta H_z \vec{S}_z + g_{\perp}\beta(H_x \vec{S}_x + H_y \vec{S}_y) + A_{\parallel}\vec{S}_z I_z + A_{\perp}(\vec{S}_x I_x + \vec{S}_y I_y) \text{ ……………… } (1.36)$$

Zero-field splitting (D and E tensors) Zero-field splitting (zfs) is the removal of spin microstate degeneracy for paramagnetic systems with S > 1/2 in the absence of an applied field. In transition metals, the spin degeneracy is removed as a consequence of dipolar interactions (spin-spin interactions), spin-orbit coupling and/or a low symmetry crystal field [26]. Zero-field splitting appears as a small energy gap of a few cm^{-1} between the spin doublets ($\pm m_s$) energy levels of the ground state (Figure 1.4). For *odd* electron systems where an EPR spectrum should be obtainable (For example; $S = 3/2$ and $S = 5/2$ with $m_s = [\pm 1/2,\ \pm 3/2]$ and $m_s = [\pm 1/2,\ \pm 3/2,\ \pm 5/2]$ respectively, which are degenerate), axial zfs (the “D” zfs parameter) removes the microstate degeneracy of m_s and produces Kramer’s doublets. Rhombic zfs (the “E” zfs parameter) splits the Kramer’s doublets. The energy barrier separating the Kramer’s doublets $\pm m_s$ is equal to $|S^2 D|$. For $S = 3/2$, the Kramer’s doublets $m_s = \pm 1/2$ and $m_s = \pm 3/2$ are separated by $2D$ whereas for $S = 5/2$, the Kramer’s doublets $m_s = \pm 1/2$ and $m_s = \pm 5/2$ are separated by $6D$ which means the separation between Kramer’s doublets

$m_s = \pm 3/2$ and $m_s = \pm 5/2$ is $4D$. These energy spacings between these Kramer's doublets are depicted in Figure 1.4.

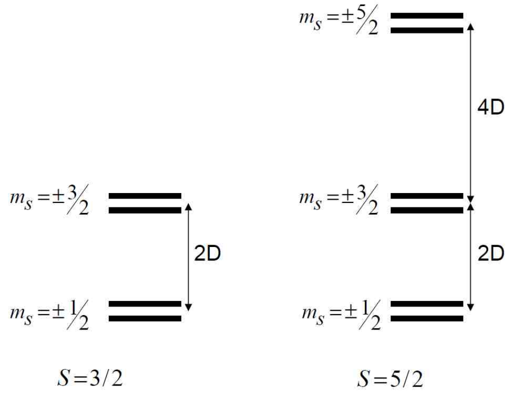

Figure 1.4: Energy level spacing showing spin systems for $S = 3/2$ and $S = 5/2$ which have $D > 0$. However, for systems with $D < 0$, the spin microstates $\pm m_s$ are reversed.

Molecules which have zero field splitting have an additional component (equation 1.37) which is added to the spin Hamiltonian of $S = 1/2$ molecules to describe it.

$$H_D = \vec{S}.D.\vec{S} \quad \text{……………………………………………………………………..(1.37)}$$

In equation (1.37), the D tensor arises from spin-spin interaction on a single paramagnetic center and has been shown to be a symmetric traceless tensor (that is, $D_{xx} + D_{yy} + D_{zz} = 0$). If the principle axes of the D and g tensors coincide, then the off diagonal tensor elements in equation (1.37) are zero which implies;

$$H_D = D_{xx} \vec{S}_x^{\,2} + D_{yy} \vec{S}_y^{\,2} + D_{zz} \vec{S}_z^{\,2} \quad \text{……………………………………………(1.38)}$$

The zfs parameters D and E are have also been defined by equations (1.39) and (1.40)

$$D = D_{zz} - \tfrac{1}{2}(D_{xx} + D_{yy}) \quad \text{…………………………………………………..(1.39)}$$

$$E = \tfrac{1}{2}(D_{xx} - D_{yy}) \quad \text{……………………………………………………..(1.40)}$$

Equations (1.39) and (1.40) clearly show that, $E/D \leq 1/3$. Substitution of equations (1.39) and (1.40) into (1.38) gives equation (1.41);

$$H_D = D\vec{S}_z^{\,2} + E(\vec{S}_x^{\,2} - \vec{S}_y^{\,2}) + \tfrac{1}{2}(D_{xx} + D_{yy})\vec{S}^{2} \quad \text{…………………………(1.41)}$$

The last term in $\vec{S}^{2}$ shifts all the energy levels equally and can be omitted since we are interested in the energy difference. This term is normally replaced by its eigen value, $-\tfrac{1}{3}DS(S+1)$ which reduces the Hamiltonian to;

$$H_D = D\left\{\vec{S}^{2}{}_{z} - \tfrac{1}{3}S(S+1)\right\} + E(\vec{S}_x^{\,2} - \vec{S}_y^{\,2}) \quad \text{…………………………………(1.42)}$$

Equation (1.42) can be written by using raising and lowering operators (shift operators (1.43) and (1.44)) to give 1.45.

$$S_+ = S_x + iS_y \quad \text{……………………………………………………………..(1.43)}$$

$$S_- = S_x - iS_y \quad \text{………………………………………………………………(1.44)}$$

$$H_D = D\left\{\vec{S}^{2}{}_{z} - \tfrac{1}{3}S(S+1)\right\} + \tfrac{1}{2}E(\vec{S}_+^{\,2} - \vec{S}_-^{\,2}) \quad \text{……………………………(1.45)}$$

However, the Hamiltonian in equation (1.45) can be solved to give the matrix elements in the $|S, M_s\rangle$ basis for $S > \frac{1}{2}$ and obtain the eigen values for the zero field energies [30,31]. The experimental D and E for transition metals contain the effects of spin-spin interaction, spin-orbit coupling and low symmetry crystal field in the total Hamiltonian (equation 1.46) that comprises the Zeeman, the hyperfine and the zero-field splitting terms. For all g-, A- and D-tensors' contributions, then the Hamiltonian is;

$$\begin{aligned} H = {} & g_{\parallel}\beta H_z \vec{S}_z + g_{\perp}\beta(H_x \vec{S}_x + H_y \vec{S}_y) + A_{\parallel}\vec{S}_z I_z + A_{\perp}(\vec{S}_x I_x + \vec{S}_y I_y) + \\ & D\left\{\vec{S}^2_z - \tfrac{1}{3}S(S+1)\right\} + E(\vec{S}_x^{\,2} - \vec{S}_y^{\,2}) \end{aligned} \quad \text{……..(1.46)}$$

The spin Hamiltonian parameters g, A, D and E are easily obtained by computer simulations. Figure 1.5 illustrates the Hamiltonian associated with these terms for D > hυ. Spin-orbit coupling and ligand field distortion are paramount in giving rise to zero field splitting compared to spin-spin interaction in transition metals. The spin-orbit coupling giving rise to zfs can either be in-state, originating from the symmetry of the ground state wavefunction or out-of state arising from spin-orbit mixing of certain excites states into the ground state. In cases where the ground state wavefunction is totally symmetric (For example $^3A_{2g}$ in O_h-d^8), spin-orbit coupling alone does not break the spin degeneracy of the ground state wavefunction (no zfs) as it results into a T_{2g} state which is also degenerate. However, ligand field distortion and spin orbit mixing of the excited state into the ground state breaks the degeneracy of the ground state resulting into zfs. The details of this, is discussed in chapter 3 for tetrahedral Co(II)-d^7.

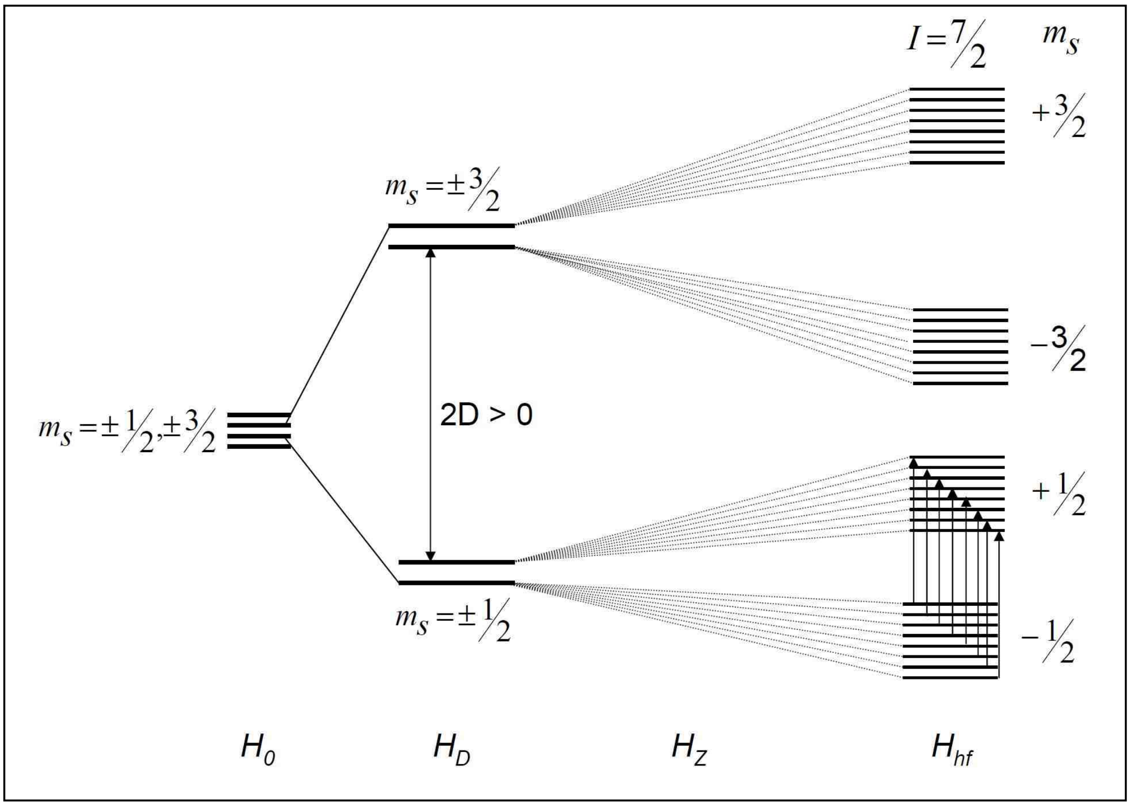

Figure 1.5: Splitting of the ground state energy levels for Co(II)-d^7 in a magnetic field ($D > h\upsilon$).Selection rules are $\Delta m_s = \pm 1$ and $\Delta m_I = 0$. Thus for I =7/2, each m_s has m_I = 2I + 1 = 8 hyperfine lines. These are m_I = -7/2, -5/2, -3/2, -1/2, 1/2, 3/2, 5/2 and 7/2 hyperfine lines.

1.1.2.3 Magnetic Circular Dichroism Spectroscopy (MCD)

Magnetic circular dichroism (MCD) spectroscopy measures the difference in absorption between left and right circularly polarized light (measured as the difference in extinction coefficients $\Delta\varepsilon = \varepsilon_{LCP} - \varepsilon_{RCP}$) induced in a sample by strong magnetic field oriented parallel to the direction of light propagation. This spectroscopic method has been proven to be extremely powerful in the analysis of the geometric and electronic structures of paramagnetic sites in biological systems, especially when coupled to electron paramagnetic resonance (EPR) [3,4,6,36-39]. However, it differs from EPR in the sense that EPR is based on resonance between spin states whereas MCD is based on wavelength dependent absorption of circularly polarized light to form excited electronic states. On the other hand, MCD and UV-vis absorption spectra of a molecular complex contain the same set of spectral bands, but bands shapes are different due to the effect of applied magnetic field and the use of differential absorbance intensity from the CD spectrometer which is used for measurement and this makes MCD a higher resolution technique than UV-vis absorption. The major applications have been in the field of transition metal ion cofactors of metalloproteins such as hemes, iron–sulfur clusters, cobalt and molybdenum [1,36,40]. The MCD selection rules are $\Delta m_J = \pm 1$. However, for right circular polarized (RCP) light the selection rule is $\Delta m_J = -1$, whereas for left circular polarized (LCP) light it is $\Delta m_J = +1$ and *J* is the total angular momentum. The total MCD intensity for a sample of randomly oriented molecules [37] can be written in the linear limit as;

$$\frac{\Delta\varepsilon}{E} = \frac{\varepsilon_{LCP} - \varepsilon_{RCP}}{E} = \frac{1}{dc}\frac{A_{LCP} - A_{RCP}}{E} = \gamma\beta H \left[(-\frac{\partial f(E)}{\partial E})\bar{A}_1 + (\bar{B}_0 + \frac{\bar{C}_0}{kT}) f(E) \right] \ldots\ldots(1.47)$$

Where $E = h\upsilon$ is the energy of the incident radiation, d is the path length, c is the concentration of the molecular species considered, γ is a collection of constants, β is the Bohr magneton, H is the magnetic flux density, $f(E)$ is a line shape function. Equation (1.47) shows that the MCD intensity is proportional to three different contributions, $\bar{A}_1$, $\bar{B}_0$ and $\bar{C}_0$ which are called Faraday terms [41], commonly designated as MCD A, B and C terms.

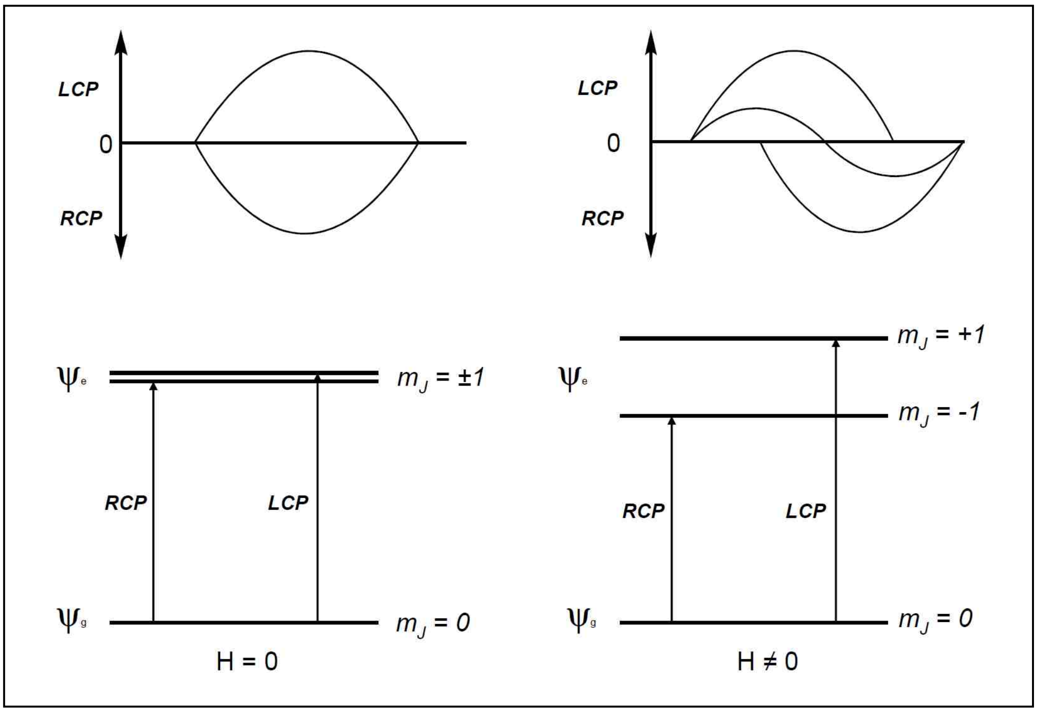

Figure 1.6: The origin of A term MCD intensity. The absorption of circularly polarized light is based on a transition from an orbitally non-degenerate ground state to an orbitally degenerate excited state within a magnetic field applied parallel to the axis of light propagation. However, when the field is zero (H = 0), the RCP and LCP light absorptions cancel each other resulting to no absorption. In the presence of an applied magnetic field (H ≠ 0), A derivative-shaped A term (right-top in Figure 1.8) is observed due to the Zeeman splitting of states and the

associated energy separation of bands absorbing RCP and LCP light based on the $m_J = \pm 1$ selection rule.

Analysis of the MCD spectra is based on an estimation of the magnitudes of these terms in equation (1.47) with the basic information derived from the Zeeman splitting of the absorption bands for LCP and RCP light for A term, the field-induced mixing of zero-field states for B term and the Zeeman splitting based ground state population adjustment for C term. However, the A-term corresponds to a signal with a derivative band shape whereas B and C terms both show an absorption band shape in MCD. The MCD C-term intensity is temperature dependent whereas the A and B terms are temperature independent. The origins of the A, B and C term mechanisms are illustrated by Figures 1.6, 1.7 and 1.8.

From Figure 1.6 above, the A term MCD intensity arises from a Zeeman splitting of an orbitally degenerate excited state resulting into a distinctive first derivative shaped band originating from the energy separation of the individual RCP and LCP transitions. It has also been shown that the A term intensity is based on the relative magnitudes of both the spin and orbital angular momenta of electrons within the ground (ψ_g) and excited (ψ_e) states, described by equation (1.48) [36,37,41].

$$A = \frac{1}{d_{\psi_g}} \sum \beta(\psi_e \left| \vec{L} + g_e \vec{S} \right| \psi_e) - \beta(\psi_g \left| \vec{L} + g_e \vec{S} \right| \psi_g)([m_{-1}{}^{\psi_g \psi_e}]^2 - [m_{+1}{}^{\psi_g \psi_e}]^2 \qquad \text{..........(1.48)}$$

Where d_{ψ_g} relates the degree of degeneracy of the excited states, $m_{-1}^{\psi_g\psi_e}$ and $m_{+1}^{\psi_g\psi_e}$ are the electric dipoles elements associated with the absorption of LCP and RCP light respectively.

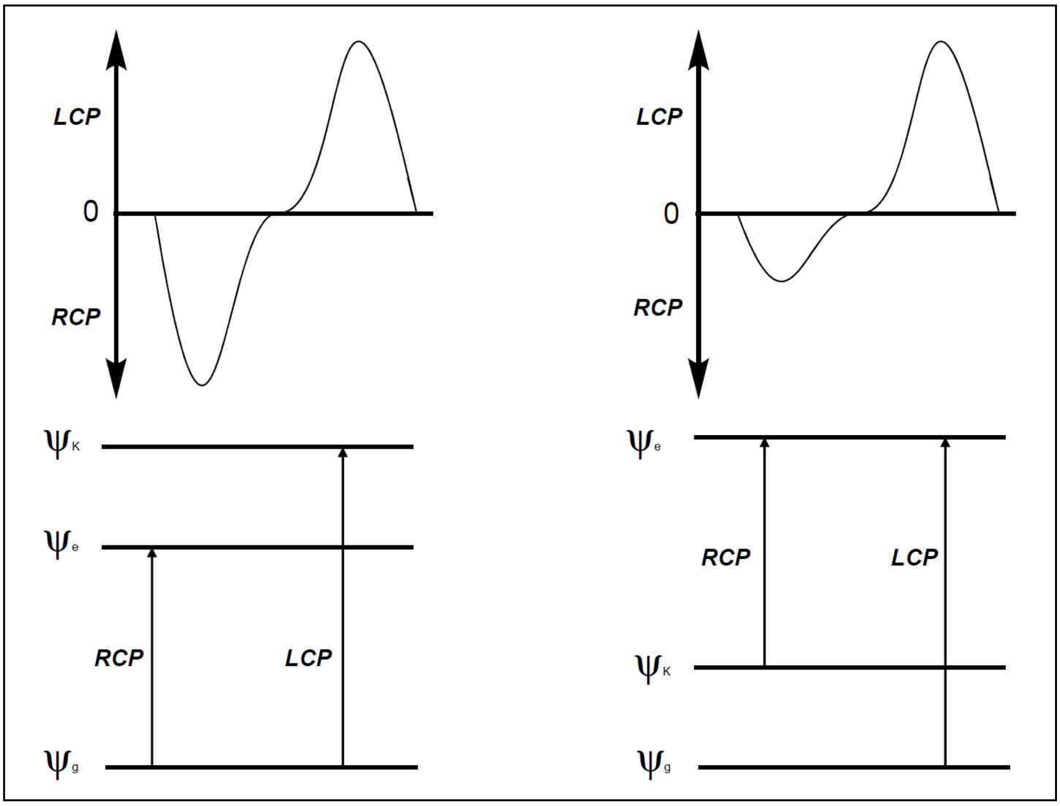

Figure 1.7: The origin of B term MCD intensity. The splitting of the negative and positive Gaussian shaped MCD signals is determined by the energy separation of the RCP and LCP light absorption bands that arise within the applied field due to field induced mixing of states via a magnetic dipole transition moment.

The Gaussian shaped, B term arises from second order effects where the magnetic field induced mixing of the excited state ψ_e with an energetically close intermediate state ψ_K occurs. As the energy gap between the excited state ψ_e and the intermediate state ψ_K decreases, the B term signal gains intensity and an A term, which is a derivative shaped absorption signal is generated. Alternatively, field induced mixing is also possible between the ground state ψ_g and an intermediate state ψ_K which results into a temperature dependent B term (Figure 1.7). B term signals dominate the MCD spectrum when there is no three fold or higher rotation axis, since there are no orbitally degenerate states that can be split due to the Zeeman effect. They are also present in high symmetry complexes' spectra but bear considerably less intensity than the A and C terms due to energy gap dependence between ψ_e and ψ_K ($\Delta E_{\psi_e \psi_K}$). The B term intensity in the absence of significant field induced mixing between the ground and excited states are given by equation (1.49) [41].

$$B = \frac{2}{d_{\psi_g}} \Re e \sum \frac{\beta(\psi_e | \vec{L} + g_e \vec{S} | \psi_K)}{\Delta E_{\psi_K \psi_e}} ([m_{-1}{}^{\psi_g \psi_e}][m_{+1}{}^{\psi_K \psi_g}] - [m_{+1}{}^{\psi_g \psi_e}][m_{-1}{}^{\psi_K \psi_g}]) \ldots\ldots. (1.49)$$

The most important mechanism for paramagnetic ions is the temperature dependent C-term. The MCD C-term intensity arises from a Boltzmann population of the degenerate ground state, which is split in the magnetic field due to the Zeeman effect and therefore shows a strong $1/kT$ temperature dependence (Equation 1.47), distinguishable from the B term temperature dependence.

Generally, degenerate ground states are due to spin degeneracy and hence, only paramagnetic compounds exhibit MCD C-term signals.

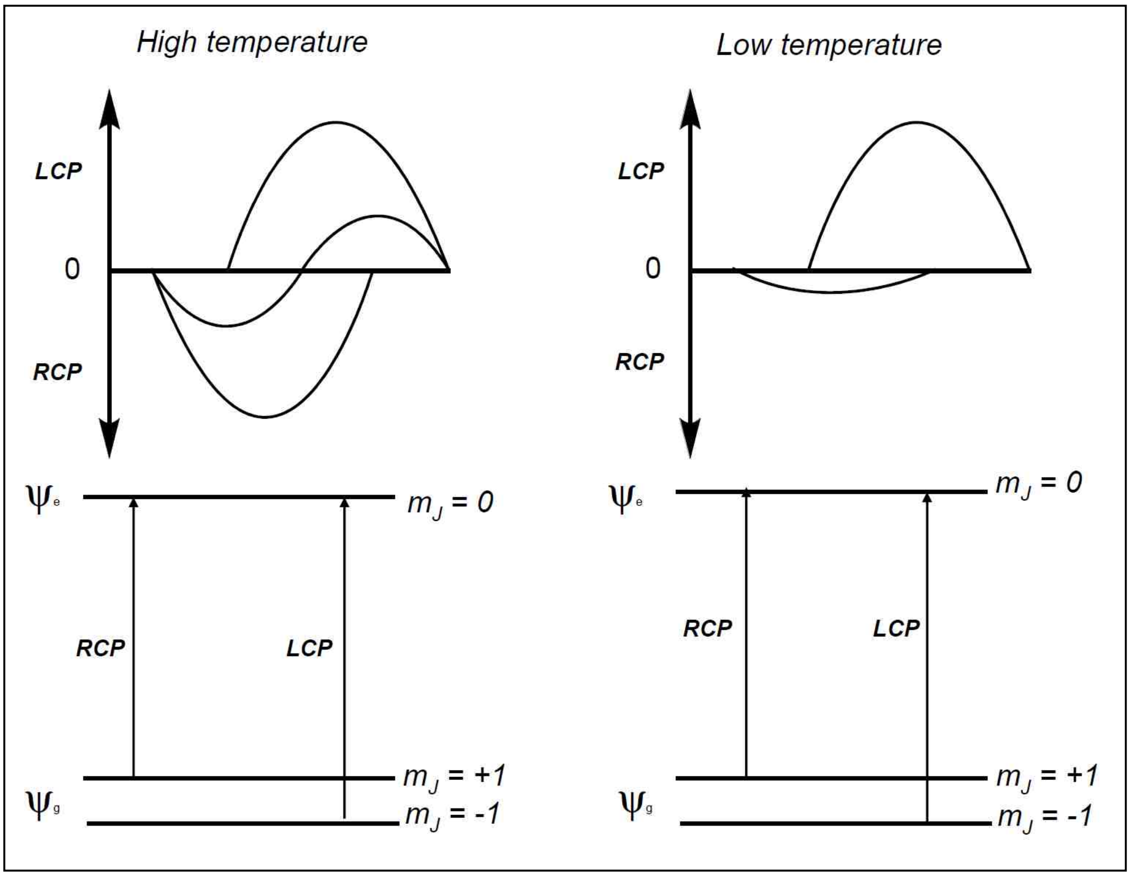
High temperature
Low temperature
LCP
0
RCP
LCP
0
RCP
ψe
$m_J = 0$
RCP
LCP
$m_J = +1$
ψg
$m_J = -1$
ψe
$m_J = 0$
RCP
LCP
$m_J = +1$
ψg
$m_J = -1$

Figure 1.8: The origin of C term MCD intensity. The C term MCD signal arises due to a transition from an orbitally degenerate ground state to an orbitally non-degenerate excited state within a magnetic field applied parallel to the axis of light propagation.

At very low temperatures and high applied magnetic fields a more intense symmetric Gaussian shaped C term signal is observed and the total MCD signal intensity is attributed to the Boltzmann population of the lowest Zeeman split state (~ 100% population). At higher temperatures, higher energy m_s states are populated and the measured C term intensity decreases. At very high temperatures, when the m_s components of the ground state become equally populated, an A-term like derivative-shaped band is observed (Figure 1.8). Closely spaced and oppositely signed B or C terms can also result into a derivative shaped band commonly designated as “pseuso A term”. Pseudo A terms arising from oppositely signed C terms are encountered for transitions originating from a Zeeman split ground state to spin-orbit split components of an orbitally degenerate excited state. These can also be distinguished from the “pseudo A terms” arising from B terms by their $1/kT$ temperature dependence. Temperature dependent B terms have a linear dependence on the magnetic field under conditions where the C terms exhibit magnetic saturation [41]. The C term intensity is given by equation (1.50).

$$C = \frac{1}{d_{\psi_g}} \sum \beta(\psi_g | \vec{L} + g_e \vec{S} | \psi_g)([m_{-1}{}^{\psi_g \psi_e}]^2 - [m_{+1}{}^{\psi_g \psi_e}]^2 \ldots\ldots\ldots\ldots\ldots\ldots\ldots\ldots (1.50)$$

In general, the basis for the observation of either an A or a C term signal in MCD spectra is the presence of orbital degeneracy either at the excited state or ground state respectively. However, for metal centers in low symmetry complexes, which are commonly encountered in biological environments, there is no orbital degeneracy since this requires at least a three fold symmetry axis. In this case, the spin-orbit coupling in low symmetry transition metal complexes is sufficiently large enough to mix states and thereby provide a mechanism for MCD intensity.

A typical example for this is explained in chapter 3 for the Co(II) substituted site in d^7 in LuxS.

Variable temperature variable field MCD(VTVH-MCD) This technique provides details of the ground state of paramagnetic centers in small molecule and metalloenzyme active sites. The technique yields information about the electronic and geometric structure in terms of g values, zero field splittings (D and E parameters) and transition polarizations [8,21,42,43]. It involves monitoring the magnetic saturation properties of discrete C term MCD bands as a function of temperature and magnetic field. In general, for a given C term MCD band, one varies the field between 0-7 Tesla at a fixed temperature and records the saturation magnetization data at that temperature. Additional scans are collected, in the same manner for at least four different temperatures in order to obtain a set of saturation curves. From equation (1.47) above, the C term MCD intensity is a function of H/T. However, this only holds if the Zeeman splitting ($g\beta H$) is $<< kT$, since the absorption of RCP and LCP light for C term MCD is a direct consequence of the Boltzmann population distribution over the Zeeman split sublevels of the ground state wavefunction. However, as H increases and/or T decreases, the MCD intensity eventually becomes H/T independent (no linear dependence) because the lowest Zeeman split component is dominantly populated and the C term intensity levels off to its saturation limit (system becomes fully saturated). Stephans [43] has shown that the MCD signal for isotropic $S = \frac{1}{2}$ ground state system ($m_S = \pm\frac{1}{2}$) varies with H/T as;

$$\frac{\Delta\varepsilon}{E} = A_{sat\lim} \tanh\left(\frac{g\beta H}{2kT}\right) f(E) \ldots\ldots\ldots\ldots\ldots\ldots\ldots\ldots\ldots\ldots\ldots\ldots\ldots\ldots\ldots\ldots(1.51)$$

Where $A_{sat\lim}$ is an MCD intensity scaling factor [43]. Thus, the ground state g value can be determined from a plot of MCD intensity versus the dimensionless variable $\beta H/2kT$ at fixed wavelength which is termed as the saturation or magnetization curve. However, complete analysis of the magnetization data for $S > \frac{1}{2}$ systems is complicated. A simulation program, which is based on the use of a standard spin Hamiltonian (equation 1.52), was developed by Neese [37] and was used in all the VTVH simulations reported in these investigations.

$$H = g_{\parallel}\beta H_z \vec{S}_z + g_{\perp}\beta(H_x \vec{S}_x + H_y \vec{S}_y) + D\left\{\vec{S}^2{}_z - \tfrac{1}{3}S(S+1)\right\} + E(\vec{S}_x{}^2 - \vec{S}_y{}^2) \ldots\ldots(1.52)$$

Here, the reference coordinate system diagonalizes the D tensor and leads to $0 \le E/D \le 1/3$. The principle coordinate system of the g matrix for $S = \frac{1}{2}$ systems is taken as a reference since there is no zero field splitting. However, the correct g values can be obtained from an EPR experiment and the zero field splitting parameters for $D > h\upsilon$ obtained from VTVH MCD simulations. The C term MCD intensity expression (equation 1.50) can be expanded to yield a relationship for transition polarizations and g values [44]. These are connected by the vector triple product in equation (1.53).

$$C\, \alpha\, g_x M_y M_z + g_y M_z M_x + g_z M_x M_y \ldots\ldots\ldots\ldots\ldots\ldots\ldots\ldots\ldots\ldots\ldots\ldots\ldots\ldots\ldots(1.53)$$

Equation (1.53) requires two mutually orthogonal transition dipoles that are in turn orthogonal to the magnetic field direction in order to observe C term MCD intensity.

Chapter 2

Spectroscopic and Electronic Structure Studies Probing the Reaction Coordinate of Xanthine Oxidase

2.1 Introduction

2.1.1 Xanthine Oxidase Family

Xanthine oxidase family comprises molybdenum-containing hydroxylases that catalyze the hydroxylation of carbon centers using oxygen derived from water, rather than from molecular oxygen, as the source of the oxygen atom incorporated into the product and generate rather than consume two reducing equivalents in the course of substrate hydroxylation (equations i and ii) [45-50].

$RH + H_2O \rightarrow ROH + 2H^+ + 2e^-$ ………………………………………….. (i)

$CO + H_2O \rightarrow CO_2 + 2H^+ + 2e^-$ ……………………..…………………….. (ii)

The members of this family include aldehyde oxidoreductase (AO), xanthine oxidoreductase (XO) and carbon monoxide dehydrogenase (CODH). This family is spread out within prokaryotic, eukaryotic and archaea organisms [47,51,52]. Both XO and AO have unusually broad range of substrate specificity ranging from purines to aromatic and aliphatic aldehydes. However, purines such as hypoxanthine and xanthine are catalyzed more efficiently by XO than AO. On the other hand, AO catalyzes more efficiently aldehydes than purines [53]. Unlike carbon monoxide dehydrogenase (CODH) that catalyzes the oxidation of carbon monoxide to carbon dioxide without cleavage of C-H bond (equation ii), aldehyde oxidoreductase and xanthine oxidoreductase catalyze the reaction that involves

C-H bond cleavage at the site of the substrate to be hydroxylated. However, CODH is included in the hydroxylase family even though the oxidation of CO to CO_2 does not represent a hydroxylation. This classification is based on its structural similarity with other members of the hydroxylase family. Full catalytic reactions for the enzymes in this family are depicted in equations (iii) to (vi).

_XO_; xanthine + $H_2O + O_2 \rightarrow$ Uric acid + $H_2O_2/O_2^{\bullet}$……………………..………. (iii)

XDH; xanthine + $H_2O + NAD^+ \rightarrow$ Uric acid + NADH………………………….. (iv)

_AO_; Aldehyde + $H_2O + O_2 \rightarrow$ Carboxylic acid + $H_2O_2/O_2^{\bullet}$………..…….……... (v)

CODH; $CO + H_2O + NAD^+ \rightarrow CO_2$ + NADH……...........……………………….. (vi)

AO enzyme is the oldest and most thoroughly studied but very little is known about the pathophysiological relevance of this enzyme todate [51]. However, its several substrates are of pharmacological and toxicological interests [51,54,55]. These include toxic metabolite of ethanol, acetaldehyde as well as antineoplastic and antiviral agents such as methotrexate, 6-mercaptopurine and famcyclovir [51,55]. AO oxidase also uses molecular oxygen as the final electron acceptor with the production of superoxide and/or hydrogen peroxide (equation (v)).

Xanthine oxidoreductase (XO) is the key enzyme involved in the catabolism of purines oxidizing hypoxanthine to xanthine and finally to uric acid. Under normal physiological conditions the enzyme is thought to be present as a dehydrogenase (XDH) but can be readily converted to an oxidase (XO) either reversibly by the oxidation of sulfhydryl residues which may easily occur during purification or irreversibly by limited proteolysis [45,52,56]. In the first case, the electrons deriving from the oxidation of the substrate reduce NAD+ to NADH (equation (iv)) whereas in the second case, electrons are transferred directly to molecular oxygen with the production of superoxide and/or hydrogen peroxide (equation (iii)) [56]. In humans, xanthine oxidoreductase (XO) has been implicated in hyperuricemia and its activity has been proposed to play a role in post ischemic or reperfusion damage in tissues which include intestine, heart, kidney, liver and brain [57]. However, the inhibition of this enzyme becomes a target of drug design, and understanding the mechanism of this enzyme is the key in the design process.

The easy conversion of mammalian XDH to XO during purification has also been hindering the direct mechanistic probe of physiological XDH and this problem has paved way to studies leading to the isolation of the similar dehydrogenase form of the enzyme from bacterial species. Recently, the isolation of XDH from *R. capsulatus* enabled detailed crystallographic and mechanistic understandings of the dehydrogenase form of xanthine oxidoreductase [58-60]. This enzyme has similar folds as mammalian XDH and is isolated purely as a dehydrogenase form and can not be converted to an oxidase form. This harbors its importance for understanding the physiological human dehydrogenase form that easily converts to an oxidase form during purification. Furthermore, mammalian XO has been extensively studied in terms of catalysis and enzyme inhibition by various substrates including aldehydes by EPR spectroscopy whereas no known inhibition EPR studies have been done on the bacterial XDH. In these investigations, we have done detailed inhibitory spectroscopic and computational studies of bovine XO and XDH from *R. capsulatus* and we have proposed new mechanistic insights for the formation of the xanthine oxidoreductase inhibited complex. Mutation studies of bacterial XDH have been done using EPR spectroscopy and have given the first spectroscopic probe of the second coordination sphere of xanthine oxidoreductase active site. Differences between the spectra of the wild type XDH and the mutant (E232A) suggest the participation of the amino acid residues at the active site with regard to the orientation and/or stability of the substrate in the binding pocket.

2.1.2 Crystal Structures of Xanthine Oxidase Family Enzymes

Four crystal structures in the molybdenum hydroxylases family have been reported: aldehyde oxidoreductase from *Desulfovibrio gigas* [61], xanthine oxidoreductase from *Bos taurus* [62], xanthine dehydrogenase from *Rhodobacter capsulatus* [58,59] and CO dehydrogenase from *Oligotropha carboxidovorans* [63,64]. These structures exist as dimmers with the monomers acting as independent subunits. Each subunit contains a Mo atom coordinated to a pyranopterine ring (Moco), two iron sulfur cluster centers (FeS(I) and FeS(II)) that are distinguished by EPR and an FAD cofactor (Figure 2.1).

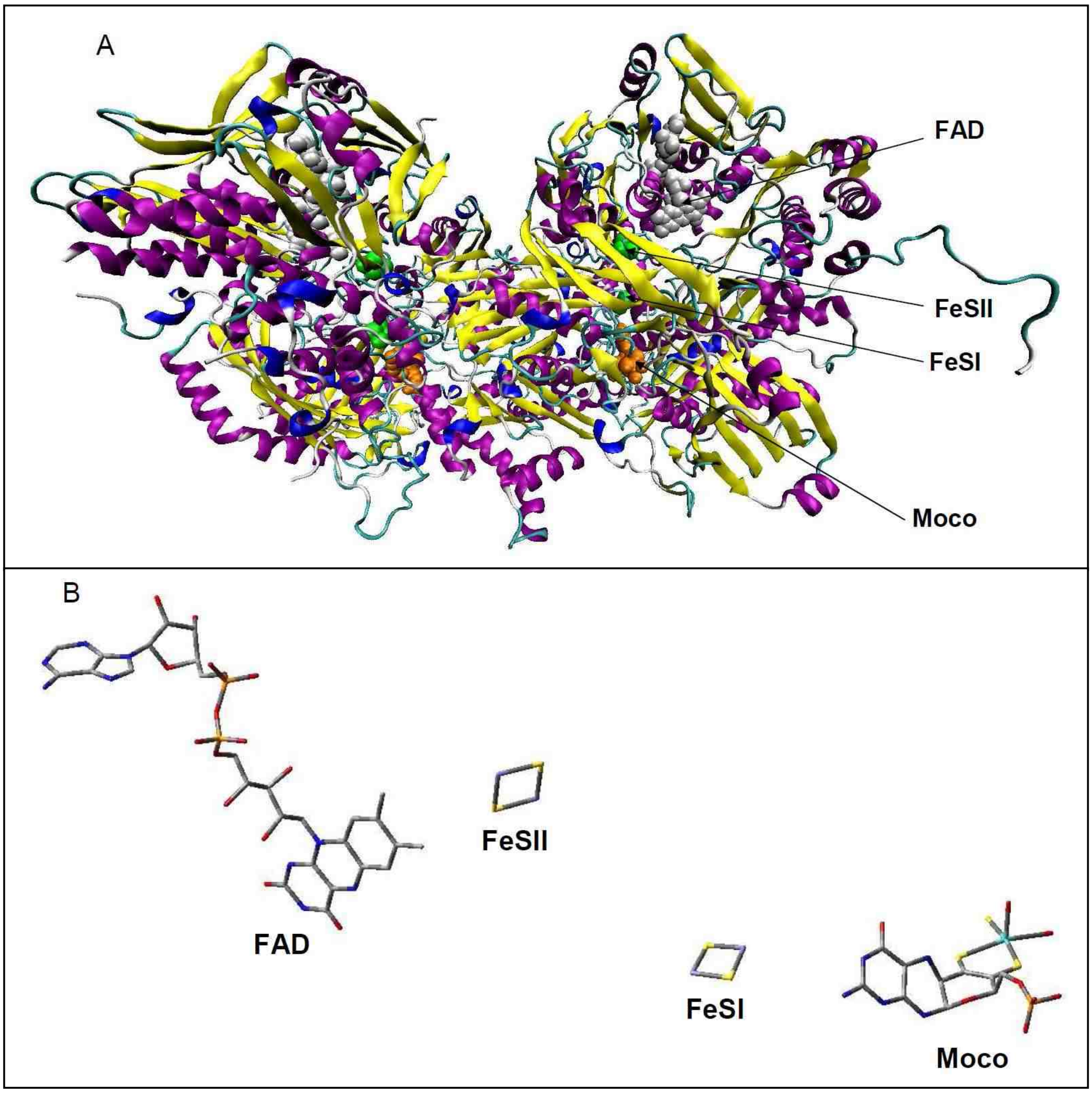

Figure 2.1: A (Top) represents the XDH dimmer isolated from bovine milk with the cofactors labeled (The structure was downloaded from PDB 1FO4. B (bottom) represents the geometrical structures of cofactors in the xanthine oxidase family [62]. Electrons flow from Moco via FeSI and FeSII to the FAD where the oxidative half reaction takes place. The FAD is on the surface of the protein where the Moco is buried deep in the protein.

Unlike AO from *D. gigas* that lacks the FAD cofactor [61], all the other cofactors are embodied in a polypeptide chain that has a similar fold in all the four crystallized enzymes. However, there are differences in the subunit composition among these crystal structures. All the cofactors of the bovine milk enzyme (XO/XDH) are bound within a continuous single polypeptide chain referred to as $(\alpha)_2$ structure. By contrast, *R. capsulatus* XDH is an $(\alpha\beta)_2$ heterotetramer with each $(\alpha\beta)$ representing one half of the active molecule. The subunit α binds the two 2Fe/2S centers and the FAD cofactor, while subunit β contains the Molybdenum cofactor [59]. In the case of CODH, the two 2Fe/2S centers are in CoxS subunit (α), FAD is in the second CoxM subunit (β) and molybdenum cofactor in the third CoxL subunit (γ) , such that the overall structure represents a dimer of trimers [63-65] Figure (2.2).

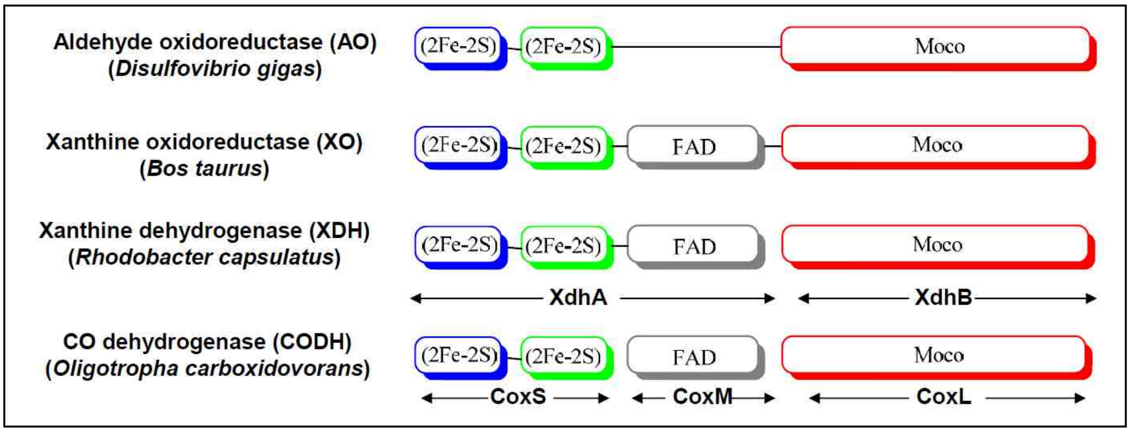
Aldehyde oxidoreductase (AO)
(Disulfovibrio gigas)
(2Fe-2S)
(2Fe-2S)
Moco
Xanthine oxidoreductase (XO)
(Bos taurus)
(2Fe-2S)
(2Fe-2S)
FAD
Moco
Xanthine dehydrogenase (XDH)
(Rhodobacter capsulatus)
(2Fe-2S)
(2Fe-2S)
FAD
Moco
XdhA
XdhB
CO dehydrogenase (CODH)
(Oligotropha carboxidovorans)
(2Fe-2S)
(2Fe-2S)
FAD
Moco
CoxS
CoxM
CoxL

Figure 2.2: Schematic representation of the homologies that exist in xanthine oxidase family. The aldehyde oxidoreductase from *D. gigas* does not have an FAD domain. In the *R. capsulatus* xanthine dehydrogenase the iron–sulfur and flavin-binding portions of the protein constitute one subunit (XdhA), and the

molybdenum-binding portion a second (XdhB). In the *O. carboxydovorans* CO dehydrogenase, the iron–sulfur centers are together in one subunit (CoxS), the flavin in a second (CoxM) and the molybdenum in a third (CoxL).

2.1.3 The Active Site of Xanthine Oxidase

The active site (Figure 2.3) possesses a catalytically labile Mo-OH group that is transferred to the substrate in the course of the hydroxylation reaction. The coordination geometry is best described as a square-pyramidal, with Mo=S, Mo-OH, and pyranopterin in the equatorial plane and Mo=O in the apical position [62,66].

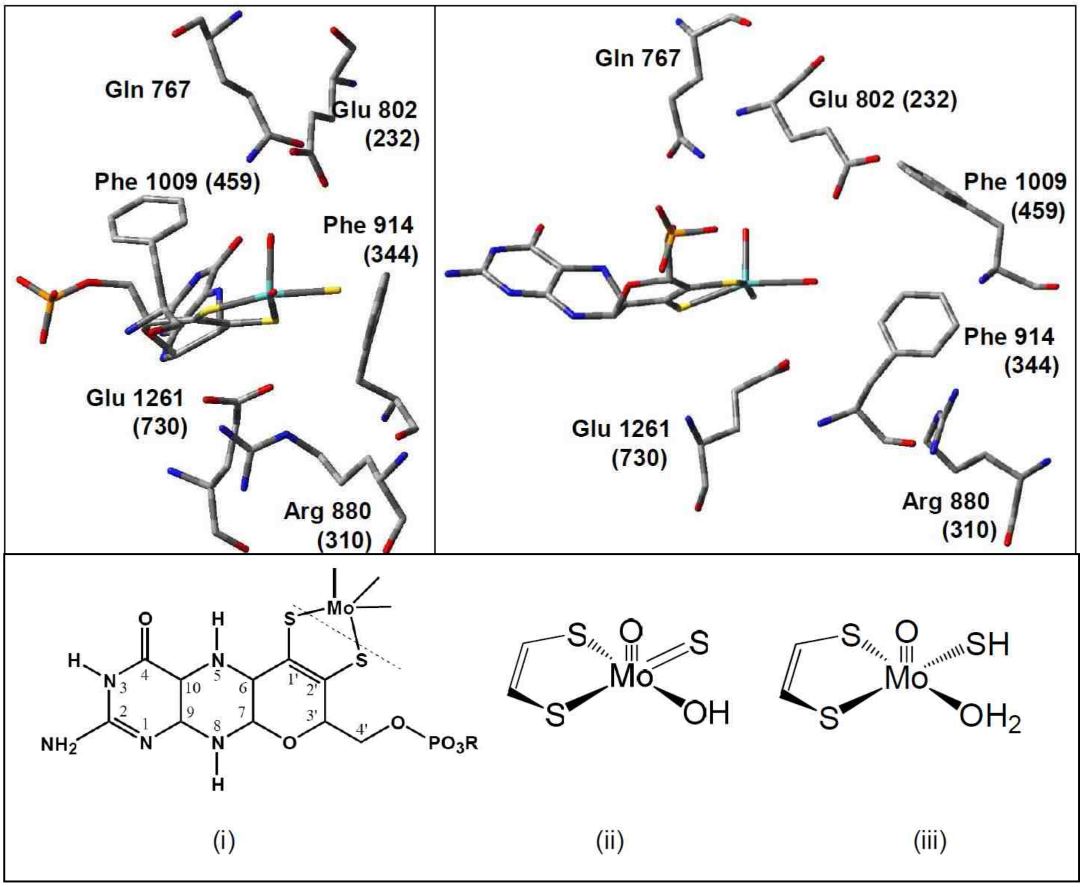
Gln 767
Glu 802
(232)
Phe 1009 (459)
Phe 914
(344)
Glu 1261
(730)
Arg 880
(310)
Gln 767
Glu 802 (232)
Phe 1009
(459)
Phe 914
(344)
Glu 1261
(730)
Arg 880
(310)
Mo
S
S
O
H
N
H
N
H
NH2
N
N
O
O
PO3R
1
2
3
4
5
6
7
8
9
10
1'
2'
3'
4'
S
O
Mo
S
S
OH
S
O
Mo
SH
S
OH2
(i)
(ii)
(iii)

Figure 2.3: Represents the active site for bovine xanthine oxidase downloaded from the PDB file with a code 1FIQ, (in parentheses is the numbering convention for the *R. capsulatus* XDH): The structure on the left (in the box) represents the orientation for the substrate channel. (i) Represents the active site for Moco, (ii) is the oxidized form at oxidation state of (VI) at the metal center and (iii) is the reduced form at an oxidation state of (IV) at the metal center.

The amino acids that have been shown to participate in substrate recognition and in the substrate tunnel leading to the molybdenum cofactor are listed in Table 2.1.

Table 2.1: Amino acids for substrates recognition.

Enzyme	Substrate recognition amino acids			Substrate channel amino acids			
Bovine-XO/XDH	Glu-802	Arg-880	Glu-1261	Leu-873	Ser-876	Phe-914	Phe-1009
R. capsulatus XDH	Glu-232	Arg-310	Glu-730	Leu-303	Pro-306	Phe-344	Phe-459

2.1.4 The Reductive Half Reaction of Xanthine Oxidase

2.1.4.1 Hydride Transfer Mechanism

The available evidence favors a mechanism (Scheme 2.2) which begins by an active site base (proposed to be a conserved glutamate residue) abstracting the proton from the Mo activated OH^-, initiating nucleophilic attack on substrate at C-8 position for xanthine [49,57]. This yields a tetrahedral transition state that breaks down by hydride transfer to the terminal sulfido resulting into a $Mo^{IV}O(SH)(OR)$ product bound species where OR represents product coordinated to the metal via the newly introduced hydroxyl group. This first observable intermediate in the reaction subsequently breaks down by electron transfer to other redox-active centers in the enzyme and displacement of product by hydroxide from solvent.

Scheme 2.1

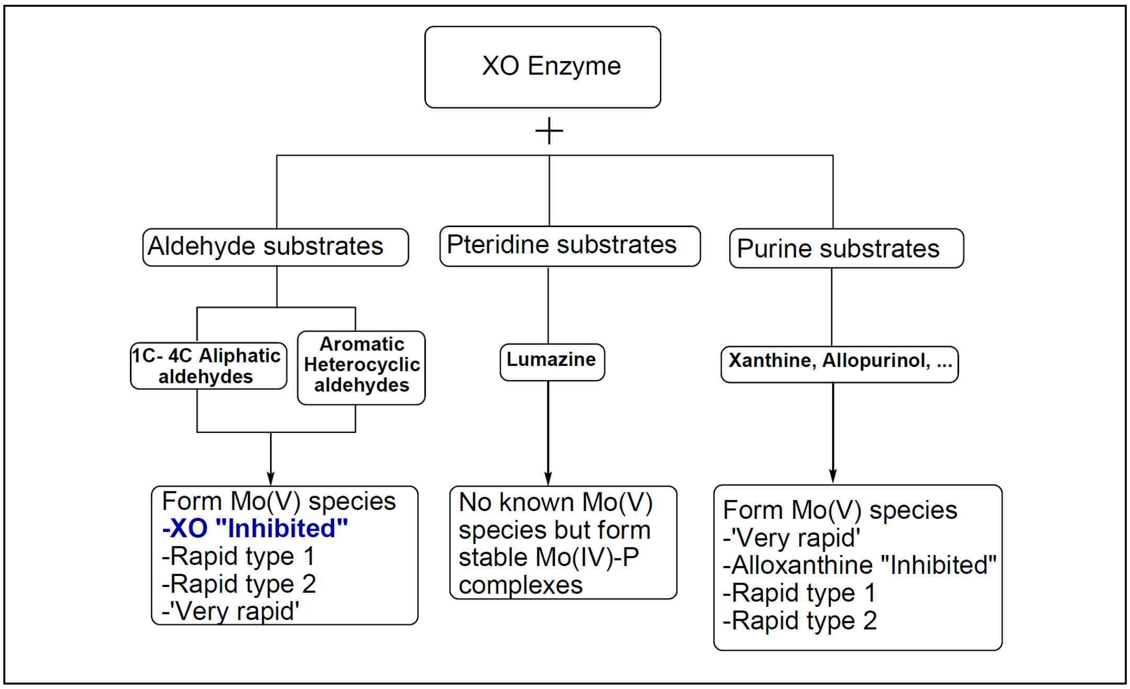
XO Enzyme
+
Aldehyde substrates
Pteridine substrates
Purine substrates
1C- 4C Aliphatic aldehydes
Aromatic Heterocyclic aldehydes
Lumazine
Xanthine, Allopurinol, ...
Form Mo(V) species
-XO "Inhibited"
-Rapid type 1
-Rapid type 2
-'Very rapid'
No known Mo(V) species but form stable Mo(IV)-P complexes
Form Mo(V) species
-'Very rapid'
-Alloxanthine "Inhibited"
-Rapid type 1
-Rapid type 2

Theoretical studies using formaldehyde and formamide as substrates confirmed this process to be a concerted reaction and occur through a tetrahedral arrangement around C8 of xanthine and the carbonyl carbon of the aldehyde and amide substrates [68]. Oxidation of the Mo(IV) reduced state, of the enzyme proceeds through two one-electron processes. An intermediate Mo(V) species, designated “very rapid” because of its short lifetime, has been detected by EPR, and has been shown to be a Mo-OR product bound species and the existence of the signal is usually taken as evidence of a reduced enzyme-product complex [66]. The Mo-OR product bound species has also been studied by electronic absorption spectroscopy with lumazine as a substrate whereby the formation of the charge transfer band at 650 nm at anaerobic conditions has been taken as evidence for the formation of the reduced Mo(IV) violapterine (oxidized lumazine) complex [69]. This charge transfer band decays upon oxygenation of the complex and this is taken as evidence for the release of the violapterine as a product and the resting state of the enzyme is regenerated (Figure 2.2).

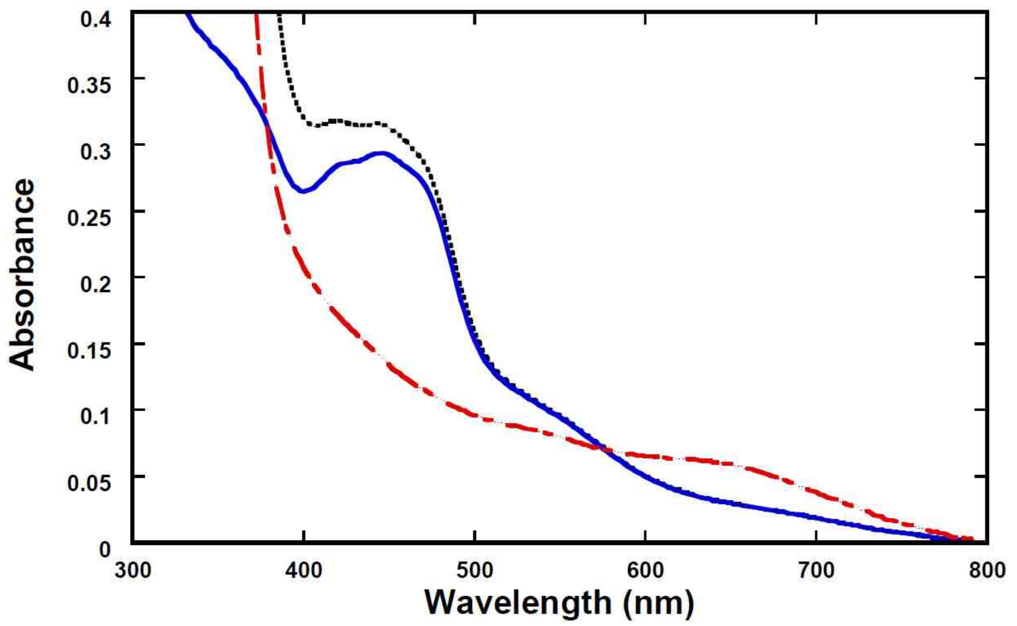

Figure 2.4: The charge transfer complex (band at 650 nm) formed between dithionite reduced xanthine oxidase with violapterine isolated from the aerobic reaction of lumazine and xanthine oxidase. The solid line (─) in blue represents oxidized enzyme at its resting state, the dashed line (-··-) in red represents the

spectrum of the violapterin and dithionite reduced enzyme with a charge transfer band at 650 nm. The dotted line (…) represents the re-oxidized enzyme from the dithionite reduced XO. Note that, the charge transfer band at 650 nm decays quickly upon exposure of the enzyme to oxygen.

Another paramagnetic enzyme form named “Inhibited” which is a dead end Mo(V) complex has also been detected by EPR from reaction of enzyme with aldehydes and is the center of this part of the investigation report. Examples of substrates and types of paramagnetic species formed in the course of catalytic reaction with xanthine oxidoreductase enzyme are illustrated in scheme 2.1.

Scheme 2.2: The proposed hydride transfer mechanism for the reductive half reaction of xanthine oxidase.

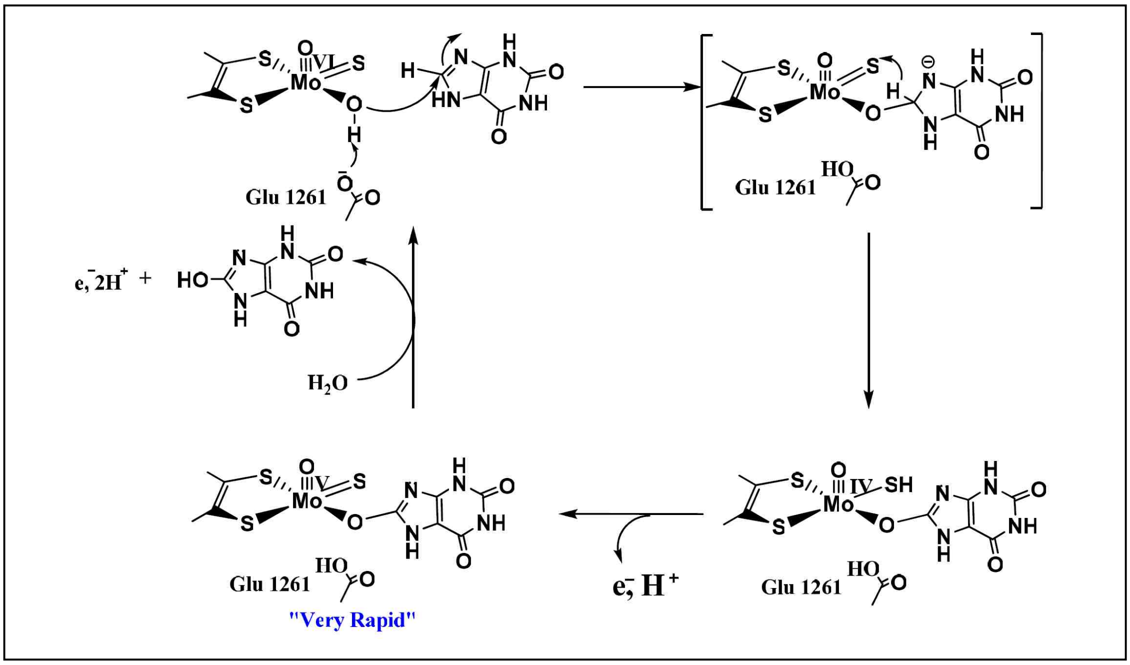

2.1.4.2 Proton Transfer Mechanism

The proton transfer mechanism was proposed based upon the results of the density functional calculations [48] that amended the hydride transfer mechanism in the hydride transfer step. However, in the hydride transfer mechanism (a charge controlled process) the calculations showed that the sulfido possesses a small net negative charge prior to the hydride transfer. This would reduce the driving force for the hydride transfer to the sulfido $d_{xy}\pi^*$ orbital which accepts two electrons.

Scheme 2.3: The proposed proton transfer mechanism for the reductive half reaction of xanthine oxidase.

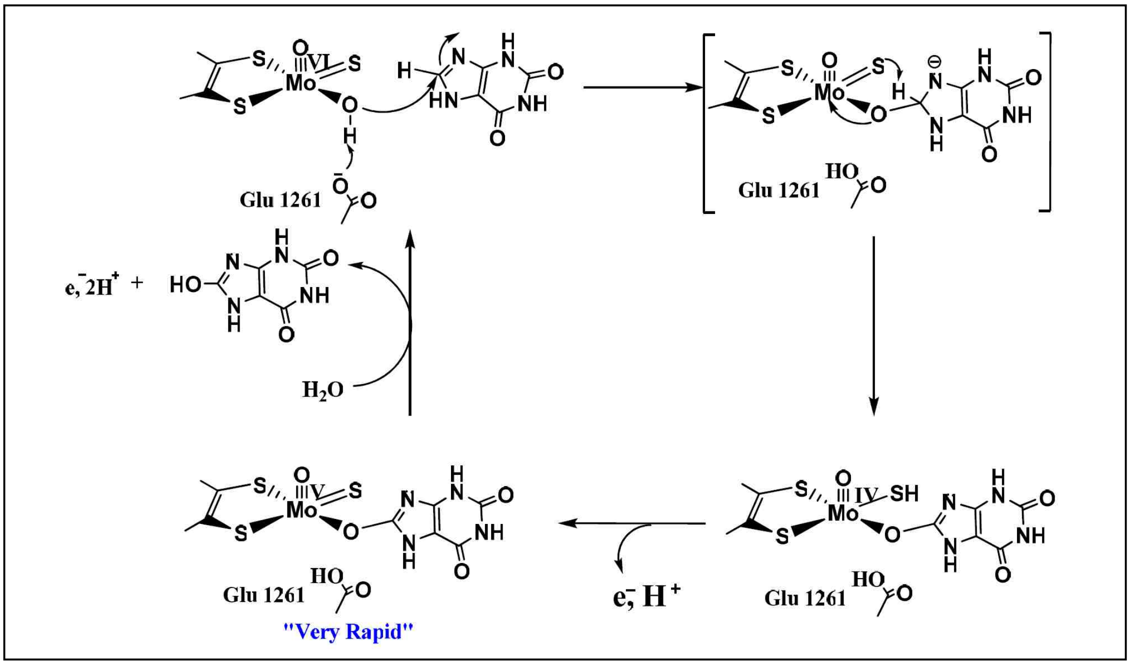

Secondly the attack of the metal bound hydroxide group to the purine carbon or aldehydic carbon of the substrate should lead to immediate deprotonation of the hydroxide proton with a concomitant proton transfer to the sulfido resulting into the formation of Mo-OR intermediate (Scheme 2.3). However, the charge transfer mechanism leading to Mo(IV)-OR intermediate was alternatively described as the inner sphere mediated by Mo-OR. The reduction of the molybdenum center by this mechanism increases the neucleophilicity of the sulfido for the proton abstraction.

2.1.5 XO "Inhibited"

The xanthine oxidase "Inhibited" is the product of the inhibitory side reaction of the oxidized enzyme with small reducing substrates such as aldehydes, formamide and methanol which is obtained upon incubation under aerobic conditions. The "inhibited" signal has been observed using EPR spectroscopy from mammalian XO and differs from other Mo(V) species observed in the reductive half reaction of XO in that, it is stable in air. For this reason the species has been the subject to extensive kinetic and spectroscopic studies but still little is known about this inhibitory reaction [70-74]. This signal develops progressively while the enzyme is turning over under steady state conditions. Studies have shown that the development of the inhibited signal is accompanied by the loss of enzyme activity and reactivation by a variety of methods including either by dithionite or ferricyanide leads to reversal inhibition presumably converting Mo(V) species to Mo(IV) or Mo(VI) respectively [70,75]. However, the activity recovered by these methods ranged from 40 to 50% [70] while quantitative recovery of xanthine oxidase activity (about 95%) was achieved by gel filtration on sephadex [75]. XO “inhibited” is important in that, along with “very rapid”, is a key paramagnetic enzyme form with substrate/product bound at the Mo site. Although XO “Very Rapid” represents a true catalytic intermediate with certain substrates, “inhibited” is a dead-end Mo(V) complex. This complex lacks the electronic and structural information despite the various forms of the “Inhibited” structures (Figure 2.5) that have been proposed by numerous researchers based on EPR/ENDOR spectroscopic and computational studies [16,72,73,76].

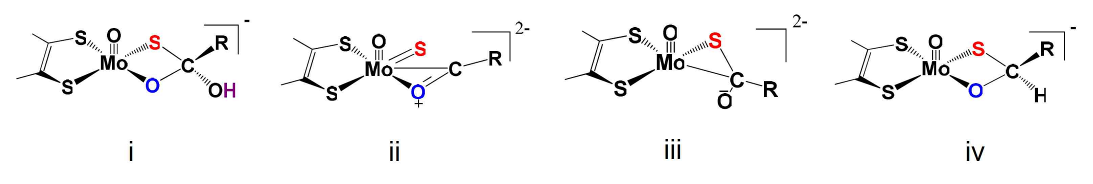

Figure 2.5: Proposed structures for xanthine oxidase “inhibited”.

However, in these investigations, we have performed detailed spectroscopic studies using EPR on the “inhibited” species generated from the reaction of mammalian XO and XDH from *R. capsulatus* with aldehyde substrates and determined the spin Hamiltonian parameters by computer simulations. We have also performed detailed computational studies using spin unrestricted DFT formalism for geometry optimizations, spin densities calculations and calculated theoretical spin Hamiltonian parameters using ORCA. The evaluation of computational results from experimentally determined parameters enabled the determination of new ^{95,97}Mo hyperfine tensor, ^{13}C hyperfine tensor and their orientations with respect to the g tensor leading to the structural elucidation of the “inhibited” species. We have also proposed new mechanisms for the generation of the “inhibited” based on the spectroscopically and computationally derived structure.

2.2 Statement of the Research Problem

Although various structures of xanthine oxidase “inhibited” have been postulated by numerous researchers, the structure of XO “inhibited” is still unknown. The mechanistic sequence by which XO “inhibited” is formed is also unknown. It is not known whether XO “inhibited” is a Mo(V) substrate or Mo(V) product complex. It is also not known whether the amino acids that surround the active site play any role on the formation of XO “inhibited”. XO “inhibited” may represent an analog of the Michaelis complex or the calculated transition state in the reductive half reaction of xanthine XO. Determining the structure of XO “inhibited” will provide deeper mechanistic insight into the reductive half reaction of XO.

2.3 Hypothesis

We hypothesize that XO “inhibited” represents a tetrahedral product or reactant molecule bound at the active site and that this binding mode results in a four member chelate ring supported via Mo-O-C and Mo-S-C linkages (Figure 2.5 (i)). We further suggest that this tetrahedral species in XO “inhibited” does not represent a highly stable geometry for heterocyclic substrates, and this is why they do not usually result in the formation of “inhibited” species. Furthermore, the tetrahedral geometry proposed for XO "inhibited" with aldehydes may mimic a tetrahedral intermediate or perhaps a tetrahedral transition state in the course of heterocyclic substrate oxidation, although without the strong C-S bond.

2.4 Materials and Methods

Xanthine oxidase and xanthine dehydrogenase from R.capsulatus enzymes. Most of bovine xanthine oxidase was purchased from Sigma Aldrich and some was isolated and purified in our laboratory from unpasteurized cow's milk by the method of Massey and co-workers [77]. On the other hand wild type xanthine dehydrogenase (XDH) and E232N-XDH mutant from *R. capsulatus* were obtained from our collaborator Silke LeimkÜhler, University of Potsdam, Institute of Biochemistry and Biology, 14476 Potsdam, Germany. Both commercial and isolated XO samples had A_{280}/A_{450} ratio of about 11.7 in bicine/NaOH buffer, pH 8.2 and had an activity to flavin ratio (AFR) of 200. (Fully functional enzyme reported by Massey et al, had an AFR of 210 and an A_{280}/A_{450} ratio of about 5.3 to 5.8) whereas XDH from *R.capsulatus* had A_{280}/A_{450} ratio of 11.5 and an AFR of 190. Enzyme concentration was determined from the absorbance at 450 nm by using the value of 37800 $M^{-1}cm^{-1}$ as the molar absorptivity of the enzyme bound FAD.

Preparation of xanthine oxidase "inhibited". The "inhibited" enzyme form was generated using the reducing substrates formaldehyde, acetaldehyde, 2-pyridinecarboxaldehyde and 3-pyridinecarboxaldehyde purchased from Sigma

Aldrich. The XO enzyme was dialyzed against 50 mM-Bicine/NaOH buffer at pH 8.2. Samples of xanthine oxidase (0.07 to 0.1 mM) were placed in EPR tubes followed by the addition of a large excess of the substrate (0.03 to 0.06 M). The mixture was then bubbled gently with oxygen gas and with frequent shaking to ensure aerobiosis. The reaction mixture was then incubated for times that ranged from minutes to hours depending on the substrate and then samples were frozen for EPR measurements after appropriate incubation times.

Electronic Absorption Spectroscopy. Electronic absorption spectra were collected using a Hitachi U-3501 UV–Vis–NIR dual-beam spectrometer capable of scanning a wavelength region between 185 and 3200 nm. XO and XDH samples (≈ 5 μM) with substrates (1mM) were prepared in 50 mM-Bicine/NaOH buffer solution at pH 8.2, and the electronic absorption spectra were measured in a 1-cm pathlength, 150 μL, black-masked, quartz cuvette (Starna Cells, Inc.) equipped with a Teflon stopper. All electronic absorption spectra were collected at room temperature.

EPR spectroscopy. EPR spectra of the frozen samples were recorded on a Bruker model EMX spectrometer operating at X-band (~9.4 GHz). A microwave power of 20 dB was used for all the inhibited experiments and spectra were collected at 40 and 100 K using an Oxford instruments liquid helium flow cryostat. Computer simulations were done using X-Sophe and the matlab toolbox EasySpin software programs.

Computational Methods. Geometry optimizations for the inhibited structures were carried out at the B3LYP level of DFT in spin-unrestricted mode using the Gaussian 03, version B.03 software package. The tetrahedral computational models of the “inhibited” structures were those originally proposed by Howes and co-workers in 1990 and 1994 [16,72], Figure 2.5. Input files were prepared using GaussView and calculations were carried out using the 6-31G* split valence basis set with added polarization functions for O, S, N, C and H and LANL2DZ basis set for Mo to probe the effective core potential. EPR parameters were calculated at the B3LYP/TZVP/ZORA level using ORCA 2.7.0 [78,79]. Relativistic corrections were incorporated self-consistently in the ORCA calculations with the ZORA scalar relativistic Hamiltonian [80,81].

2.5 Results and Analysis

2.5.1 Reduction of Mammalian XO and Bacterial XDH Enzymes by Substrates

Electronic absorption spectroscopy was used to study the reactivity of XO and XDH enzymes with substrates and use the results to calibrate EPR experiments. The electronic absorption spectra of the oxidized XO and XDH enzymes upon anaerobic reduction by the substrates are shown in figures 2.6, 2.7, 2.8 and 2.9.

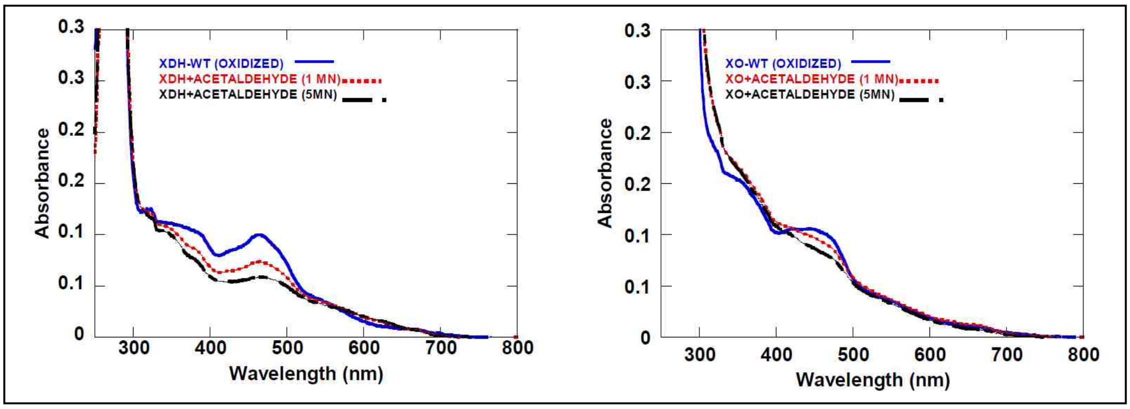

Figure 2.6: Reaction of oxidized XO/XDH with acetaldehyde

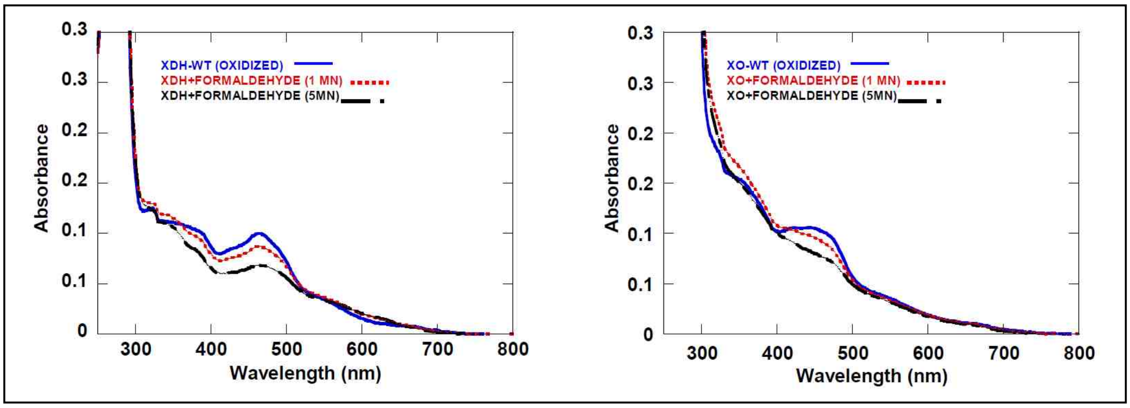

Figure 2.7: Anaerobic reaction of oxidized XO/XDH with formaldehyde

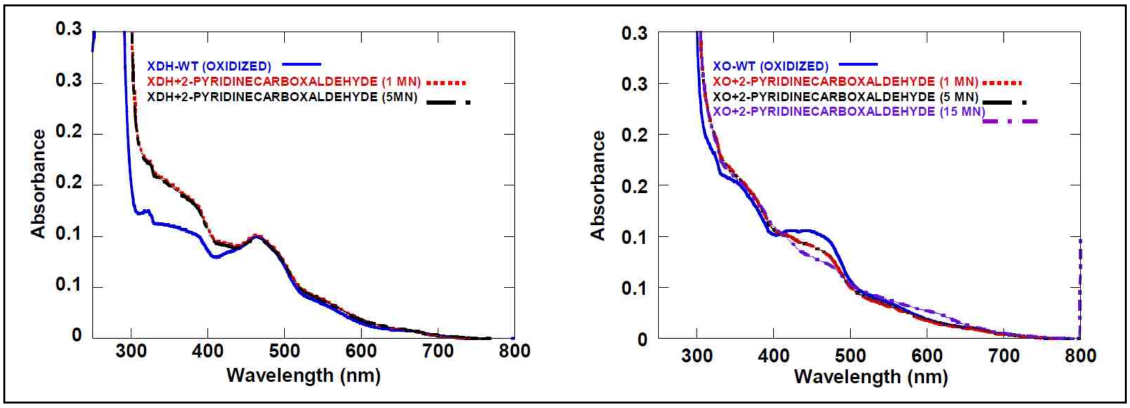

Figure 2.8: Anaerobic reaction of oxidized XO/XDH with 2-pyridinecarboxaldehyde

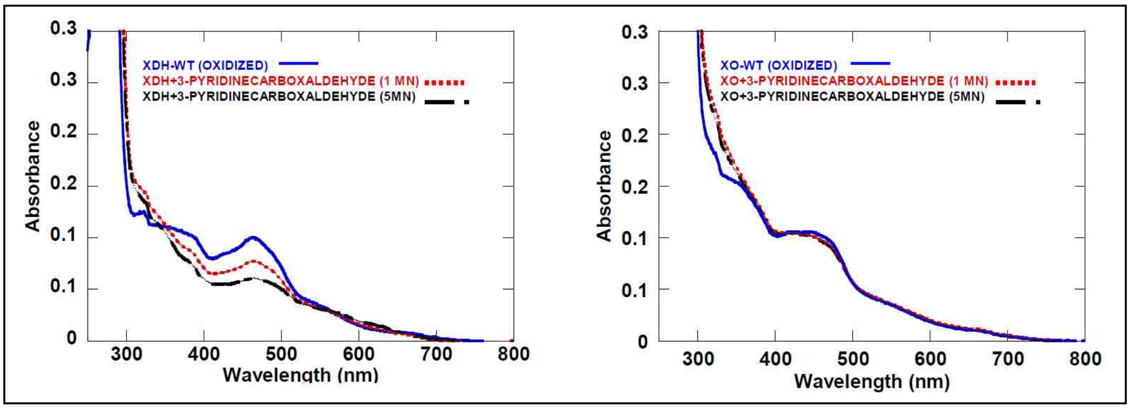

Figure 2.9: Anaerobic reaction of oxidized XO/XDH with 3-pyridinecarboxaldehyde

The reactions were carried out using 5 μM of the XO/XDH enzyme and 1 mM of the substrate and the spectra were taken within 1 to 15 minutes after mixing with substrates. The results indicated a rate dependence on the substrates as measured by change in absorbance between the oxidized and the reduced enzyme at 450 nm. Thus acetaldehyde is the fastest reducing substrate whereas 2-pyridinecarboxaldehyde is the slowest reducing substrate. The results also indicate an enzyme dependence on the rate of the reaction, with XDH being more quickly reduced by substrates than XO.

2.5.2 Inhibited Signals and ^{95,97}Mo Hyperfine Analysis

The EPR spectra obtained from the reaction of bovine xanthine oxidase and xanthine dehydrogenase from *R. capsulatus* with various aldehydes are shown in figures 2.10 and 2.11 respectively. Experiment with formaldehyde and 3-

pyridinecarboxaldehyde display well resolved ^{95,97}Mo hyperfine splitting due to the I = 5/2 nuclei.

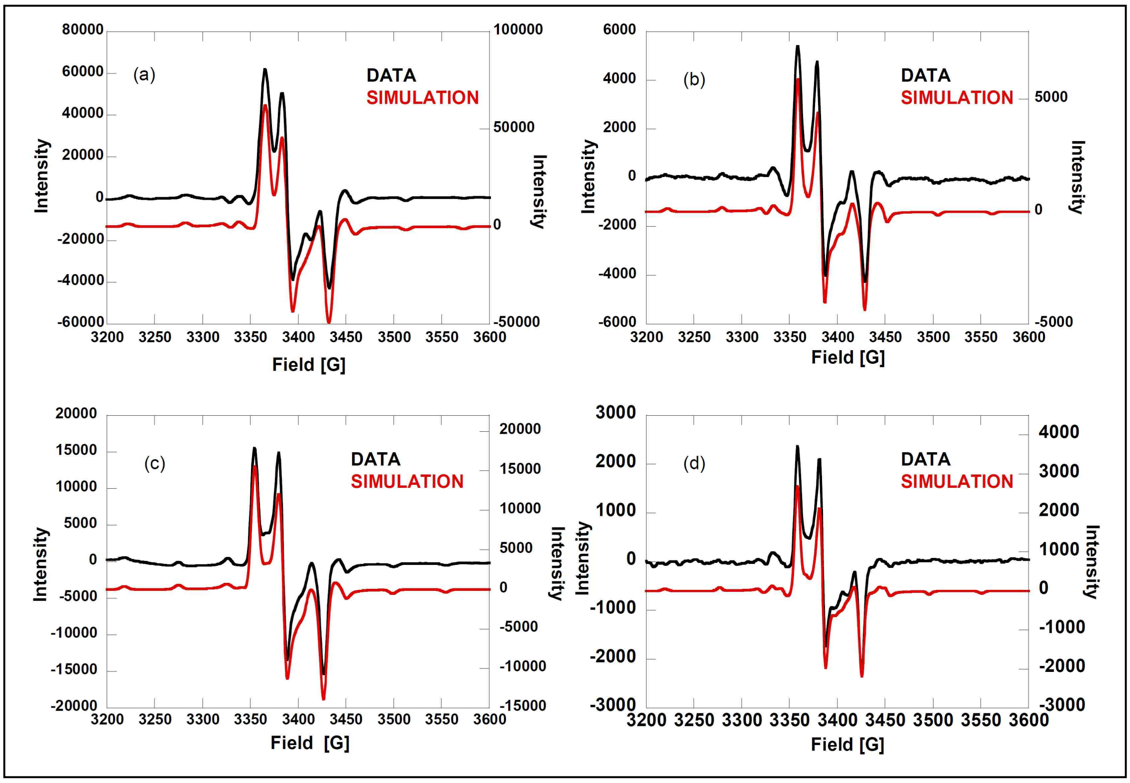

Figure 2.10: Electron paramagnetic resonance (EPR) signals for various aldehydes at 9.41 GHz during reaction with xanthine oxidase (0.07 mM) in 50 mM Bicine/NaOH buffer, pH 8.2. The aldehydes used for spectra (a), (b), (c) and (d) are respectively formaldehyde (0.20 M), 2-pyridinecarboxaldehyde (0.03 M), 3-pyridinecarboxaldehyde (0.03 M) and acetaldehyde (0.50 M). Their incubation times with xanthine oxidase are 6, 0.5, 1.5 and 0.12 hours respectively. The black spectra (upper) represent data whereas the red spectra (below) are their corresponding simulations.

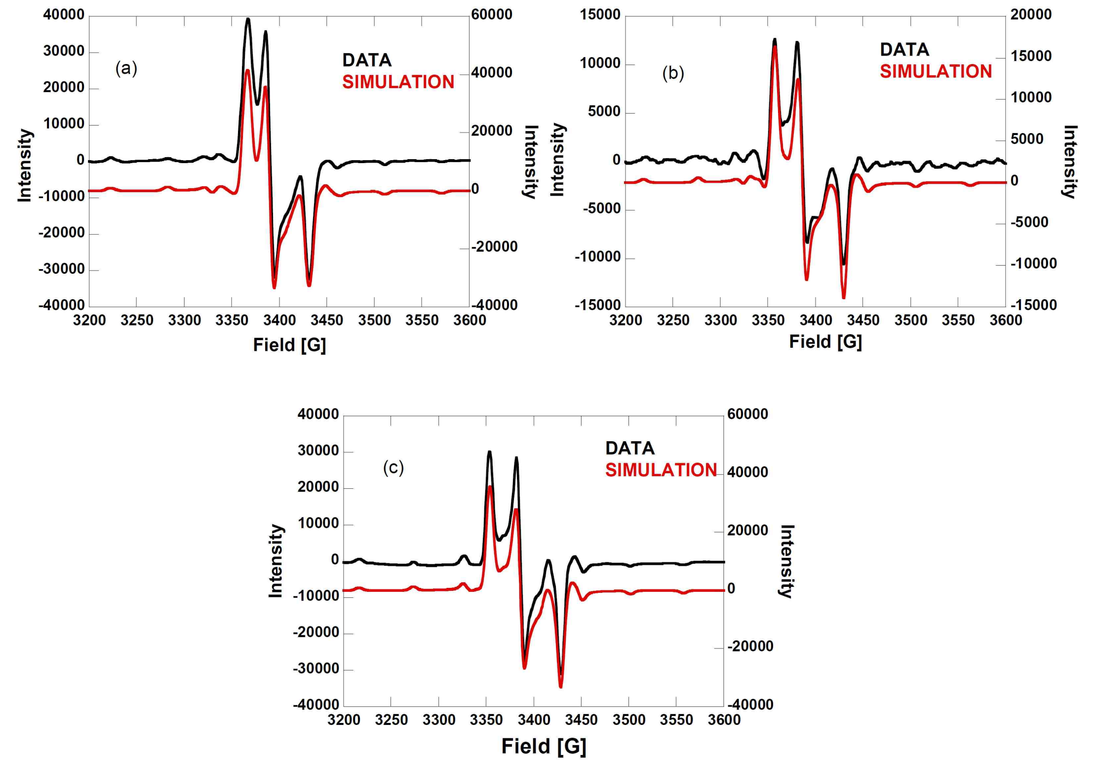

Figure 2.11: Electron paramagnetic resonance (EPR) signals for various aldehydes at 9.42 GHz during reaction with XDH (0.07mM) in 50 mM Bicine/NaOH buffer, pH 8.2. The aldehydes used for spectra (a), (b) and (c) are respectively formaldehyde (0.20 M), 2-pyridinecarboxaldehyde (0.03M) and 3-pyridinecarboxaldehyde (0.03 M). Their incubation times with xanthine oxidase are 0.25, 0.50 and 0.17 hours respectively. The black spectra (upper) represent data whereas the red spectra (below) are their corresponding simulations.

The spin Hamiltonian parameters for various aldehydes upon reactions with mammalian XO and XDH from *R. capsulatus* are summarized in tables 2.2 and 2.3 respectively. Both enzymes give identical spectra. However, the incubation times for the formation of the “inhibited” species differ markedly between the mammalian XO and bacterial XDH enzymes. The bacterial XDH forms “inhibited” much faster than the mammalian XO.

The rhombic nature of the g tensor anisotropy for the “inhibited” spectra is characteristic of the lower symmetry ligand field distortions at the molybdenum center. However, there are slight differences in values of the EPR parameters of the “inhibited” signal which is a function of the chemical nature of the aldehyde group (R) forming the inhibited species (Tables 2.2 and 2.3).

Table 2.2: EPR Parameters for XO Inhibited (bovine)

	Axis			Average	Euler Angles		
Parameters	z	y	x		α	β	γ
Formaldehyde							
g	2.0002	1.9856	1.9610	1.9823			
A(^{95,97}Mo) x 10^{-4} cm^{-1}	59.50	23.00	22.50	35.00	86.75	138.59	8.28
A(^{13}C) x 10^{-4} cm^{-1}	12.33	16.67	16.00	15.00	90.00	69.15	56.58
A(^{1}H) x 10^{-4} cm^{-1}	5.00	3.33	3.33	3.89	9.51	102.89	-81.87
2-Pyridinecarboxaldehyde							
g	2.0025	1.9878	1.9614	1.9839			
A(^{95,97}Mo) x 10^{-4} cm^{-1}	57.00	22.33	21.67	33.67	69.00	137.00	17.62
3-Pyridinecarboxaldehyde							
g	2.0048	1.9872	1.9626	1.9849			
A(^{95,97}Mo) x 10^{-4} cm^{-1}	56.33	20.67	20.67	32.56	72.00	140.00	12.00

Table 2.3: EPR Parameters for XDH Inhibited (*R. capsulatus*)

	Axis			Average	Euler Angles		
Parameters	z	y	x		α	β	γ
Formaldehyde							
g	1.9995	1.9854	1.9614	1.9821			
A(^{95,97}Mo) x 10^{-4} cm^{-1}	59.33	23.00	22.67	35.00	86.75	138.59	8.28
A(^{13}C) x 10^{-4} cm^{-1}	12.33	15.00	16.67	14.67	90.00	69.15	56.58
A(^{1}H) x 10^{-4} cm^{-1}	5.00	3.33	3.33	3.89	9.51	102.89	-81.87
2-Pyridinecarboxaldehyde							
g	2.0039	1.9867	1.9614	1.9840			
A(^{95,97}Mo) x 10^{-4} cm^{-1}	57.67	23.33	21.00	34.00	69.00	137.00	17.62
3-Pyridinecarboxaldehyde							
g	2.0068	1.9878	1.9629	1.9858			
A(^{95,97}Mo) x 10^{-4} cm^{-1}	57.00	20.67	20.67	32.78	72.00	140.00	10.00

Table 2.4: EPR Parameters for E232A-XDH Inhibited (*R. capsulatus*)

	Axis			Average	Euler Angles		
Parameters	z	y	x		α	β	γ
3-Pyridinecarboxaldehyde							
g	2.0050	1.9863	1.9621	1.9845			
A(^{95,97}Mo) x 10^{-4} cm^{-1}	58.67	22.00	20.67	33.78	72.00	140.00	10.00

In particular, this depends on the electron density at the aldehydic carbon of the substrate which is a result of either the donating or withdrawing effects of the R group (Figure 2.5). If the carbon is more positive, there is spin delocalization into it resulting into greater Mo-C covalency and higher values of g in the z-direction (magnetic field direction) are obtained and vice versa. The formaldehyde “inhibited” EPR spectrum shows evidence for ^{1}H coupling to the molybdenum center that results in increased spectral line broadening (R = H in Figure 2.5 (i) and (iv)). This proton (I = ½) splits the molybdenum peak signals into doublets. The doublet splitting was clearly observed after three hours incubation of enzyme and formaldehyde substrate and disappeared upon longer incubation times due to increased intensities (Figure 2.12). This strongly coupled proton is not evident in the 3-pyridinecarboxaldehyde and 2-pyridinecarboxaldehyde spectra, and this indicates that the aldehydic R group is oriented upwards in the Mo≡O direction. The EPR experiments for the wt-XDH and E232A-XDH strongly suggest that the R group of 3-pyridinecarboxaldehyde is oriented in the up direction such that it can potentially interact with the carboxylate side chain of the glutamate 802/232 (Figure 2.3). The difference between the formaldehyde spectra obtained after 1 hour and 6 hours incubation times (Figure 2.12) resulted into the ‘rapid type’ signal. In general, the generation of the “inhibited” signal is always preceded by the ‘rapid type’ signal formation which disappears upon further oxygenation of the sample. Additionally, the formaldehyde Inhibited EPR spectrum displays well-resolved ^{13}C (I=1/2) hyperfine splitting when using $H^{13}COH$. The magnitude and nature of the ^{13}C tensor (Figure 2.13 and Table 2.3) is consistent with the delocalization of unpaired spin from the Mo center to the C atom that derives from the carbonyl carbon of the aldehyde substrate. This also suggests a unique orientation of the carbon sp hybrid orbital with respect to the molybdenum d orbital.

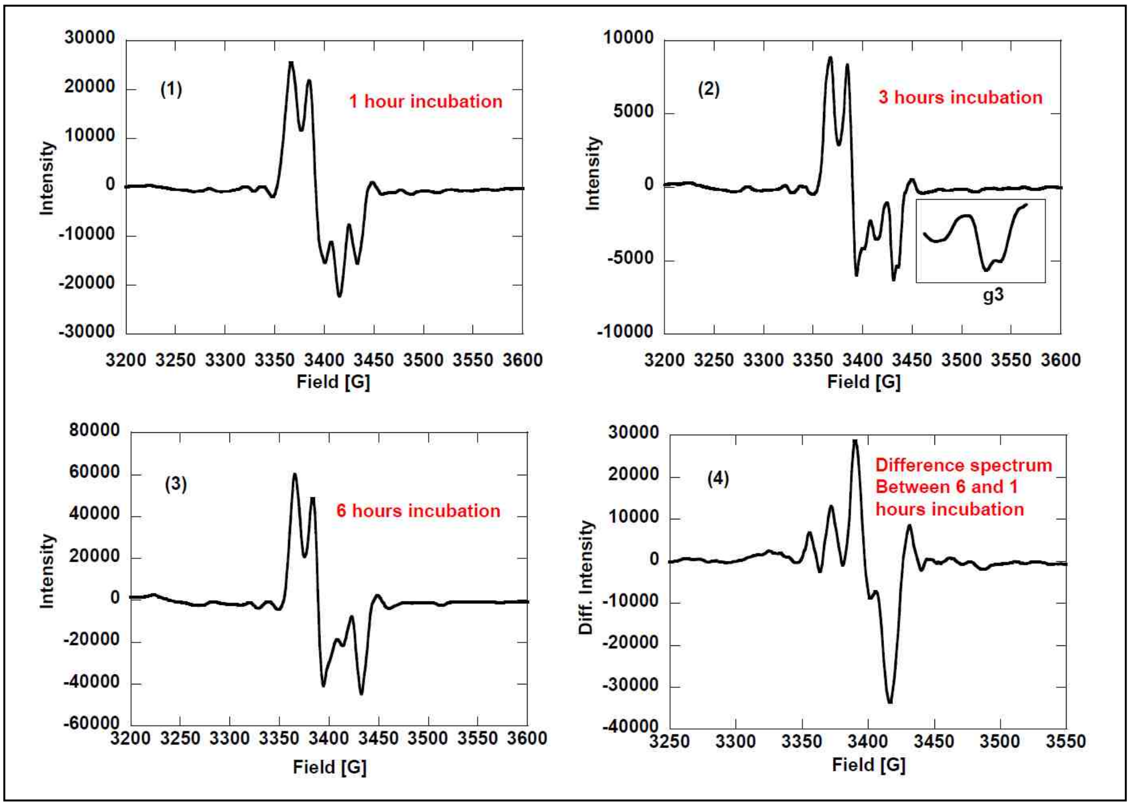

Figure 2.12: Electron paramagnetic resonance (EPR) signals at 9.41GHz during reaction of xanthine oxidase (0.07 mM) with formaldehyde (0.20 M) in 50 mM Bicine/NaOH buffer, pH 8.2. At intervals, samples were bubbled with oxygen in the EPR tubes and frozen for EPR measurement. Reaction times for (1), (2) and (3) were respectively 1, 3 and 6 hours. Spectrum (4) represents a ‘rapid type’ signal which is the difference spectrum obtained from subtracting (1) from (3). The insert in (2) shows the proton splitting at g_x at lower concentrations of the “inhibited” species.

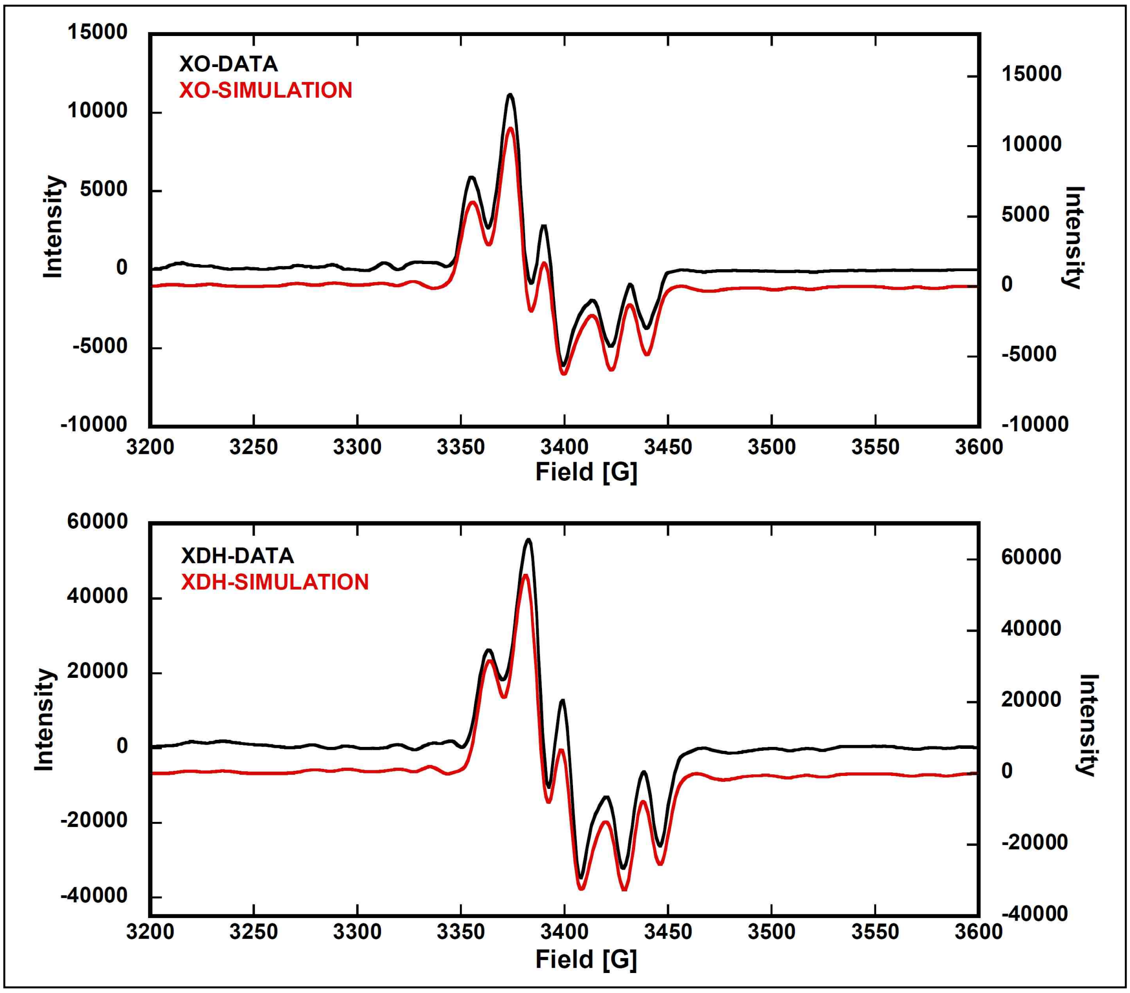

Figure 2.13: Electron paramagnetic resonance (EPR) signal at ≈ 9.4 GHz during reaction of 0.07 mM XO (top) and 0.07 mM XDH (bottom) with ^{13}C-labeled formaldehyde (0.20 M) in 50 mM Bicine/NaOH buffer pH 8.2 and its corresponding simulation. The reaction mixture was bubbled with oxygen in an EPR tube for 15 minutes and then frozen for EPR measurement. The black spectrum (upper) is the data whereas the red spectrum (below) is the simulation in each set.

Furthermore, an EPR spectrum of XDH mutant (E232A) with 3-pyridinecarboxaldehyde substrate was collected and is the first spectroscopic probe of the catalytic role of the active site residues in the secondary coordination sphere at the active site (Figure 2.14). A comparison with the wt-XDH 3-pyridinecarboxaldehyde “inhibited” spin-Hamiltonian parameters indicates that the E232A mutant possesses slightly larger A tensor and slightly smaller g1 values when compared to the wt enzyme, and this is consistent with a structural perturbation that results in a reduced covalency at the Mo site (Figure 2.15 and Table 2.4).

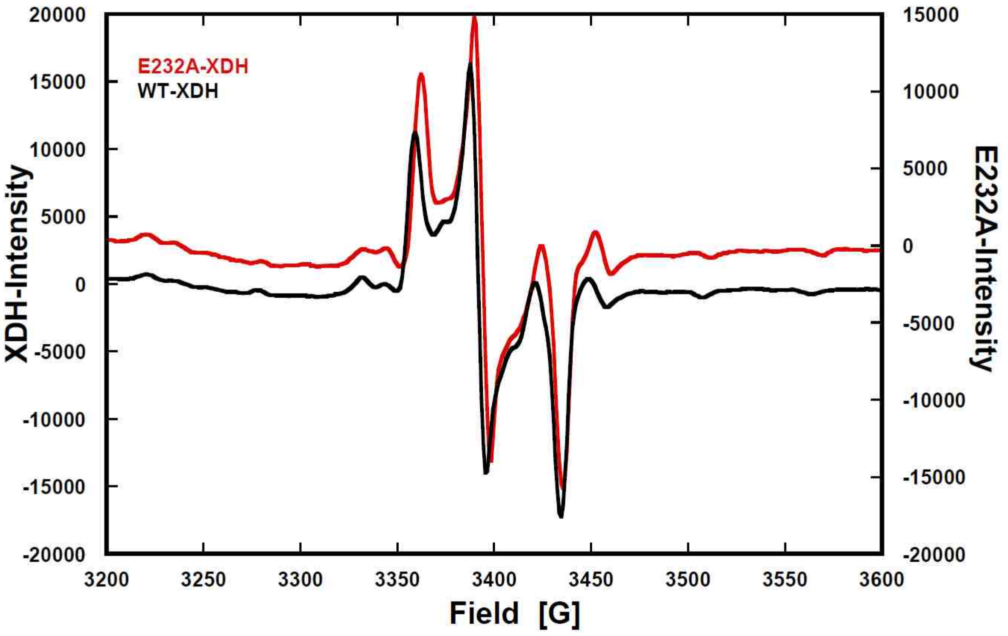

Figure 2.14: Electron paramagnetic resonance (EPR) signals at 9.41GHz during reactions of 0.07 mM wild type xanthine dehydrogenase from *R. capsulatus* (black spectrum - below) and 0.07 mM of E232A-xanthine dehydrogenase (red

spectrum – upper) with 3-pyridinecarboxaldehyde (0.03 M) in 50 mM Bicine/NaOH buffer, pH 8.2. Note; the E232A-XDH (red spectrum) is relatively shifted to higher field compared with the wild type XDH (black spectrum).

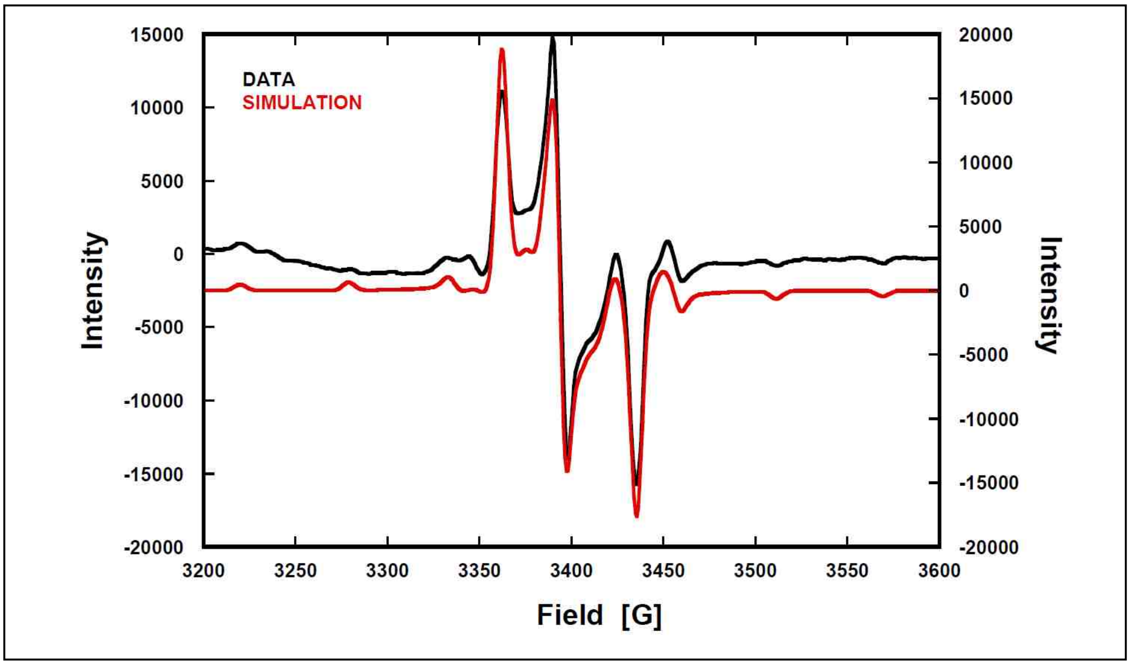

Figure 2.15: Electron paramagnetic resonance (EPR) signal at 9.439 GHz during reaction of E232A-xanthine dehydrogenase (0.07 mM) with 3-pyridinecarboxaldehyde (0.03 M) in 50 mM Bicine/NaOH buffer pH 8.2 and its corresponding simulation. The reaction mixture was incubated in an open EPR tube for 10 minutes and then frozen for EPR measurement. The black spectrum (upper) is the data whereas the red spectrum (below) is the simulation.

A previous EPR study of XO "inhibited" utilized an EPR spectrum from ^{95}Mo isotope enrichment to obtain the hyperfine parameters A_{iso} = 42.72 x 10^{-4} cm^{-1}

and A_{dip} = [+9.83, -19.67, +9.83] x 10^{-4} cm^{-1} [70]. The anisotropy in the dipolar term A_{dip} is unusual, and indicative of a Mo_{dz^2} singly occupied molecular orbital (SOMO) ground state wave function. In order to better understand the nature of the ground state wave function we carried out computational calculations which also facilitated structural determination of the “inhibited” signal giving species in xanthine oxidase.

2.5.3 Structural Insights of the “Inhibited” Species

Four structures were considered for investigation of the structure of the “inhibited” signal giving species (Figure 2.5). While this study was ongoing, a ^{1,2}H pulsed ENDOR studies on formaldehyde “inhibited” XO appeared in the literature and provided evidence for structure (iv) in Figure 2.5 [18]. This recent ENDOR study did not explicitly exclude the possibility of structure (i) particularly if this geometry is present in 1:1 mixture of R and S configurations with respect to the chiral carbon atom derived from the carbonyl of other substrates besides formaldehyde. Computational analysis of both structures (i) and (iv) indicate very similar electronic properties (Table 2.5) which suggests that either one could be the structure. Structure (i) is consistent with the accepted proposed XO mechanism which results into a product bound species whereas structure (iv) represents a Michael’s complex. Furthermore, the EPR catalytic events observed for purines are very similar to those leading to the formation of the “inhibited” signal indicating that the substrate is turning over to product. Thus, structure (i) can be hypothesized to represent a more stable geometry of the “inhibited” species than structure (iv) and hence its consideration for further analysis against the two other structures (ii) and (iii). However, structures (i) to (iii) were optimized as formaldehyde "inhibited" (R = H) using a spin unrestricted DFT formalism and their spin densities calculated (Figure 2.16). Structure (i) has about 97% of its spin density distributed on molybdenum and about 2% distributed on formaldehyde carbon. The calculated s and p spin densities for the R configuration are 0.43% and 1.74% respectively whereas the calculated s spin density for S configuration is about 0.78% and the calculated p spin density is about 1.11%.

Table 2.5: Comparison between "inhibited" proposed structures (i) and (iv).

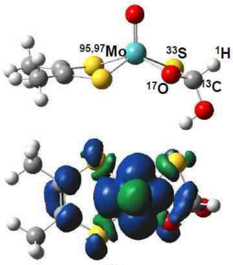

(i)

g-values	^{95,97}Mo A-values	^{13}C; A-values	^{1}H; A-values	^{17}O; A-values	^{33}S; A-values
g_z = 1.9971772	54.14	14.72	5.84	-5.88	2.76
g_y = 1.9801995	18.64	11.69	3.97	-2.63	1.08
g_x = 1.9525335	17.97	11.34	3.65	-1.67	-0.38
Spin density Populations (%)	100.85	2.18	0.68	1.17	-1.66

^{95,97}Mo-Aiso = 30.25, ^{95,97}Mo-Adipol = 23.89, -11.61, -12.28

^{13}C-Aiso = 12.58, ^{13}C-Adipol = 2.14, -0.89, -1.24

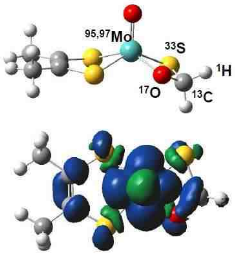

(iv)

g-values	^{95,97}Mo A-values	^{13}C; A-values	^{1}H; A-values (up/down)	^{17}O; A-values	^{33}S; A-values
g_z = 1.9938339	54.43	15.37	5.16/-1.86	-6.61	7.52
g_y = 1.9802818	19.11	12.71	3.27/-1.74	-1.71	-1.40
g_x = 1.9508757	17.50	12.39	2.96/-0.51	-0.61	0.36
Spin density Populations (%)	99.48	2.03	0.86	1.91	-0.57

^{95,97}Mo-Aiso = 30.35, ^{95,97}Mo-Dipol = 24.08, -11.24, -12.85

^{13}C-Aiso = 13.49, ^{13}C-Adipol = 1.88, -0.78, -1.10

Structures (ii) and (iii) yielded very similar electronic structure properties and both have about 9% of the spin density distributed on molybdenum and 72% distributed on the formaldehyde carbon. They both give an s spin density of about 10.33% and p spin density of about 61.60%. However, the p orbital ($2p_x$) that is interacting with the molybdenum orbital in structure (i) is in the equatorial plane of the molecule whereas for structures (ii) and (iii) the orbital ($2p_z$) is oriented perpendicular to this plane and parallel with Mo≡O bond. Bond order calculations reveal no Mo-C bond formation in all the proposed structures (Figure 2.16).

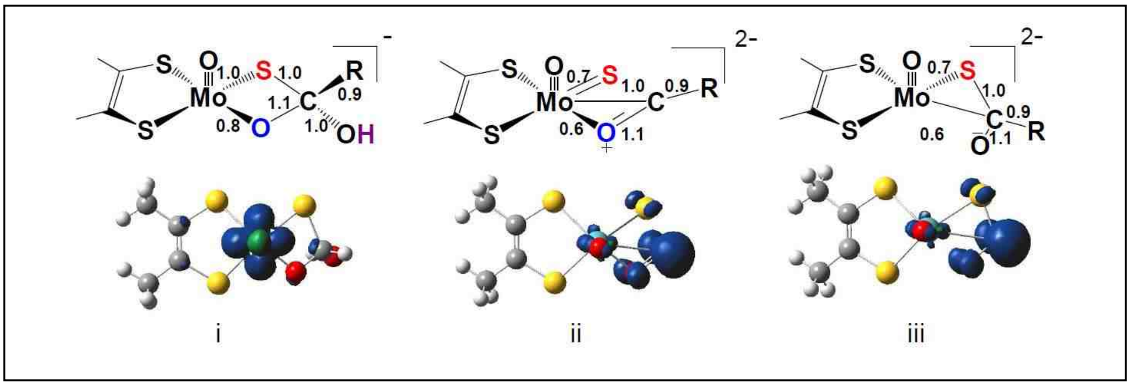

i ii iii

Figure 2.16: Proposed xanthine oxidase structures and their spin density maps (R = H). The numbers between the atoms are Mayer bond orders. Notice, Structure (i) has its spin density localized on molybdenum whereas structures (ii) and (iii) are identical and have their spin densities mostly localized on the aldehydic carbon. Secondly, there is no Mo-C bond order calculated in all the proposed structures.

Calculated spin Hamiltonian parameters for both the R and S configurations of structure (i) indicate strong agreement with the experimentally determined spin Hamiltonian parameters. However, the two differ markedly in the calculated proton hyperfine values (Tables 2.6 and 2.7). The proton hyperfine values predicted from the R configuration are in a very good agreement with the observed values (Table 2.3) which suggests that the alkyl group (R) is in the "up" orientation parallel to the Mo≡O group. This is also consistent with the observed results for E232A-XDH.

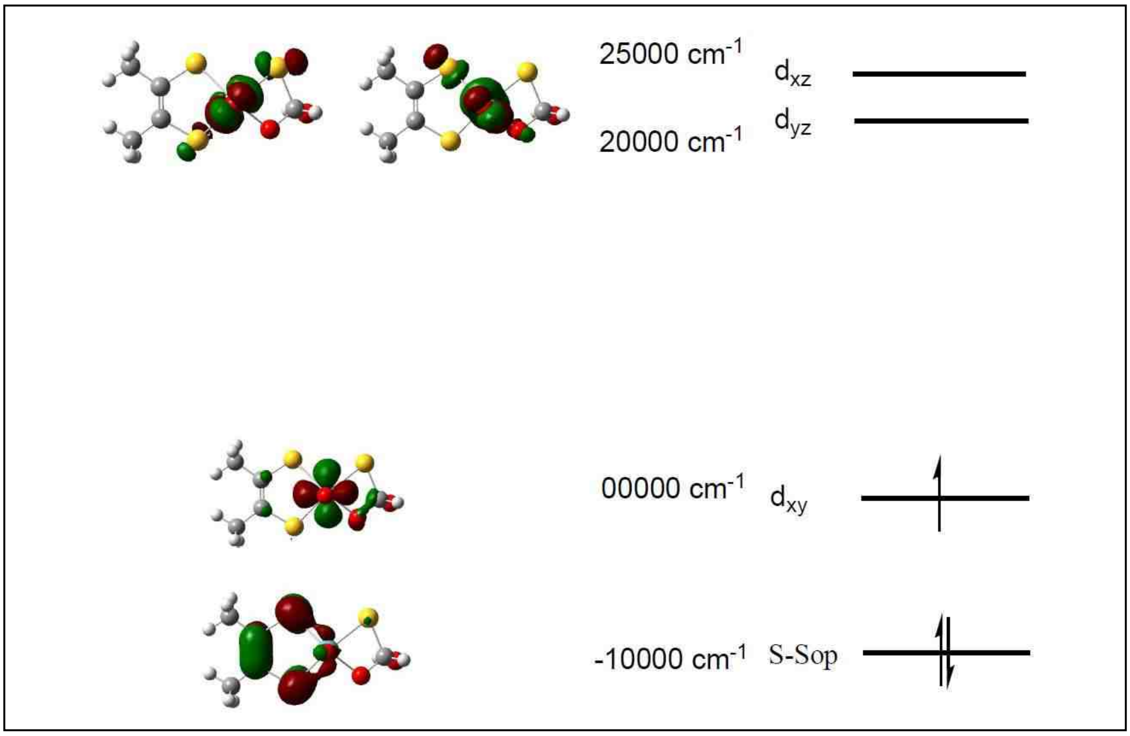

Figure 2.17: The energy level diagram for the proposed "inhibited" structure (i) showing the presence of unpaired electron in the Mo-d_{xy} orbital (SOMO).

Table 2.6: Theoretical spin Hamiltonian parameters for “inhibited” species (S-configuration)

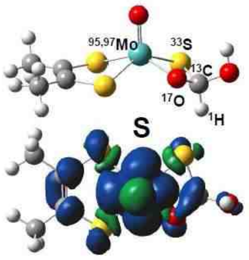

g-values	^{95,97}Mo A-values	^{13}C; A-values	^{1}H; A-values	^{17}O; A-values	^{33}S; A-values
g_z = 1.9982998	53.43	16.55	-1.42	-6.44	3.08
g_y = 1.9802235	18.06	14.31	-1.35	-2.35	0.68
g_x = 1.9595245	16.86	14.00	0.69	-1.34	-0.11
Spin density %	96.67	1.90	-0.15	1.70	-0.24

^{95,97}Mo-Aiso = 29.45, ^{95,97}Mo-Dipol = 23.98, -11.39, -12.59

^{13}C-Aiso = 14.95, ^{13}C-Adipol = 1.60, -0.64, -0.95

Table 2.7: Theoretical spin Hamiltonian parameters for “inhibited” species (R-configuration)

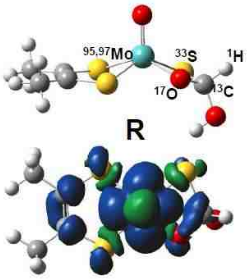

g-values	^{95,97}Mo A-values	^{13}C; A-values	^{1}H; A-values	^{17}O; A-values	^{33}S; A-values
g_z = 1.9971772	54.14	14.72	5.84	-5.88	2.76
g_y = 1.9801995	18.64	11.69	3.97	-2.63	1.08
g_x = 1.9525335	17.97	11.34	3.65	-1.67	-0.38
Spin density %	100.85	2.18	0.68	1.17	-1.66

^{95,97}Mo-Aiso = 30.25, ^{95,97}Mo-Adipol = 23.89, -11.61, -12.28

^{13}C-Aiso = 12.58, ^{13}C-Adipol = 2.14, -0.89, -1.24

Molecular orbital analysis indicates the presence of the unpaired electron being located in a Mo d_{xy} orbital (SOMO). DFT calculations using a spin restricted open shell formalism show that this orbital is separated by about 22,400 cm^{-1} from the nearly degenerate and empty Mo-d_{xz}/d_{yz} orbitals (Figure 2.17). Consequently, the g shift, $\Delta g = g_e - g_{obs}$ is relatively small (Table 2.8) with $g_{obs} < g_e$ [82]. The experimental EPR spectrum, which is highly rhombic, strongly indicates the presence of a unpaired electron in an orbital which is metal character consistent with the theoretical calculations (Figure 2.19; experimental vs. theoretical (i)).

The ^{1}H, ^{17}O and ^{33}S hyperfine tensors were also calculated (Tables 2.6 and 2.7) for formaldehyde generated "inhibited" species for comparison with either reported or observed results. Except for ^{33}S, these also gave a good agreement with the observed/reported hyperfine tensors (Table 2.8).

Table 2.8: Formaldehyde "inhibited" present data vs. reported.

FORMALDEHYDE INHIBITED - EXPERIMENTAL (PRESENT WORK)						
g-values	^{95,97}Mo A-values X10^{-4}cm^{-1}	^{13}C; A-values X10^{-4}cm^{-1}	^{1}H; A-values X10^{-4}cm^{-1}	^{17}O; A-values X10^{-4}cm^{-1}	^{33}S; A-values X10^{-4}cm^{-1}	Mo- (ZxZ) Euler Angles (Axg^{-1})
g_z = 1.9995	59.33	12.33	4.83	-	-	α = 86.75
g_y = 1.9854	23.00	15.00	3.33	-	-	β = 138.59
g_x = 1.9614	22.67	16.67	4.33	-	-	γ = 8.28
g_{iso} = 1.9821	A_{iso}= 35.00	A_{iso}= 14.67	A_{iso}= 4.16	-	-	
FORMALDEHYDE INHIBITED - THEORETICAL (PRESENT WORK; R-GEOMETRY)						
g_z = 1.9972	54.14	14.72	5.84	-5.86	2.42	α = 70.74
g_y = 1.9802	18.45	11.69	3.97	-2.06	0.85	β = 139.53
g_x = 1.9525	17.97	11.34	3.65	-1.09	-0.47	γ = -3.27
g_{iso} = 1.9766	A_{iso}= 30.19	A_{iso}= 12.58	A_{iso}= 4.49	A_{iso}= -3.00	A_{iso}= 0.93	
FORMALDEHYDE INHIBITED – EXPERIMENTAL (REPORTED)						
g_1 = 1.9911	52.53	17.50	4.06	0.55/1.06	0.55	-
g_2 = 1.9772	23.04	13.53	3.59	2.86/1.06	0.28	-
g_3 = 1.9513	52.53	13.53	5.16	1.57/1.29	1.84	-
g_{iso} = 1.9732	A_{iso}= 42.70	A_{iso}= 14.83	A_{iso}= 4.27	A_{iso}= 1.66/1.14	A_{iso}= 0.92	-
Bray and Gutteridge (1982)[87]	Pick et al (1971) [70]	Howes et al (1996) [73]	Pick et al (1971) [70]	Bray and Gutteridge (1982)[87]	Malthouse et al(1981) [74]	

The spin Hamiltonian parameters calculated for structures (ii) and (iii) showed very poor agreement with the observed values (Table 2.9). Analysis of the singly occupied molecular orbital (SOMO) wavefunction using restricted open shell DFT for these proposed structures indicate the presence of unpaired electron in a substrate carbon orbital (organic radical). Thus, the Mo(V) center has been reduced by one electron to a Mo(IV) state and the formaldehyde carbon has been oxidized by one electron (Figure 2.18).

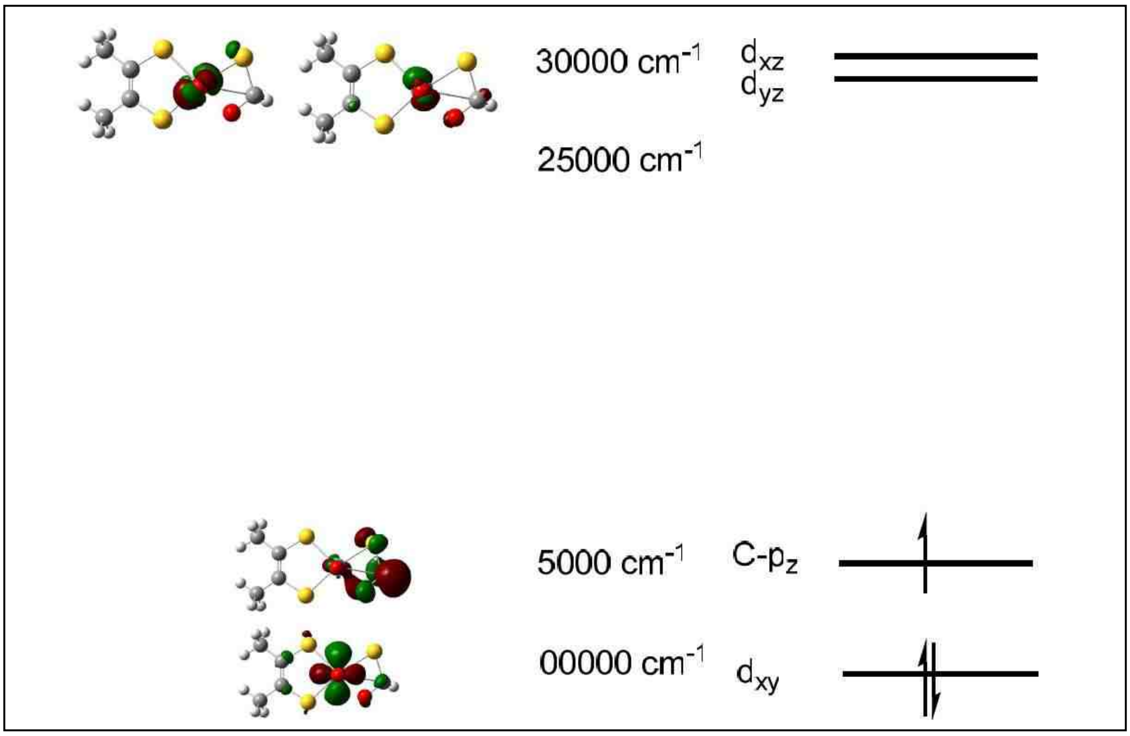

Figure 2.18: The energy level diagram for the proposed “inhibited” structures (ii) and (iii) showing the presence of unpaired electron in the carbon $2p_z$ orbital (SOMO).

However, for most organic radicals, the ground state has zero orbital angular momentum and the g-factors are very close to the free electron value (g_e = 2.0023). The g shift, $\Delta g = g_{obs} - g_e$ is consequently small. The calculated higher g values (Table 2.9) of the “inhibited” structures (ii) and (iii) is presumably due to mixing of the SOMO (singly occupied orbital (C_{pz})) and the next orbital of different symmetry which is closest in energy [83]. The SOMO for structure (ii) or (iii) is separated from the next higher lying orbitals Mo-d_{xz}/d_{yz} by approximately 25,000 cm^{-1} suggesting a significant reduction of mixing between the C_{pz} and the Mo-$d_{xz/yz}$ orbitals. However, this SOMO is separated by only 5300 cm^{-1} from HOMO-1 (Mo-d_{xy}) which suggests a significant interaction between these two orbitals. It has been shown that for free radicals, the mixing of the singly occupied molecular orbital (SOMO) with an orbital of lower energy leads to $g_{obs} > g_e$ and mixing with an orbital of higher energy leads to $g_{obs} < g_e$ as illustrated by equation (vii) which holds true under the conditions $\zeta_A << \Delta E_A$ [83].

$$g_{obs} - g_e = \sum_A \rho_A \zeta_A \Big/ \Delta E_A \quad \text{..(vii)}$$

Where summation is over all the atoms A in the radical, ρ_A is the spin density on atom A, ζ_A is the spin orbit coupling constant for atom A and ΔE_A is the energy difference between a SOMO and the next orbital of different symmetry closest in energy. Figure 2.19 shows poor agreement between the experimental and theoretical EPR spectra ((ii) and (iii)) of these proposed structures.

Table 2.9: Theoretical EPR parameters for Mo(V) proposed “inhibited” structures

	Axis			Average	Euler Angles		
Parameters	z	y	x		α	β	γ
Proposed structure (i) (charge = -1)							
g	1.9972	1.9802	1.9525	1.9766			
A(^{95,97}Mo) x 10^{-4} cm^{-1}	54.14	18.45	17.97	30.19	70.74	139.53	-3.27
A(^{13}C) x 10^{-4} cm^{-1}	14.72	11.69	11.34	12.58	90.00	69.15	56.58

A(^{1}H) x 10^{-4} cm^{-1}	5.84	3.97	3.65	4.49	9.51	102.89	-81.87
Proposed structure (ii) (charge = -2)							
g	2.0128	2.0046	1.9708	1.9960			
A(^{95,97}Mo) x 10^{-4} cm^{-1}	5.91	-2.09	1.75	1.86	-12.64	57.25	39.86
A(^{13}C) x 10^{-4} cm^{-1}	102.72	45.70	45.46	64.63	-23.28	20.28	-19.38
A(^{1}H) x 10^{-4} cm^{-1}	18.11	6.34	-0.55	7.97	-53.95	56.43	1.17
Proposed structure (iii) (charge = -2)							
g	2.0128	2.0046	1.9708	1.9961			
A(^{95,97}Mo) x 10^{-4} cm^{-1}	5.90	-2.10	1.76	1.85	-12.82	57.45	40.02
A(^{13}C) x 10^{-4} cm^{-1}	102.75	45.73	45.49	64.66	-23.10	20.28	-19.20
A(^{1}H) x 10^{-4} cm^{-1}	18.12	6.35	-0.53	7.98	-53.19	56.29	1.17

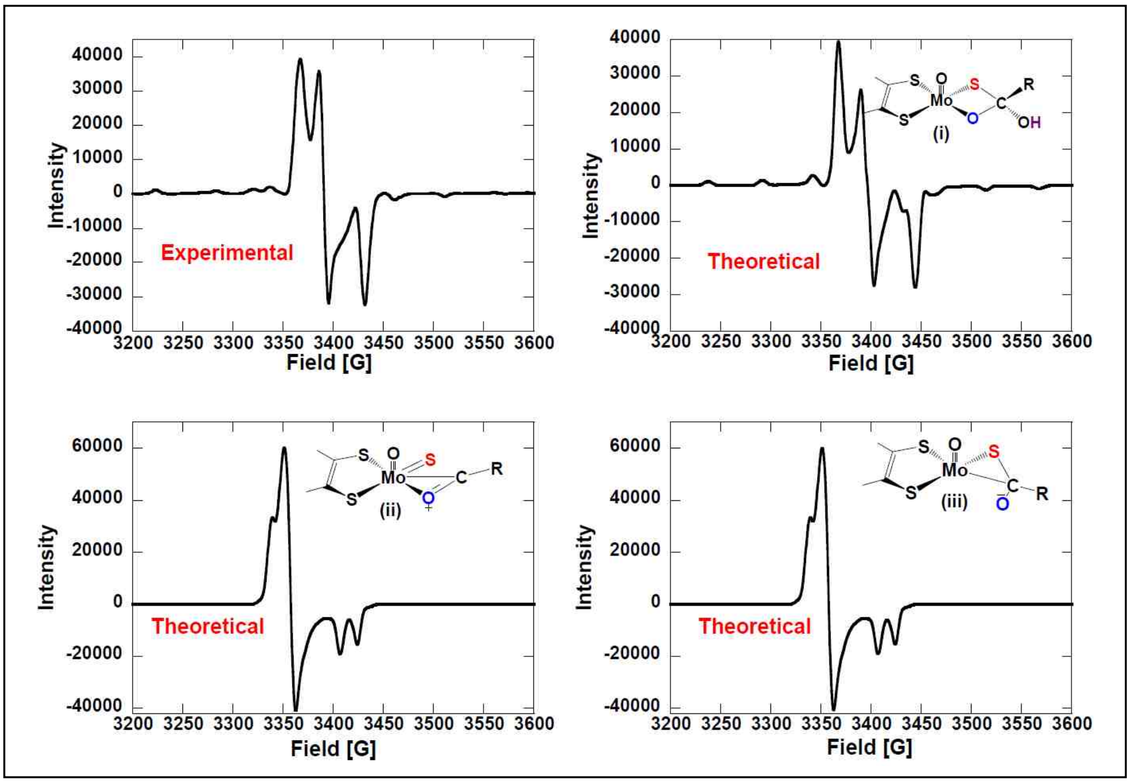

Figure 2.19: Comparison of the theoretical formaldehyde (R = H) “inhibited” EPR spectra of the proposed xanthine oxidase structures with the observed formaldehyde generated xanthine dehydrogenase “inhibited” spectrum. Notice; structure (i) is in a very good agreement with the observed EPR spectrum whereas structures (ii) and (iii) (organic radicals) are identical and do not agree with the experimental spectrum. The little rhombicity for structures (ii) and (iii) indicates reduction of metal character and increase in ligand character. The splitting at g_x is due to a formaldehyde proton (R = H).

Figure 2.20 shows the comparison between theoretical and experimental EPR spectra of isotopically labeled ^{13}C-formaldehyde, 3-pyridinecarboxaldehyde, 2-pyridinecarboxaldehyde and acetaldehyde generated xanthine oxidase “inhibited” for structure (i). There is also a good agreement between the calculated and observed spectra for all these substrates. However, in this “inhibited” structure, the aldehyde is bound in a tetrahedral fashion stabilized by C-S bond formation and excludes the assertion that there is Mo-C bond in the “inhibited” species.

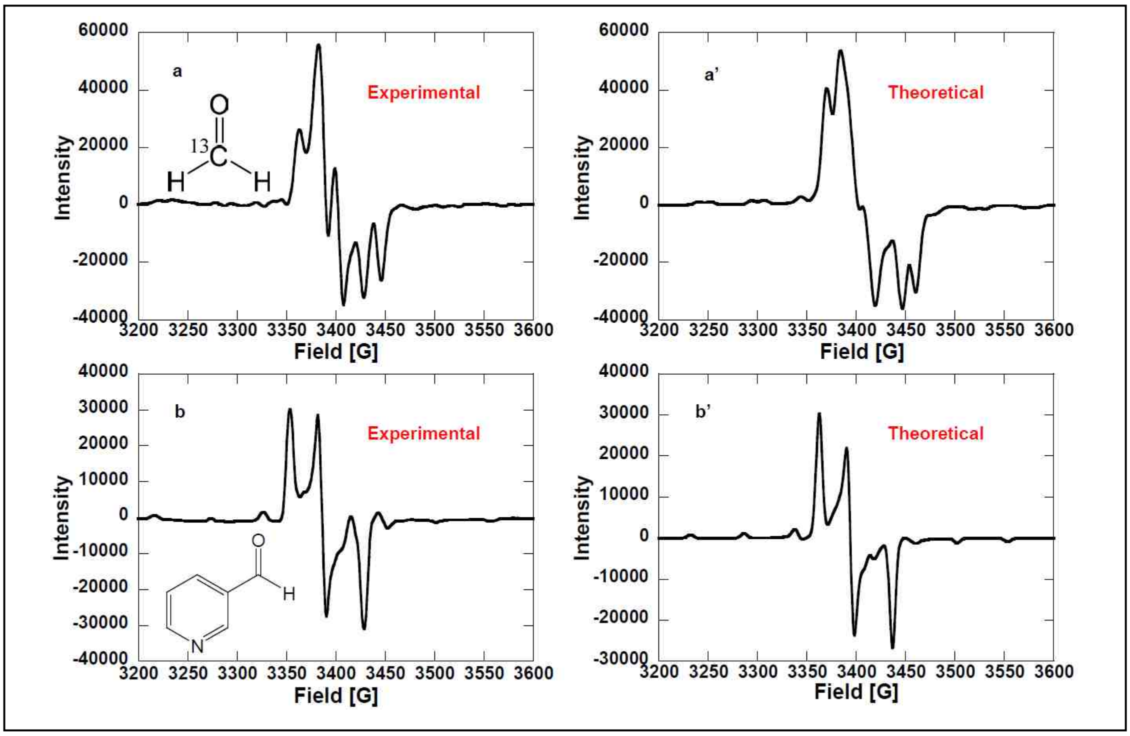
a
Experimental
a'
Theoretical
b
Experimental
b'
Theoretical
Intensity
Field [G]
O
13
C
H
H
N
H
60000
40000
20000
0
-20000
-40000
30000
10000
-10000
-30000
3200 3250 3300 3350 3400 3450 3500 3550 3600

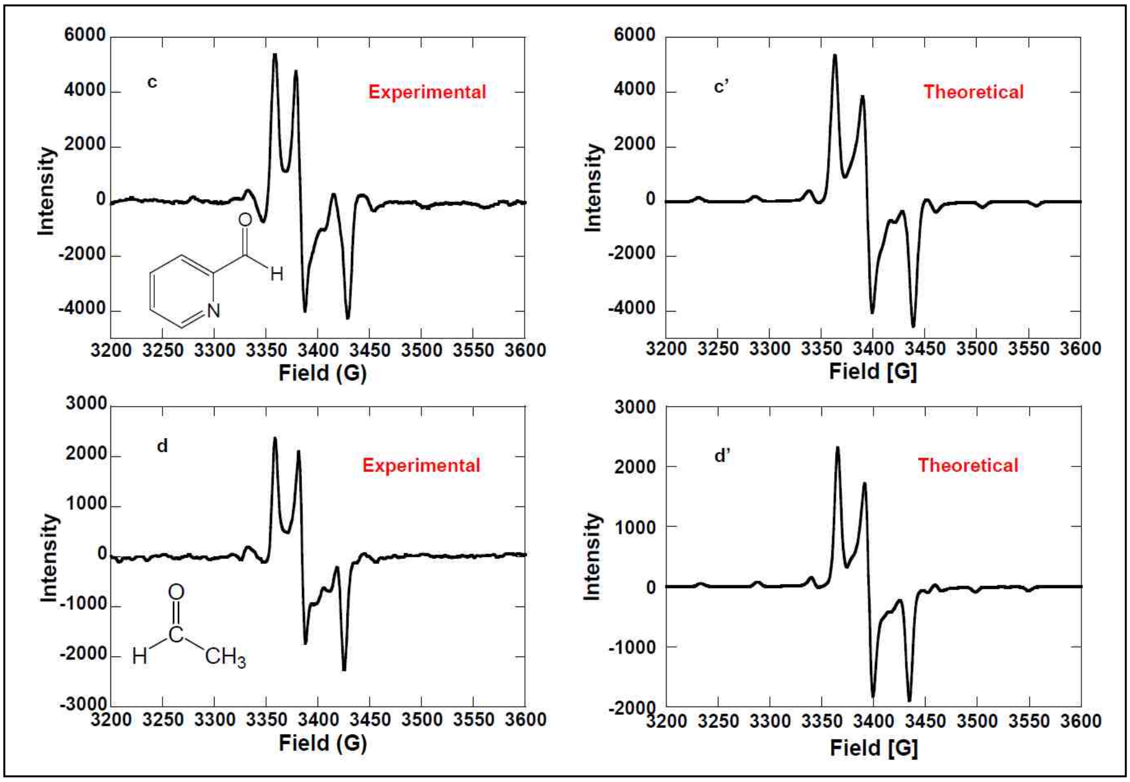
c
Experimental
c'
Theoretical
d
Experimental
d'
Theoretical
Intensity
Field (G)
Field [G]
O
H
N
C
CH_3
6000
4000
2000
0
-2000
-4000
3000
1000
-1000
-3000
3200 3250 3300 3350 3400 3450 3500 3550 3600

Figure 2.20: Comparison of the theoretical with the observed “inhibited” spectra for (a) ^{13}C-formaldehyde (b) 3-pyridinecarboxaldehyde, (c) 2-pyridinecarboxaldehyde and (d) acetaldehyde generated XO/XDH. (a’), (b’), (c’) and (d’) are their corresponding theoretical spectra respectively.

2.5.4 Molecular Orbital Description of XO/XDH Derived “Inhibited” Structure

2.5.4.1 Ligand Field Splitting and Nature of the β-LUMO

The density functional theory calculations using spin unrestricted formalism for the “inhibited” species shows a splitting of the t_{2g} sublevel that results in the isolation of the lowest unoccupied Mo-d_{xy} orbital (LUMO) which is separated by ~ 14000 cm^{-1} from the higher lying d_{yz}/d_{xz} orbitals (Figure 2.21).

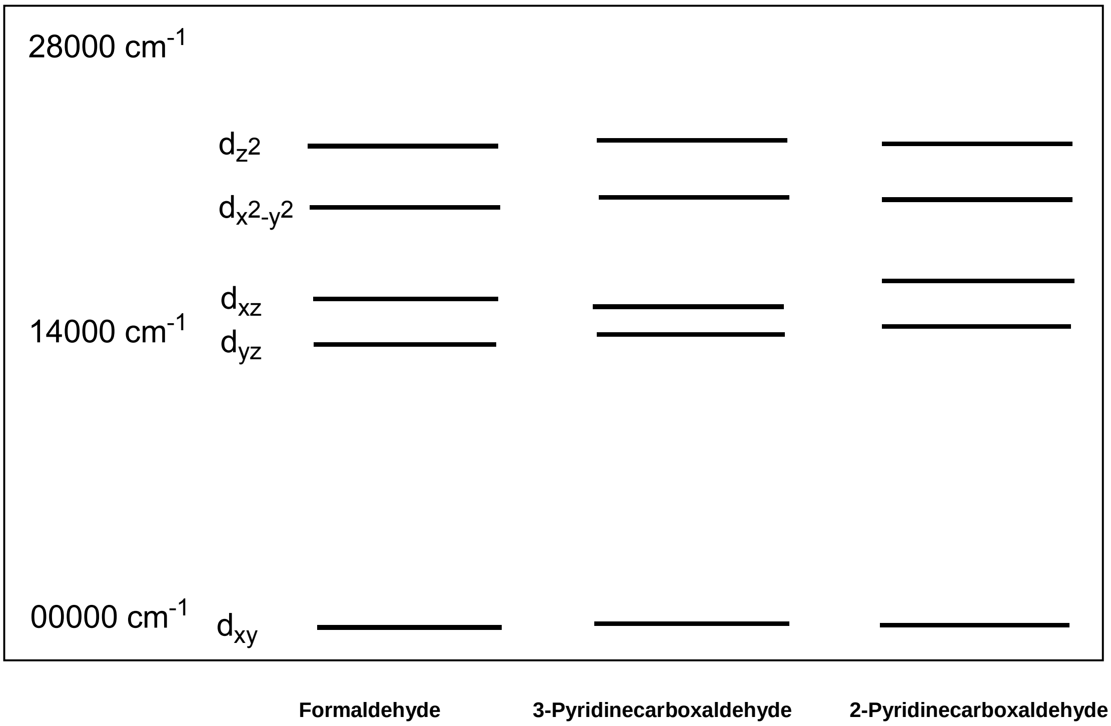
28000 cm^{-1}
d_{z^2}
$d_{x^2-y^2}$
d_{xz}
14000 cm^{-1}
d_{yz}
00000 cm^{-1}
d_{xy}
Formaldehyde
3-Pyridinecarboxaldehyde
2-Pyridinecarboxaldehyde

Figure 2.21: calculated ligand field molecular orbital energies for formaldehyde, 3-pyridinecarboxaldehyde and 2-pyridinecarboxaldehyde XO/XDH “inhibited” structures. The molecular orbital energies have been normalized to Mo-d_{xy} orbital (LUMO).

This splitting of the t_{2g} sublevel originates primarily from the strong interactions of the apical oxo ligand with the Mo-d_{xz} and d_{yz} orbitals. Further separation of the Mo-d_{xy} redox orbital from Mo-d_{xz} and d_{yz} orbitals in “inhibited” species is consistent with stabilization of the Mo-d_{xy} at a Mo(IV) state of XO enzyme during its turnover. At this state, the orbital interacts with thiol leading to a stabilization of about 7.4 kcal/mol relative to Mo(VI) state which strongly π interacts with a sulfido (Figure 2.32). However, during enzyme turnover the sulfido is converted to sulfurhydryl when the enzyme is reduced to Mo(IV). The ligand field splitting depicting the position of the redox orbital for different substrates is presented in Figure 2.21. Its orbital composition is proportional to the amount of its spin density. Comparison of the LUMO and spin density maps for formaldehyde, 3-pyridinecarboxaldehyde, 2-pyridinecarboxaldehyde and acetaldehyde “inhibited structures are summarized in Tables 2.10 and 2.11 respectively.

Table 2.10: Mo d_{xy} (β – LUMO) composition for the “inhibited” species

	Mo%	S-S%	S%	μ-O%	O%	C%
Formaldehyde	79.82	6.37	2.07	2.34	0.27	2.11
3-Pyridinecarboxaldehyde	77.02	7.17	2.41	2.19	0.29	2.39
2-Pyridinecarboxaldehyde	77.30	6.92	2.37	2.16	0.28	2.41
Acetaldehyde	78.98	6.61	2.23	2.44	0.27	2.35

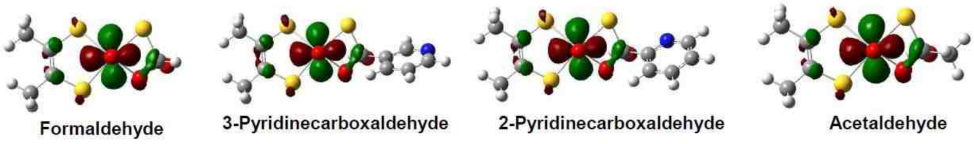
Formaldehyde
3-Pyridinecarboxaldehyde
2-Pyridinecarboxaldehyde
Acetaldehyde

Table 2.11: Spin density composition for the “inhibited” species

	Mo%	S-S%	S%	μ-O%	O%	C%
Formaldehyde	100.85	-1.60	-1.66	1.17	-6.75	2.18
3-Pyridinecarboxaldehyde	96.00	0.26	-1.06	1.33	-5.54	2.23
2-Pyridinecarboxaldehyde	96.44	-0.08	-1.08	1.31	-5.52	2.25
Acetaldehyde	98.21	-0.79	-1.33	1.49	-5.80	2.33

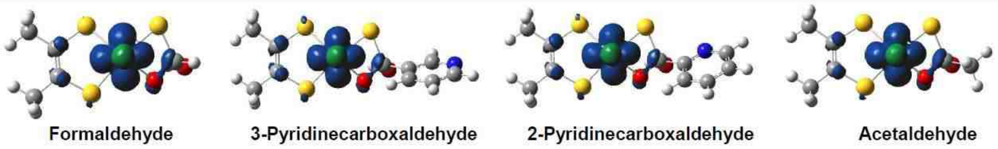
Formaldehyde
3-Pyridinecarboxaldehyde
2-Pyridinecarboxaldehyde
Acetaldehyde

Formaldehyde generated XO/XDH “inhibited” has the largest spin population on Mo, and this directly correlates with the magnitude of the observed hyperfine tensor (Tables 2.2 and 2.3). Formaldehyde also shows the smallest spin delocalization to thiol S and C atoms compared to the other substrates, which directly correlates to the reduced covalency to these atomic orbitals.

Consequently, the g tensor for formaldehyde generated “inhibited” is comparably smaller whereas the A tensor is comparably larger.

2.5.4.2 The Magnitude and Orientations of the g and Hyperfine Tensors for ^{95,97}Mo, ^{13}C, ^{1}H, ^{17}O and ^{33}S of the “Inhibited” Structure

All g- and A-tensor calculations have been performed for the following cartesian coordinate system defined as the molecular frame: The vector along the Mo=O bond defines the Z direction. The X and Y axes lie along the plane perpendicular to the Z axis with X axis bisecting the dithiolenes (Figure 2.22 and 2.23). The orientations of the g- and A-tensors relative to this molecular frame were calculated using using the program EasySpin [204] which utilizes a ZYZ convention. The results are presented in Figures 2.22 and 2.23. The calculated g and hyperfine tensors for ^{95,97}Mo, ^{13}C, ^{1}H, ^{17}O and ^{33}S of the “inhibited” derived structure are tabulated in Table 2.7. The orientations of g- and A-tensors with respect to the molecular frame are depicted in Figures 2.22 (top view), 2.23 (side view) drawn from ORCA output files in Figure 2.24. Figure 2.22 shows that, the structure of “inhibited” possesses a pseudo mirror plane (XZ) that bisects the dithiolene sulfur donors and contains the Mo≡O unit. The orientation of the g-tensor (g_x g_y g_z) from the calculation is such that $g_x \neq g_y \neq g_z$. The ZYZ convention indicates rotations of about α = 65^0, β = 137^0 and γ = -88^0 relative to the molecular frame (X Y Z) (Figures 2.22 and 2.23). The g-tensor is also rotated off the A-tensor by α = 70.74, β = 139.53, γ = -3. These larger rotations of the g-tensor relative to the A-tensor have previously been shown to result from increased Mo-ligand covalency [84-86].

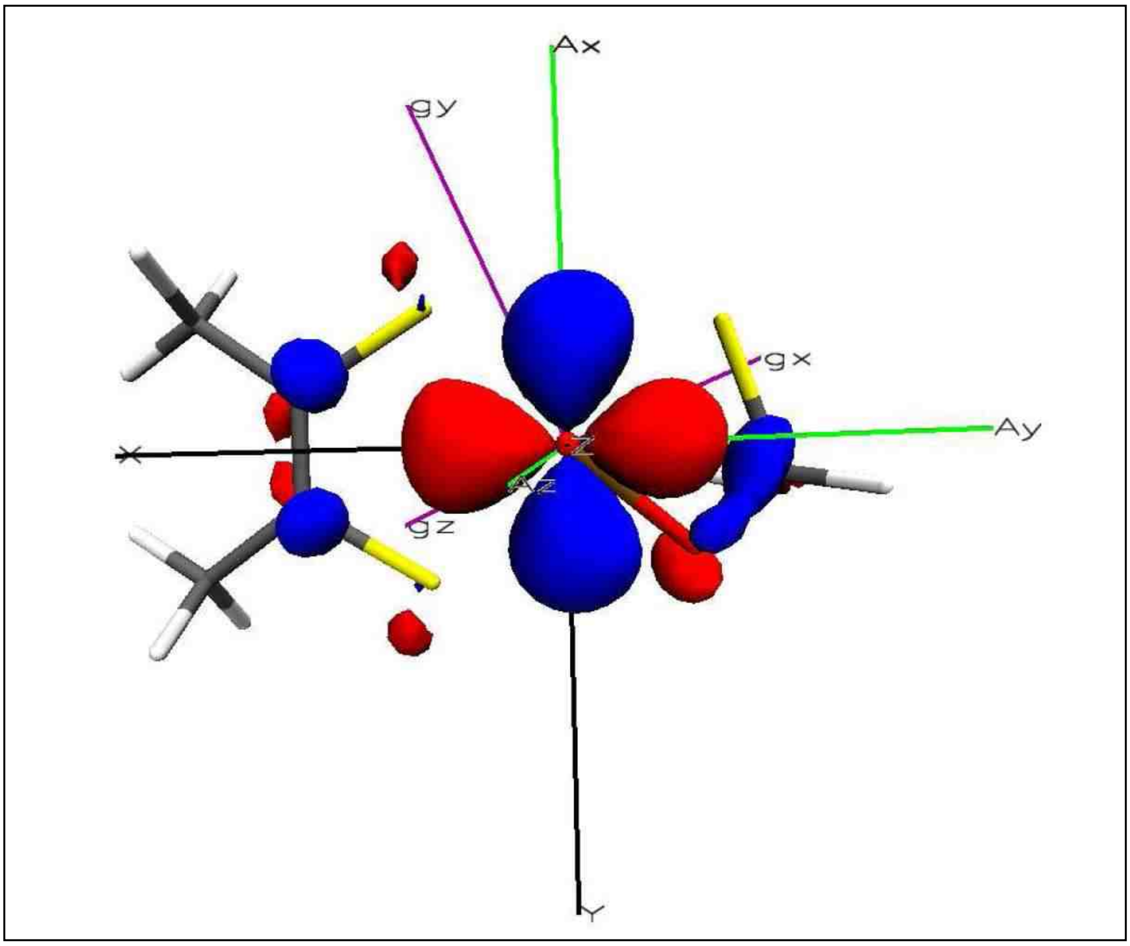

Figure 2.22: Schematic representation of the top view (Z coming out of the plane) of the molecular frame (X Y Z) relative to the laboratory frames for g (g_x g_y g_z) and A (A_x A_y A_z) tensors as drawn from the orientation matrices in ORCA output files. The g-tensor is highly rotated from the symmetry axes (X Y Z) of the “inhibited” complex compared to the A-tensor. Using the ZXZ convention, the largest value of the A- tensor is rotated 4.75^0 away from Z direction (Mo=O)

whereas the largest value of the g-tensor (g_z) that has the smallest Δg shift is rotated 137^0 from Z-direction (Mo=O).

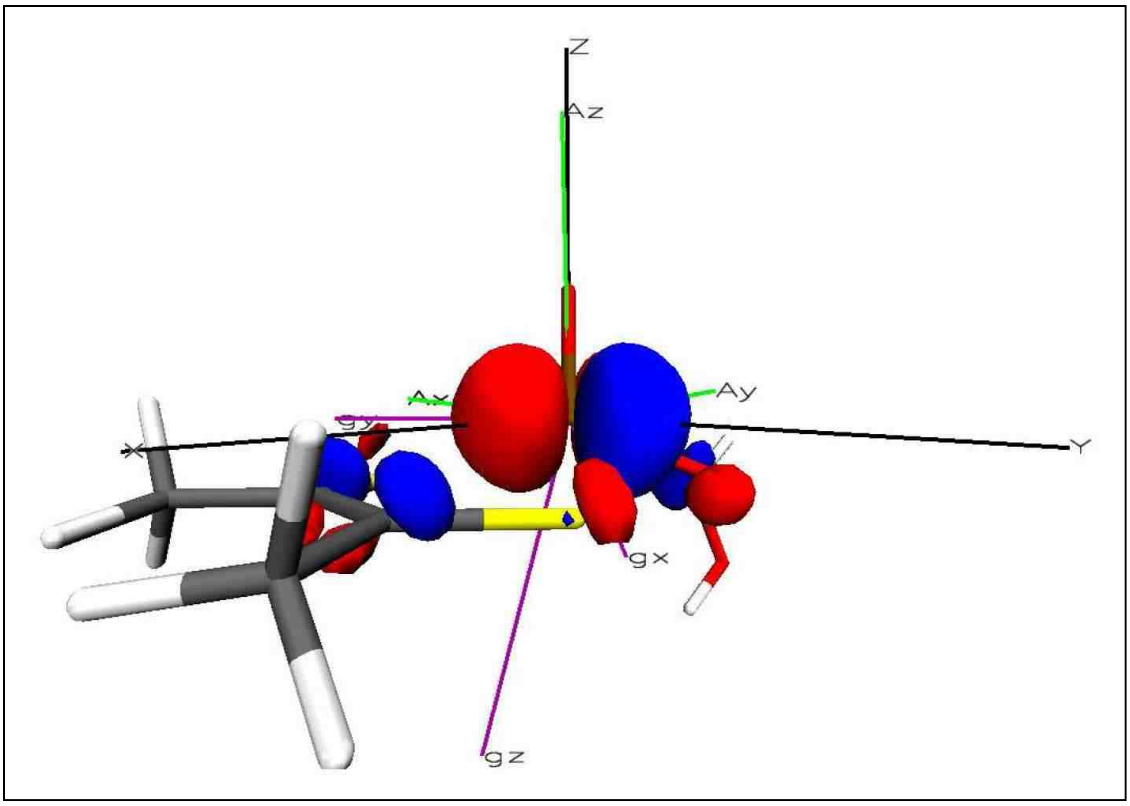

Figure 2.23: Schematic representation of the side view of the molecular frame (X Y Z) relative to the laboratory frames for g (g_x g_y g_z) and A (A_x A_y A_z) tensors as drawn from the orientation matrices in ORCA output files.

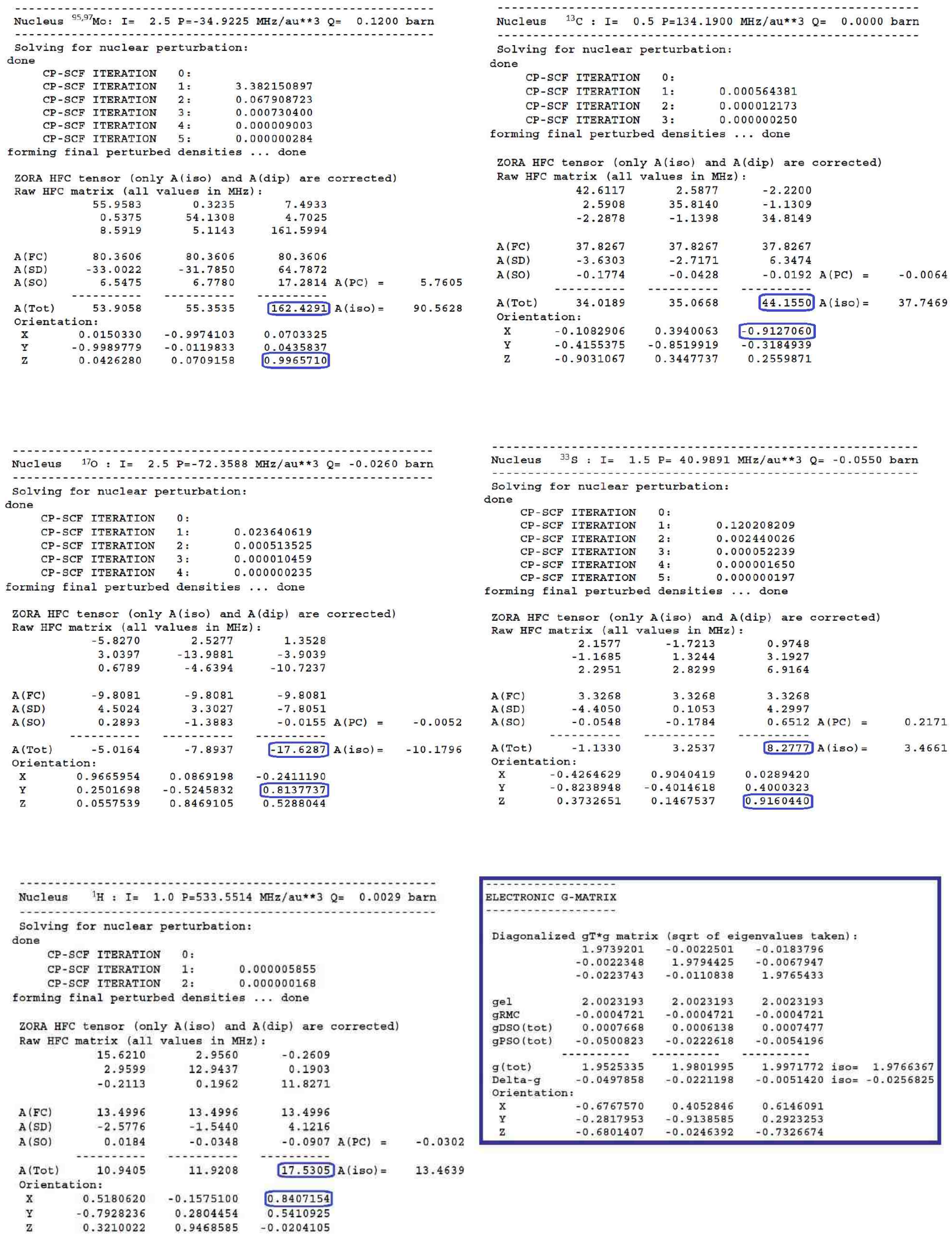

```
 ---------------------------------------------------------
 Nucleus 95,97Mo: I=  2.5 P=-34.9225 MHz/au**3 Q=  0.1200 barn
 ---------------------------------------------------------
 Solving for nuclear perturbation:
done
     CP-SCF ITERATION   0:
     CP-SCF ITERATION   1:      3.382150897
     CP-SCF ITERATION   2:      0.067908723
     CP-SCF ITERATION   3:      0.000730400
     CP-SCF ITERATION   4:      0.000009003
     CP-SCF ITERATION   5:      0.000000284
forming final perturbed densities ... done

 ZORA HFC tensor (only A(iso) and A(dip) are corrected)
 Raw HFC matrix (all values in MHz):
            55.9583       0.3235       7.4933
             0.5375      54.1308       4.7025
             8.5919       5.1143     161.5994

 A(FC)      80.3606      80.3606      80.3606
 A(SD)     -33.0022     -31.7850      64.7872
 A(SO)       6.5475       6.7780      17.2814 A(PC)  =     5.7605
        ----------   ----------   ----------
 A(Tot)     53.9058      55.3535     162.4291 A(iso)=    90.5628
 Orientation:
  X       0.0150330   -0.9974103    0.0703325
  Y      -0.9989779   -0.0119833    0.0435837
  Z       0.0426280    0.0709158    0.9965710
```

```
 ---------------------------------------------------------
 Nucleus   13C : I=  0.5 P=134.1900 MHz/au**3 Q=  0.0000 barn
 ---------------------------------------------------------
 Solving for nuclear perturbation:
done
     CP-SCF ITERATION   0:
     CP-SCF ITERATION   1:      0.000564381
     CP-SCF ITERATION   2:      0.000012173
     CP-SCF ITERATION   3:      0.000000250
forming final perturbed densities ... done

 ZORA HFC tensor (only A(iso) and A(dip) are corrected)
 Raw HFC matrix (all values in MHz):
            42.6117       2.5877      -2.2200
             2.5908      35.8140      -1.1309
            -2.2878      -1.1398      34.8149

 A(FC)      37.8267      37.8267      37.8267
 A(SD)      -3.6303      -2.7171       6.3474
 A(SO)      -0.1774      -0.0428      -0.0192 A(PC)  =    -0.0064
        ----------   ----------   ----------
 A(Tot)     34.0189      35.0668      44.1550 A(iso)=    37.7469
 Orientation:
  X      -0.1082906    0.3940063   -0.9127060
  Y      -0.4155375   -0.8519919   -0.3184939
  Z      -0.9031067    0.3447737    0.2559871
```

```
 ---------------------------------------------------------
 Nucleus   17O : I=  2.5 P=-72.3588 MHz/au**3 Q= -0.0260 barn
 ---------------------------------------------------------
 Solving for nuclear perturbation:
done
     CP-SCF ITERATION   0:
     CP-SCF ITERATION   1:      0.023640619
     CP-SCF ITERATION   2:      0.000513525
     CP-SCF ITERATION   3:      0.000010459
     CP-SCF ITERATION   4:      0.000000235
forming final perturbed densities ... done

 ZORA HFC tensor (only A(iso) and A(dip) are corrected)
 Raw HFC matrix (all values in MHz):
            -5.8270       2.5277       1.3528
             3.0397     -13.9881      -3.9039
             0.6789      -4.6394     -10.7237

 A(FC)      -9.8081      -9.8081      -9.8081
 A(SD)       4.5024       3.3027      -7.8051
 A(SO)       0.2893      -1.3883      -0.0155 A(PC)  =    -0.0052
        ----------   ----------   ----------
 A(Tot)     -5.0164      -7.8937     -17.6287 A(iso)=   -10.1796
 Orientation:
  X       0.9665954    0.0869198   -0.2411190
  Y       0.2501698   -0.5245832    0.8137737
  Z       0.0557539    0.8469105    0.5288044
```

```
 ---------------------------------------------------------
 Nucleus   33S : I=  1.5 P= 40.9891 MHz/au**3 Q= -0.0550 barn
 ---------------------------------------------------------
 Solving for nuclear perturbation:
done
     CP-SCF ITERATION   0:
     CP-SCF ITERATION   1:      0.120208209
     CP-SCF ITERATION   2:      0.002440026
     CP-SCF ITERATION   3:      0.000052239
     CP-SCF ITERATION   4:      0.000001650
     CP-SCF ITERATION   5:      0.000000197
forming final perturbed densities ... done

 ZORA HFC tensor (only A(iso) and A(dip) are corrected)
 Raw HFC matrix (all values in MHz):
             2.1577      -1.7213       0.9748
            -1.1685       1.3244       3.1927
             2.2951       2.8299       6.9164

 A(FC)       3.3268       3.3268       3.3268
 A(SD)      -4.4050       0.1053       4.2997
 A(SO)      -0.0548      -0.1784       0.6512 A(PC)  =     0.2171
        ----------   ----------   ----------
 A(Tot)     -1.1330       3.2537       8.2777 A(iso)=     3.4661
 Orientation:
  X      -0.4264629    0.9040419    0.0289420
  Y      -0.8238948   -0.4014618    0.4000323
  Z       0.3732651    0.1467537    0.9160440
```

```
 ---------------------------------------------------------
 Nucleus    1H : I=  1.0 P=533.5514 MHz/au**3 Q=  0.0029 barn
 ---------------------------------------------------------
 Solving for nuclear perturbation:
done
     CP-SCF ITERATION   0:
     CP-SCF ITERATION   1:      0.000005855
     CP-SCF ITERATION   2:      0.000000168
forming final perturbed densities ... done

 ZORA HFC tensor (only A(iso) and A(dip) are corrected)
 Raw HFC matrix (all values in MHz):
            15.6210       2.9560      -0.2609
             2.9599      12.9437       0.1903
            -0.2113       0.1962      11.8271

 A(FC)      13.4996      13.4996      13.4996
 A(SD)      -2.5776      -1.5440       4.1216
 A(SO)       0.0184      -0.0348      -0.0907 A(PC)  =    -0.0302
        ----------   ----------   ----------
 A(Tot)     10.9405      11.9208      17.5305 A(iso)=    13.4639
 Orientation:
  X       0.5180620   -0.1575100    0.8407154
  Y      -0.7928236    0.2804454    0.5410925
  Z       0.3210022    0.9468585   -0.0204105
```

```
-------------------
ELECTRONIC G-MATRIX
-------------------

 Diagonalized gT*g matrix (sqrt of eigenvalues taken):
             1.9739201   -0.0022501   -0.0183796
            -0.0022348    1.9794425   -0.0067947
            -0.0223743   -0.0110838    1.9765433

 gel         2.0023193    2.0023193    2.0023193
 gRMC       -0.0004721   -0.0004721   -0.0004721
 gDSO(tot)   0.0007668    0.0006138    0.0007477
 gPSO(tot)  -0.0500823   -0.0222618   -0.0054196
          ----------   ----------   ----------
 g(tot)      1.9525335    1.9801995    1.9971772 iso=  1.9766367
 Delta-g    -0.0497858   -0.0221198   -0.0051420 iso= -0.0256825
 Orientation:
  X         -0.6767570    0.4052846    0.6146091
  Y         -0.2817953   -0.9138585    0.2923253
  Z         -0.6801407   -0.0246392   -0.7326674
```

Figure 2.24: Part of ORCA output files showing the orientation of the g-tensor (in a box) and the largest component of the hyperfine tensors relative to the molecular frame for ^{95,97}Mo, ^{13}C, ^{1}H, ^{17}O and ^{33}S isotopes. The numbers circled in

blue on the **A (Tot)** and in the **orientation** matrix represent the largest hyperfine component and its orientation coordinate respectively. When the hyperfine tensor is perfectly oriented along either X or Y or Z coordinated then its value is a unit.

The ^{95,97}Mo hyperfine tensor components are axial and all positive, with the largest component of the ^{95,97}Mo hyperfine tensor (A_z) oriented 4.75^0 away from Mo≡O bond. The A-tensor yields A_{iso} = 30.25 x 10^{-4} cm^{-1} and A_{dip}: A_z = 23.89 x 10^{-4} cm^{-1}, A_y = -11.61 x 10^{-4} cm^{-1}, A_x = -12.28 x 10^{-4} cm^{-1}. The anisotropy in the dipolar term, A_{dip}, is indicative of a $Mo_{d_{xy}}$ type singly occupied molecular orbital (SOMO) wave function. The analysis of ^{13}C hyperfine tensor also yields an axial pattern with all signs of the hyperfine tensor components being positive. The largest ^{13}C hyperfine tensor component is oriented along the X direction of the molecular frame such that one lobe of the $Mo_{d_{xy}}$ orbital, which bisects the dithiolene sulfurs, points in the direction of the tetrahedral C sp_x hybrid orbital. These $Mo_{d_{xy}}$ and C sp_x orbitals are aligned for a potential net pseudo-sigma bonding interaction, although, the calculated Mo-C Mayer bond order is zero. This explains the nature of the ^{13}C hyperfine tensor. The isotropic value (A_{iso}) is 12.58 x 10^{-4} cm^{-1} whereas the anisotropic values ($A_{dipolar}$) are A_z = 2.14 x 10^{-4} cm^{-1}, A_y = -0.89 x 10^{-4} cm^{-1}, A_x = -1.24 x 10^{-4} cm^{-1}. The calculated ^{1}H hyperfine tensor has all positive components of the tensor with the major component oriented along X direction of the molecular frame and yields A_{iso} = 4.49 x 10^{-4} cm^{-1} and $A_{dipolar}$: A_z = 1.35 x 10^{-4} cm^{-1}, A_y = -0.52 x 10^{-4} cm^{-1}, A_x = -0.84 x 10^{-4} cm^{-1}. The ^{17}O analysis yielded all negative hyperfine tensor components (A_z,A_y,A_x) = (-

5.88,-2.63,-1.67) which give A_{iso} = -3.39 x 10^{-4} cm^{-1} and $A_{dipolar}$: A_z = -2.49 x 10^{-4} cm^{-1}, A_y = -0.76 x 10^{-4} cm^{-1}, A_x = -1.72 x 10^{-4} cm^{-1}. On the other hand the ^{33}S isotope yielded the smallest values of the hyperfine tensor components, (A_z,A_y,A_x) = (2.76,1.08,-0.38) which are rhombic with a negative component along the X direction (A_x). However, the major component of the hyperfine tensor lies along the Z direction. Further analysis of this tensor indicated a larger contribution from the anisotropic part, $A_{dipolar}$: A_z = 1.61 x 10^{-4} cm^{-1}, A_y = -0.07 x 10^{-4} cm^{-1}, A_x = -1.53 x 10^{-4} cm^{-1} than the isotropic contribution, A_{iso} = 1.15 x 10^{-4} cm^{-1}.

2.6 Discussion

2.6.1 The Structure of XO/XDH "Inhibited" Signal Giving Species

The origin of the derived structure lies on earlier work done by Howes et al, 1990 [16] who proposed it based on ^{1}H-ENDOR with incorporation of ideas from the basic structure deduced by Bray et al, 1988 [15] (hyperfine coupling tensors of $^{95,97}Mo$, ^{17}O, ^{33}S of the 'very rapid' and 'rapid' type species from multifrequency EPR), to ^{17}O hyperfine coupling [87] and ^{33}S hyperfine coupling [74] of the "inhibited" species. However, later in 1994 and 1996, this structure was excluded and a different structure involving a Mo-C bond formation in "inhibited" species was proposed [72,73] (Figure 2.5 (ii)). This was based on strong ^{13}C hyperfine coupling tensors (A_1 = 17.50 x 10^{-4} cm^{-1}, A_2 = 13.53 x 10^{-4} cm^{-1}, A_3 = 13.53 x 10^{-4} cm^{-1}; A_{iso} = 14.83 x 10^{-4} cm^{-1}) of the formaldehyde carbon to the molybdenum spin observed from ^{13}C-ENDOR. His analysis of the dipolar coupling components of this tensor indicated Mo-C distances of about 1.9Å and hence the proposal of structure (ii) in Figure 2.5. Deeth and co-workers [76] performed calculations on various “inhibited” models with Amsterdam Density Functional (ADF) program and a local density approximation functional (LDA) for geometry optimizations. He compared his results with the short Mo-C distance estimated from Howes and his co-workers and thus proposed structure (iii) in Figure 2.5. He obtained a relatively short Mo-C bond length of about 2.2 Å for structure (iii) and also strongly suggested the existence of Mo-C bond formation. However, Manikandan et al, 2001 [88] criticized the method used by Howes et al, to estimate the short Mo-C bond length and consequently the existence of Mo-C bond in the “inhibited” species. Manikandan and his co-workers employed the same, point dipolar model used by Howes et al, for approximation of the distance r of a given nucleus located at a distance r from a dipole but considered a different point of view [88]. In their analysis, they accounted for the local contribution from spin density on carbon which gives rise to both isotropic and anisotropic hyperfine coupling as opposed to Howes et al who considered anisotropic contribution for estimation of Mo-C distance as entirely arising from nonlocal interaction between the unpaired spin density on Mo and the ^{13}C. The information extracted from his analysis based on the magnitudes of the ^{13}C hyperfine tensor observed by Howes et al, indicated unrealistic sp hybridization of ^{13}C for a Mo-C distance of 1.95Å. The reasonable sp^2 hybridization indicated a Mo-C bond distance of about 2.4Å whereas the sp^3 hybridization indicated a Mo-C distance greater than 4Å. However, in this work, geometry optimization for the “inhibited” derived structure at the B3LYP level of DFT in spin-unrestricted mode reveal a Mo-C bond length of about 2.75Å and a Mayer's bond order of zero between Mo and C. The s and p spin densities calculations at ^{13}C nucleus indicate an approximately sp^2 and sp^3 hybridization for S and R geometries respectively at ^{13}C reasonably consistent to Manikandan et al work and therefore strongly suggests the absence of the Mo-C bond formation in the "inhibited" species. However, analyses of the Mo-C overlap integral for the β-LUMO (that has a direct correlation to the spin density) using overlap population density of states (OPDOS) indicates strong anti-bonding character between Mo-d_{xy} and the C-p orbitals (Figure 2.25).

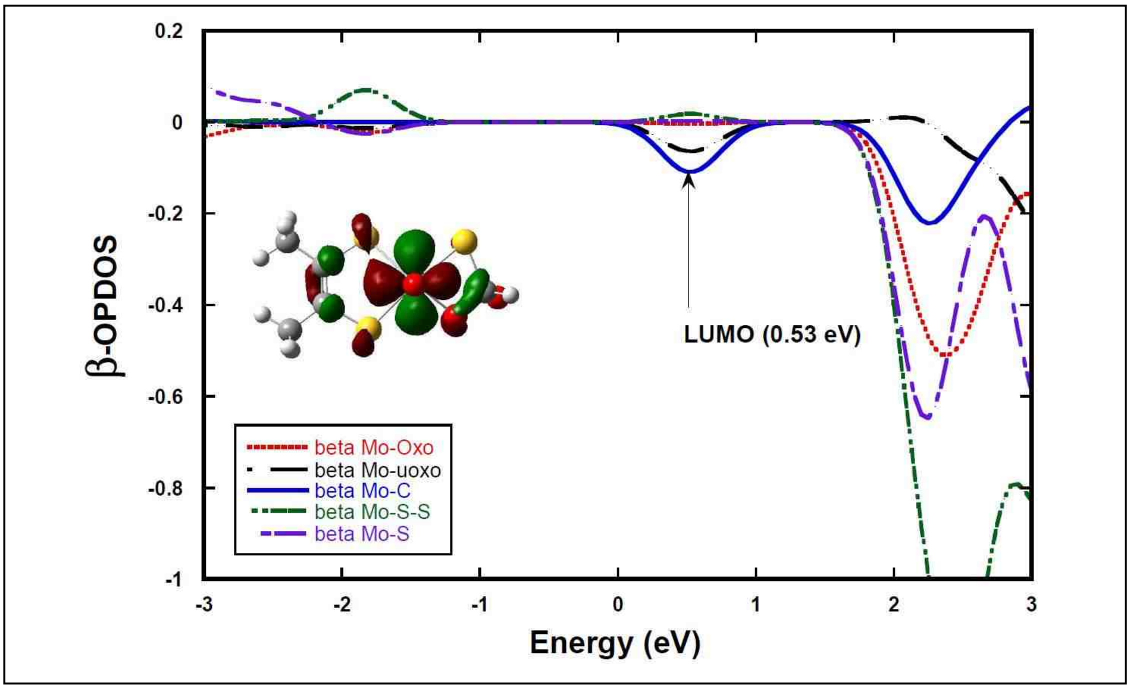

Figure 2.25: Overlap population density of states (OPDOS) plot showing the magnitude and nature of anti-bonding between Mo and C atoms. This overlap is indicated by the solid line in blue and is the strongest interaction in the β-LUMO.

Hence, these calculations indicate that the observed large value of the hyperfine tensor comes from the orientation of the ^{13}C hyperfine tensor principle axis which lies along the plane of the molecule perpendicular to the Mo=O (Z direction) and points directly to the Mo-dxy orbital. Secondly, the ^{13}C hyperfine tensor is a direct result of a large isotropic Fermi contact term that originates from direct C s-orbital character being admixed into the β-LUMO/α-SOMO wavefunction consistent with the work done by Shanmugan and co-workers [18].

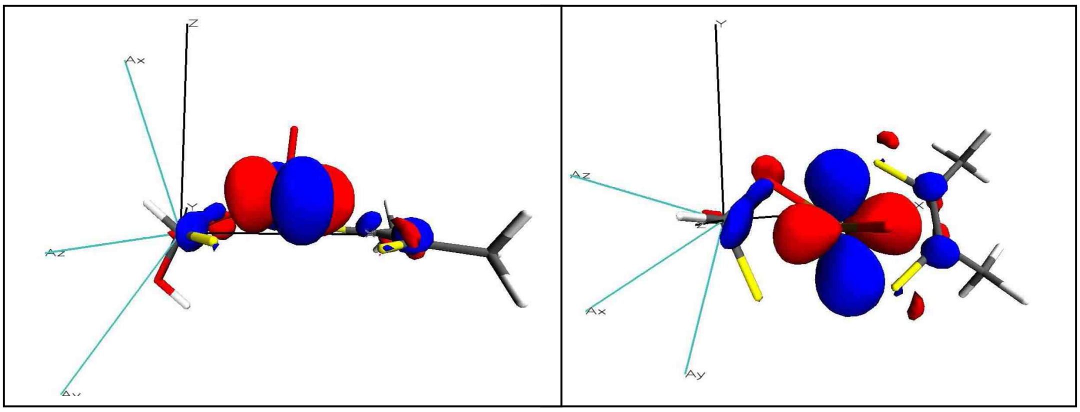

Figure 2.26: Schematic representation of the side view (left) and top view (right) showing the orientation of the ^{13}C hyperfine tensor (A_x, A_y, A_z) relative to molecular frame (X, Y, Z) drawn from the orientation matrices in ORCA output files. The largest ^{13}C hyperfine tensor component A_z lies along the XY plane and interacts in the anti-bonding fashion with the Mo-d_{xy} orbital.

2.6.2 The Stability and Oxygen Dependence of XO/XDH "Inhibited" Species

There is an oxygen requirement for the formation of the "inhibited" species. This indicates that one electron reoxidation of the initially formed two electron reduced enzyme is necessary before the "inhibited" signal appears. The intensity of the "inhibited" signal with well resolved ^{95,97}Mo hyperfine structure was found to increase with increasing time of exposure to oxygen/air. However, Morpeth and Bray [75] reported the formation of the "inhibited" species for some substrates under anaerobic conditions and in the presence of sodium dithionite.

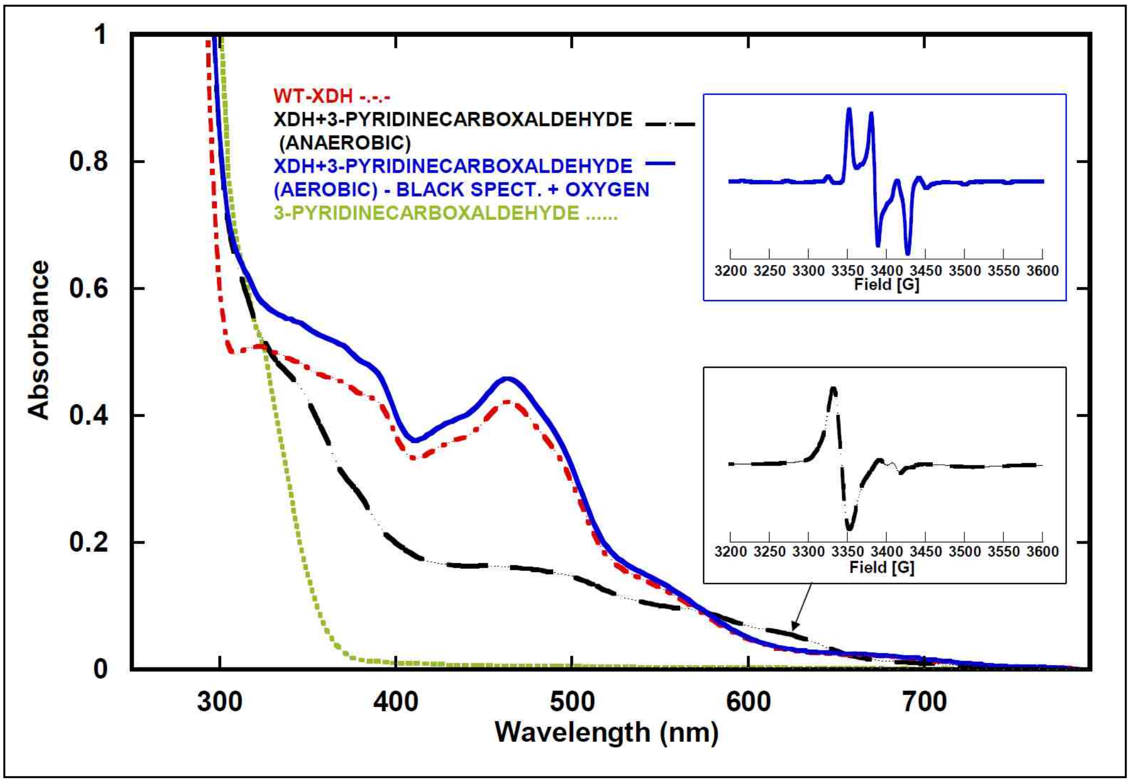

Figure 2.27: Electronic absorption spectra representing anaerobic incubation of 3-pyridinecarboxaldehyde with xanthine dehydrogenase (XDH) from *R.*

capsulatus. The inserts are the corresponding EPR spectra obtained for XDH + 3-pyridinecarboxaldehyde at anaerobic conditions (black: ─···─) and then adding oxygen to XDH + 3-pyridinecarboxaldehyde kept at anaerobic conditions that immediately forms the "inhibited" spectrum (blue: ─). The band at 620 nm (shown by an arrow) has been confirmed to represent the absorption for a flavin semiquinone (The black (─···─) EPR spectrum).

Attempts to form the "inhibited" species under anaerobic conditions using 3-pyridinecarboxaldehyde as a substrate resulted into a dominant flavin semiquinone and a trace of the rapid type 1 EPR signal (Figure 2.27). Attempts to also form the "inhibited" signal at anaerobic conditions in the presence of 1mM sodium dithionite also resulted into the flavin semiquinone EPR spectrum (Figure 2.28). It is well known that dithionite fully reduces the enzyme. However, dithionite in the presence of 3-pyridinecarboxaldehyde resulted in a partial reduction of the enzyme (Figure 2.28) suggesting the presence of both the oxidized and the reduced forms of enzyme cofactors. There is strong evidence for the presence of either Mo(VI) or Mo(IV) "inhibited" species from the work done by Morpeth and Bray [75] on this inhibitory reaction under anaerobic conditions. Attempts to investigate the presence of these Mo(VI) and Mo(IV) species in this work by a difference technique using electronic absorption spectroscopy proved difficult due to the dominant absorptions of the two 2Fe-2S clusters and FAD (absorbances at 420, 470 and 550 nm are for 2Fe-2S clusters whereas absorbances at 360 and 450 nm are for FAD (Figures 2.27 and 2.28)).

Unfortunately, these species are diamagnetic and can't be detected by EPR spectroscopy. Upon oxygenation of the anaerobic 3-pyridinecarboxaldehyde-XDH enzyme complex (Figure 2.27, black spectrum), the flavin semiquinone signal disappeared and the "inhibited" signal quickly appeared indicating the conversion of Mo(IV) to the Mo(V) "inhibited" species. Once the "inhibited" species is formed, it is stable for several hours as long as it is kept under cold conditions (4^0C) to avoid protein degradation. Four substrates, formaldehyde, acetaldehyde, 2-pyridinecarboxaldehyde and 3-pyridinecarboxaldehyde were investigated with regard to the formation of the "inhibited" species under aerobic conditions. However, formaldehyde and 3-pyridinecarboxaldehyde easily formed the "inhibited" species and gave cleaner EPR spectra with nicely resolved molybdenum hyperfine when compared with acetaldehyde and 2-pyridinecarboxaldehyde. The stability of these "inhibited" species with regard to the formation of a strong covalent C-S bond was theoretically investigated by performing geometry optimizations of the inhibited structure followed by single point energy calculations. Mayer's bond order analysis between C and S atoms shows a bond order of ~ 1 for aldehyde substrates and a bond order of zero for purine (xanthine) and pterine (lumazine) (Table 2.12) indicating that xanthine and lumazine substrates are unstable with respect to the formation of a strong C-S bond under these conditions. However, there is kinetic evidence for the breakdown of formaldehyde, acetaldehyde, 2-pyridinecarboxaldehyde, 3-pyridinecarboxaldehyde and other "inhibited" species accompanied by reappearance of xanthine oxidase activity [75]. The results of Morpeth et al, indicated a strikingly fast rate of breakdown for 2-pyridinecarboxaldehyde ($k = 5.2\ h^{-1}$) compared with 3-pyridinecarboxaldehyde ($k = 0.8\ h^{-1}$) and 4-pyridinecarboxaldehyde ($k = 0.7\ h^{-1}$). Their results could not be explained by our computational results. However, we attribute the observed differences in stability between these substrates as being due to solubility factors in the protein environment. These include hydrogen bonding between the substrate and the secondary coordination sphere at the active site, presence of nitrogen atoms and their respective positions in the R group of the aldehyde, which results in different interactions with the protein second coordination sphere (For example, 2 and 3 nitrogen positions in pyridinecarboxaldehyde substrates). The 3-pyridinecarboxaldehyde inhibited EPR results for the E232A-XDH mutant (Figure 2.14) confirmed these interactions with the secondary coordination sphere.

Table 2.12: Calculated Mayer C-S bond order for various XO substrates.

Substrate	Mo%	Mayer B.Order	Substrate	Mo%	Mayer B.Order
Formaldehyde	**78.07**	**0.934**	**2-Pyridinecarboxaldehyde**	**77.30**	**0.931**
Acetaldehyde	**78.98**	**0.929**	**3-Pyridinecarboxaldehyde**	**77.48**	**0.945**
Propanaldehyde	78.91	0.928	4-Pyridinecarboxaldehyde	76.44	0.942
Butyraldehyde	78.79	0.929	3-Indolecarboxaldehyde	77.48	0.945
Indole-5-acetaldehyde	77.87	0.923	Benzaldehyde	77.42	0.935
			2-Amino-4-hydroxy-6-formylpteridine	74.26	0.935
Formamide	79.05	0.941			
			Lumazine	74.21	0.000
Xanthine	75.76	0.000			

The extension of the theoretical study to include purine and pterine substrates such as xanthine and lumazine respectively (Table 2.12) has confirmed that these substrates are not potential candidates for the formation of the “inhibited”. That is why purines, exemplified by xanthine are not known to form any “inhibited” species whereas pterine substrates such as lumazine are known to form stable Mo(IV) product bound species [69,89,90].

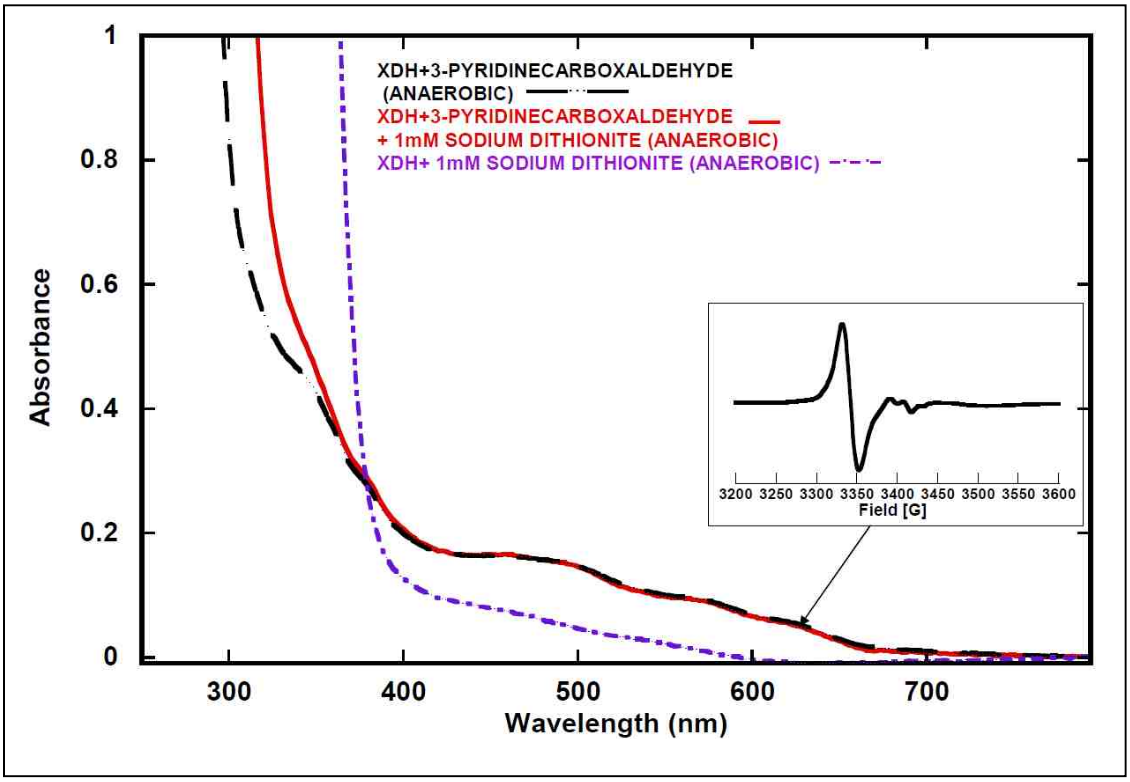

Figure 2.28: Electronic absorption spectra representing anaerobic incubation of 3-pyridinecarboxaldehyde with xanthine dehydrogenase (XDH) from *R. capsulatus* in and without the presence of 1mM dithionite. The insert is the corresponding EPR spectrum obtained for XDH + 3-pyridinecarboxaldehyde at

anaerobic conditions with and without 1mM dithionite which are represented by red (─) and black (─···─) spectra respectively.

Studies on the stability of “inhibited” species included also pH dependency. These indicated increasing magnitudes of signal intensities on going from pH 8 to 12 (Figure 2.29). We implicated these results to the presence of the ionizable group(s) in the immediate vicinity of the molybdenum site whose ionization is intimately associated with the reduction of the molybdenum center. Previously, pH dependent studies associated with the reduction of the enzyme at the active site were reported by Ryan and co-workers [91] who also observed an increase in the overall magnitude of the molybdenum absorption on going from pH 6 to 10.

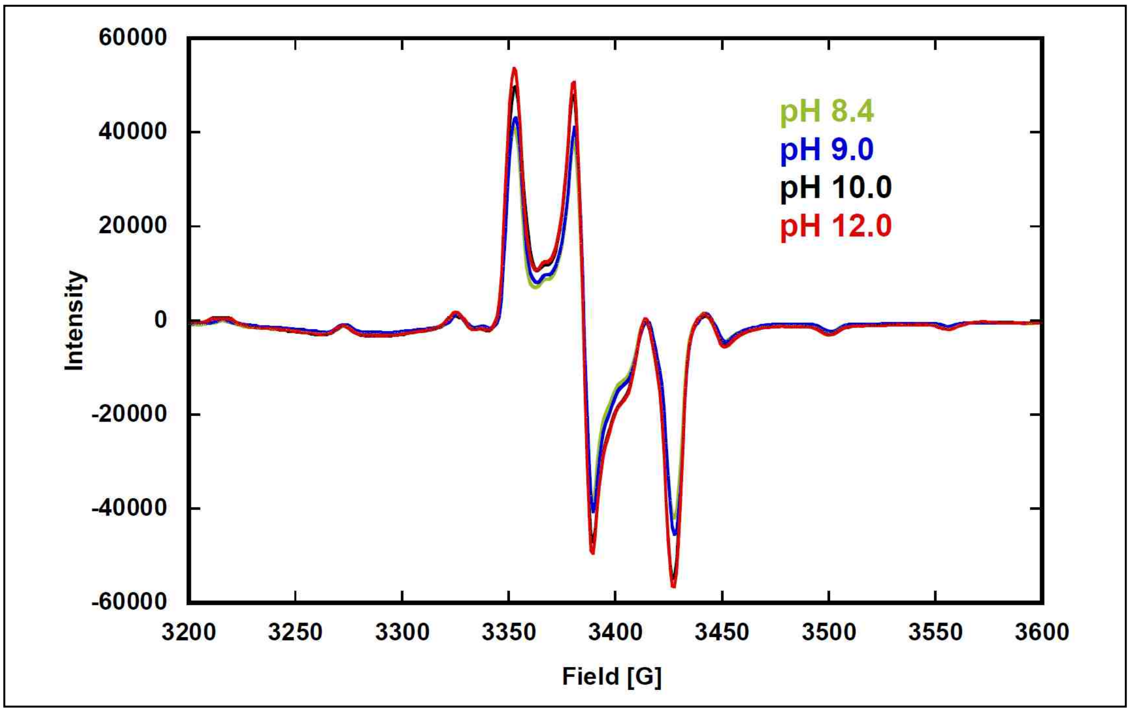

Figure 2.29: EPR pH dependent studies for 3-pyridinecarboxaldehyde generated xanthine dehydrogenase "inhibited" from *R. capsulatus*. The EPR intensity increases from pH 8 to pH 12. Notice; from pH 9 to pH 10, there is a dramatic increase in intensity. However, pH 8 and pH 9 are close in signal intensities and on the other hand pH 10 and pH 12 are close with higher intensities than pH 8 and pH 9.

The results of Ryan agree very well with our EPR pH dependent studies. However, the results pose a question as to which ionizable amino acid groups are involved in the molybdenum center reduction. Nonetheless, if the structure of the inhibited is that of a product bound species, these results exclude ionization of the bound carboxylic acid at the active site as this would break down the "inhibited" resulting to the disappearance of the signal.

2.6.3 Mechanistic Insights for the Generation of XO "Inhibited" Species

The catalytic sequence of XO/XDH enzymes begin at the molybdenum site where electrons are introduced by the substrate into the molybdenum cofactor, which is reduced from Mo(VI) to Mo(IV) [92]. Electrons are then transferred one at a time to the more proximal of the two 2Fe-2S clusters, positioned approximately 15 Å away. Each electron then moves approximately 12 Å to the second cluster, and finally each is passed 8 Å to the FAD, forming $FADH^{\bullet}$ and then $FADH_2$ prior to reaction with an electron acceptor, which is oxygen for XO and either oxygen or NAD+ for XDH [65,93]. However, in the absence of an electron acceptor, total reduction of the enzyme requires 6 electrons; 2 for the molybdenum center, 2 for the two 2Fe-2S clusters and 2 for FAD (Scheme 2.4). Scheme 2.5 depicts the various oxidation states for the FAD and the two 2Fe-2S clusters. The oxidized 2Fe-2S cluster form has a singlet spin electronic structure (S = 0) resulting from anti-ferromagnetic coupling of two Fe(III) ions with a spin quantum number S = 5/2 [94-96] whereas the reduced 2Fe-2S is low spin with S = ½ [97].

Scheme 2.5

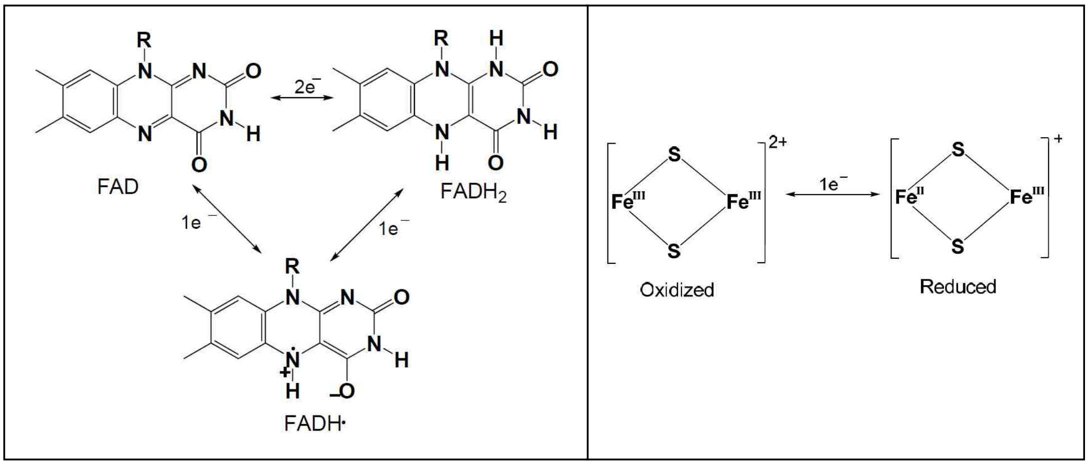

EPR and electronic absorption results for anaerobic incubation of XDH with 3-pyridinecarboxaldehyde (Figure 2.28 and 2.30) indicate a partial reduction of the enzyme signifying a mixture of Mo(VI),Mo(IV) and Mo(V) at the molybdenum center and a mixture of reduced and oxidized 2Fe-2S clusters and FAD. There is a Mo(V) signal in the EPR spectrum (Figure 2.30) at around 3420G which is a 'rapid' type signal as this is always formed prior to the formation of the "inhibited" species and disappears upon oxygenation of the sample. Figure 2.30 (solid black spectrum and the insert) also shows reduced FeSI and dominant FADH$^{\bullet}$ signals. There could also be an FeSII signal, but this is usually observed at 15K. In general, the catalytic events taking place during the reaction of XO/XDH enzyme with aldehydes giving the “inhibited” signal are closely related to the catalytic events taking place upon the reaction of XO enzyme with purine and pteridine substrates such as xanthine and 2-amino-4-hydroxy-6- formylpteridine which give the ‘very rapid’ and ‘rapid’ signals [71,74,98-100].

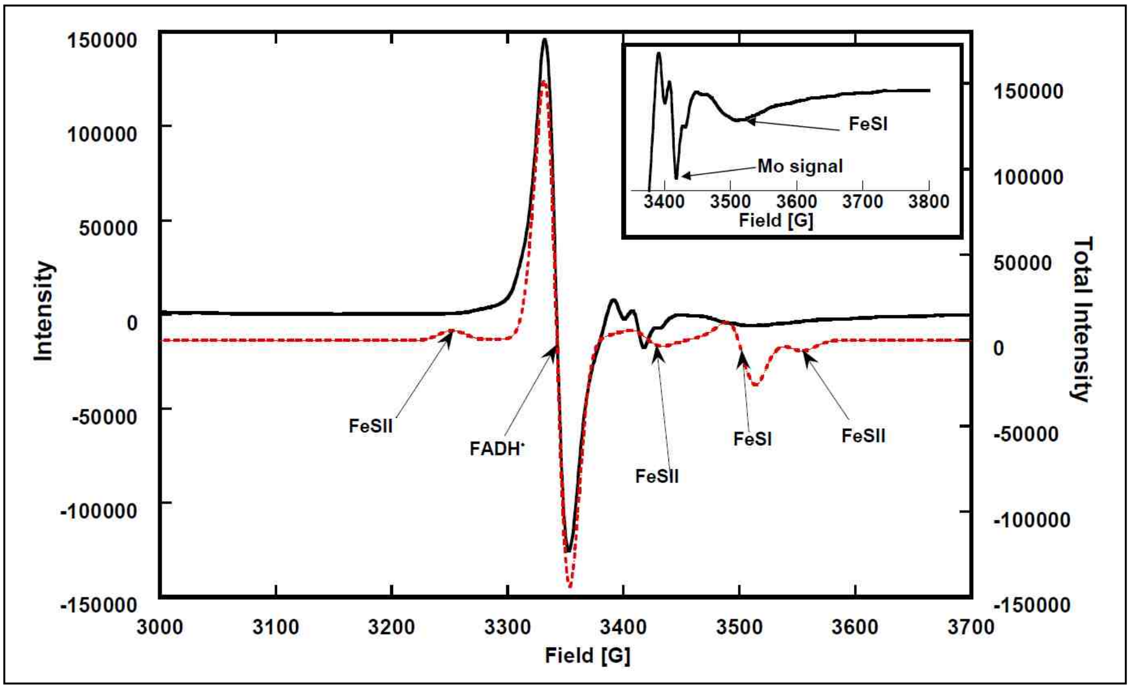

Figure 2.30: Low temperature EPR spectra for anaerobic incubation of XDH with 3-pyridinecarboxaldehyde at 9.436 GHz and 40K. Solid black spectrum is the data whereas the dashed red spectrum is the simulation. The g-values for FADH$^{\bullet}$ derived from EPR simulation are $g_x = g_y = g_z = 2.0170$. The g-values for FeSI and

FeSII were adapted from Leimkuhler et al, 2003 [101] which are $g_x = g_y = 1.9217$, $g_z = 2.0222$ for FeSI and $g_x = 1.8964$, $g_y = 1.9711$, $g_z = 2.0730$ for FeSII. These (g-values for FeSI and FeSII) were obtained from a reduction of XDH by sodium dithionite at anaerobic conditions.

This observation suggests a very similar catalytic pathway for purines and aldehyde species. With purines, the ‘rapid’ signal can be generated prior to substantial accumulation of the ‘very rapid’ signal (scheme 2.5) whereas in aldehydes, the “inhibited” signal appears after the ‘rapid’ signal (scheme 2.6).

Scheme 2.5

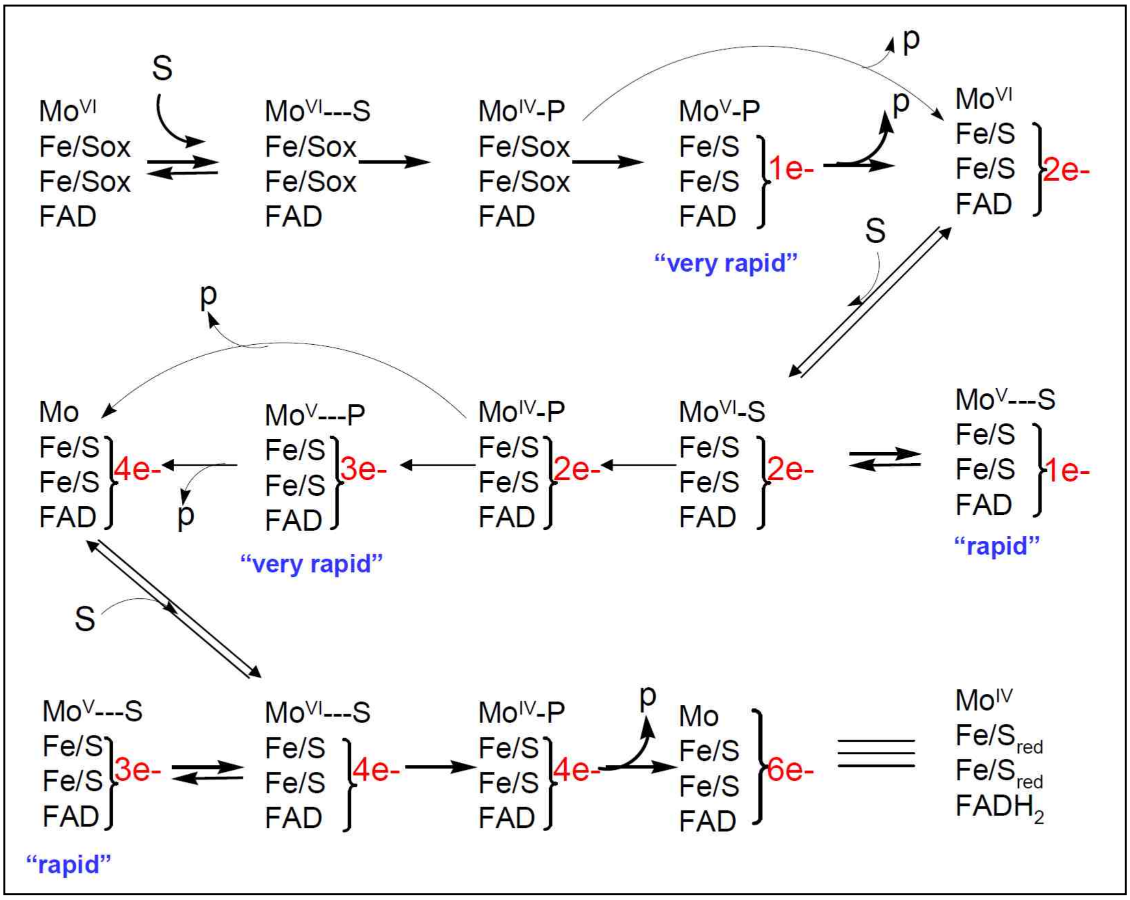
S
Mo^VI Fe/Sox Fe/Sox FAD
Mo^VI---S Fe/Sox Fe/Sox FAD
Mo^IV-P Fe/Sox Fe/Sox FAD
Mo^V-P Fe/S Fe/S FAD 1e-
p
p
Mo^VI Fe/S Fe/S FAD 2e-
“very rapid”
S
p
Mo Fe/S Fe/S FAD 4e-
p
Mo^V---P Fe/S Fe/S FAD 3e-
Mo^IV-P Fe/S Fe/S FAD 2e-
Mo^VI-S Fe/S Fe/S FAD 2e-
Mo^V---S Fe/S Fe/S FAD 1e-
“very rapid”
“rapid”
S
Mo^V---S Fe/S Fe/S FAD 3e-
Mo^VI---S Fe/S Fe/S FAD 4e-
Mo^IV-P Fe/S Fe/S FAD 4e-
p
Mo Fe/S Fe/S FAD 6e-
Mo^IV Fe/S_red Fe/S_red FADH_2
“rapid”

EPR and ENDOR spectroscopic methods have confirmed the ‘very rapid’ is the Mo(V)-product bound species [10,88,102] whereas the ‘rapid’ type signal has been suggested to arise from the complex of unreacted substrate with a partially reduced enzyme that possesses a Mo(V) center [103] (Scheme 2.5).

Scheme 2.6

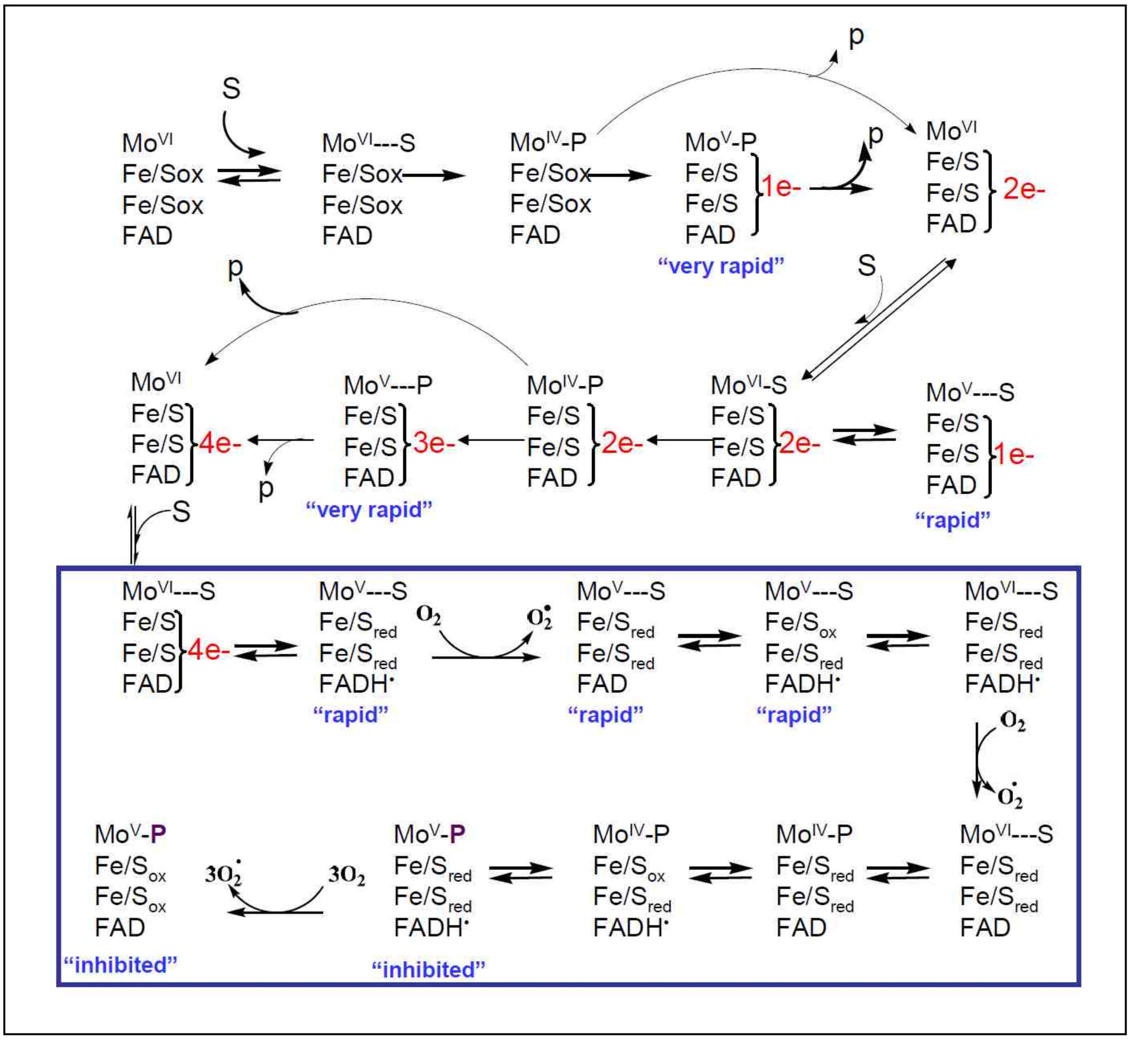
S
p
Mo^VI Fe/Sox Fe/Sox FAD
Mo^VI---S Fe/Sox Fe/Sox FAD
Mo^IV-P Fe/Sox Fe/Sox FAD
Mo^V-P Fe/S Fe/S FAD 1e-
"very rapid"
Mo^VI Fe/S Fe/S FAD 2e-
Mo^VI Fe/S Fe/S FAD 4e-
Mo^V---P Fe/S Fe/S FAD 3e-
"very rapid"
Mo^IV-P Fe/S Fe/S FAD 2e-
Mo^VI-S Fe/S Fe/S FAD 2e-
Mo^V---S Fe/S Fe/S FAD 1e-
"rapid"
Mo^VI---S Fe/S Fe/S FAD 4e-
Mo^V---S Fe/S_red Fe/S_red FADH•
"rapid"
O2
O2•
Mo^V---S Fe/S_red Fe/S_red FAD
"rapid"
Mo^V---S Fe/S_ox Fe/S_red FADH•
"rapid"
Mo^VI---S Fe/S_red Fe/S_red FADH•
Mo^VI---S Fe/S_red Fe/S_red FAD
Mo^IV-P Fe/S_red Fe/S_red FAD
Mo^IV-P Fe/S_ox Fe/S_red FADH•
Mo^V-P Fe/S_red Fe/S_red FADH•
"inhibited"
3O2
3O2•
Mo^V-P Fe/S_ox Fe/S_ox FAD
"inhibited"

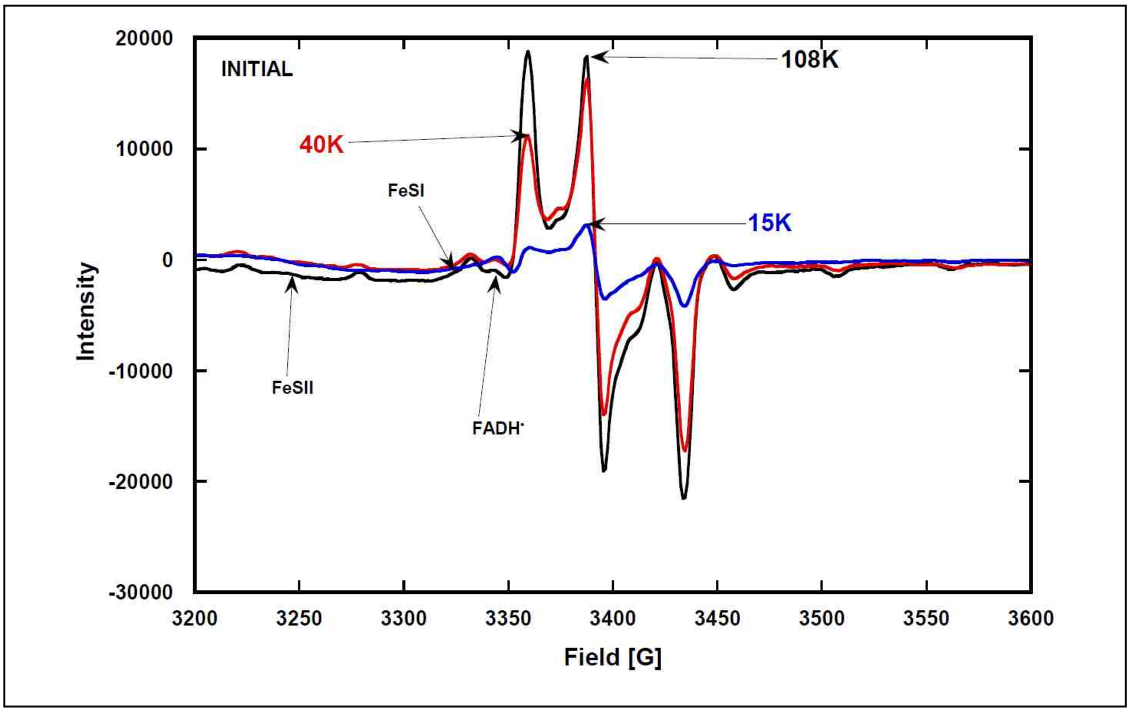

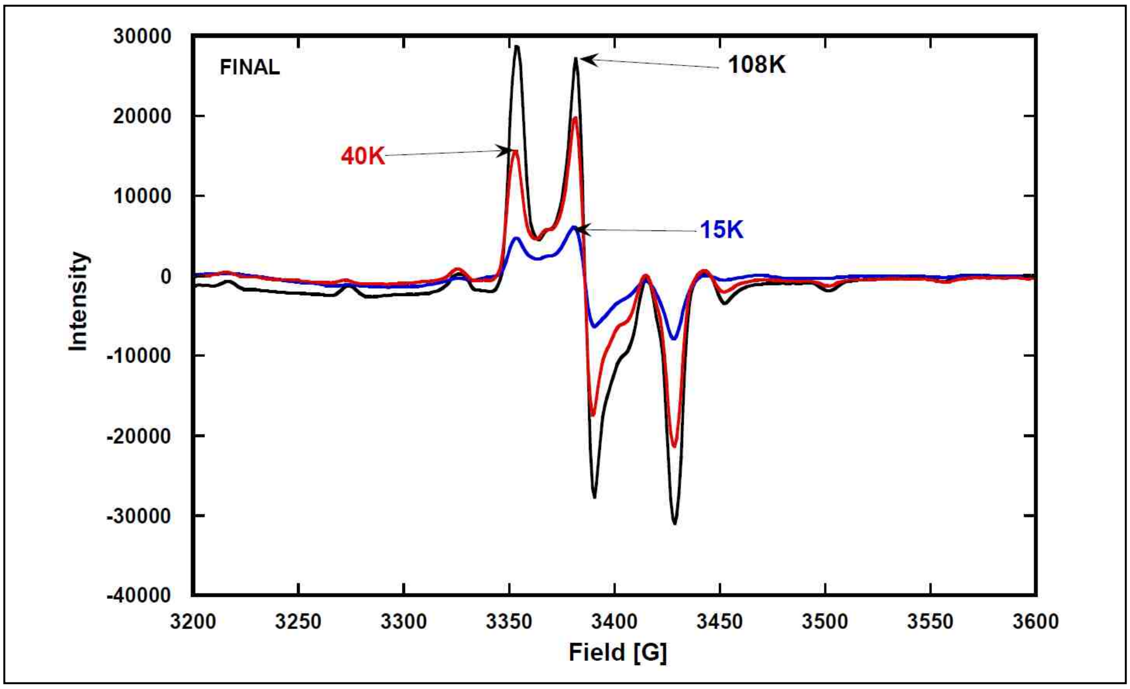

Figure 2.31: EPR spectra showing the presence and absence of the 2Fe-2S clusters and FADH$^{\bullet}$ obtained upon exposure to oxygen at different times. The **INITIA**L spectra (7 minutes incubation) contain all spin states for the three

cofactors whereas the **FINAL** spectra (further 5 minutes incubation) contain only the molybdenum cofactor after further oxygenation of the sample.

However, computational and EPR spectroscopic studies from this work also support an “inhibited” species that is a Mo(V)-product bound species, and spectral observations have enabled us to propose new scheme 2.6 for the reaction of xanthine oxidase with excess aldehyde substrate generating the “inhibited” species. In the proposed catalytic scheme 2.6, “inhibited” is formed when the enzyme is operating by shuttling six electrons, 2 in fully reduced 2Fe-2S clusters, 2 in fully reduced FAD and 2 in a Mo(VI) substrate complex in the presence of oxygen as an electron acceptor. However, an electron becomes transferred from a Mo(IV)-product bound species to a nearby oxidized 2Fe-2S cluster while the other 2Fe-2S cluster and an FAD remain almost fully reduced. These processes slow down product release (Scheme 2.6) and thus provide an opportunity for the formation the “inhibited” species. The EPR spectrum collected after the initial aerobic incubation is composed of a mixture of the spin states from molybdenum center (“inhibited” signal and sometimes a trace of ‘rapid’ type I), $FADH^{\bullet}$ and the 2Fe-2S clusters. However, the $FADH^{\bullet}$ and the 2Fe-2S cluster signals disappear after further oxygenation of the sample and the “inhibited” signal appears and gains intensity as more oxygen is bubbled into the sample (Figures 2.31). We could not obtain, however, any trace of the “inhibited” signal at stoichiometric conditions of enzyme and substrate suggesting that all substrates are converted to products resulting to no inhibition under these conditions. This suggests that substrate inhibition giving the “inhibited” signal occurs only under those circumstances when the enzyme is over-reduced leading to slow release of the product and thus supports the proposed scheme 2.6. These findings agree well with the observations of Morpeth F.F, 1983 [71] on substrate inhibition seen at high substrate concentration which cause the enzyme to operate less effectively.

Scheme 2.7

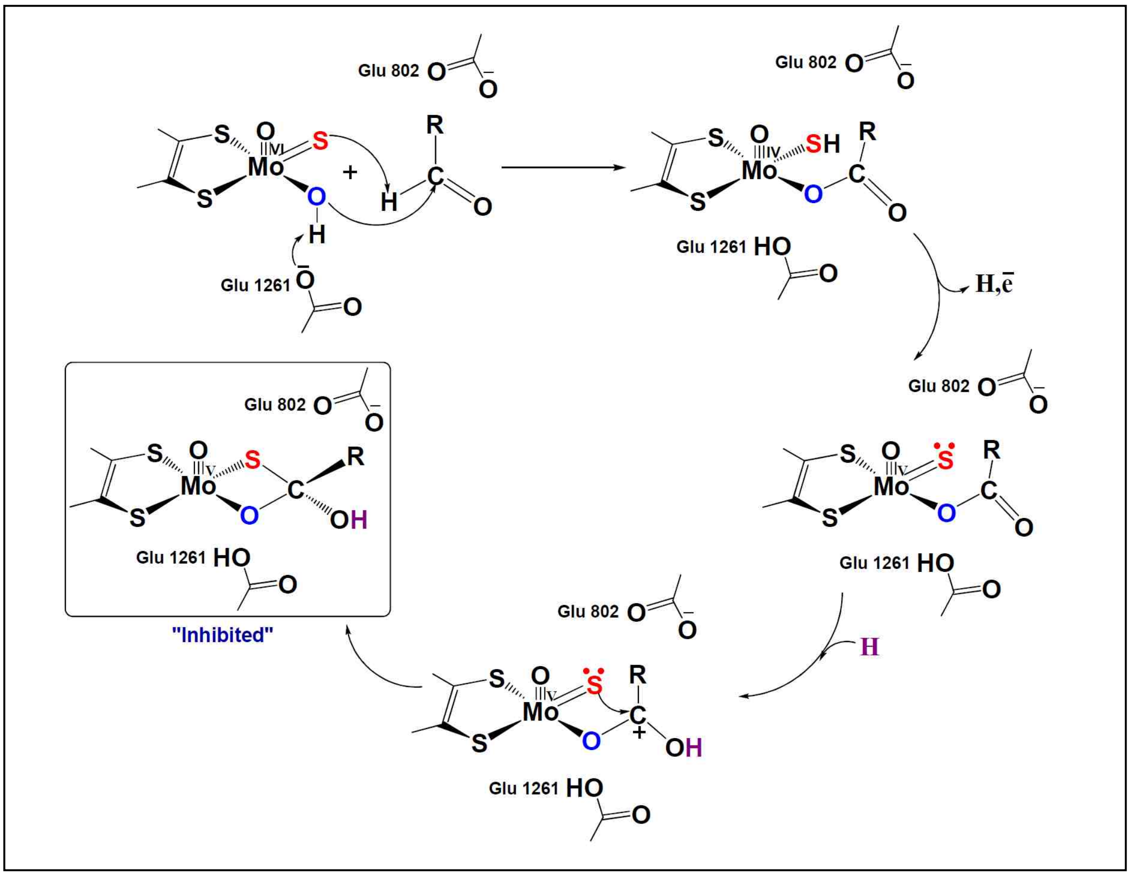
Glu 802
Glu 1261
Mo
VI
V
IV
S
SH
O
OH
R
C
H
+
H,e̅
"Inhibited"

Scheme 2.8

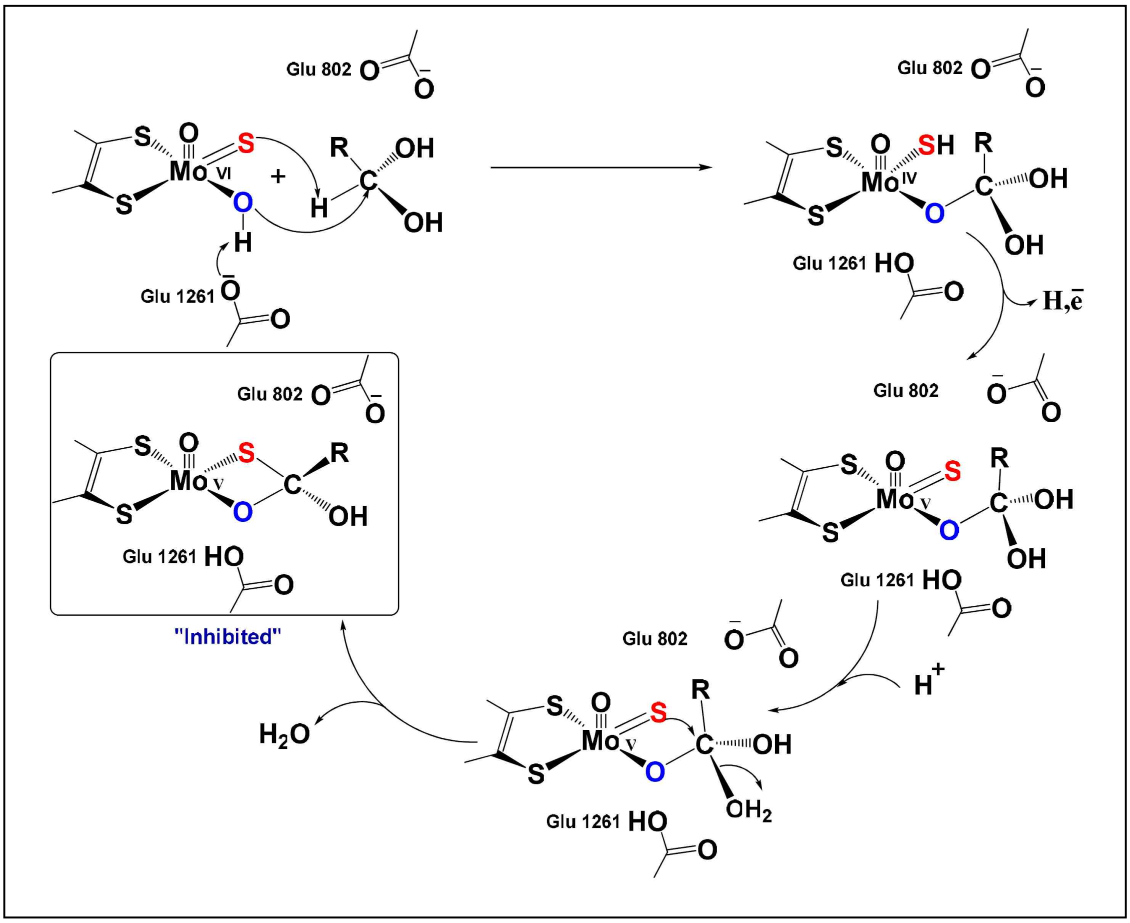

On the basis of the “inhibited” derived structure, we have also proposed two new possible mechanisms (Schemes 2.7 and 2.8) for the generation of the “inhibited” species which are directly related to the proposed catalytic mechanisms for the reductive half reaction of xanthine oxidase depicted on schemes 2.2 and 2.3 for the hydride and proton transfer respectively. These mechanisms account for the existence of two forms, aldehyde functional group (scheme 2.2) and the gem-diol (scheme 2.3) obtained when an aldehyde is dissolved in water/buffer. Formaldehyde exists almost exclusively (99.9%) as a gem-diol in water whereas

58 % of acetaldehyde is a gem-diol [104]. Both mechanisms can be related to the proposed catalytic mechanism for the reductive half reaction of xanthine oxidase. They both involve a reaction in which the initial molybdenum bound water molecule is converted into OH^- by proton transfer to Glu 1261/730 near the molybdenum active site. The second step is a nucleophilic attack on the substrate-aldehydic carbon by metal-coordinated OH^- and a hydride/proton transfer from the substrate to the metal sulfido giving the Mo(IV)-product bound species.

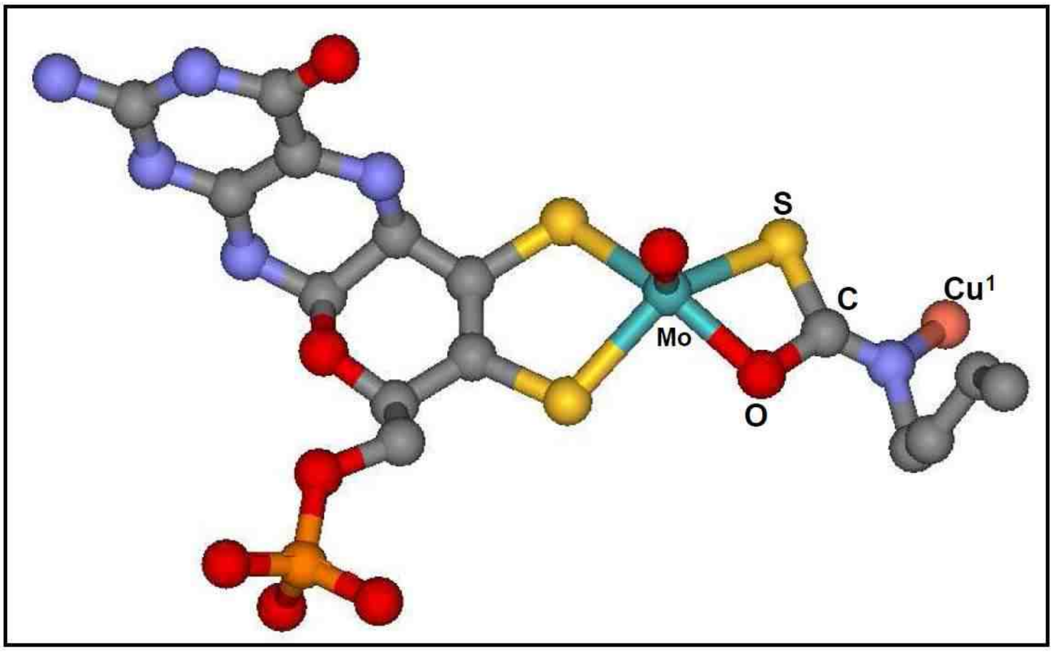

Figure 2.32: 1.09Å crystal structure of n-butylisocyanide “inhibited” CODH. The molybdenum center is at the oxidation state of (IV). Notice, both XO (schemes 2.7 and 2.8) and CODH “inhibited” form Mo-S-C and Mo-O-C bonds, however, substrate C in XO “inhibited” complex is tetrahedral whereas in CODH is a trigonal planar.

Thermodynamic properties from quantum mechanical calculations indicated that the formation of the “inhibited” derived structure is uphill. Attempts to include the participation of amino acid residues (Glu 1261 and 802), which are in the vicinity of the active site, proved difficult due to the electrostatic repulsion between oxygen atoms. These repulsive forces can be overcome by QM-MM methods, which have become popular alternatives for the study of enzymatic reactions at an affordable computational cost and reasonable accuracy. Recently, QM-MM calculations have provided theoretical mechanistic insights on xanthine oxidase and aldehyde oxidase catalytic mechanisms by including the effects of protein or solvent environments. These methods have accounted for the participation of the glutamates 1261 and 802 for xanthine oxidase and glutamate 869 for aldehyde oxidase and have provided a theoretical support to the proposed catalytic mechanisms of xanthine and aldehyde oxidase [104,106]. Thus, we suggest that these protein or solvent effects from the bulky of the protein structure also play some role during this inhibitory reaction and favor stabilization of the “inhibited” derived structure. Thus, a QM-MM study is worth doing in the future in order to delineate between the proposed mechanisms. There is crystal structure evidence for the formation of Mo-S-C and Mo-O-C bonds in CO dehydrogenase (which is also a member of xanthine oxidase family) upon reaction with the inhibitor n-butylisocyanide [64] (Figure 2.32).

2.6.4 Relationship between “Inhibited” and the Calculated Transition State in the Proposed XO Catalytic Mechanism

XO “inhibited” possesses structural features that are common to the putative tetrahedral intermediate calculated for aldehydes (**IM** in Scheme 2.9) and other heterocyclic aromatic substrates, which include pterine and purine substrates along the reaction coordinate (Schemes 2.2 and 2.3). These include the presence of Mo-S-R(H) ligation in place of a terminal sulfido (Mo=S), an Mo-O-R linkage, and a tetrahedral carbon center that derives from the substrate. Linear transit calculations with formaldehyde as a substrate indicate an electronic structural similarity between formaldehyde “inhibited” and active site structures that evolve along the **IM**→**P** reaction coordinate, particularly those evolving between **TS**→**P** (Scheme 2.9 and Figure 2.33). Along this reaction coordinate (Scheme 2.9), the Mo atom is reduced formally from oxidation state VI to IV, while the formaldehyde substrate is oxidized. Thus, XO “inhibited” can be thought to represent a paramagnetic analogue of enzyme structures found between the **TS** and **P** (Figure 2.33). The calculated **IM**→**TS** activation energy, ΔE, is found to be 14.77 kcal/mol. The **IM**→**P** reaction profile is represented as a function of formaldehyde C-H distance in Figure 2.33. The transition state **TS** was verified by the observation of a single large negative eigenvalue, -1062.5 cm^{-1} in the frequency calculation which corresponded to the C-H stretching mode. Similar results were obtained with acetaldehyde as a substrate. This gave an eigenvalue of -572 cm^{-1} in the frequency calculation and **IM**→**TS** activation energy, ΔE of 12.6 kcal/mol [107].

Scheme 2.9

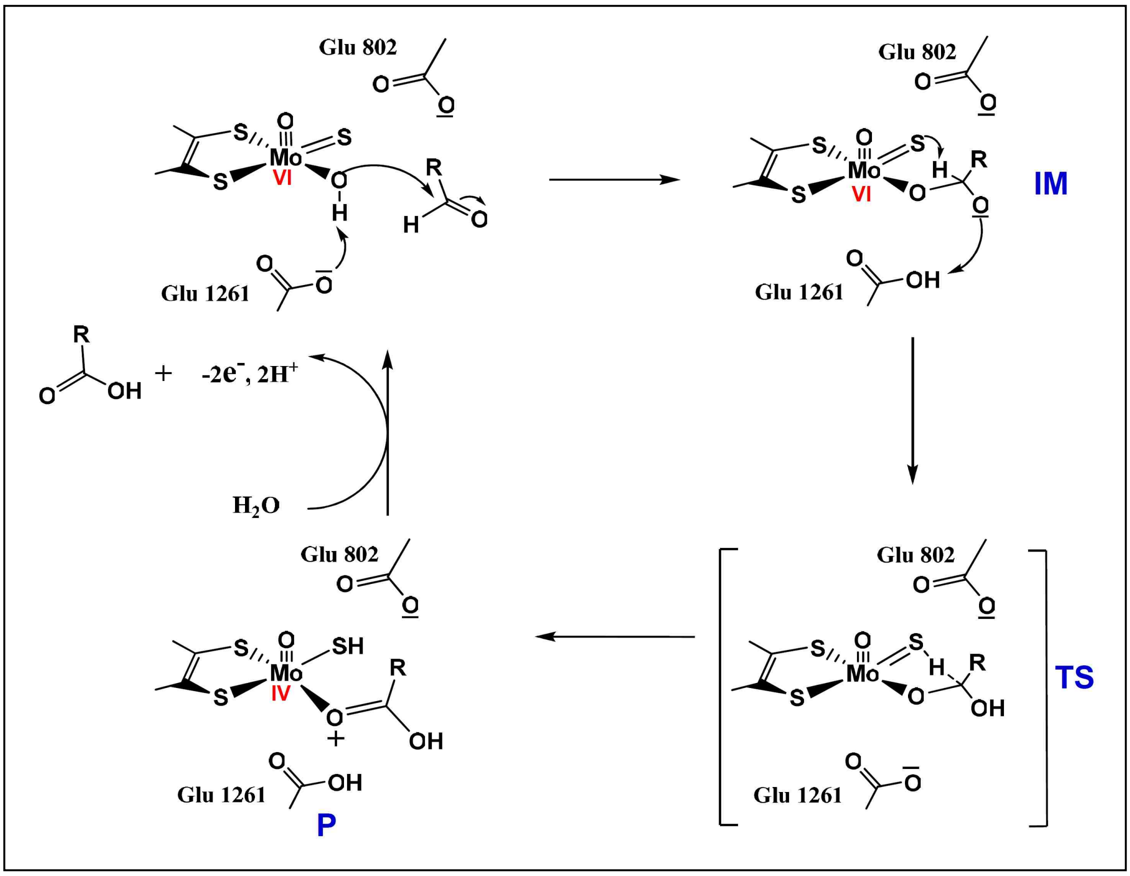

Mulliken atomic charges. The characterization of the charge flow along the reaction coordinate for the reduction of Mo center (from **IM**→**TS**→**P**) and oxidation of formaldehyde is presented in Figure 2.34. The Mo center becomes less positive as the reaction proceeds from **IM** to **TS** and eventually to **P** indicating a reduction to a Mo(IV) center. This reduction is concomitant with the migration of H from C to the sulfido (S). However, the hydrogen (H) becomes more negative and reaches climax at the **TS**. At this point (**TS**), the sulfido (S) is most positive indicating strong attraction between S and H centers and becomes negative as the reaction proceeds to the **P** state indicating charge neutralization leading to the formation of the S-H bond. On the other hand, the C becomes more positive as the reaction proceeds to the **P** state. The “inhibited” carries also a positive charge at the carbon center comparable to that observed in geometric structures found between the transition state and the product.

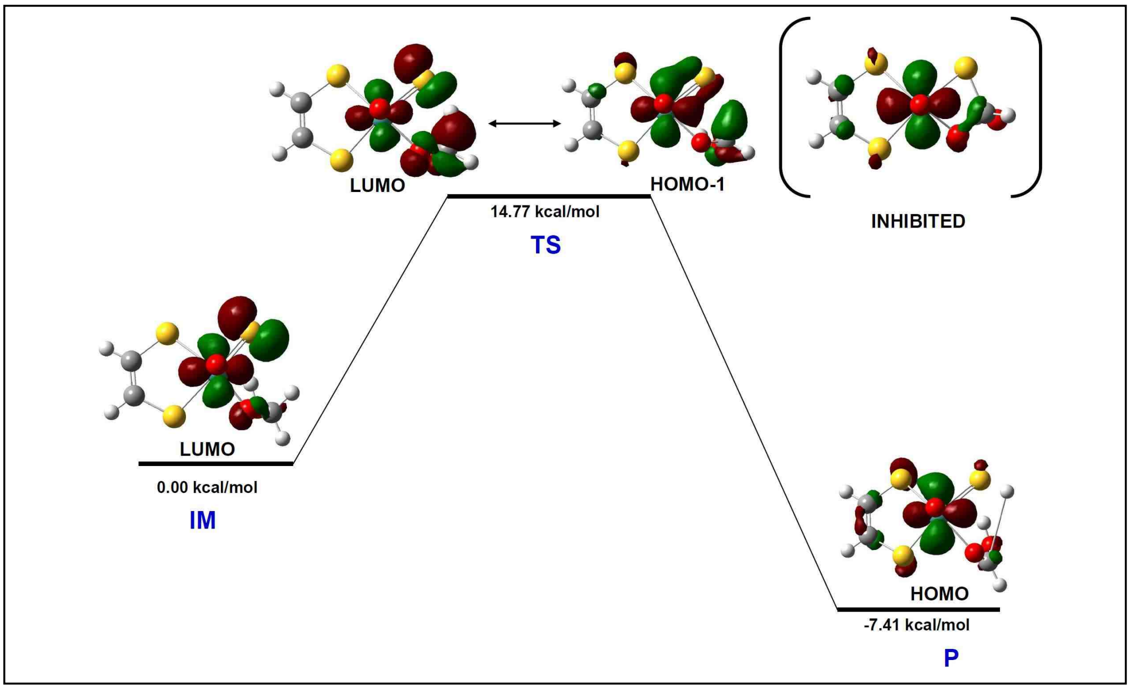
LUMO
HOMO-1
14.77 kcal/mol
TS
INHIBITED
LUMO
0.00 kcal/mol
IM
HOMO
-7.41 kcal/mol
P

Figure 2.33: The reaction profile for formaldehyde substrate as a function of C-H bond distance.

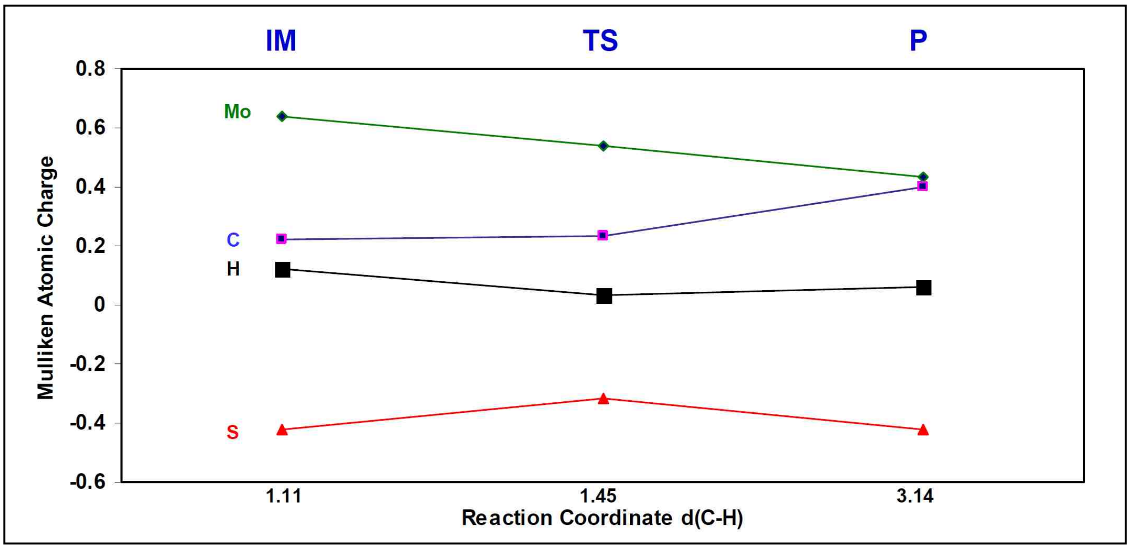

Figure 2.34: Mulliken charge distributions along formaldehyde pathway at the **IM**, **TS** and **P**.

2.7 Conclusion

These investigations provide considerable new information on the nature of the inhibitory reaction between aldehydes and the molybdenum center of xanthine oxidase (XO) and xanthine dehydrogenase (XDH). The derived structure (Figure 2.5 (i)) represents a transition state analogue proposed in schemes 2.2 and 2.3 by which an oxidized substrate is bound at the active site. This has allowed for an evaluation of the proposal that metal activated water undergoes nucleophilic attack at a substrate carbon to yield a tetrahedral transition state that breaks down by formal hydride transfer to the terminal sulfido ligand (Schemes 2.2 and 2.3). This work also provides new interpretations of the observed spin Hamiltonian parameters of the “inhibited” signal giving species particularly the magnitudes and orientations of ^{95,97}Mo and the ^{13}C hyperfine parameters. In addition to the magnitudes of the principal components of g- and A- tensors, the work also provides their orientations relative to each other, and relative to the molecular frame. The orientation of A- and particularly g-tensors with respect to the molecular frame, or the experimentally relative orientations of g- and A-tensors appears to be very sensitive probes of the local symmetry and coordination of the “inhibited” species. This detailed analysis of spin Hamiltonian parameters for the “inhibited” signal giving species has enabled its structural derivation which has been under debate for about three decades. The work has also proposed new mechanistic insights derived on the basis of the observed EPR spectral features and altogether have given deeper understanding of the reductive and oxidative half reactions mechanisms for XO/XDH. The proposed mechanisms for the generation of the “inhibited” structure opens also a new room for future theoretical investigations and analysis to further understand the reaction coordinate of xanthine oxidase family.

Chapter 3

Ground and Excited State Spectroscopy of LuxS

3.1 Introduction

3.1.1 S-Ribosylhomocysteinase (LuxS)

S-Ribosylhomocysteinase (LuxS) is a homodimeric enzyme with a fold that incorporates two identical tetrahedral metal-binding sites that are formed at the dimer interface, Figure 3.1. LuxS has been isolated and crystallized from diverse bacterial species including *Bacillus subtilis, Helicobacter pylori, Haemophilus influenzae, Deinococcus radiodurans* that show very similar overall structure and a totally conserved active site [108-110].

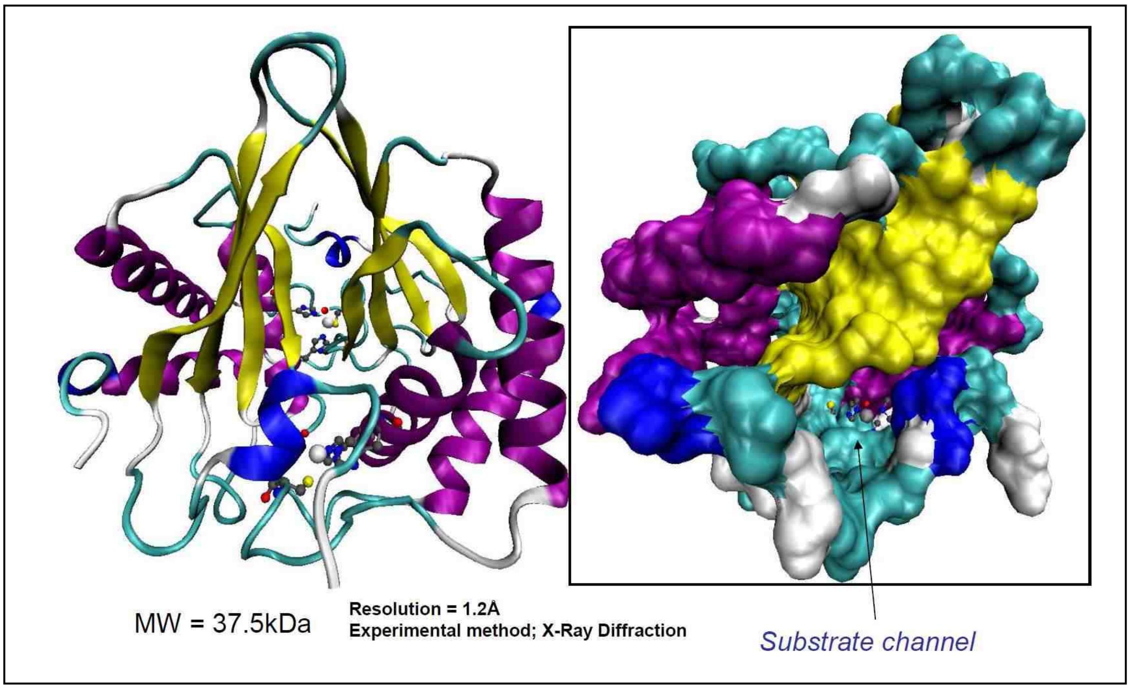
MW = 37.5kDa
Resolution = 1.2Å
Experimental method; X-Ray Diffraction
Substrate channel

Figure 3.1: A stereo representation of the luxS dimmer showing the two active sites with Fe^{2+} coordinated to His-54, His-57, Cys-126 and a H_2O/OH^- in *Bacillus*

subtilis luxS. On the right hand side is a stereo representation of the van der Waals surface of the luxS dimmer showing the substrate channel. The protein was downloaded from the protein data bank (PDB) 1J6X.

This metalloenzyme is encoded by *luxS* gene in *Bacillus subtilis*. Early studies showed Zn^{2+} as the active central metal, but the Zn^{2+} form only possesses ~10% of the activity of the native enzyme [108-110]. Recently it has been shown that an Fe^{2+} ion is present at the active site and is coordinated by two histidines (His-54, His-58), Cys-126 and either a hydroxide or water molecule in *Bacillus subtilis* LuxS [109,111] Interestingly, substitution of Co^{2+} for Fe^{2+} preserves full catalytic activity and is considerably more stable with respect to oxidation to the +3 state in air. LuxS catalyzes the cleavage of the thioether linkage of S-ribosylhomocysteine (SRH) to produce L-homocysteine and 4,5-dihydroxy-2,3-pentanedione (DHPD), a key step in the biosynthetic pathway of the type II autoinducer (AI-2) utilized by both Gram-positive and Gram-negative bacteria for interspecies communication (quorum sensing) [111,112].

Quorum sensing can be defined as cell-to-cell communication by which bacteria control their gene expression in response to cell density [113-115]. It is a wide spread system of intercellular communication among bacteria achieved through synthesis, release and detection of small signaling molecules, called autoinducers (AIs) in their environment [116-119]. However, by monitoring the local density of cells of the same (intra-species, type-1 autoinducers, AI-1) or different (inter-species; type-2 autoinducers, AI-2) species, bacteria can respond by altering gene expression and, ultimately, their behavior to best exploit their new environment [120,121]. This results in the formation of complex biofilm communities that can be very resistant to antibiotics [122]. The formation of bacterial biofilms and bacterial virulence pose significant medical and agricultural threats that make quorum sensing critically important [123-127]. It is theorized that a pathogen is prevented by quorum sensing from prematurely alerting the host's immune system at low numbers and only turns virulent when present in numbers large enough to overwhelm the host's immune response [128,129]. Biofilm development depends on quorum sensing pathways and inhibition of biofilm formation would make pathogens more sensitive to conventional antibiotics [122,130]. For example, *Pseudomonas aeruginosa* forms multicellular aggregates (biofilms) that are highly resistant to most antibiotics and can be life threatening to cystic fibrosis patients [117]. Also, crop pests such as *Erwinia carotovora*, *Ralstonia solanacearum*, and *Agrobacterium tumefaciens* require an intact quorum sensing pathway for pathogenicity [108,130]. The luxS gene is present and highly conserved in a wide variety of bacterial species including significant human pathogens such as *Haemophilus influenzae*, *Helicobacter pylori*, *Staphylococcus aureus* and *Streptococcus pneumoniae* and thus makes quorum sensing pathways attractive targets for the inhibition and development of novel antibacterial agents [131-134]. This background formed the basis for detailed spectroscopic and computational investigations carried out on the luxS active site. Its electronic structure and the effects of the secondary coordination sphere on catalysis have been explored in depth. This work reports novel electronic structure studies of the wild type luxS active site and two mutants (C84A and C84D) using electronic absorption, magnetic circular dichroism (MCD), variable temperature variable field magnetic circular dichroism (VTVH-MCD) and electron paramagnetic resonance (EPR) spectroscopies. It also reports qualitative comparisons of luxS with small molecule Co(II) analogues using the same spectroscopic methods in order to address the correlations between the electronic and geometric structures of the luxS enzyme and mutants. The complexes (PATH)CoBr and (PATH)CoNCS were synthesized (Prof. David Goldberg, Johns Hopkins University) as models for Co(II)His2CysL metalloproteins. Spectroscopic studies have shown that these models are remarkably similar to *wt* luxS, and C84A and C84D mutants,. The amino acid residue, cysteine 84 in the secondary coordination sphere has been proposed to play a role in abstracting a proton from the incoming substrate during catalysis. Our experimental results are strongly supported by computational work that indicates C84 plays a major role in the maintenance of the luxS catalytic geometry. Mutation of C84 to either alanine (C84A) or aspartic acid (C84D) resulted in active site geometries with different spectroscopic properties. Activity analysis of these two mutants indicated that C84A is completely inactive whereas C84D possesses a greater than 220 fold reduction in catalytic efficiency [111]. These significant electronic changes of the active site observed upon C84 mutation are a confirmation of the conserved catalytic geometry of the wild type luxS.

3.6.2 The Proposed Catalytic Mechanism of LuxS.

The active site possesses an Fe^{2+} ion coordinated with either water or a hydroxide ligand which is displaced by the substrate in the initial step of catalysis [110-112,132,135,136]. Other than the metal ligands, the active site also contains highly conserved residues, Ser-6, His-11, Arg-39, Glu-57 and Cys-84. However, mutation of Glu-57 and Cys-84 resulted in significant reduction of catalytic efficiency with the C84A mutation completely inactivating the enzyme and E57A possessing only a trace amount of activity [111].

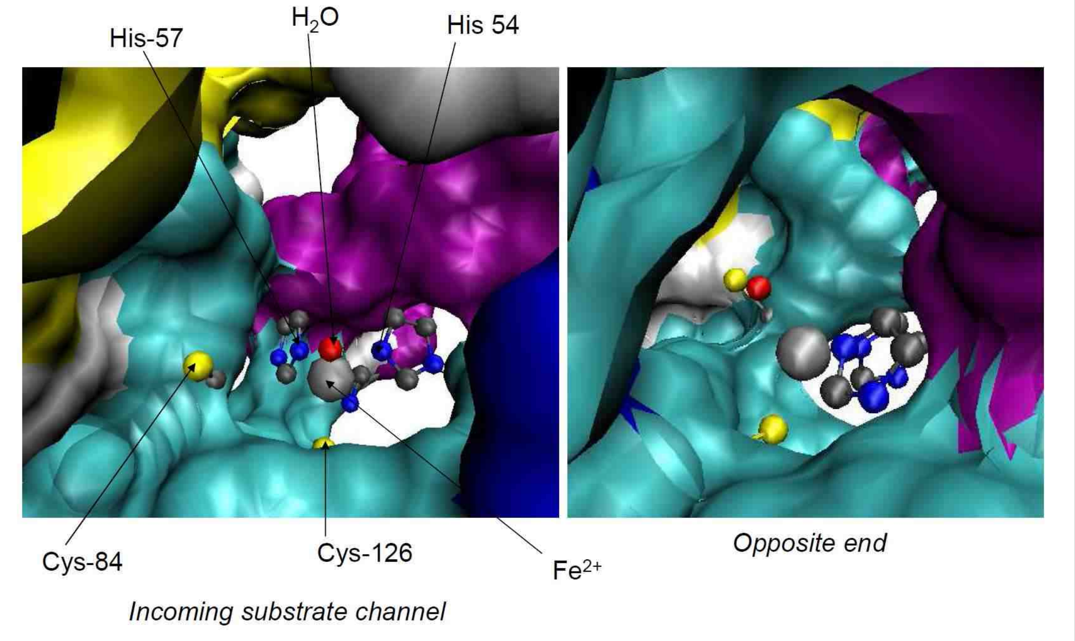

Figure 3.2: A magnified stereo representation of the of the van der Waals surface of the luxS dimmer showing the substrate channel with Fe^{2+} at the active site coordinated to His-54, His-57, Cys-126 and a H_2O/OH^- in *Bacillus subtilis* luxS. The position of Cys-84 is also shown (4.86 Å from Fe^{2+} metal center). On

the right hand side is the opposite end of the channel. The protein structure was downloaded from the protein data bank (PDB) 1J6X

Both C84 and E57 have been proposed to participate in the luxS catalytic mechanism as general acids/bases [136]. However, Ser-6 and His-11 are involved in substrate/intermediate binding through hydrogen bonding interactions, [137] whereas Arg-39 has been proposed to stabilize the thiolate anion in Cys-84 [135]. Figure 3.2 shows the substrate channel containing the active site (Fe^{2+} coordinated to His-54, His-58, Cys-126 and a hydroxide/water molecule in *Bacillus subtilis* luxS) and the positions of amino acid residues Arg-39 and Glu-57 are shown in Figure 3.3.

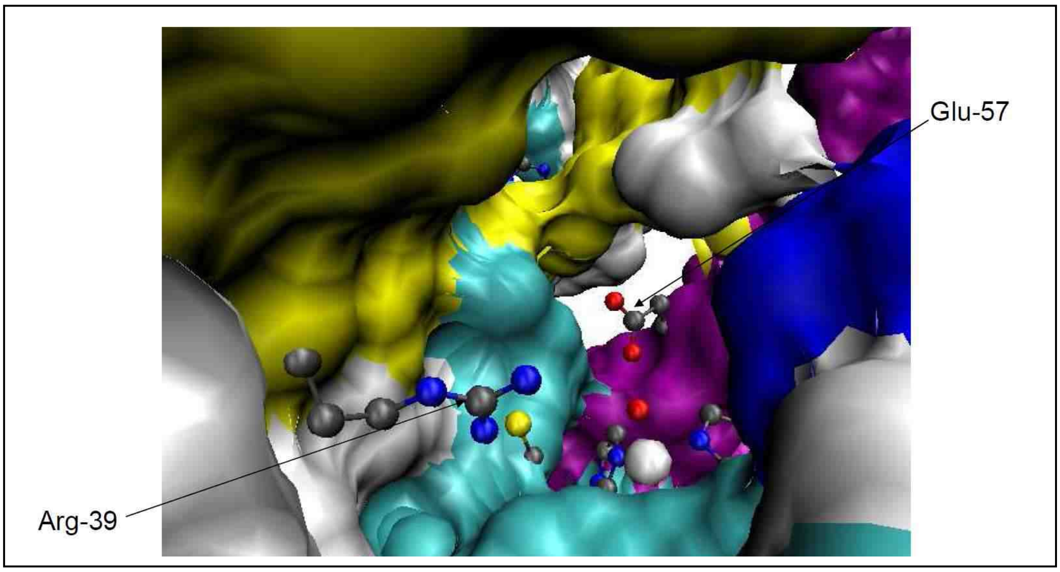

Figure 3.3: A magnified stereo representation of the of the van der Waals surface of the luxS dimmer showing the substrate channel with Fe^{2+} at the active site coordinated to His-54, His-57, Cys-126 and a H_2O/OH^- in *Bacillus subtilis*

luxS. The positions of Arg-39 and Glu-57 are shown. Arg-39 is located at 4.04 Å from Cys-84 and Glu-57 is located at 4.67 from Fe^{2+} metal center.

Scheme 3.1

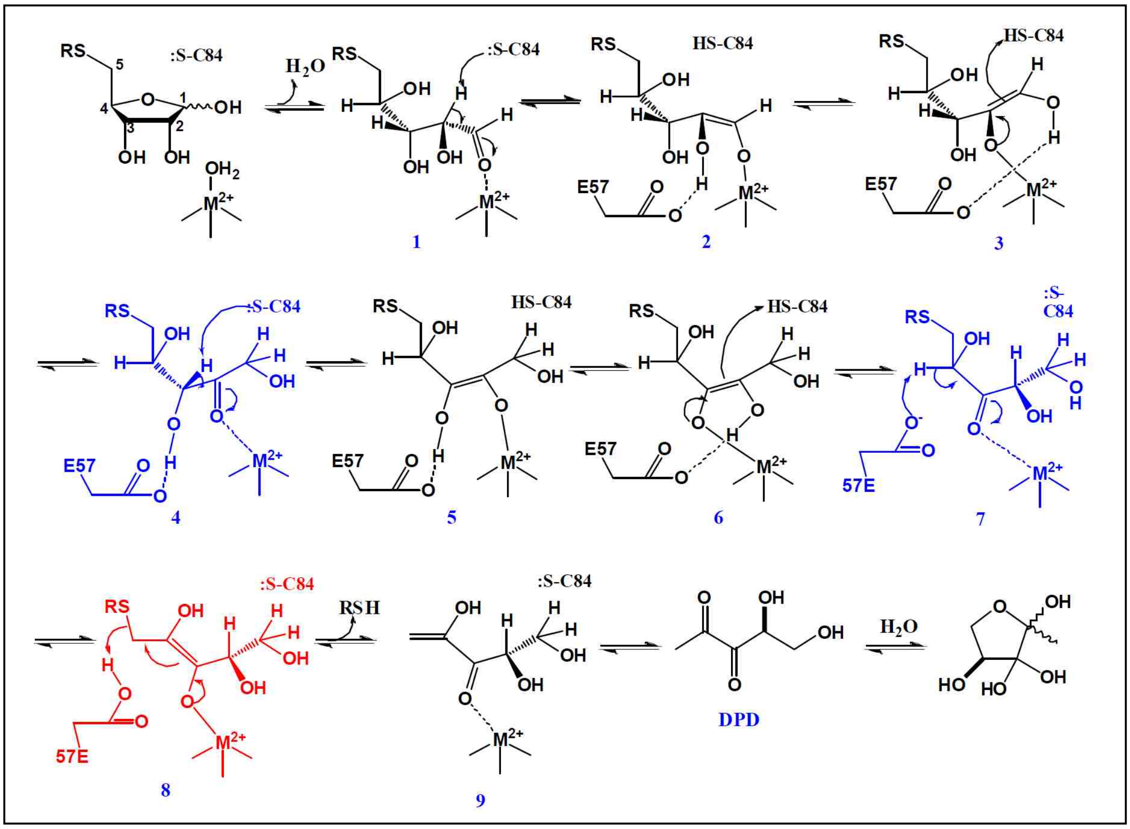

The LuxS proposed catalytic mechanism is a metal-catalyzed aldose-ketose isomerization reaction involving two consecutive carbonyl migrations followed by a β-elimination of the thioether linkage at C5 (Scheme 3.1) [135]. The substrate, S-ribosylhomocysteine (SRH), exists predominantly in its hemiacetal form; however, it was proposed that binding to the LuxS active site would open the ribose ring so that the carbonyl oxygen of the aldehyde binds to the metal ion, displacing a water/hydroxide molecule bound at the active site [132].

A general base, likely Cys-84 in BsLuxS, is proposed to abstract a proton from the C2 position generating a cis-enediolate intermediate 2. This step is followed by the ligand exchange from the C1 to C2-OH group, presumably assisted by a second base/acid that is proposed to be Glu-57 via a five membered ring transition state, giving enediolate 3. Reprotonation at C1 by Cys-84 followed by enol-keto tautomerism generate a 2-keto intermediate 4. A repetition of this isomerization reaction results into the migration of the carbonyl group to the C3 position to give a 3-keto intermediate 7. Step 7 is followed by β-elimination at C5, and is probably catalyzed by Glu-57 releasing homocysteine (Hcys) and the enol form of 4,5-dihydroxy-2,3-pentanedione (DHPD) 9 which tautomerizes to the keto form. However, this mechanism is supported by substantial experimental evidence, including the experimental observation of ketones 4 and 7 by broadband-decoupled ^{13}C NMR spectroscopy [112], direct coordination of the 2-keto oxygen of intermediate 4 to the metal ion is observed by x-ray crystallography from co-crystallization of the inactive C84A mutant of Co^{2+}-substituted *Bacillus subtilis* LuxS with the 2-ketone intermediate [137], and confirms of the proposed stereochemical course of the proton transfer reactions [136].

3.7 Statement of the Research Problem

LuxS plays a key role in quorum sensing making its investigation an attractive target for inhibition and the development of novel antibacterial agents. It is also an intriguing enzyme mechanistically because it catalyzes the non-redox cleavage of a stable thioether bond, a difficult reaction from chemist's perspective. However, the electronic structure of the LuxS active site is unknown. It is not known whether the substrate displaces a hydroxide or water bound molecule at the active site in the proposed catalytic mechanism. It is also not known whether C84 in the secondary coordination sphere is important for maintaining the catalytic geometry of LuxS active site. Therefore detailed spectroscopic investigations coupled with bonding calculations will help explain the nature of the electronic transitions for this tetrahedrally coordinated metalloenzyme and account for the existence of either the hydroxide or water bound molecule at the active site. These studies will also explain observed differences in catalytic efficiency of mutant and wild type enzyme as probably being due to geometrical distortions of the active site caused by mutation of the amino acid residue cysteine 84.

3.3 Hypotheses

The substrate displaces metal bound water and not a hydroxide in wt-LuxS. Secondly, mutation of C84 induces geometric changes at the active site of LuxS that reduces its catalytic efficiency.

3.4 Materials and Methods

Protein samples. Purified wt-luxS samples and mutants (C84A and C84D) were obtained from our collaborator Dehua Pei from The Ohio State University.

UV-vis Spectra. UV-vis luxS samples were prepared in 23% w/v polyethylene glycol 8000 (2.3 g PEG/10ml HEPES buffer) and the HEPES buffer was ensured to be a Cl^- free to avoid binding of Cl^- to the metal center which would in turn interfere with the native spectrum. Higher concentrations of PEG 8000 in UV-vis experiments scattered light. The final concentration of the luxS protein in the UV-vis sample cell was about 5 μM in 20 mM HEPES buffer admixed in PEG 8000 (23% w/v PEG 8000), pH 8. The spectra were recorded using a U-3501 double beam spectrophotometer at room temperature.

MCD experiments. An optically transparent glass is required for low temperature MCD measurements. This was achieved by preparing the protein samples in 140% w/v polyethylene glycol 8000 (14g PEG/10ml HEPES buffer). The sample was always prepared in a Cl^- free buffer to avoid binding to the metal center that would produce interference with the native spectrum. The final concentration of the luxS protein in the MCD sample cell ranged from 15 to 25 μM in 20 mM HEPES buffer, pH 8. Low temperature MCD spectra were measured in an applied magnetic field of 7 T using a JASCO J-810 spectropolarimeter that is interfaced to a computer and an Oxford Instruments Spectromagnet 4000-7 split-coil superconducting magnet system.

EPR spectroscopy. EPR spectra of the frozen samples were recorded on a Bruker model EMX spectrometer operating at X-band (~9.4 GHz). A microwave power of 20 dB was used for all the luxS experiments and spectra were collected at 4K, 8K and 20K for high spin Co^{2+} (S = 3/2) using a liquid helium flow cryostat. Computer simulations were done using xsophe software program.

Computational Methods. Geometry optimizations for the luxS computational models were carried out at the B3LYP level of DFT in spin-unrestricted mode using the Gaussian 03, version B.03 software package. Ammonia ligands were used to approximate the coordination environment of the two histidines and methyl thiolate to approximate the coordination environment of a cysteine at the enzyme's tetrahedral Co^{2+} metal site and with the fourth ligand as either water or hydroxide. Calculations were carried out using the 6-31G* basis set with p and d polarization functions. *Angular overlap method (AOM)* calculations were made using *AOMX* (a FORTRAN program developed by Hoggard for d^3 transition metal ions and extended to d^n systems by Adamsky [6,138]). The input file contained luxS Cartesian coordinates of the crystal structure downloaded from PDB 1IE0. However, during fitting, the Cartesian coordinates remained fixed and the program was set up to calculate the best fit to the observed d-d transition energies by varying B (Racah parameter), ξ (spin-orbit coupling constant), $e\sigma$ and $e\pi$.

3.5 Results and Analysis

3.5.1 Ligand Field Transitions in Tetrahedral Co(II) – d^7

The free ion energy terms for Co^{2+} (d^7)-tetrahedral are ^4F, ^4P, ^2H, ^2G, ^2F, (2)^2D, ^2P. However, as predicted by Hund's rule, the ^4F term is the ground state of the Co^{2+} ion with the quartet term (^4P) occurring at higher energy and separated by 15B. B is a Racah parameter, which is a measure of electron-electron repulsion between terms of the same multiplicity. B has been determined for the free Co^{2+} ion to be 970 cm^{-1}. When the ligand field is introduced as a perturbation on the system due to the tetrahedral ligand field, the symmetry is lowered from spherical (R_3) to tetrahedral (T_d) and splits the ^4F term into three new terms, $^4A_2$, $^4T_2$, and $^4T_1$ whereby the $^4A_2$ term becomes the ground state. The energy differences between the $^4A_2$, $^4T_2$, and $^4T_1$ (F) terms depend on the strength of the ligand field. The ^4P term does not split but becomes another $^4T_1$ term often denoted as $^4T_1$ (P). However, three spin allowed ligand field transitions from the ground state, $^4A_2$ (F) to the three excited states, $^4T_2$ (F), $^4T_1$ (F) and $^4T_1$ (P) are expected for a Co^{2+} ion possessing a tetrahedral geometry. These are $^4A_2$ (F) → $^4T_2$ (F), $^4A_2$ (F) → $^4T_1$ (F) and $^4A_2$ (F) → $^4T_1$ (P) which occur in the infra-red (3,000 – 5,000 cm^{-1}), near infra-red (6,000 – 12,000 cm^{-1}) and visible regions (13,900 – 20,000 cm^{-1}) respectively. The $^4T_1$ (F) and $^4T_1$ (P) energy states interact by symmetry and they are mixed by the following 2 X 2 matrix elements:

$$\begin{array}{ccc} & {}^4T_1(F) & {}^4T_1(P) \\ {}^4T_1(F) & 2\Delta + 3B - E & 6B \\ {}^4T_1(P) & 6B & \Delta + 12B - E \end{array}$$

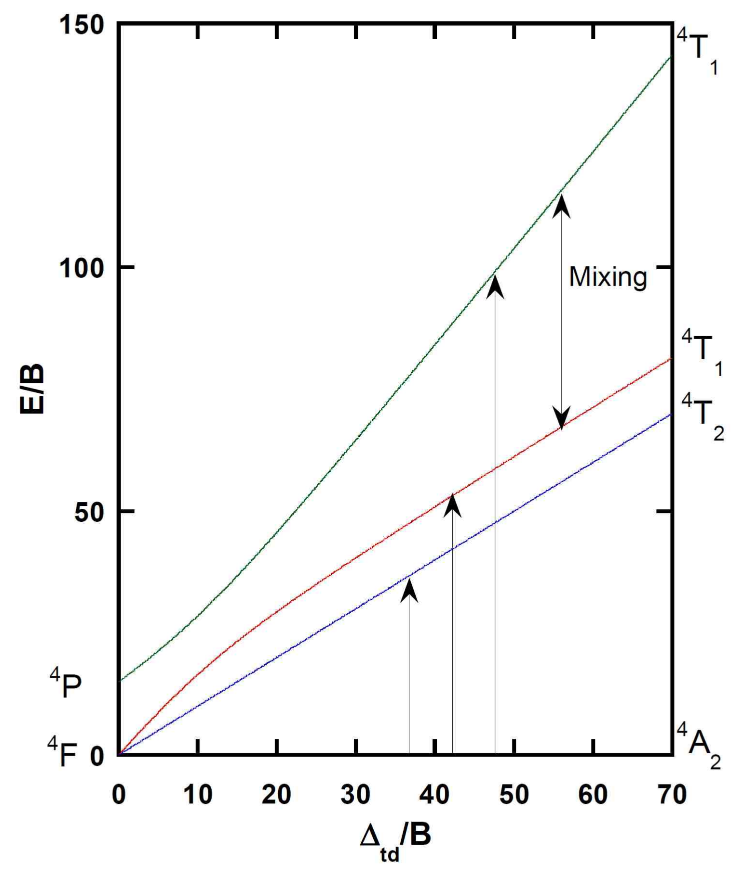

Figure 3.4: Simplified Tanabe sugano diagram showing the energy differences between terms of the three spin allowed ligand field transitions occurring in tetrahedral d^7 Co^{2+} complex.

Solving the quadratic equation: $(2\Delta^2 + 27B\Delta) - E(3\Delta + 15B) + E^2 = 0$ resulting from the matrix above in E and worked out for E/B gives two linear equations (i) and (ii) corresponding to $^4A_2$ (F) → $^4T_1$ (F) and $^4A_2$ (F) → $^4T_1$ (P) transitions. Thus equation (iii) corresponds to the $^4A_2$ (F) → $^4T_2$ (F) transition; the ligand field parameter (Δ), and B is the Racah parameter which is the measure of the repulsion between terms of the same multiplicity. Figure 3.4 depicts these three spin allowed electronic transitions in a simplified Tanabe Sugano diagram which plots the transitional energies (E), including inter-electronic repulsions (B) as a function of the strength of the ligand field (Δ).

$$E2/B = 1/2\{15 + 3(\Delta/B) - \sqrt{}(225 - 18(\Delta/B) + (\Delta/B)^2)\}\ldots\ldots\ldots\ldots(i)$$

$$E3/B = 1/2\{15 + 3(\Delta/B) + \sqrt{}(225 - 18(\Delta/B) + (\Delta/B)^2)\}\ldots\ldots\ldots\ldots(ii)$$

$$E1/B = \Delta/B\ldots\ldots\ldots\ldots\ldots\ldots\ldots\ldots\ldots\ldots\ldots\ldots(iii)$$

A series of spin forbidden transitions may also appear due to electronic transitions to the excited states derived from the ^2H, ^2G, ^2F, (2)^2D or ^2P terms and these would make band assignments very difficult. The lowest energy configuration (the ground state term, $^4A_2$) of tetrahedral Co^{2+} has four electrons in the degenerate e orbitals ($\pi + \sigma$ orbitals) which are paired and three unpaired electrons in the t_2 degenerate orbitals ($\sigma + \pi$ orbitals) (Figure 3.5). However, its spin state, S = 3/2 which has $m_s = \pm 1/2, \pm 3/2$ degenerate spin microstates in tetrahedral symmetry is subject to zero field splitting. This is the removal of spin microstate degeneracy of the ground state in the absence of magnetic field as a consequence of a distortion from tetrahedral symmetry (T_d) to lower symmetry geometries such as C_{3v}, or C_{2v}, and spin orbit coupling which mixes the excited states into the ground state.

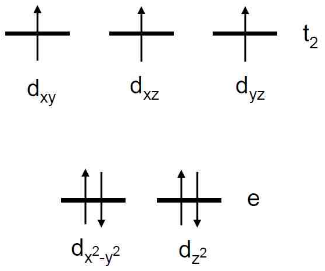

Figure 3.5: Splitting diagram for tetrahedral Co^{2+} complex – ground state configuration.

However, the ground state $^4A_2$ is non degenerate and their are low lying degenerate excited states, $^4T_2$ (F) and $^4T_1$ (F). This ground state can not be split by in state spin orbit coupling but is subject to splitting by out of state spin orbit coupling and low-symmetry ligand field distortions. Both excited states have orbital angular momentum and are split by in state spin orbit coupling producing twelve wavefunctions (Figure 3.6). However, the out of state orbit coupling interaction that mixes them into the ground state must transform as $A_2 \times T_2 = T_1$ or $A_2 \times T_1 = T_2$. Since the spin orbit coupling operator (this operator transforms as the rotations (R_x. R_y, R_z) in the character Table 3.1) transforms as T_1, then the spin orbit coupling mixes $^4T_2$ into the ground state $^4A_2$ ($A_2 \times T_1 = T_2$). Ligand field distortions will break the excited states degeneracy of $^4T_2$ (into ^4E and $^4A_1$ in C_{3v} and $^4B_2$, $^4B_1$ and $^4A_1$ in C_{2v} symmetry) and of $^4T_1$, (into ^4E and $^4A_2$ in C_{3v} and $^4B_2$, $^4B_1$ and $^4A_2$ in C_{2v} symmetry). Low symmetry distortions coupled with out of state spin orbit coupling partially removes the spin degereracy in the $^4A_2$ ground state. Consequently, the m_s microstate degeneracy of the ground term is removed and results in a zero field splitting (the energy difference between the two Kramers doublets, |S, m_s> = |3/2, ±1/2> and |3/2, ±3/2> depicted in Figure 3.6) of the ground state. The order of spin orbit coupling and distortion is immaterial and produces the same resultant effect. However Figure 3.6 illustrates this effect in the order of low-symmetry distortion followed by spin orbit coupling and then the Zeeman effect (magnetic field application). The energetics of the lower symmetry excited states terms in C_{3v} and C_{2v} point groups were not considered in this illustration. It also shows the terms that result from T_d symmetry upon distortion to lower symmetry geometries and the multiplets which result from T_d symmetry terms upon spin orbit coupling of the excited states. However, the diagram does not correlate the energetics of the two effects.

Table 3.1: Character table for tetrahedral symmetry (T_d)

T_d	E	$8C_3$	$3C_2$	$6S_4$	$6\sigma_d$		
A_1	1	1	1	1	1		
A_2	1	1	1	-1	-1		
E	2	-1	2	0	0		$(2z^2 - x^2 - y^2, x^2 - y^2)$
T_1	3	0	-1	1	-1	(R_x, R_y, R_z)	
T_2	3	0	-1	-1	1	(x, y, z)	(xy, xz, yz)

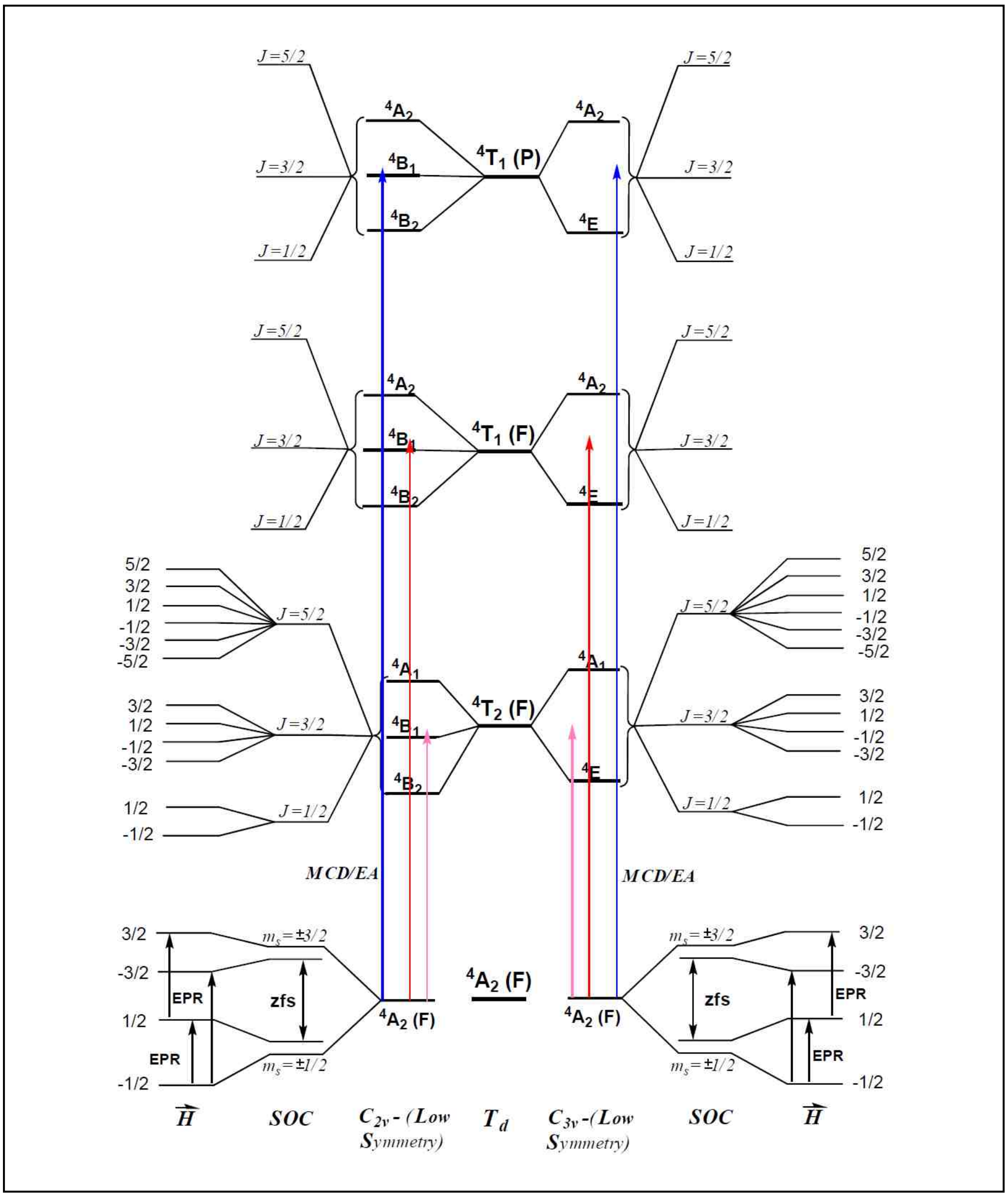
J=5/2
J=3/2
J=1/2
4A2
4B1
4B2
4T1 (P)
4E
4T1 (F)
4A1
4T2 (F)
5/2
3/2
1/2
-1/2
-3/2
-5/2
MCD/EA
ms=±3/2
ms=±1/2
EPR
zfs
4A2 (F)
H
SOC
C2v - (Low Symmetry)
Td
C3v -(Low Symmetry)

Figure 3.6: Splitting of the T_d terms with both distortions (C_{2v}, C_{3v}) and spin orbit coupling (SOC) followed by splitting of each multiplet due to magnetic field (H) for Co^{2+}, d^7. The higher excited states, $^4T_1$ (F) and $^4T_1$ (P) also split in the same way as $^4T_2$ (F) upon application of the magnetic field (H) though not shown. The splitting of the ground state term due to both low symmetry and spin orbit coupling (SOC) results into zero field splitting zfs which can be probed by EPR

spectroscopy and VTVH-MCD. Transitions to higher excited states $^4T_2$ (F), $^4T_1$ (F) and $^4T_1$ (P) can be probed by electronic absorption (EA) and magnetic circular dichroism (MCD).

Figure 3.6 illustrates these two distortions from T_d symmetry. However, if the tetrahedral active site of luxS (Co^{2+}) is distorted to C_{3v} symmetry, transitions to $^4A_2$ and ^4E are expected which will appear as a C term and pseudo A term in the MCD spectra particularly for the near infra-red transitions ($^4A_2$ (F) → $^4T_1$ (F)) which have very little or no mixing with the spin forbidden doublet transitions. On the other hand, a distortion to C_{2v} symmetry will show transitions to $^4B_2$, $^4B_1$ and $^4A_2$ excited states which will all appear as C terms in the MCD spectra. The near infra-red region is more sensitive to the geometric distortion than the visible region due to a greatly reduced mixing with spin forbidden doublet transitions. If departures from T_d symmetry are severe, then the interpretation of the spectra on the basis of a simple perturbation of the T_d geometry becomes complicated. However, distortions in luxS suggesting a C_{3v} distortion splitting T states into ^4E and $^4A_2$ terms were observed in the near infra-red region ($^4A_2$ (F) → $^4T_1$ (F)) for both wild type and mutant enzyme forms.

3.5.2 Observed Ligand Field Transitions in LuxS, C84A and C84D

Both the absorption and MCD spectra for the wild-type luxS and the two mutants (C84A and C84D) (Figures 3.7, 3.8 and 3.9) revealed absorption bands in the near infra red and visible regions derived from $^4A_2$ (F) → $^4T_1$ (F), $^4A_2$ (F) → $^4T_1$

(P) ligand field transitions ($\epsilon \approx 300\ M^{-1}cm^{-1}$). Transitions associated with $^4A_2$ (F) → $^4T_2$ (F) which occur in the infra-red region were not observed due to instrumental limitations. The $^4A_2$ (F) → $^4T_1$ (F) transitions for wt-luxS were observed at 7,950 and 10,451 cm^{-1} (Figure 3.7). The transition at 7,950 cm^{-1} appeared as a pseuso A term in the MCD (with a positive C term at 7404 cm^{-1} and a negative C term at 8404 cm^{-1}) whereas the transition at 10,451 cm^{-1} appeared as a negative C term in the MCD (Figure 3.7). These same transitions for the mutants were observed at 7,836 (positive C term at 7351 cm^{-1} and a negative C term at 8241 cm^{-1}) and 10,451 cm^{-1} for C84A (Figure 3.8), whereas for C84D the bands occurred at 8,010 (positive C term at 7366 cm^{-1} and negative C term at 8487 cm^{-1}) and 10,436 cm^{-1} (Figure 3.9). However, the splitting pattern in the wild type and mutants in the near infra-red region suggests a distortion from the tetrahedral (T_d) symmetry to either C_{2v} ($^4A_1$ + $^4B_1$ + $^4B_2$) or C_{3v} symmetry whereby the $^4T_1$ (F) state is proposed to split axially by the low symmetry distortion into an E and an A state. No appreciable differences in transition energies were observed in the NIR region among wt-luxS, C84A and C84D indicating only small perturbation of the ligand field. The $^4T_1$ (P) state showed a more complex splitting pattern for the wt and mutants which we attribute it to low symmetry distortions, spin-orbit coupling, and the presence of charge transfer transitions. Computational probes of low energy charge transfer transitions were made using DFT (section 3.5.5.1) methods and an angular overlap model (AOMX) (section 3.5.5.2) enabled the assignment of the ligand field transitions for wt-luxS and mutants. The $^4A_2$ (F) → $^4T_1$ (P) transitions for the wt-luxS were observed at 15,386, 16,105 and 17,500 cm^{-1} (Figure 3.7).

Table 3.2: Energy states and observed transitions for wt, C84A and C84D

Energy State	**WT LuxS**	**LuxS C84A**	**LuxS C84D**
$^4A_2 \rightarrow {}^4T_2(F)$	Not observed	Not observed	Not observed
$^4A_2 \rightarrow {}^4T_1(F)$	7,950 cm^{-1}	7,836 cm^{-1}	8,010 cm^{-1}
	10,451 cm^{-1}	10,451 cm^{-1}	10,436 cm^{-1}
$^4A_2 \rightarrow {}^4T_1(P)$	15,386 cm^{-1}	15,391 cm^{-1}	15,228 cm^{-1}
	16,105 cm^{-1}	16,147 cm^{-1}	16,122 cm^{-1}
	17,500 cm^{-1}	17,600 cm^{-1}	17,246 cm^{-1}

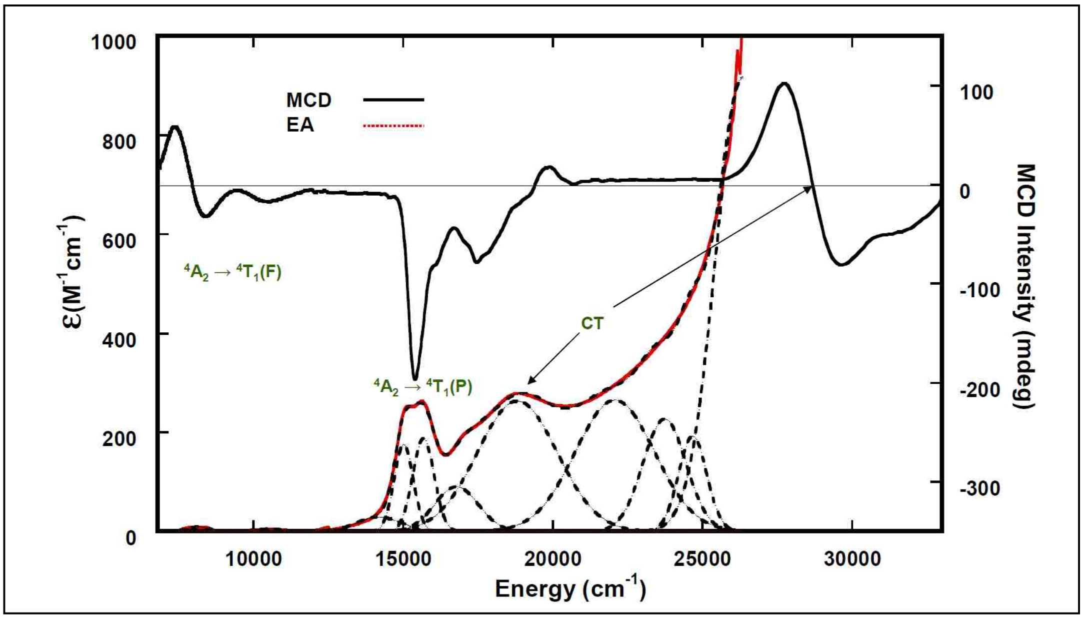

Figure 3.7: MCD and electronic absorption (EA) spectra overlays for wt-luxS

All these bands appeared as temperature dependent negative C terms in the MCD. In C84A, these transitions were observed at 15,391, 16,147 and 17,600 cm^{-1} (Figure 3.8) whereas in C84D they were observed at 15,228, 16,122 and 17,246 cm^{-1} (Figure 3.9). Table 3.2 summarizes the energy states and their corresponding observed transitions for wild type and mutant enzyme forms. However, the splitting pattern in the $^4T_1$ (P) state suggests the presence of C_{2v} symmetry where all the three terms, $^4A_1$, $^4B_1$ and $^4B_2$ appear as negative C terms in the MCD spectra.

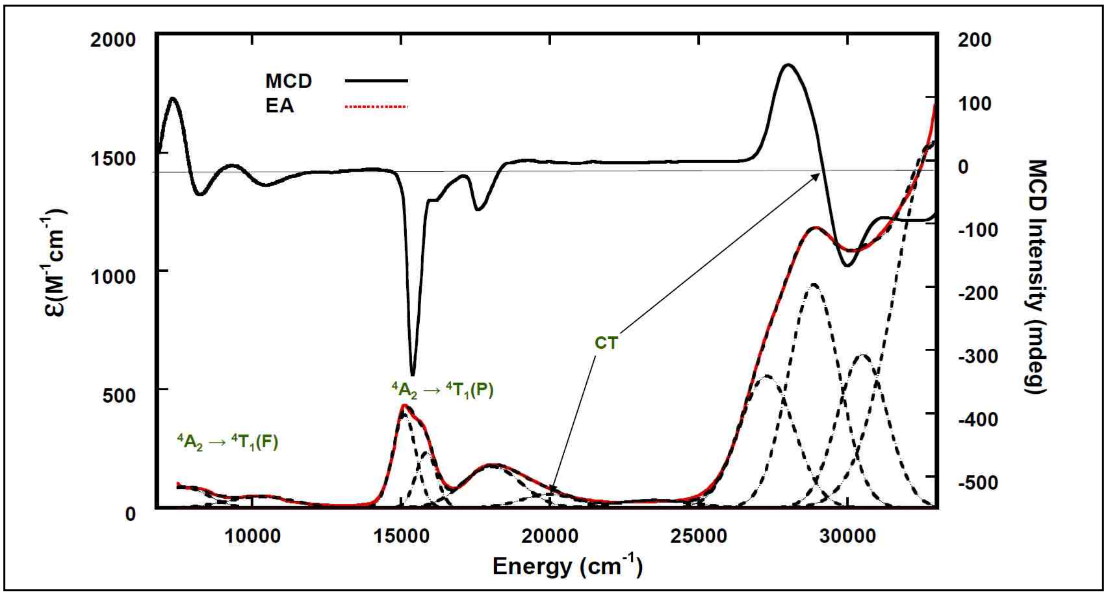

Figure 3.8: MCD and electronic absorption (EA) spectra overlays for luxS-C84A

Since the $^4T_1$(P) state is a very sensitive probe of Co^{2+} ligand field, this same splitting can be implicated in the NIR giving $^4A_1$, $^4B_1$ and $^4B_2$ components where one of these terms is positive C term (lowest in energy) and the other two terms are negative C terms.

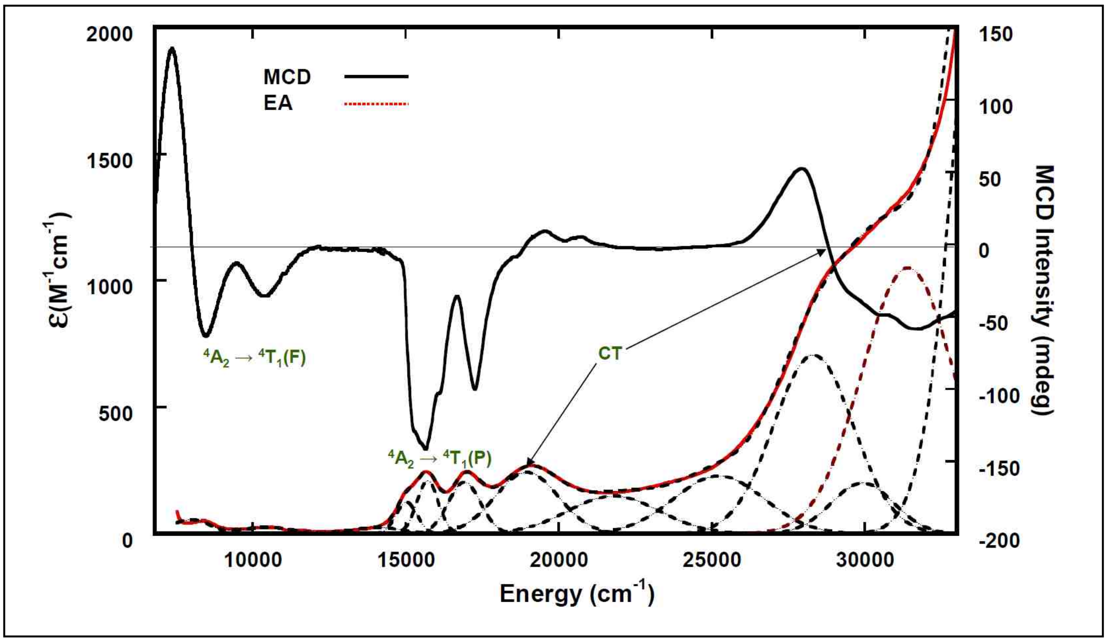

Figure 3.9: MCD and electronic absorption (EA) spectra overlays for luxS-C84D

The high-energy region is comprised of bands that arise from charge-transfer (CT) transitions. These bands, while intense in the electronic absorption spectrum, carry considerably less MCD intensity than the ligand-field transitions. These have been assigned as S → Co charge transfer transitions. For wt-luxS, these CT bands were observed at 19,866 and 28,641 cm^{-1} whereas in C84A at 19,169 and 29,164 cm^{-1} while in C84D at 19,517 and 28,758 cm^{-1} (Figures 3.7, 3.8 and 3.9).

3.5.3 Determination of Spin Hamiltonian and the Zero Field Splitting Parameters Using VTVH-MCD

The EPR spectrum of wt-luxS appears as if it were a mixture of the C84A and C84D spectra (Figure 3.13). Therefore, VTVH MCD data have only been collected for the C84A and C84D mutants. The VT-MCD spectra for wt, C84A and C84D luxS were collected at 5K, 10K and 20K and showed that all MCD bands are temperature dependent C terms (Figure 3.10). The VTVH-MCD magnetization curves for C84A and C84D were collected at three selected wavelengths as indicated in Figures 3.11 and 3.12.

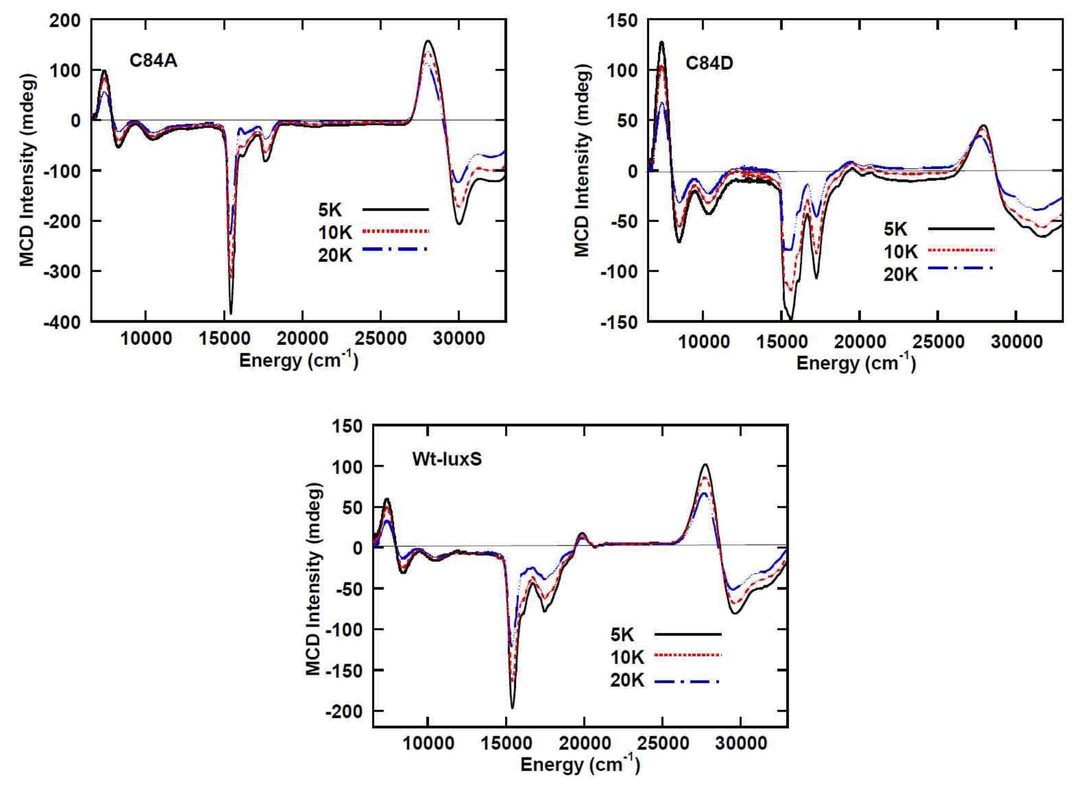

Figure 3.10: VT-MCD for wt-luxS, C84A and C84D collected at 5, 10 and 20K. The MCD intensities for all bands increase with decreasing temperature, which is a characteristic of C-term behavior.

The MCD signal intensity at a selected wavelength was measured at four different temperatures (≈ 1.8, 3, 5, and 10 K) as a function of magnetic field between (0 - 7 T). The resulting sets of magnetization curves for C84A and C84D are shown in Figures 3.11 and 3.12 respectively. The NIR 1364 nm VTVH-MCD data set for C84A showed almost no nesting (Figure 3.6) whereas the other two magnetization data sets in the ultraviolet-visible region, at 357 and 650 nm showed larger nesting indicating mixing of the ±3/2 ground spin state with the ±1/2 excited spin state. In contrast, the corresponding VTVH-MCD data set for the NIR band at 1354 nm in C84D showed nesting, and this suggests differences in zfs values between C84A and C84D. The remaining two data sets for C84D in the visible region at 580 and 638 nm showed nesting similar to those observed for C84A (Figure 3.6).

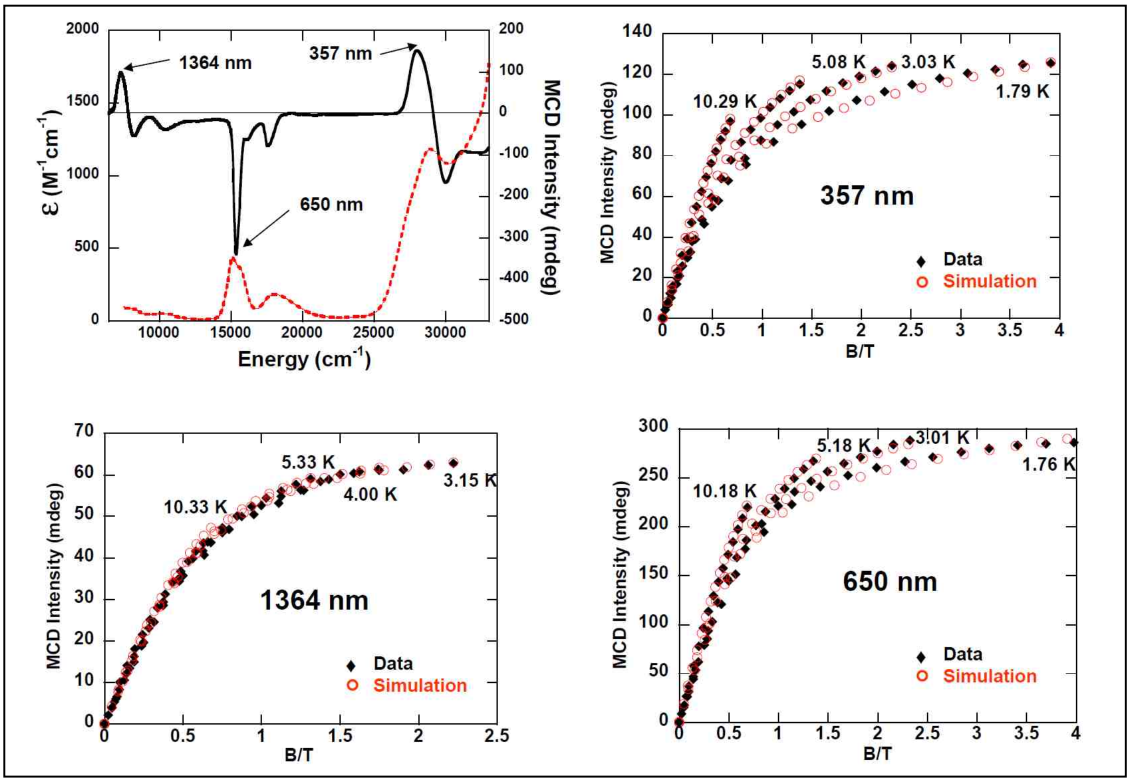

Figure 3.11: MCD magnetization curves of the luxS-C84A mutant at 357, 650 and 1364 nm. Spectral simulation has been achieved with $g_x = 2.300$, $g_y = 2.300$, $g_z = 1.800$, $S = 1.5$, $D = -10\ cm^{-1}$, $E/D = 0.095\ cm^{-1}$; polarizations are: xy = 1.000, xz = yz = 0.900 at 430 nm, xy = 1.000, xz = 0.000, yz = 0.400 at 1364 nm, and xy = 0.600, xz = 0.700, yz = 1.000 at 357 nm.

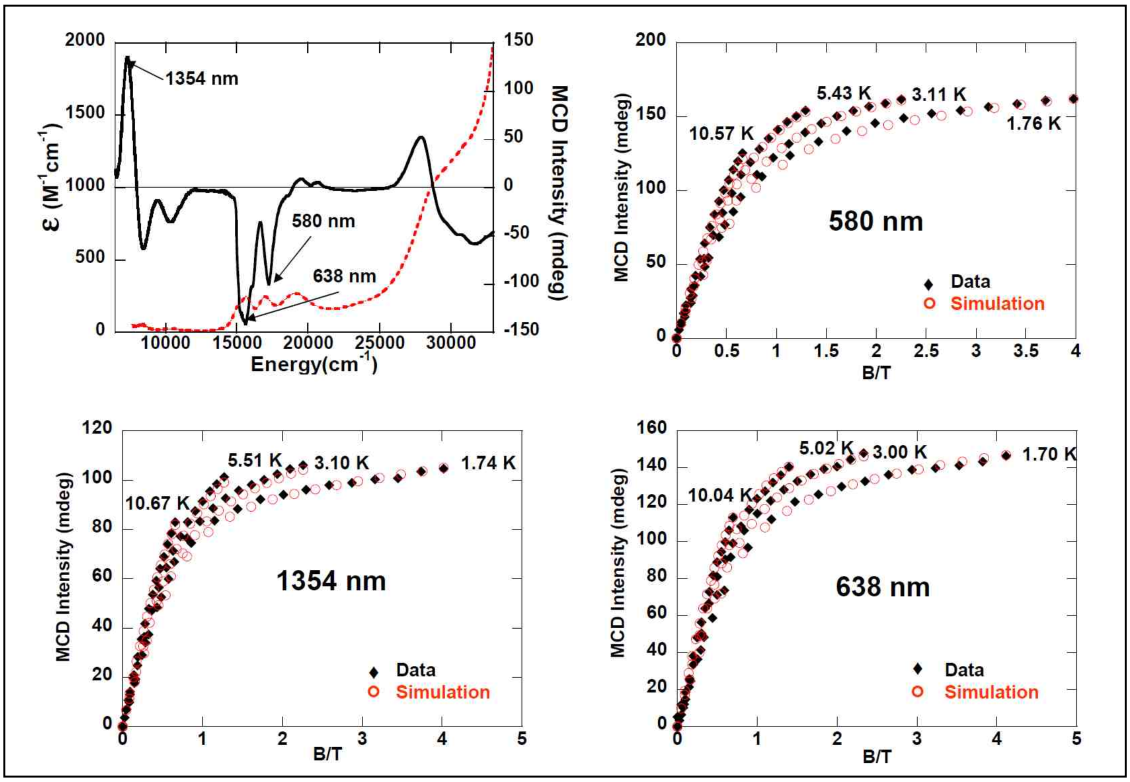

Figure 3.12: MCD magnetization curves of the luxS-C84D mutant at 580, 638 and 1354 nm. Spectral simulation has been achieved with $g_x = 2.180$, $g_y = 2.180$, $g_z = 2.115$, $S = 1.5$, $D = 8$ cm^{-1}, $E/D = 0.045$ cm^{-1}; polarizations are: xy = xz = 0.000, yz = 1.000 at 638 nm, xy = 1.000, xz = 0.900, yz = 0.000 at 1354 nm, and xy = xz = 1.000, yz = 1.000 at 580 nm.

The VTVH-MCD spectral simulation yielded the following spin Hamiltonian parameters for luxS-C84A: $D = -10$ cm^{-1}, $E/D = 0.095$ cm^{-1}, $g_x = 2.300$, $g_y = 2.300$ and $g_z = 1.800$ whereas luxS-C84D gave $D = 8$ cm^{-1}, $E/D = 0.045$ cm^{-1}, $g_x = 2.180$, $g_y = 2.180$ and $g_z = 2.115$. These same parameters were used for the simulation of their corresponding EPR spectra.

3.5.4 Determination of Spin Hamiltonian by EPR Spectroscopy

The EPR spectra of wt-luxS, C84A, and C84D were collected as frozen solutions in 50 mM Hepes buffer, pH 8 at 4, 8 and 20K using a 9.416 GHz X-band frequency. However, the maximum signal intensity is observed at 4K and above 20K the signal becomes reduced and eventually disappears indicating relaxation processes are operative.

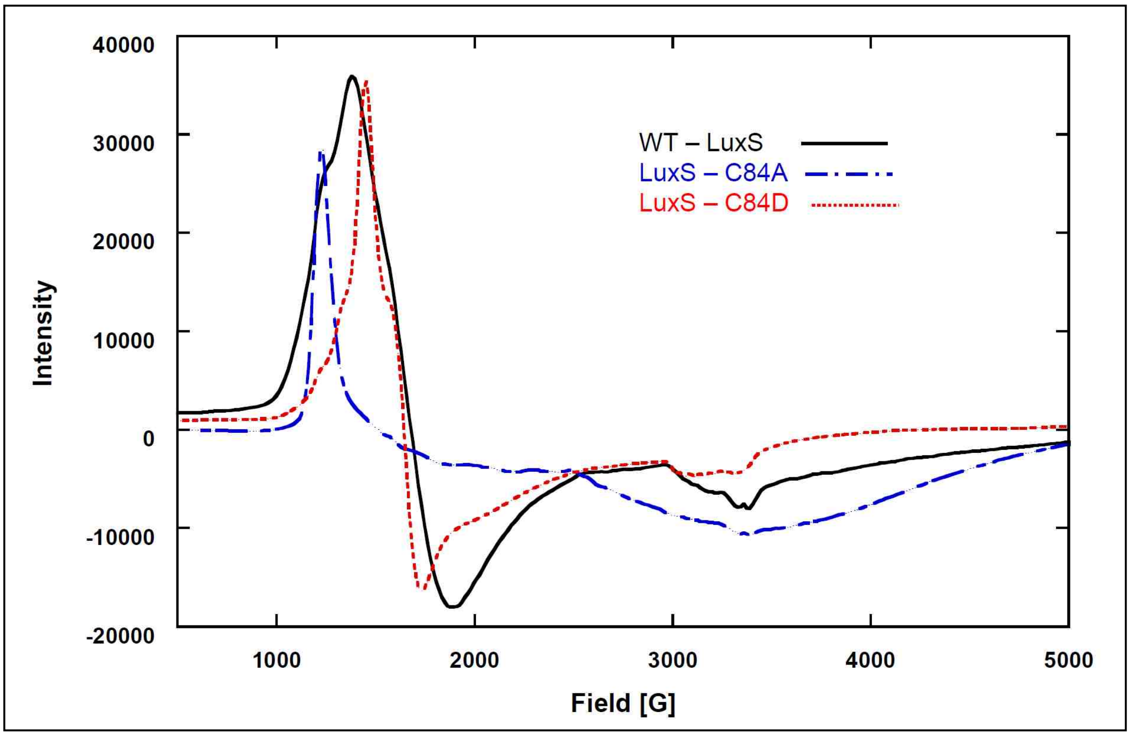

Figure 3.13: EPR spectral overlays for the wt, C84A and C84D-luxS at 4K and 20 dB.

The EPR spectral overlay of the wt, C84A and C84D enzyme forms indicated that wt enzyme appears as a mixture of C84A and C84D type spectra (Figure 3.13). Spectral simulation revealed that luxS-C84A is characterized by three resonances with g-values $g_x = 2.300$, $g_y = 2.300$ and $g_z = 1.800$ with E/D of 0.095 whereas C84D gave g-values; $g_x = 2.180$, $g_y = 2.180$ and $g_z = 2.115$ with E/D of 0.045 and completely resolved hyperfine coupling (51×10^{-4} cm^{-1}) at g_z for $^{59}Co^{2+}$, I = 7/2. The EPR spectra of C84A and C84D indicate an approximate axial symmetry for the cobalt ion at the active site.

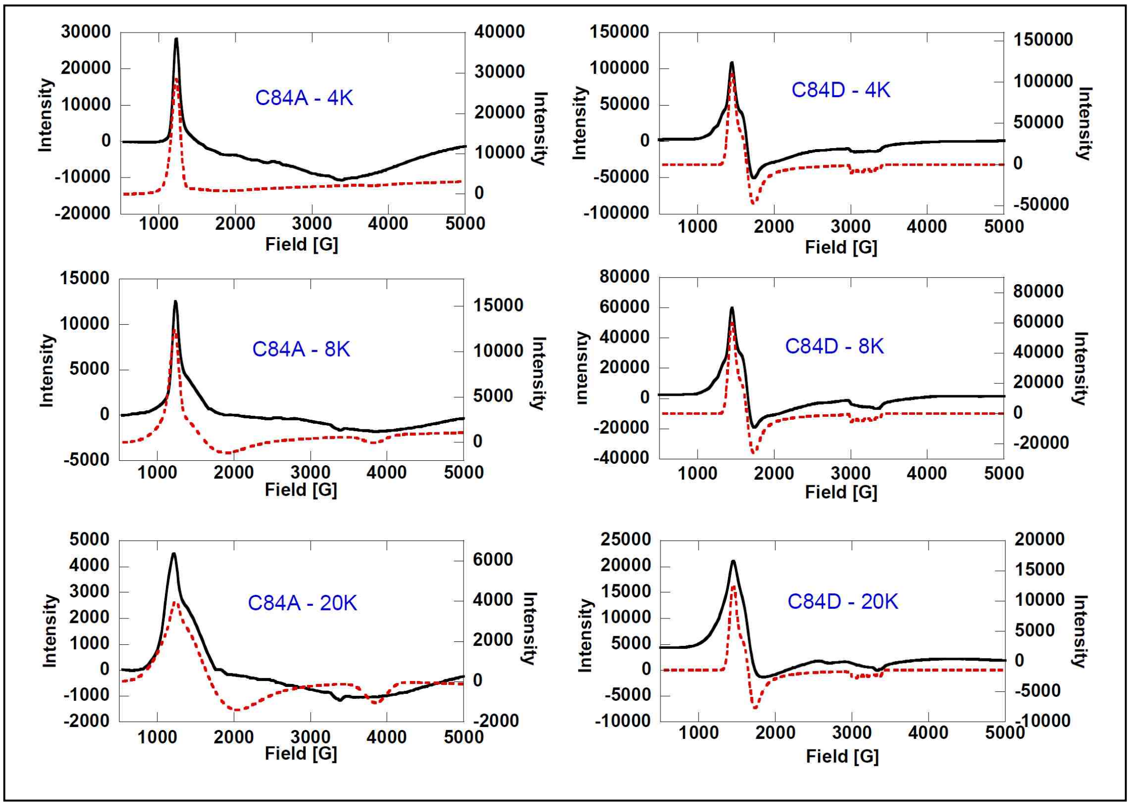

Figure 3.14: Temperature dependent EPR spectral data (____) and simulations (.........) overlays for C84A and C84D mutants collected and simulated at 4, 8 and 20K.

However, C84A (E/D = 0.095) shows evidence for a greater distortion from tetrahedral symmetry than C84D (E/D = 0.045). Both variable temperature EPR and MCD-VTVH simulations strongly suggest the value of D for C84A as -10 cm^{-1} which implies that the m_s = ±3/2 Kramers doublet is the ground state doublet (lower in energy) whereas the m_s = ±1/2 Kramers doublet is the excited state (higher in energy). The features observed in the low field region (1000 – 2000G) of the C84A variable temperature EPR spectra at 4, 8 and 20K were reasonably reproduced by computer simulations using the same set of spin Hamiltonian parameters (Figure 3.14).

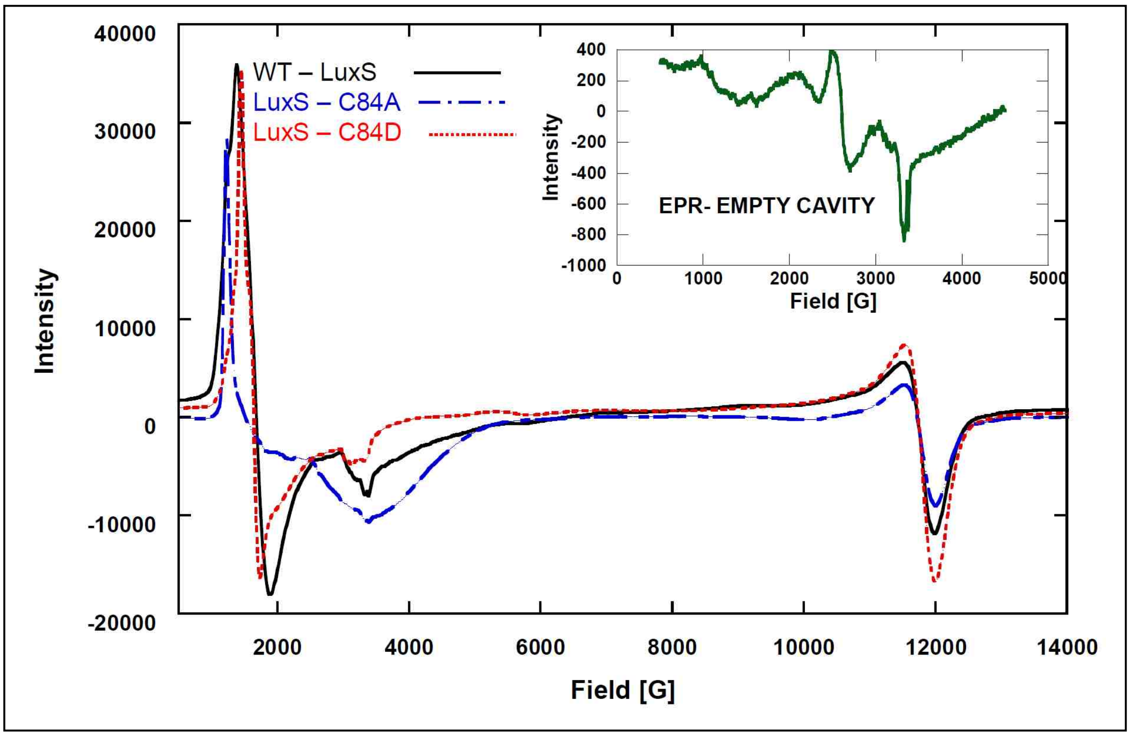

Figure 3.15: Full width EPR spectral overlays for the wt, C84A and C84D-luxS at 4K and 20 dB. The derivative shaped signal at 12000G represents the absorption for the paramagnetic oxygen. The insert represents the signal for the empty cavity at 4K, which interferes with the sample signals (visible between 2000 and 4000G in sample spectra).

The signal in the 3368G region possesses an interference from the empty cavity (The insert in Figure 3.15). The m_s = ±1/2 Kramers doublet, visible in the simulation at 3800G for 8 and 20K in Figure 3.13 is buried in the corresponding region of the data which is too broad, between 3000 and 4500G. This signal is parallel with the one at 1228G, which results from the m_s = ±3/2 Kramers doublet and is observed as a sharp peak seen clearly at 4K. The low temperature lines originating from the ±3/2 Kramers doublet are visibly sharper (line widths up to 250G) than their high temperature counterparts originating from the ±1/2 Kramers doublet (line widths up to 1300G). On the other hand, the C84D EPR spectra indicated a degree of active site heterogeneity by having C84A type resonances as a minor component (extra broadness visible at 1000 – 1300 G in C84D variable temperature EPR, Figure 3.14). Particularly, the broadness of the C84D EPR data at 20K results from C84A high temperature transitions originating from the ±1/2 Kramers doublet. However, The MCD-VTVH simulated value of D for C84D is 8 cm^{-1} which implies that m_s = ±1/2 Kramers doublet is the ground state (lower in energy) whereas the m_s = ±3/2 Kramers doublet is the excited state (higher in energy). All other visible features in the C84D EPR spectra were nicely reproduced by computer simulations and the transitions originate from m_s = ±1/2 Kramers doublet. These were less sensitive to temperature variations compared to corresponding transitions in C84A. Figures 3.16 and 3.17 represents energy level diagrams for C84A and C84D generated for the three canonical field orientations (X, Y and Z) using the same set of spin Hamiltonian parameters in order to facilitate the interpretation of these results.

C84A however, has temperature dependent features at 9900 and 11000G originating from m_S = ±1/2 Kramers doublet which were not observed in the data probably due to being obscured by a very intense transition arising from paramagnetic oxygen which occurs at 12000G (Figure 3.15).

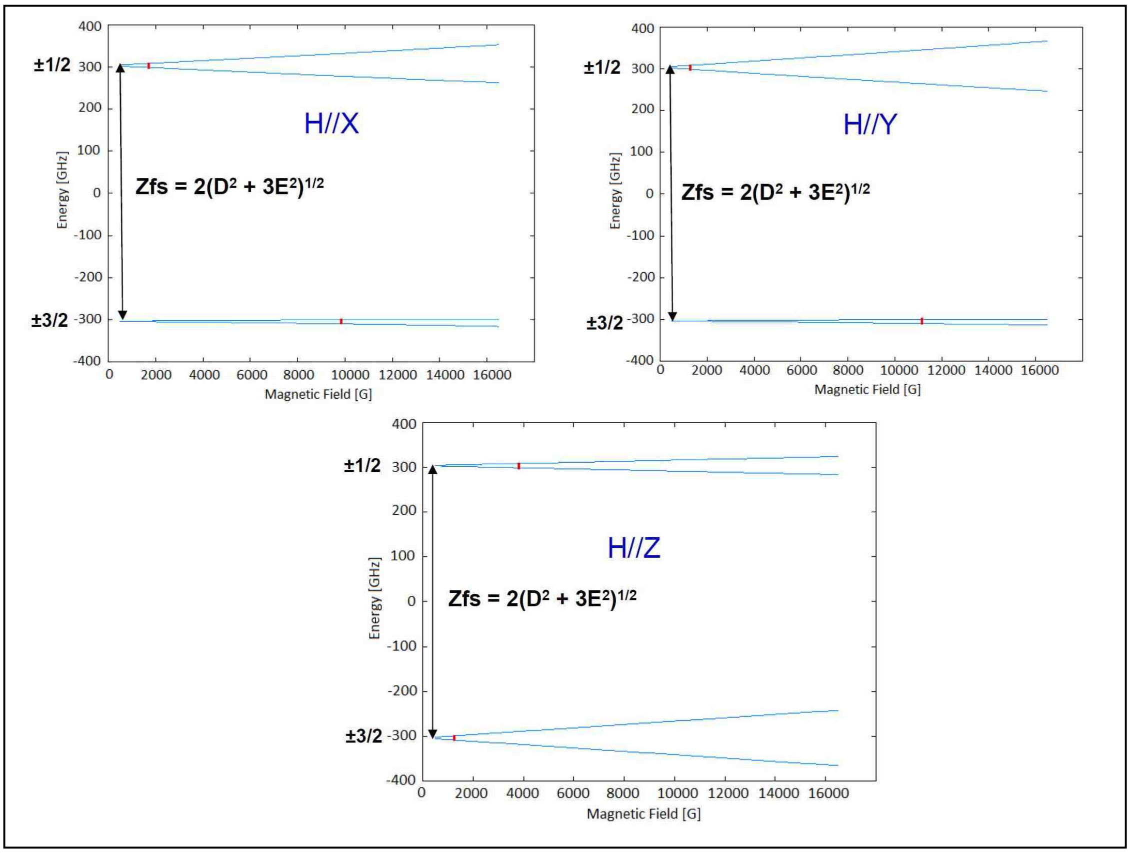

Figure 3.16: Energy levels as a function of magnetic field for the three canonical orientations of the field relative to the principal zfs axis calculated for C84A using the same set of EPR spin Hamiltonian parameters. Observed EPR transitions are marked with red bars. However, there are four transitions in H//X and H//Y, two originating from m_S = ±1/2 Kramers doublet and two from m_S = ±3/2 Kramers doublet.

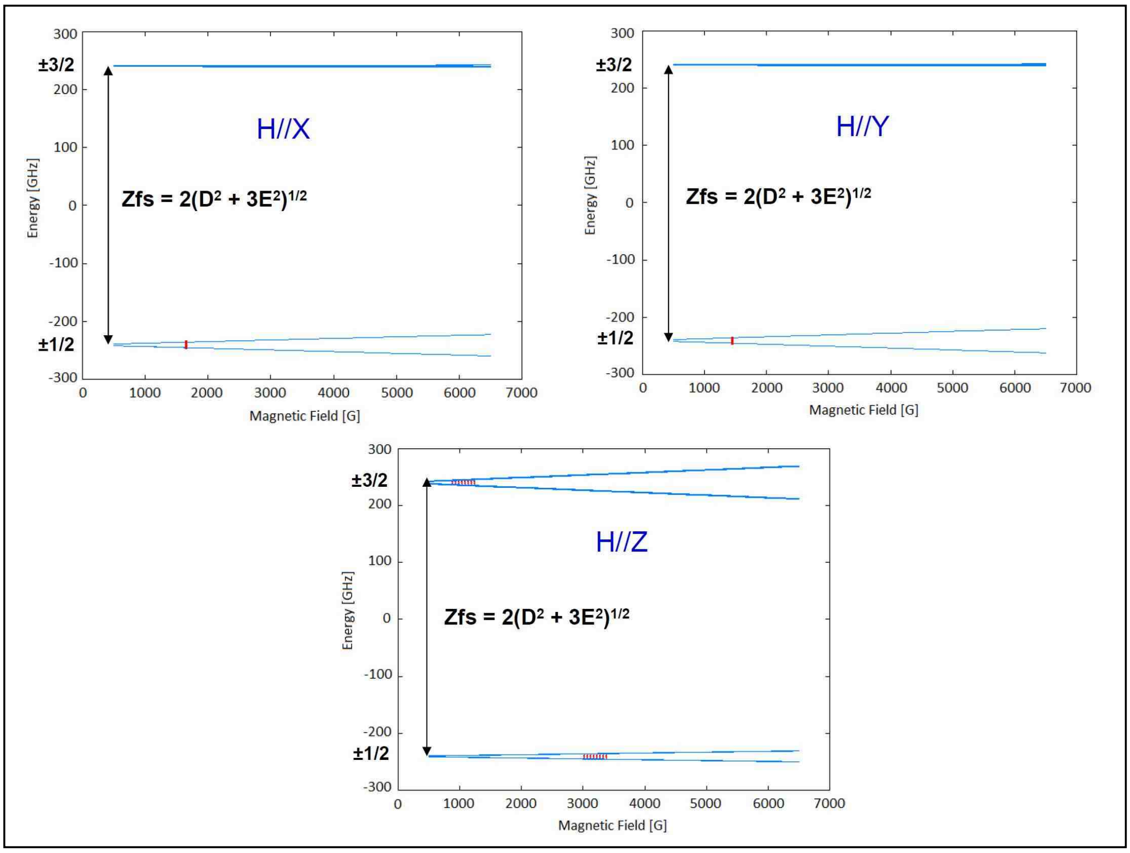

Figure 3.17: Energy levels as a function of magnetic field for the three canonical orientations of the field relative to the principal zfs axis calculated for C84D using the same set of EPR spin Hamiltonian parameters. Observed EPR transitions are marked with red bars. However, there are two transitions for H//X and H//Y both originating from m_S = ±1/2 Kramers doublet and two transitions for H//Z, one originating from m_S = ±1/2 and the other from m_S = ±3/2 Kramers doublets.

There are two transitions for H//Z. One originates from the m_S = ±3/2 Kramers doublet, and is more intense and sharper, and the other is from m_S = ±1/2 Kramers doublet. Transitions in the H//X and H//Y directions are very sensitive to E/D compared to transitions in the H//Z direction. Furthermore transitions within the $m_s = \pm 1/2$ Kramers doublet are more sensitive to temperature than transitions in the $m_s = \pm 3/2$ Kramers doublet. At 4K the $m_s = \pm 3/2$ Kramers doublet transitions are the most intense and the intensity is reduced as the temperature is changed to 8 and to 20K due to populating the excited state, $m_s = \pm 1/2$ Kramers doublet.

3.5.5 Theoretical Calculations of Electronic Structure of LuxS Active Site.

3.5.5.1 Density Functional Theory on LuxS-C84A and LuxS-C84D

The complex splitting pattern of the $^4T_1$ (P) state for the wt and mutants has been attributed as being due to a combination of low symmetry distortions, spin-orbit coupling, and the presence of charge transfer (CT) transitions (Figure 3.18). An angular overlap model was used to assign the ligand field transitions (section 3.5.5.2) and charge transfer transition were probed using spin unrestricted DFT calculations and Time-Dependent DFT (TD-DFT) for wt-luxS, C84A and C84D.

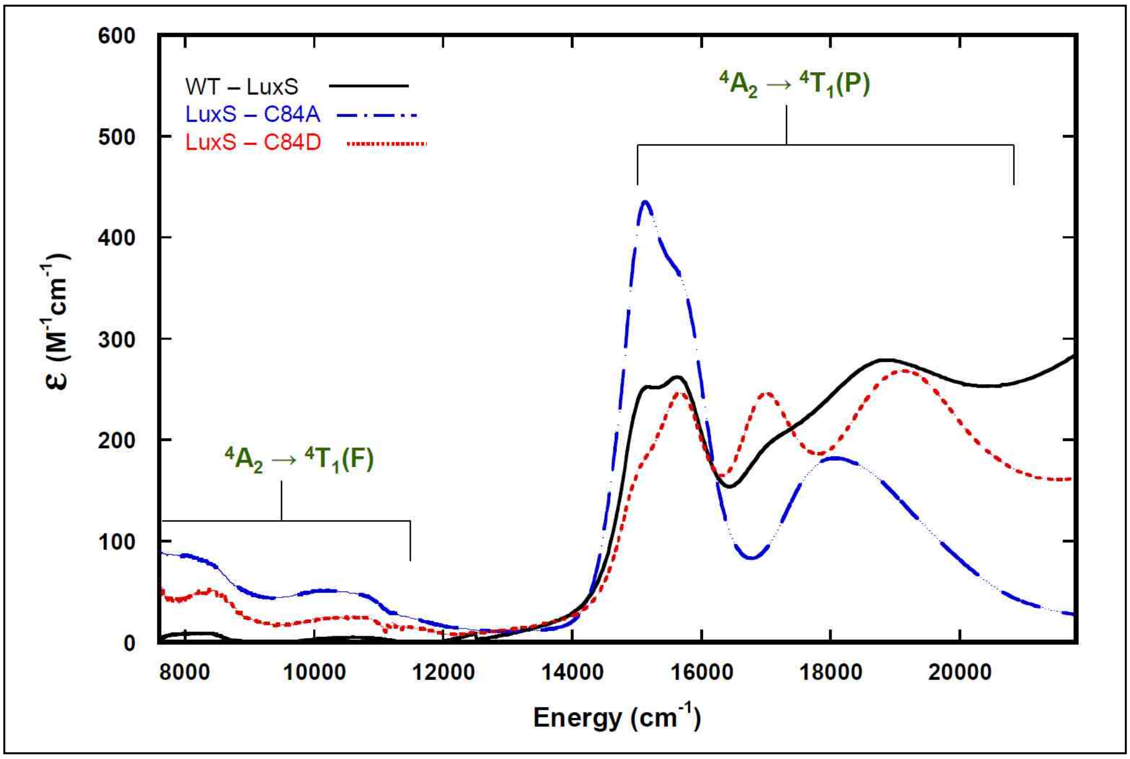

Figure 3.18: Electronic absorption spectra overlays for wt, C84A and C84D showing the splitting of the $^4T_1$(F) and $^4T_1$ (P) states.

Previous pH dependent studies suggested that C84A possesses a hydroxide ligand whereas C84D possesses a water bound to Co(II) [135]. The geometries of the computational complexes modeling the active sites of these two mutants are displayed in Figure 3.19. Selected bond lengths and bond angles (angles and bond lengths directly coordinated to Co(II)) were frozen to acquire *B. subtillis* crystal structure geometry and partial optimization was performed on the hydrogens and imidazole rings. Methyl substituted imidazole rings were chosen as models for the two histidines and methyl thiolate was chosen to model the cysteine ligand. A hydroxide at the luxS-C84A and water at luxS-C84D active sites round out the first coordination environment.

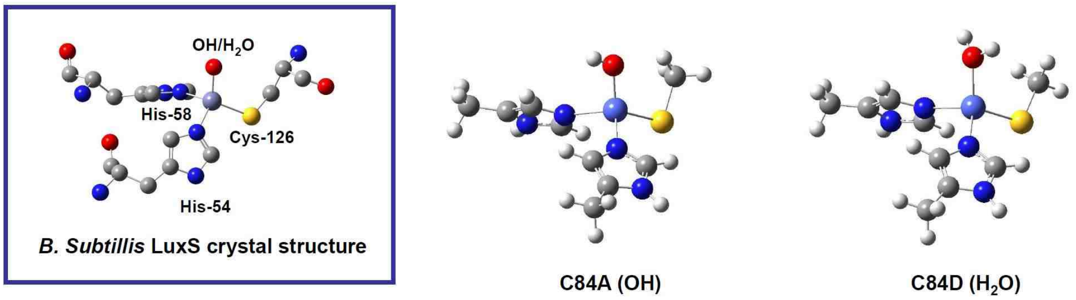

	C84A (OH)	C84D (H_2O)
Co – OH/H_2O	1.852	2.062
Co – S_{126}	2.270	2.270
Co – N_{54}	2.060	2.060
Co – N_{58}	2.130	2.130
OH/H_2O – Co – S_{126}	116.30	116.30
OH/H_2O – Co – N_{54}	112.70	112.70
OH/H_2O – Co – N_{58}	101.60	101.60
N_{54} – Co – S_{126}	105.00	105.00
N_{58} – Co – S_{126}	116.30	116.30
N_{54} – Co – N_{58}	104.60	104.60

Figure 3.19: Selected bond distances (Å) and bond angles (degrees) for computational models of C84A and C84D which have been partially optimized by freezing the first coordination sphere with *B. subtillis* wt-luxS crystal structure values [109,110]. The Co-OH/H_2O bond lengths were allowed to optimize. However, the crystal structure value for the Co-O bond length is 1.93 Å. The crystal structure values have been downloaded from the protein data bank (PDB 1IE0).

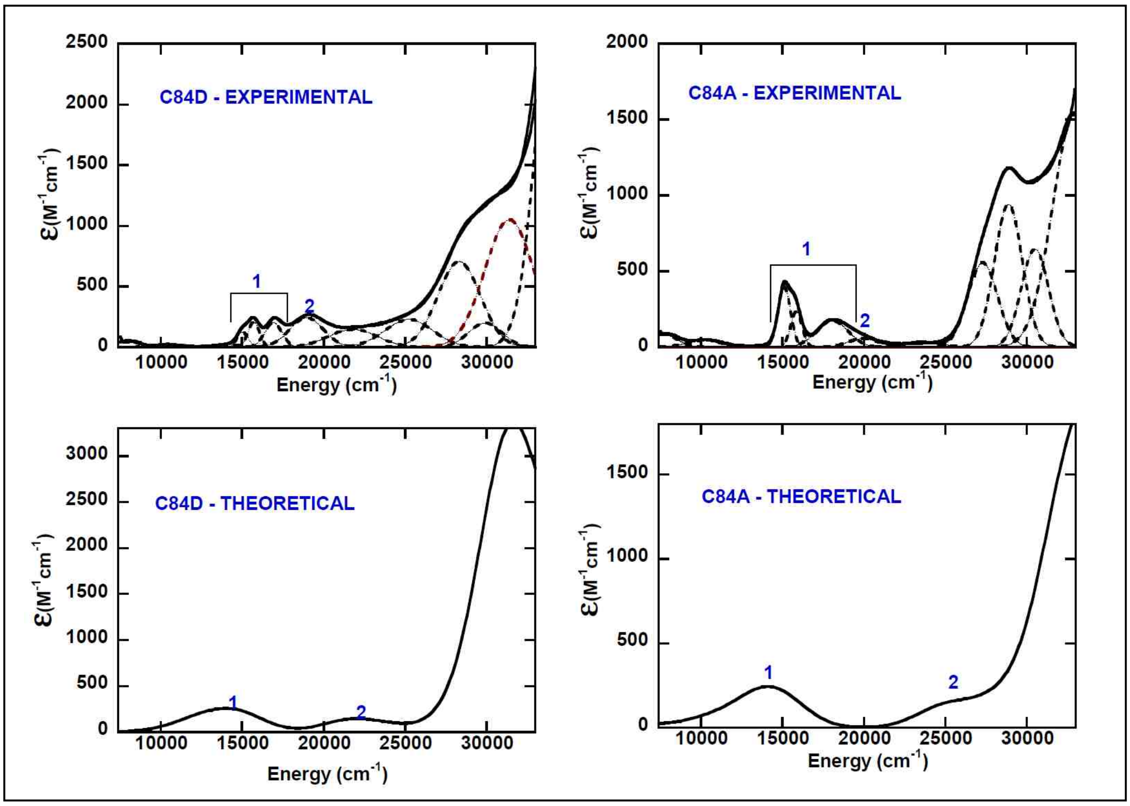

Figure 3.20: Experimental electronic absorption (top) and theoretical absorption spectra (bottom) obtained from TD-DFT computed transitional energies and oscillator strengths for C84D and C84A mutants.

Figure 3.20 shows a comparison between the theoretical/calculated electronic absorption spectra and the experimental spectra for the C84A and C84D mutants. Computational analysis of bands 1 and 2 (Figures 3.21-3.24) in the visible region ($^4T_1$ (P) state) using electron density difference maps (EDDMS), revealed that for C84D, band 1 is a ligand field (d-d) transition whereas band 2 is a S → Co charge transfer transition (Figure 3.23). Dark red and green represent the loss and gain of electron density respectively.

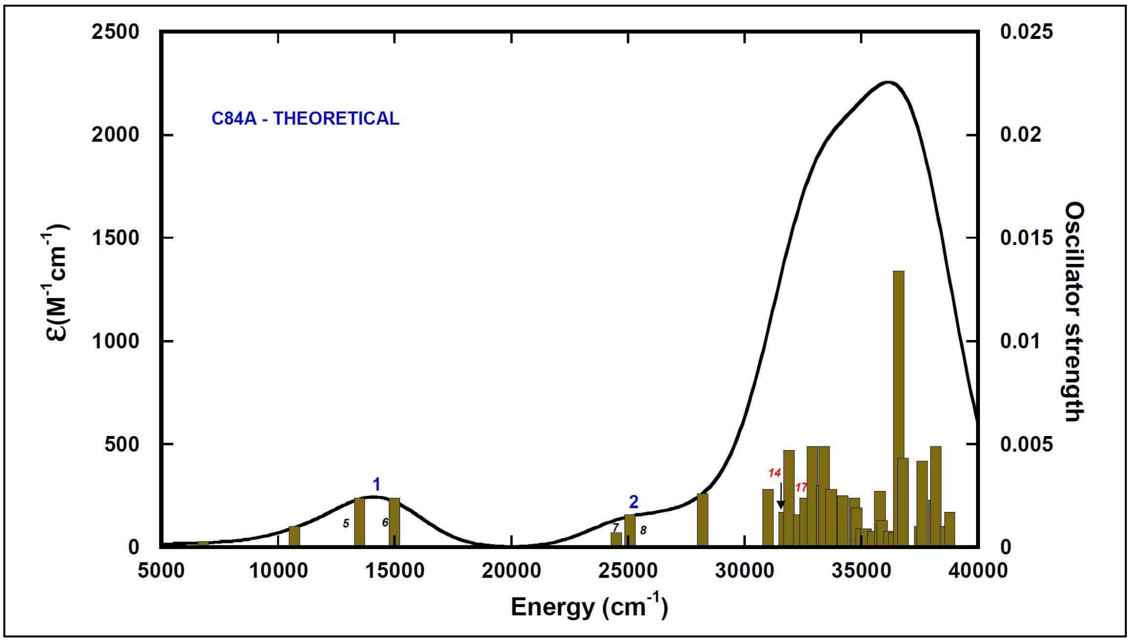

Figure 3.21: C84A TD-DFT calculated absorption spectrum from 40 excited states depicted by bars. Excited states 5 and 6 constitute band 1 whereas excited states 7 and 8 constitute band 2. Excited states 14 and 17 are the two components of the pseudo A term in the MCD for S → Co charge transfer transitions mixed with LLCT.

In C84A, bands 1 and 2 are mixtures of ligand field (d-d), S → imidazole rings (LLCT), and S → Co charge transfer transitions (Figure 3.24). However, band 2 in C84A, has an increased amount of LLCT character which makes it reasonably to assigned this band as a LLCT transition. In general, C84A wavefunctions contain many mixed transitions an make the analysis difficult, whereas the C84D wavefunctions are simpler and more straightforward to analyze. It is known that TD-DFT cannot account fully for the nature and splitting pattern of ligand field transitions observed in tetrahedral transition metal complexes due to large spin orbit coupling and the presence of coupled two electron transitions [206]. TD-DFT only accounts for single electron transitions and is therefore perhaps better suited for describing charge transfer transitions that result from one electron promotions between donor and acceptor orbitals.

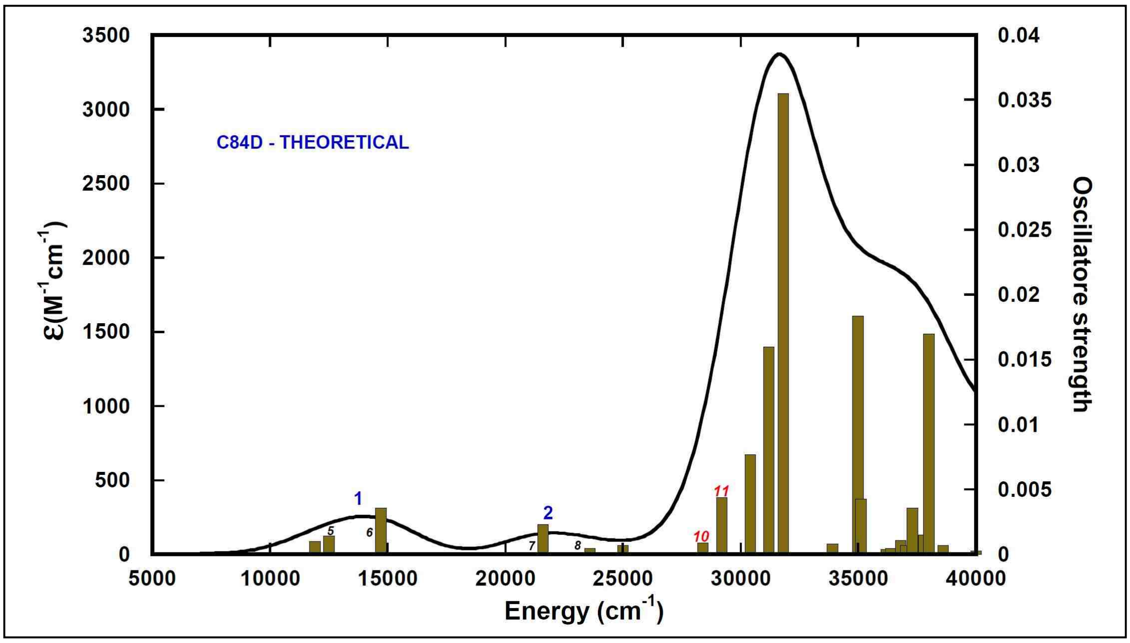

Figure 3.22: C84D TD-DFT calculated absorption spectrum from 40 excited states depicted by bars. Excited states 5 and 6 constitute to band 1 whereas excited states 7 and 8 constitute to band 2. Excited states 10 and 11 are the two components of the pseudo A term in the MCD for S → Co charge transfer transitions.

The TD-DFT calculations overestimate the S → Co CT band 2 in C84D by about 3000 cm^{-1} whereas in C84A band 2 (LLCT) is overestimated by about 6000 cm^{-1}. An energy adjustment is therefore needed to obtain reasonable agreement between experimental and calculated absorption spectra for both C84A and C84D. Figures 3.21 and 3.22 depict the 40 TD-DFT calculated excited states for C84A and C84D.

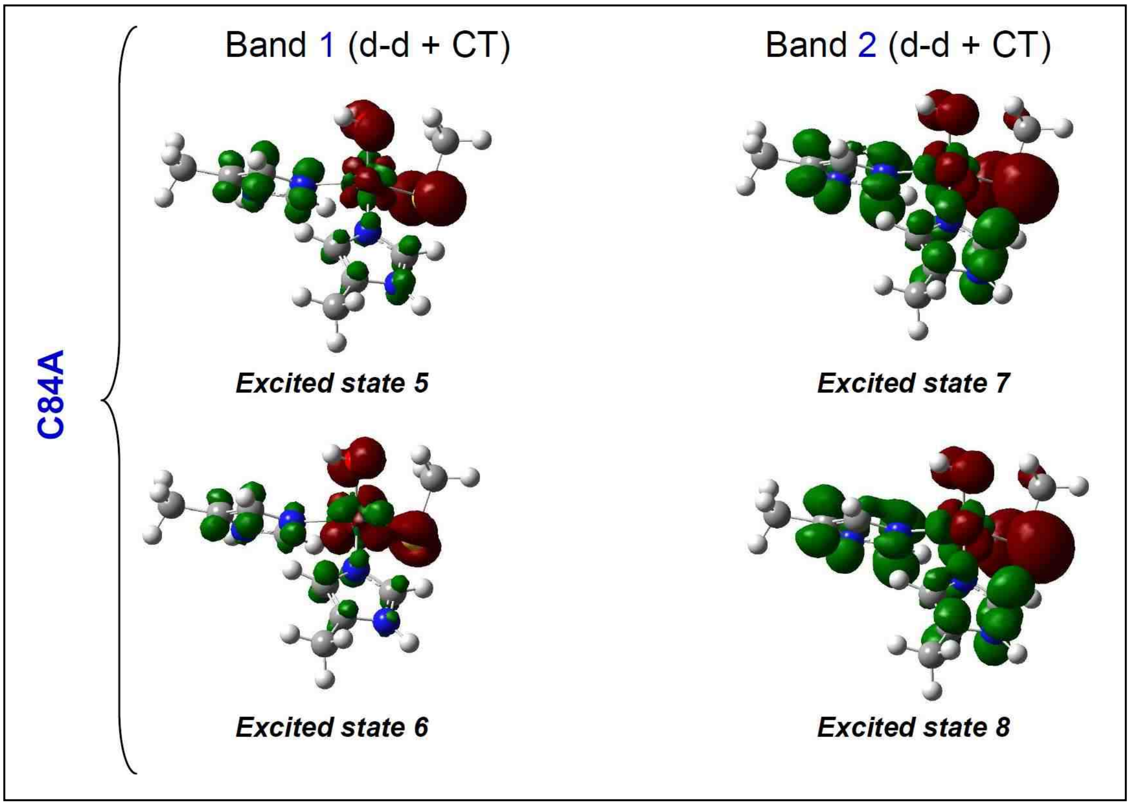
C84A
Band 1 (d-d + CT)
Band 2 (d-d + CT)
Excited state 5
Excited state 7
Excited state 6
Excited state 8

Figure 3.23: Electron density difference maps (EDDMs) for C84A where dark red represents loss of electron density and green represents gain of electron density.

The higher energy transition that is observed as pseudo A term band in the MCD spectra has also been calculated and assigned as a second S → Co charge transfer transition. Proper assignment of this isolated transition is important in delineating the presence of either the hydroxide or water at the active sites of C84A and C84D. It is expected that the presence of the hydroxide ligand (σ and π donor) would destabilize both the t and e orbitals of the Td Co ion to a greater extent than water, consistent with the spectrochemical series. Consequently, the S → Co charge transfer transition is expected to occur at higher energy for the Co-OH species than for Co-OH_2 (σ donor only), as water destabilizes only the σ orbitals of the metal ion. However, for C84A, the S → Co CT is observed at 29140 cm-1 whereas the two calculated energy components (excited states 14 and 17) of the pseudo A term are 31677 and 32637 cm^{-1}.

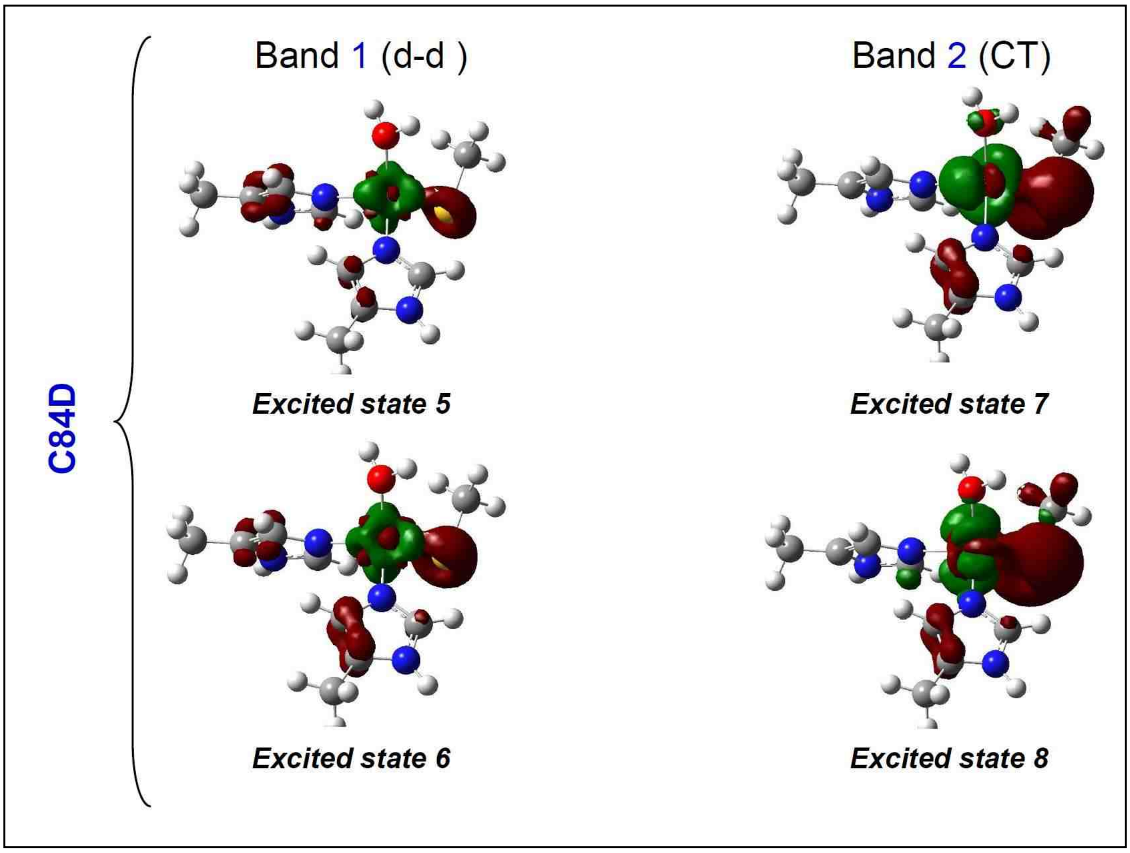
C84D
Band 1 (d-d)
Band 2 (CT)
Excited state 5
Excited state 7
Excited state 6
Excited state 8

Figure 3.24: Electron density difference maps (EDDMs) for C84D where dark red represents loss of electron density and green represents gain of electron density.

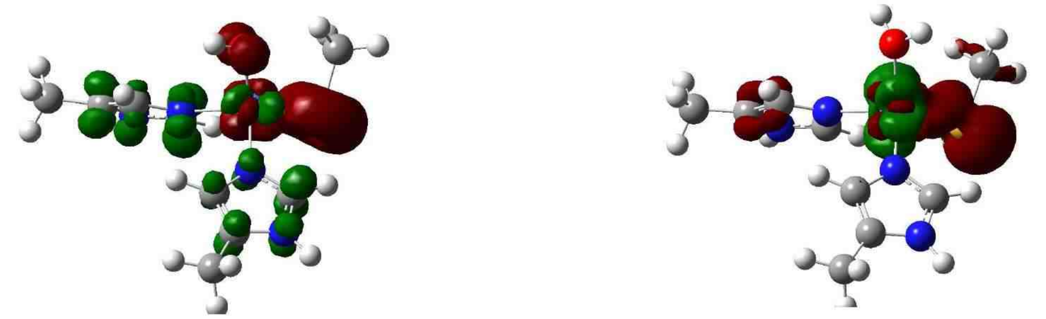

Excited state 14

Excited state 10

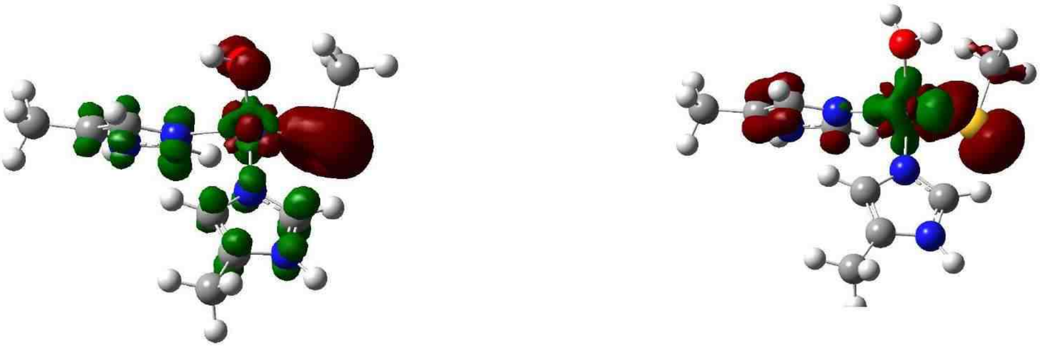

Excited state 17

Excited state 11

Figure 3.25: Electron density difference maps (EDDMs) for S → Co charge transfer transitions of C84A and C84D. Dark red represents loss of electron density and green represents gain of electron density.

In the C84D mutant, the S → Co CT band is observed at 28816 cm^{-1} whereas the two calculated energy components (excited states 10 and 11) of the pseudo A term are found at 28432 and 29213 cm^{-1}. These findings are in reasonable agreement with the presence of a hydroxide in C84A and coordinated water in C84D. Figures 3.25 and 3.26 depict the EDDMS and nature of the transitions involved respectively for C84A and C84D.

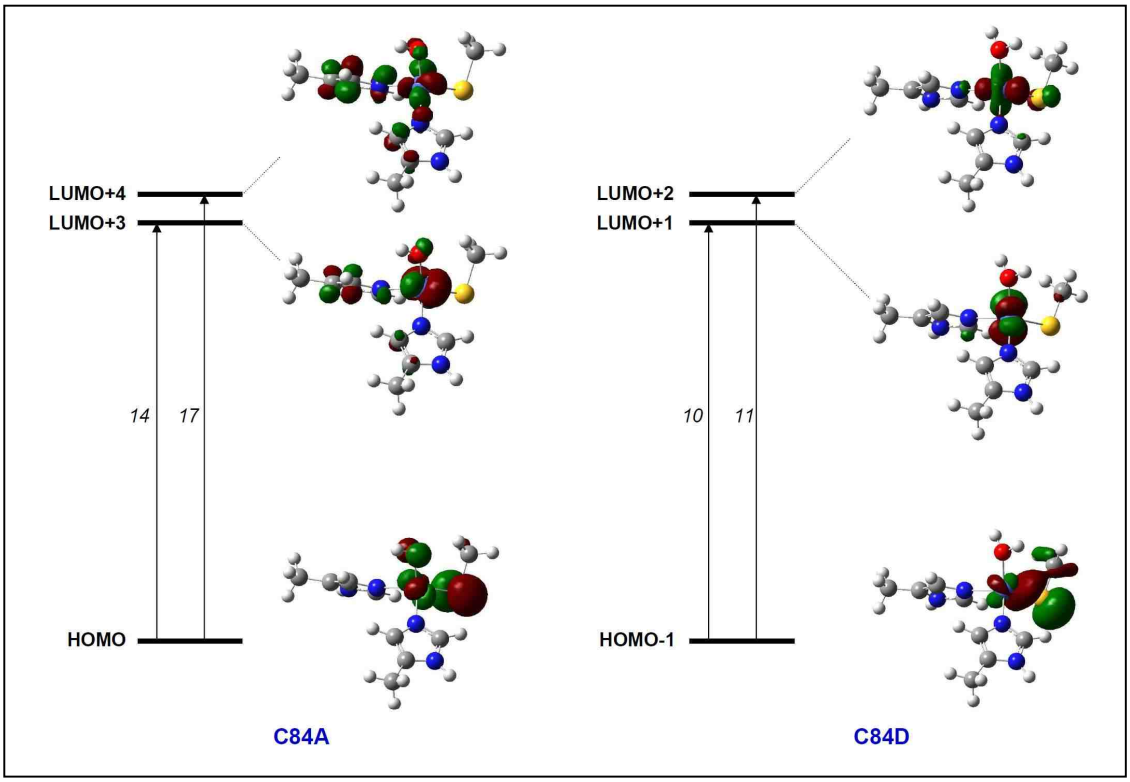

Figure 3.26: S → Co charge transfer transitions for C84A and C84D. The two transitions, excited states 14 and 17 for C84A occur at 31677 and 32637 cm^{-1} whereas for C84D these transitions (excited states 10 and 11) occur at 28432 and 29213 cm^{-1}.

3.5.5.2 Angular Overlap Model (AOM) Applied to Wt-luxS, LuxS-C84A and LuxS-C84D

The AOM method calculates the d-orbital splitting in terms of weak covalent σ- and π- bonding interactions denoted by the bonding parameters $e\sigma$ and $e\pi$, where $e\sigma$ and $e\pi$ denote the metal–ligand interactions in a σ- and π- fashion respectively (Figure 3.27). The basic assumption is that the strength of a bond formed between two atomic orbitals is related to the magnitude of overlap between the two orbitals.

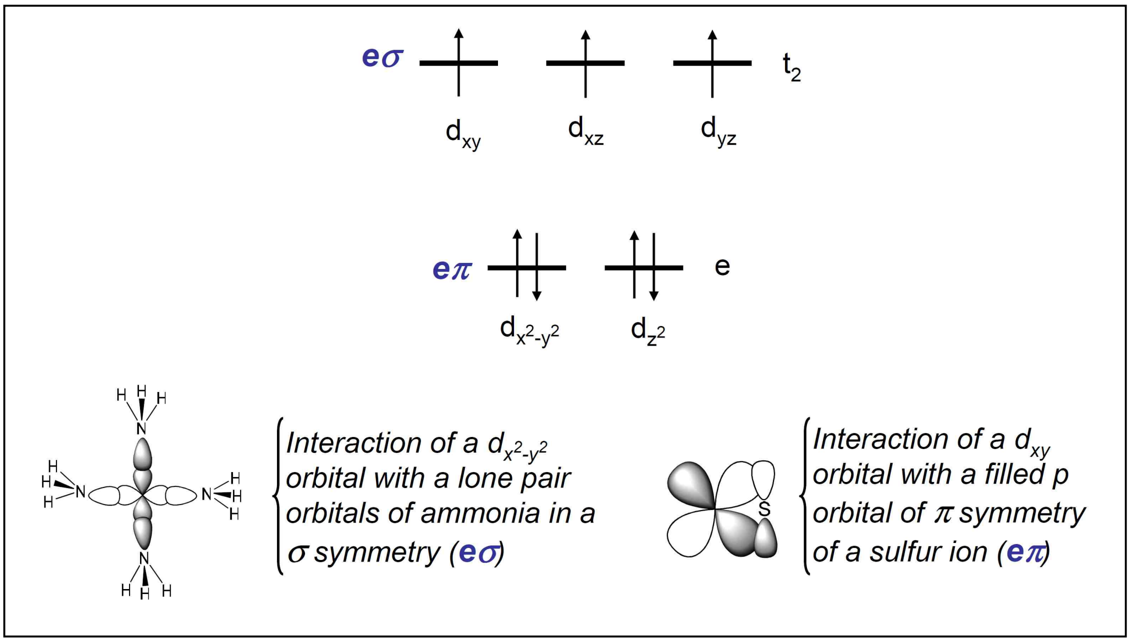
eσ
t2
dxy
dxz
dyz
eπ
e
dx2-y2
dz2
Interaction of a dx2-y2 orbital with a lone pair orbitals of ammonia in a σ symmetry (eσ)
Interaction of a dxy orbital with a filled p orbital of π symmetry of a sulfur ion (eπ)
H
N
S

Figure 3.27: Explanation of metal-ligand interactions in a tetrahedral Co(II) – d^7 by AOM.

The input data are the Cartesian coordinates for metal center (Co), two histidine nitrogens (N), one cysteine sulfur (S) and the oxygen (O) from either water or hydroxide of the active site crystal structure downloaded from PDB 1IE0. These coordinates remained fixed throughout the calculations and the best fits to d-d transition energies for wt-luxS, C84A and C84D were obtained by varying the Racah parameter (B), spin orbit coupling constant (ξ), eσ and eπ. The values for eσ and eπ for N, S and O were within the range of values tabulated elsewhere [139,140]. When the spin orbit coupling constant is set to zero, there are three spin allowed transitions $^4A_2$ (F) → $^4T_2$ (F), $^4A_2$ (F) → $^4T_1$ (F) and $^4A_2$ (F) → $^4T_1$ (P). The AOM method also calculates the spin forbidden transitions arising from the ^2G free ion term that overlap in energy with the $^4A_2$ (F) → $^4T_1$ (P) transition. All of these transitions are labeled for easy identification when the spin orbit coupling constant (ξ) is set to zero. However, when ξ is non-zero, all of the spin allowed transitions split into six transitions and are no longer labeled together with the spin forbidden transitions which creates a possibility of mis-assigning a spin-allowed band arising from $^4A_2$ (F) → $^4T_1$ (P) to a transition arising from ^2G that is spin-forbidden. This problem was avoided by pre-fitting the d-d transitions first with ξ set to zero and then extract the corresponding six transition energies when ξ is non-zero. However, there are no possible spin-forbidden transitions that could be mistaken for the $^4A_2$ (F) → $^4T_2$ (F) and $^4A_2$ (F) → $^4T_1$ (F) d-d transitions which occur in the infrared and near-infrared regions respectively. The value of the spin-orbit coupling constant had very little effect ($\Delta \approx 100$ cm^{-1}) on the energies of the calculated transitions due to the broadness of the experimental bands. Table 3.3 summarizes the calculated AOMX transition energies for wt-luxS, C84A and C84D and AOMX using the parameters that generate the best fit to the experimental data.

Table 3.3: Observed vs. AOMX-calculated d-d transitions for wt, C84A and C84D

Wt-LuxS		
Energy State	**Observed**	**AOMX – Calculated**
$^4A_2 \rightarrow {}^4T_2$(F)	Not observed	4652 cm^{-1}
$^4A_2 \rightarrow {}^4T_1$(F)	7404 cm^{-1}	7410 cm^{-1}
$^4A_2 \rightarrow {}^4T_1$(F)	8404 cm^{-1}	8444 cm^{-1}

${}^4A_2 \rightarrow {}^4T_1$(F)	10,451 cm^{-1}	10443 cm^{-1}
${}^4A_2 \rightarrow {}^4T_1$(P)	15,386 cm^{-1}	15366 cm^{-1}
${}^4A_2 \rightarrow {}^4T_1$(P)	16,105 cm^{-1}	16141 cm^{-1}
${}^4A_2 \rightarrow {}^4T_1$(P)	17,500 cm^{-1}	17511 cm^{-1}
C84A		
${}^4A_2 \rightarrow {}^4T_2$(F)	Not observed	4511 cm^{-1}
${}^4A_2 \rightarrow {}^4T_1$(F)	7351 cm^{-1}	7255 cm^{-1}
${}^4A_2 \rightarrow {}^4T_1$(F)	8241 cm^{-1}	8331 cm^{-1}
${}^4A_2 \rightarrow {}^4T_1$(F)	10451 cm^{-1}	10453 cm^{-1}
${}^4A_2 \rightarrow {}^4T_1$(P)	15391 cm^{-1}	15403 cm^{-1}
${}^4A_2 \rightarrow {}^4T_1$(P)	16147 cm^{-1}	16135 cm^{-1}
${}^4A_2 \rightarrow {}^4T_1$(P)	17600 cm^{-1}	17604 cm^{-1}
C84D		
${}^4A_2 \rightarrow {}^4T_2$(F)	Not observed	4778 cm^{-1}
${}^4A_2 \rightarrow {}^4T_1$(F)	7366 cm^{-1}	7525 cm^{-1}
${}^4A_2 \rightarrow {}^4T_1$(F)	8487 cm^{-1}	8520 cm^{-1}
${}^4A_2 \rightarrow {}^4T_1$(F)	10436 cm^{-1}	10440 cm^{-1}
${}^4A_2 \rightarrow {}^4T_1$(P)	15228 cm^{-1}	15288 cm^{-1}
${}^4A_2 \rightarrow {}^4T_1$(P)	16122 cm^{-1}	16035 cm^{-1}
${}^4A_2 \rightarrow {}^4T_1$(P)	17246 cm^{-1}	17238 cm^{-1}

BEST FIT AOMX PARAMETERS			
Parameter	**Wt-LuxS**	**C84D**	**C84A**
N; eσ	5300 cm^{-1}	5300 cm^{-1}	5340 cm^{-1}
S; eσ, eπ	1900, 1350 cm^{-1}	2200, 1400 cm^{-1}	1720, 1430 cm^{-1}
O; eσ, eπ	4800, 0 cm^{-1}	4800, 0 cm^{-1}	4900, 120 cm^{-1}
B	638 cm^{-1}	620 cm^{-1}	649 cm^{-1}
Dq	465 cm^{-1}	478 cm^{-1}	451 cm^{-1}
ξ, |zfs = 2D|	500, 18.7 cm^{-1} (D=9.5)	500, 17 cm^{-1} (D=8.5 vs. *8.0 from VTVH*)	500, 20 cm^{-1} (D=10 vs. *-10 from VTVH*)

Quality fits for C84A could only be generated with using both eσ and eπ parameters for the coordinated oxygen atom, indicating the potential presence of a hydroxide ligand coordinated to the metal center. It is known from metal-ligand interactions that a hydroxide is both a σ and π donor whereas water is a σ donor. The AOMX ligand field parameters obtained strongly suggest that C84A is coordinated by hydroxide whereas C84D is coordinated by water. The calculations for the ligand field strength yields 10Dq/B values of 7.3, 7.0 and 7.7 for the wt, C84A and C84D respectively, indicating that the strength of the oxygen atom coordinated to the metal center of the wt-luxS lies between that of C84A (hydroxide bound) and C84D (water bound). These findings are in line with the observed EPR results for the wt and the two mutants that show wt enzyme is a mixture of coordinated water and hydroxide (Figure 3.13). Additional support is also provided by the calculated eσ values for S in wt and mutants (C84A and C84D) which indicate that the strength of the bond between S and Co for wt lies between that of C84A and C84D.

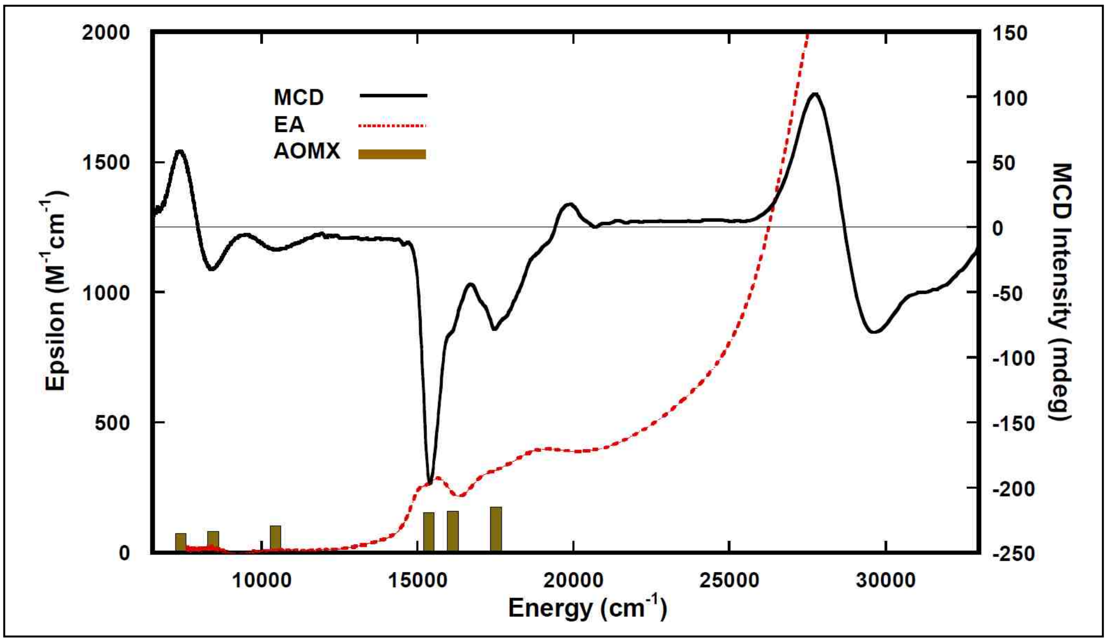

Figure 3.28: MCD, electronic absorption (EA) and AOMX overlays for wt-luxS

Figures 3.28, 3.29 and 3.30 depict the overlays between the d-d transitions observed in the MCD and electronic absorption spectra and the calculated values from AOMX for the wt, C84A and C84D. Taken together, these results indicate a very important role for C84 in catalysis.

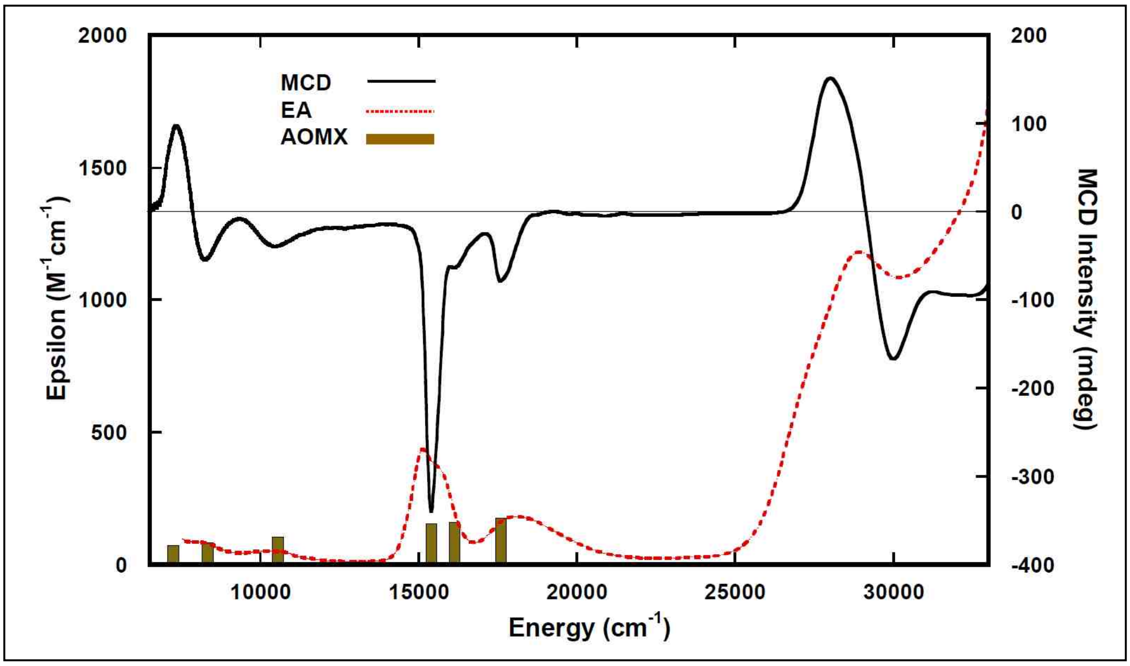

Figure 3.29: MCD, electronic absorption (EA) and AOMX overlays for C84A

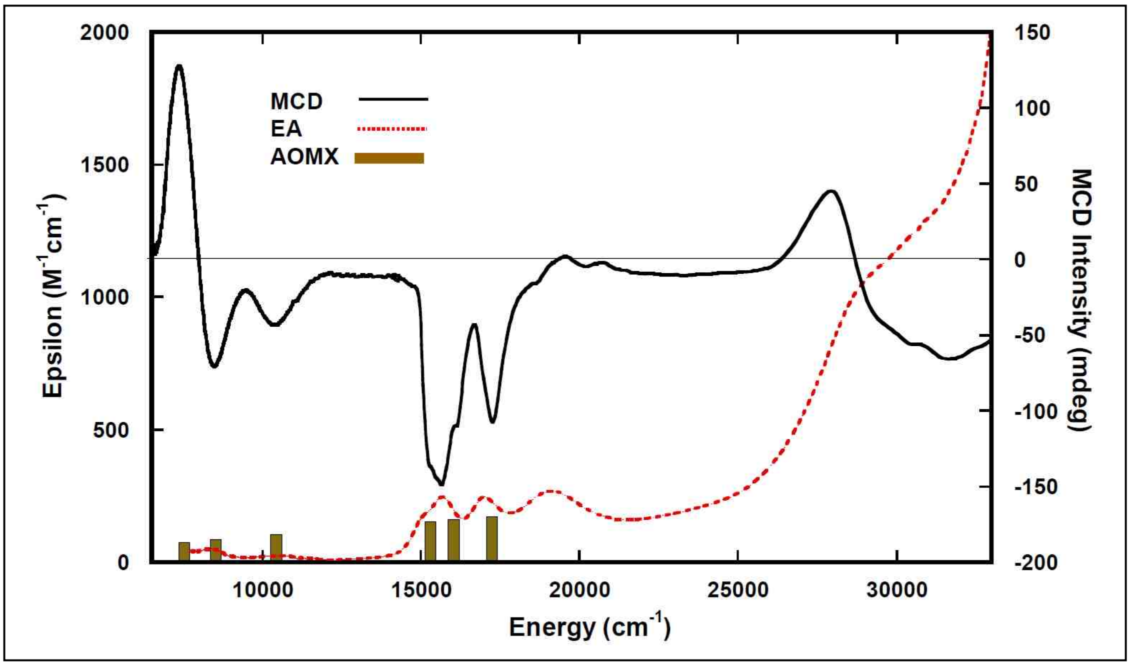

Figure 3.30: MCD, electronic absorption (EA) and AOMX overlays for C84D.

Thus, mutation of C84 affects the electronic and geometric structures of the active site, likely by modifying the pKa of the bound water ligand and the catalytic efficiency which leads to a complete disappearance of luxS activity in C84A as observed by Zhu and co-workers [111]. This is supported by the calculated eσ values for S using AOMX (Table 3.3) which show that mutation of C84 in the secondary coordination sphere affect the nature of bound water ligand in wt leading to increased pKa of water bound for C84A and a decreased pKa for C84D.

3.5.6 Spectroscopic and Computational Study of the LuxS Model Compounds (PATH)CoBr and (PATH)CoNCS.

3.5.6.1 (PATH)CoBr and (PATH)CoNCS and Their Observed Transitions

The effects of the low symmetry ligand field, spin-orbit coupling and the possibility of spin forbidden transitions can make interpretations of Co(II) electronic spectra very difficult. Single crystal spectroscopic measurements which are made directly on crystallographically defined Co(II) sites can provide definitive correlations of the electronic and geometric structures of Co(II) chromophores. These studies are inconveniently labor intensive and are generally technically infeasible for metalloproteins. Consequently, small molecule analogues such as (PATH)CoBr and (PATH)CoNCS have been synthesized [141] to mimic metalloprotein active sites having Co(II)His$_2$CystL coordination like we observe in luxS. These small molecule analogues (Figure 3.46) possess spectra that are remarkably similar to the luxS enzyme spectra. The spectroscopic data have allowed for an increased understanding of the electronic and geometric structures of luxS, particularly in the visible $^4A_2(F) \rightarrow {}^4T_1(P)$ region which is difficult to interpret in the enzyme and mutants. Electronic absorption and MCD spectra for (PATH)CoBr and (PATH)CoNCS (Figures 3.31 and 3.32) revealed electronic transitions in the near infrared and visible regions that derive from $^4A_2$ (F) → $^4T_1$ (F) and $^4A_2$ (F) → $^4T_1$ (P) ligand field transitions ($\epsilon \approx 500$ M^{-1}cm^{-1}). These transitions occurred in the region between 6000 and 18500 cm^{-1} and are relatively weak in the electronic absorption but intense in the MCD. As in the wt-luxS and mutants, the higher energy region is comprised of bands that arise from charge transfer transitions. These are observed as pseudo A terms in the MCD at 25461 and 25500 for (PATH)CoBr and (PATH)CoNCS respectively and were both assigned as S → Co charge transfer transitions. The $^4A_2$ (F) → $^4T_1$ (F) transitions for (PATH)CoBr were observed at 6573, 8442 and 11062 cm^{-1} (Figure 3.31). These three distinctive transitions observed in the electronic absorption spectrum (Figure 3.31) appeared as a positive C term (lowest in energy) followed by two negative C terms in the MCD spectrum (Figure 3.31). The corresponding transitions for the (PATH)CoNCS were observed at 6817 cm^{-1} (positive C term in the MCD), 8772 cm^{-1} (positive C term in the MCD) and at 11521 cm^{-1} (negative C term in the MCD) (Figure 3.31 and 3.32). However, the splitting pattern in the near infra-red region and visible regions of these model compounds suggest a distortion from tetrahedral (T_d) symmetry to C_{2v} where both the $^4T_1$(F) and $^4T_1$(P) states are split into $^4A_1$, $^4B_1$ and $^4B_2$ orbital singlet states. Comparing these results with the observed results for wt-luxS, C84A and C84D suggest the presence of a C_{2v} distortion in wt-luxS and the mutants. Table 3.4 summarizes the nature of the transitions and their corresponding observed transition energies for (PATH)CoBr and (PATH)CoNCS.

Table 3.4: Observed transitions for (PATH)CoBr and (PATH)CoNCS.

Energy State	**(PATH)CoBr Observed**	**(PATH)CoNCS Observed**
$^4A_2 \rightarrow {}^4T_2(F)$	Not observed	Not observed
$^4A_2 \rightarrow {}^4T_1(F)$	6573 cm^{-1}	6817 cm^{-1}
$^4A_2 \rightarrow {}^4T_1(F)$	8442 cm^{-1}	8772 cm^{-1}
$^4A_2 \rightarrow {}^4T_1(F)$	11062 cm^{-1}	11521 cm^{-1}
$^4A_2 \rightarrow {}^4T_1(P)$	14877 cm^{-1}	14873 cm^{-1}
$^4A_2 \rightarrow {}^4T_1(P)$	15965 cm^{-1}	16737 cm^{-1}
$^4A_2 \rightarrow {}^4T_1(P)$	17895 cm^{-1}	18404 cm^{-1}

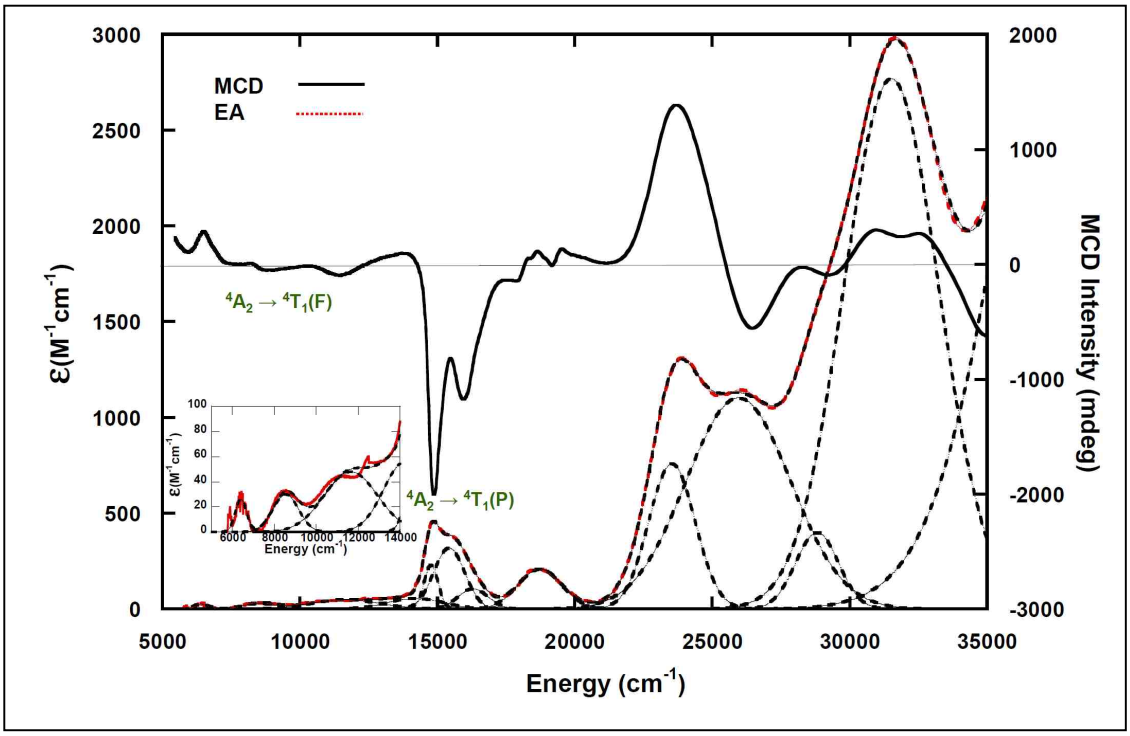

Figure 3.31: MCD and electronic absorption (EA) spectra overlays for (PATH)CoBr. The insert represents the enlarged NIR ligand field absorption bands depicting the splitting pattern for $^4A_2$ (F) → $^4T_1$ (F).

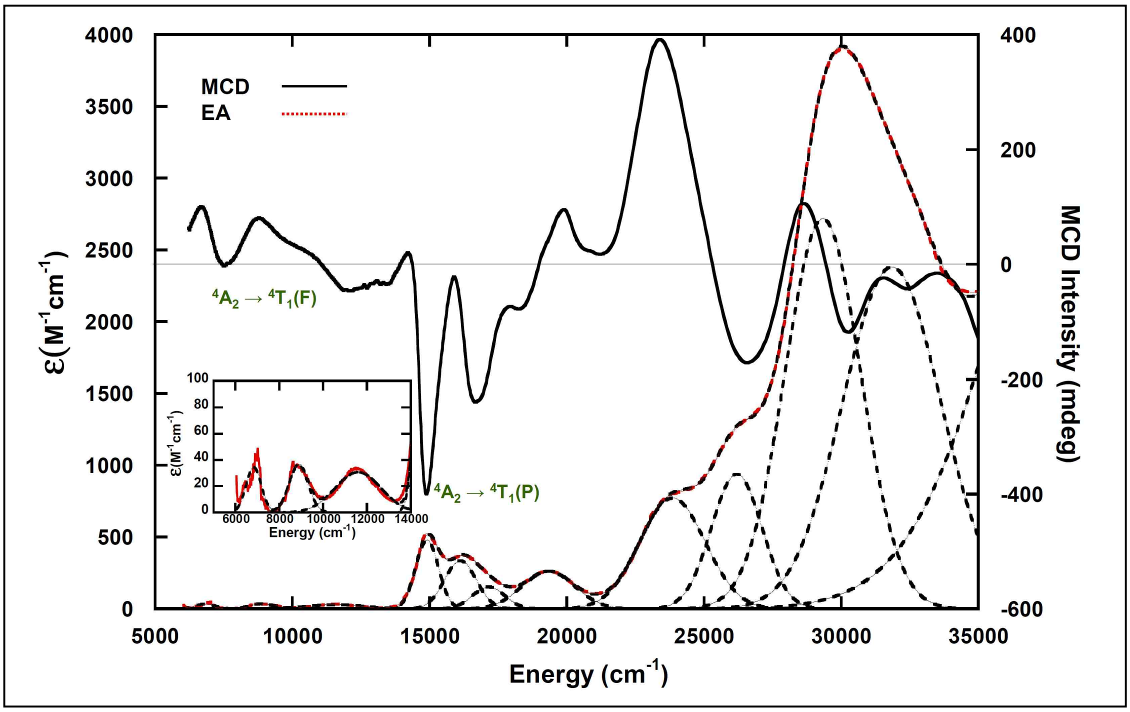

Figure 3.32: MCD and electronic absorption (EA) spectra overlays for (PATH)CoNCS. The insert represents the enlarged NIR ligand field absorption bands depicting the splitting pattern for $^4A_2$ (F) → $^4T_1$ (F). The shoulder at 10600 cm^{-1} in the MCD spectrum (positive C term or possibly a pseudo A term) could be originating from the spin forbidden doublet transition ^2E.

The high-energy region is comprised of bands that arise from charge-transfer (CT) transitions that are similar to the transitions observed in wt-luxS and the C84A and C84D mutants.

3.5.6.2 Determination of Spin Hamiltonian and Zero Field Splitting Parameters by VTVH-MCD

VTVH-MCD magnetization curves for (PATH)CoBr and (PATH)CoNCS were collected on three temperature dependent C term bands as indicated in Figures 3.33 and 3.34. The signal intensity was measured at four different temperatures (≈ 1.8, 3, 5, and 10 K) as a function of magnetic field between 0 and 7 T. The resulting sets of magnetization curves for (PATH)CoBr and (PATH)CoNCS are shown in Figures 3.35 and 3.36 respectively.

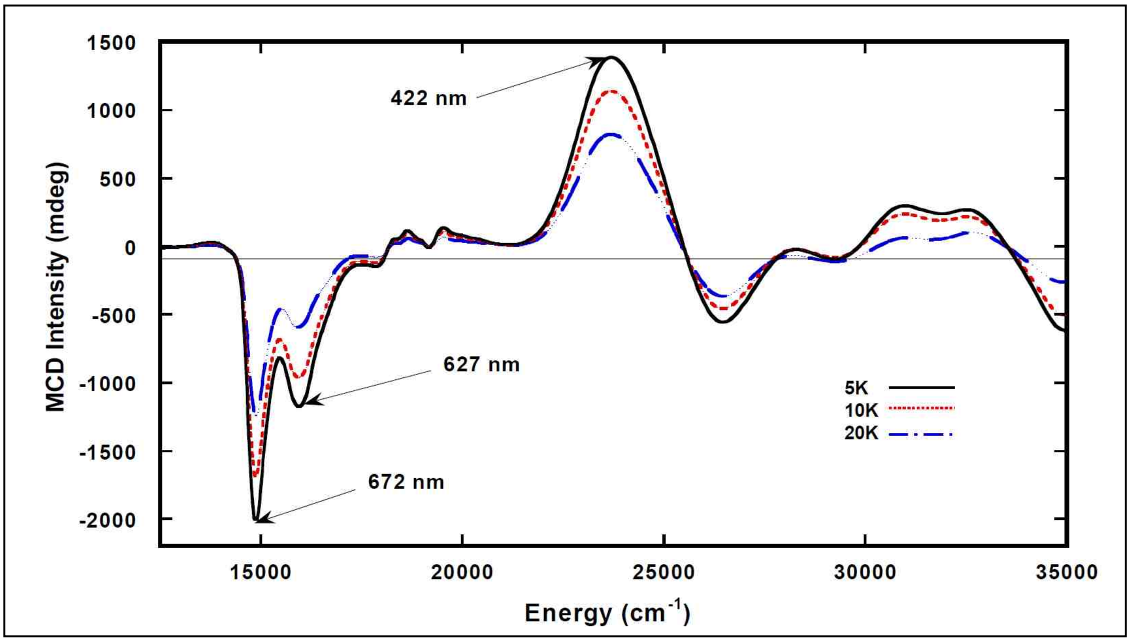

Figure 3.33: VT-MCD for (PATH)CoBr collected at 5, 10 and 20K. Bands 672, 627 and 422 nm were used for collection of VTVH-MCD magnetization data. The MCD intensities for all bands increase with decreasing temperature, a characteristic of C-term behavior.

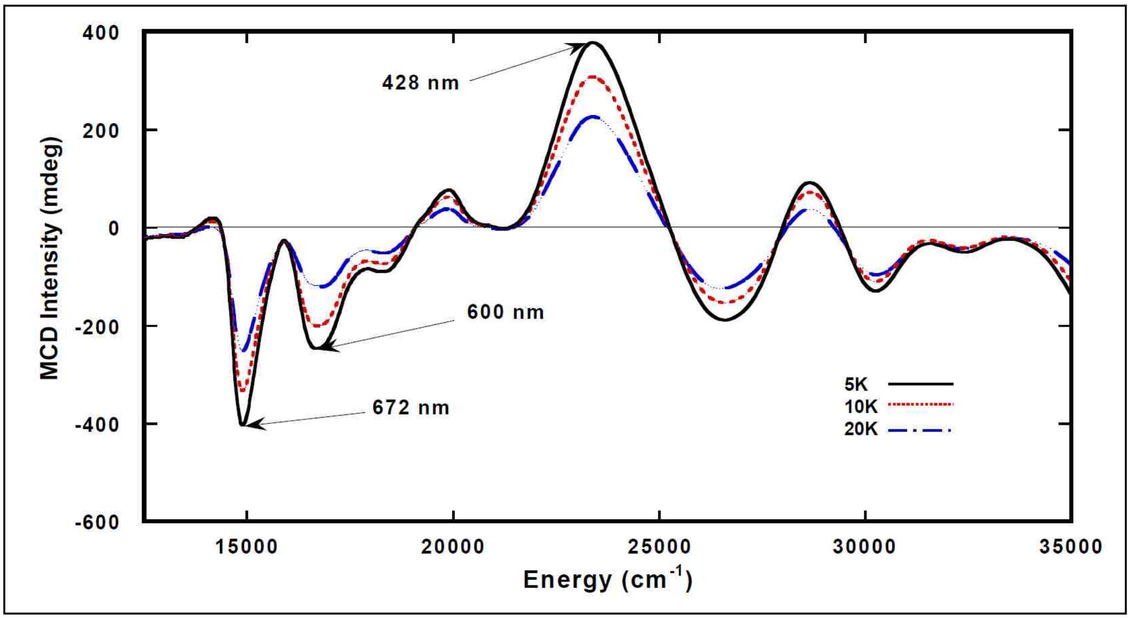

Figure 3.34: VT-MCD for (PATH)CoNCS collected at 5, 10 and 20K. Bands 672, 600 and 428 nm were used for collection of VTVH-MCD magnetization data. The MCD intensities for all bands increase with decreasing temperature, a characteristic of C-term behavior.

The 627 and 600 nm VTVH-MCD data sets for (PATH)CoBr and (PATH)CoNCS showed no nesting whereas the remaining data sets at 672 and 428 nm for (PATH)CoBr and 672 and 422 nm for (PATH)CoNCS showed nesting. The nesting is similar to the observed pattern for the luxS-C84A mutant. However, the VTVH-MCD derived spin Hamiltonian parameters for (PATH)CoBr gave D = -12 cm^{-1}, E/D = 0.05 cm^{-1}, g_x = 2.380, g_y = 2.030 and g_z = 2.025 whereas (PATH)CoNCS gave D = -12 cm^{-1}, E/D = 0.085 cm^{-1}, g_x = 2.300, g_y = 1.900 and g_z = 1.980. These same parameters were used for the simulation of their corresponding EPR spectra.

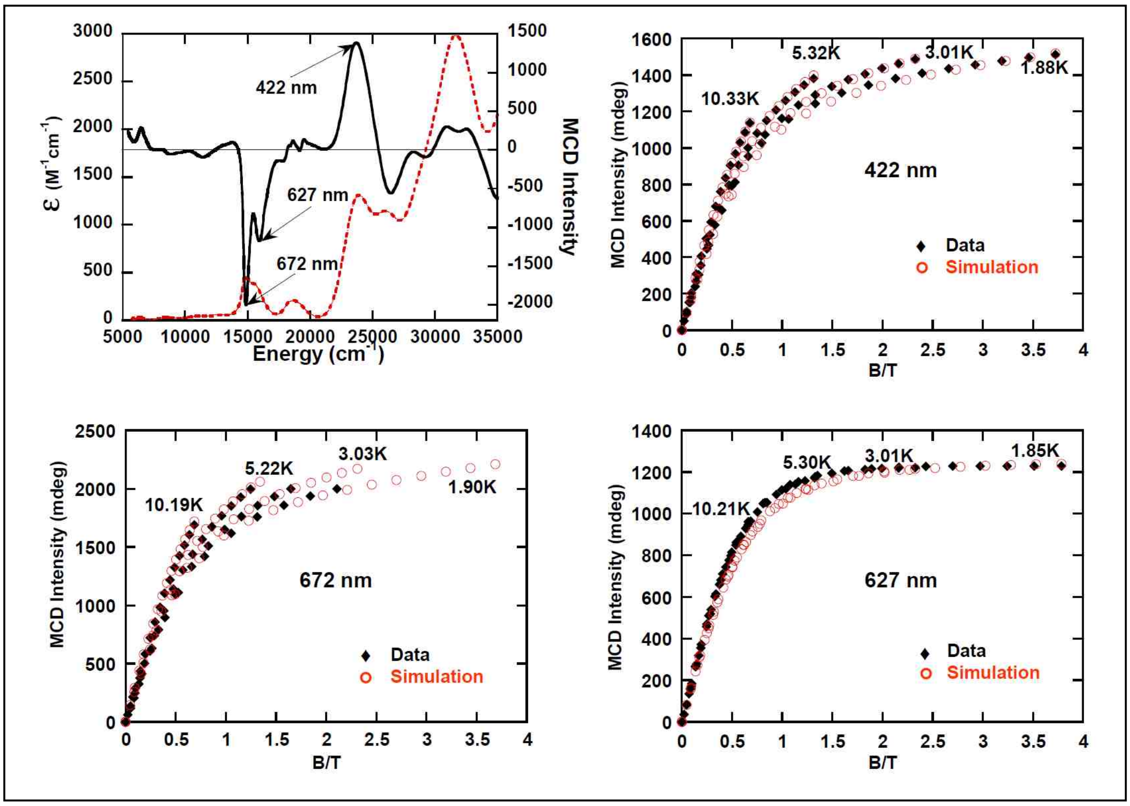

Figure 3.35: MCD magnetization curves for (PATH)CoBr at 422, 627 and 672 nm. Spectral simulation has been achieved with $g_x = 2.380$, $g_y = 2.030$, $g_z = 2.025$, $S = 1.5$, $D = -12$ cm^{-1}, $E/D = 0.05$ cm^{-1}; polarizations are: xy = 1.000, xz = yz = 0.700 at 422 nm, xy = 1.000, xz = yz = 0.100 at 627 nm, and xy = 1.000, xz = yz = 0.700 at 672 nm.

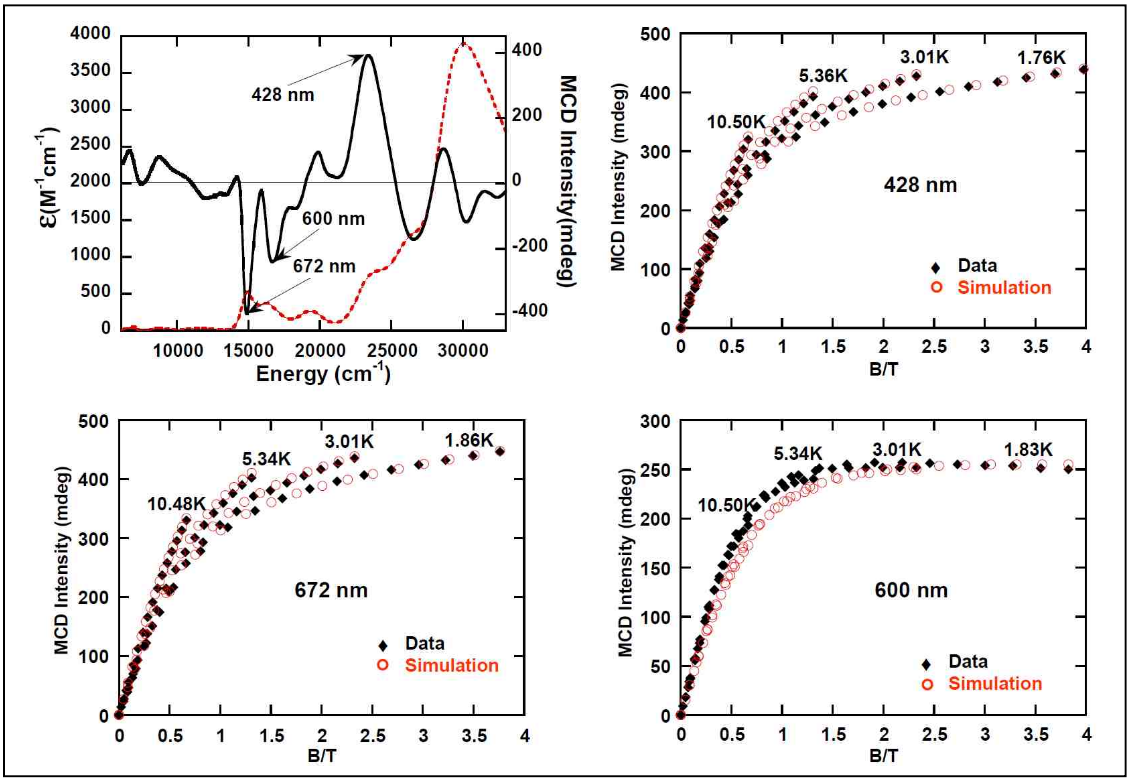

Figure 3.36: MCD magnetization curves for (PATH)CoNCS at 428, 600 and 672 nm. Spectral simulation has been achieved with $g_x = 2.300$, $g_y = 1.900$, $g_z = 1.980$, $S = 1.5$, $D = -12$ cm^{-1}, $E/D = 0.085$ cm^{-1}; polarizations are: xy = 1.000, xz = 0.500, yz = 1.000 at 428 nm, xy = 1.000, xz = yz = 0.000 at 600 nm, and xy = 1.000, xz = 0.700, yz = 1.000 at 672 nm.

3.5.6.3 Determination of Spin Hamiltonian Parameters by EPR Spectroscopy

EPR spectra for (PATH)CoBr and (PATH)CoNCS were collected as frozen solutions in methanol at 15K using a 9.397 GHz X-band frequency. The EPR spectrum of (PATH)CoBr is characterized by three broad resonances with g-values; g_x = 2.380, g_y = 2.030 and g_z = 2.025 and an E/D of 0.05, whereas (PATH)CoNCS gave three broad resonances with g-values at g_x = 2.300, g_y = 1.900 and g_z = 1.980 with an E/D of 0.085. Both sets of g values were obtained from computer simulations. Both the (PATH)CoBr and (PATH)CoNCS EPR spectra were simulated using two ^{59}Co hyperfine parameter that split the g_y and g_z lines. These are estimated values, since they are not resolved in the spectra. In the case of (PATH)CoBr a resolved hyperfine coupling for the I = 7/2 ^{59}Co nucleus was observed on g_z. The simulated principle hyperfine components for (PATH)CoBr at g_y and g_z are 88 x 10^{-4} cm^{-1} and 50 x 10^{-4} cm^{-1} respectively whereas for (PATH)CoNCS, the values are 80 x 10^{-4} cm^{-1} and 50 x 10^{-4} cm^{-1} at g_y and g_z respectively. An accurate value of D for both compounds was determined from the fitting of equations to the VTVH-MCD data and gave D = -12 cm^{-1} for both compounds implying that the m_s = ±3/2 Kramers doublet is the ground state doublet (lower in energy) whereas the m_s = ±1/2 Kramers doublet is the excited state (higher in energy) doublet. The transitions involved in these model compounds are similar to the transitions observed in luxS-C84A.

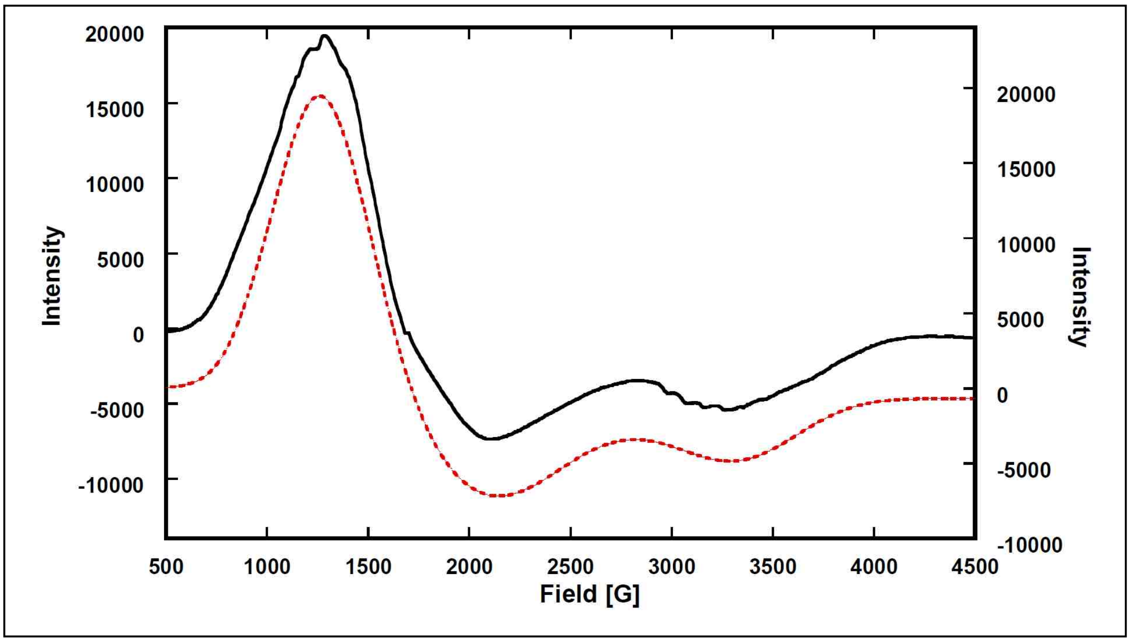

Figure 3.37: (PATH)CoBr EPR spectral data (——) and simulation (.........) collected and simulated at 15K and 20dB. The parameters used for this simulation are exactly the same as those used for VTVH-MCD simulation. Notice, the resolved hyperfine structure on the g_z resonance position to the I = 7/2 ^{59}Co nucleus.

Temperature dependent studies would be very informative as we showed for luxS-C84A, unfortunately these were not collected. Figures 3.37 and 3.38 depicts the overlays of (PATH)CoBr and (PATH)CoNCS EPR data and simulations at 15K and 20dB respectively.

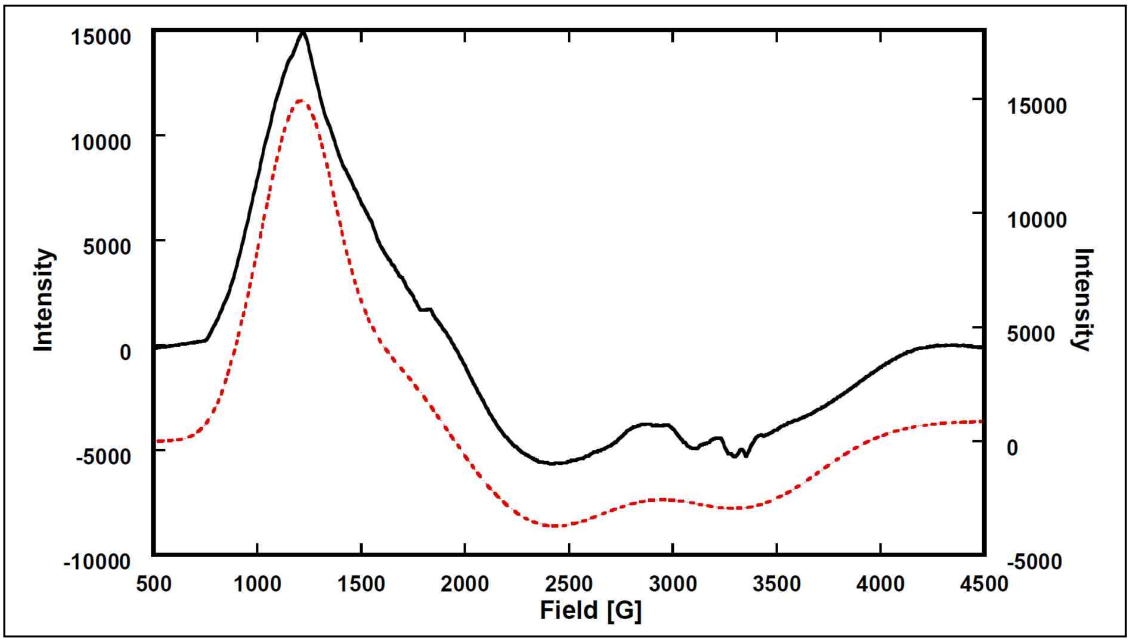

Figure 3.38: (PATH)CoNCS EPR spectral data (_____) and simulation (.........) overlay collected and simulated at 15K and 20dB. The parameters used for this simulation are exactly the same as those used for VTVH-MCD simulation. Features at g_z resonance position could be from hyperfine coupling due to I = 7/2 of ^{59}Co and possibly the impurity from the empty cavity.

3.5.6.4 Density Functional Theory (DFT) Calculations

(PATH)CoBr and (PATH)CoNCS were also analyzed computationally for the presence of charge transfer bands in the $^4T_1(P)$ state (visible) region of the spectrum in order to to make accurate assignments of the ligand field bands and for evaluation of the luxS enzyme results. TD-DFT computed transition energies and oscillator strengths were used to simulate absorption spectra in order to facilitate comparison with the spectroscopic data (Figure 3.39). This provided a tentative assignment of band 2 as a LLCT charge transfer transition for both

(PATH)CoBr and (PATH)CoNCS.. Computational model geometries for these model compounds were adapted from their corresponding crystal structures reported by Chang and co-workers [141]. The crucial bond lengths and bond angles (angles and bond lengths directly coordinated to Co(II)) were frozen at the crystal structure geometries.

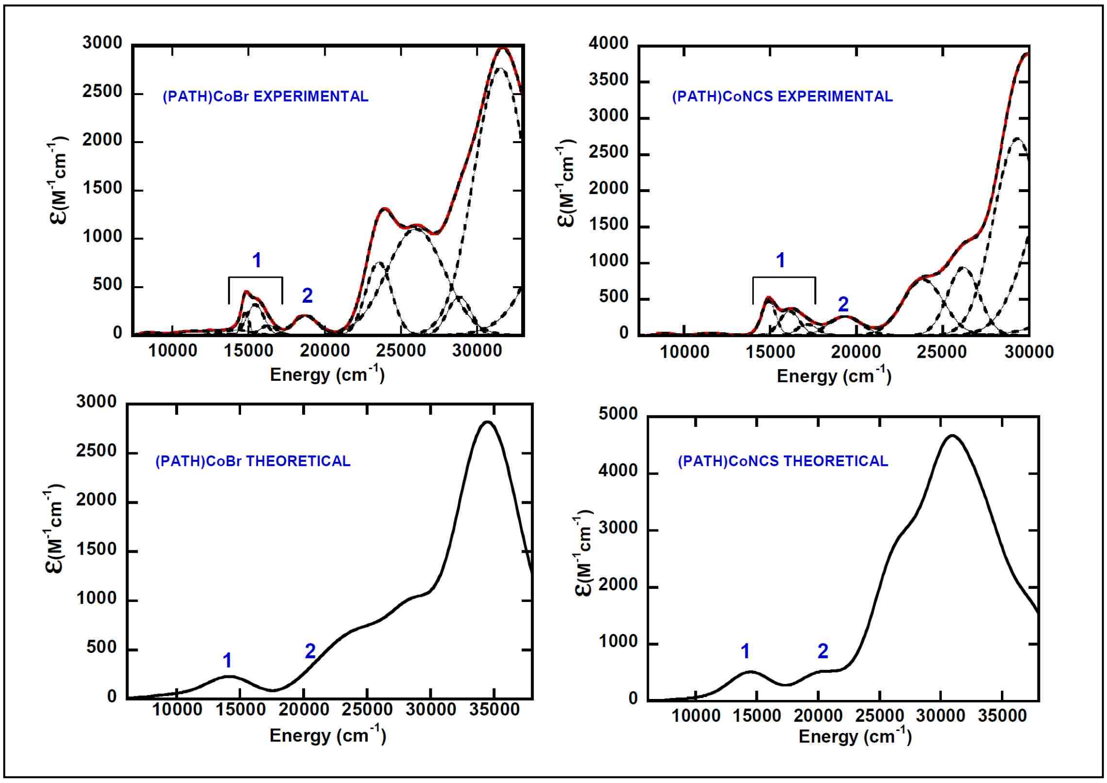

Figure 3.39: Experimental electronic absorption (top) and theoretical absorption spectra (bottom) from computed TD-DFT transitional energies and oscillator strengths for (PATH) CoBr and (PATH)CoNCS.

However, TD-DFT overestimates band 2 by about 2000 cm^{-1} whereas band 1(d-d transition) is underestimated by about 1000 cm^{-1}. This minor adjustment leads to reasonable agreement between experimental and calculated absorption spectra for both (PATH)CoBr and (PATH)CoNCS. Figures 3.40 and 3.42 depicts all 40 TD-DFT calculated excited states for (PATH)CoBr and (PATH)CoNCS. In particular, excited states under bands 1 and 2 are described by electron density difference maps (EDDMs), where dark red and green represent the loss and gain of electron density in the transition, respectively (Figures 3.41 and 3.43).

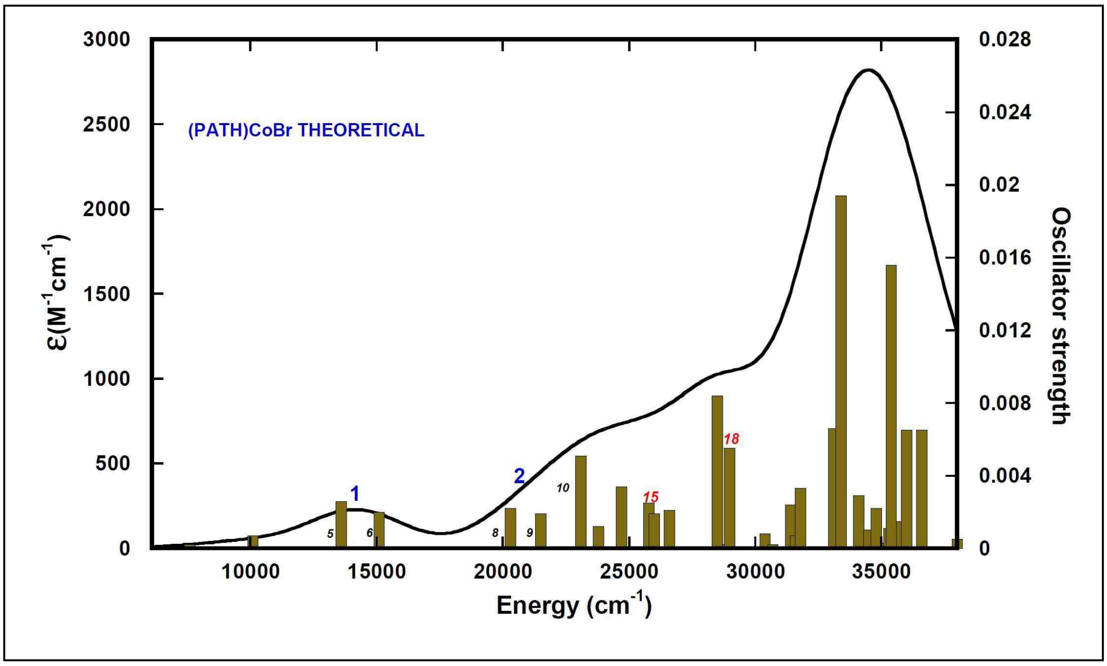

Figure 3.40: TD-DFT calculated absorption spectrum for (PATH)CoBr from 40 excited states depicted by bars. Excited states 5 and 6 constitute band 1 whereas excited states 8, 9 and 10 constitute band 2. Excited states 15 and 18 are the two components of the pseudo A term in the MCD for S → Co charge transfer transitions.

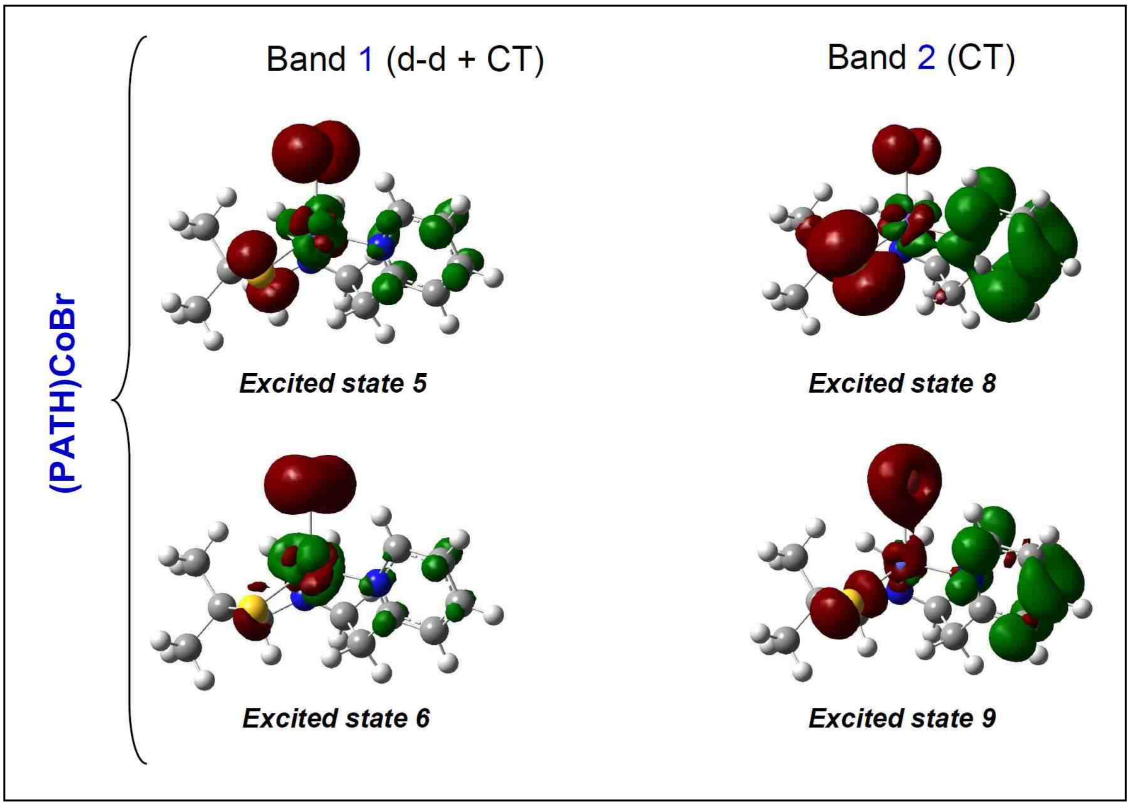
(PATH)CoBr
Band 1 (d-d + CT)
Band 2 (CT)
Excited state 5
Excited state 8
Excited state 6
Excited state 9

Figure 3.41: Electron density difference maps (EDDMs) for (PATH)CoBr where dark red represents a loss of electron density and green represents a gain of electron density in the transition.

The electronic transitions contributing to band 1 in (PATH)CoBr predominantly includes those from d-d and charge transfer transitions assigned as S → Co and Br → Co whereas electronic transitions contributing to band 2 are predominantly intra-ligand charge transfer transitions commonly denoted as LLCT and assigned as S → Py (pyridine ring). Similarly, electronic transitions contributing to band 1 in (PATH)CoNCS includes also those arising from d-d transitions and charge transfer transitions (S → Co and NCS → Co) whereas electronic transitions contributing to band 2 are predominantly intra-ligand charge transfer transitions from S and NCS to the pyridine ring.

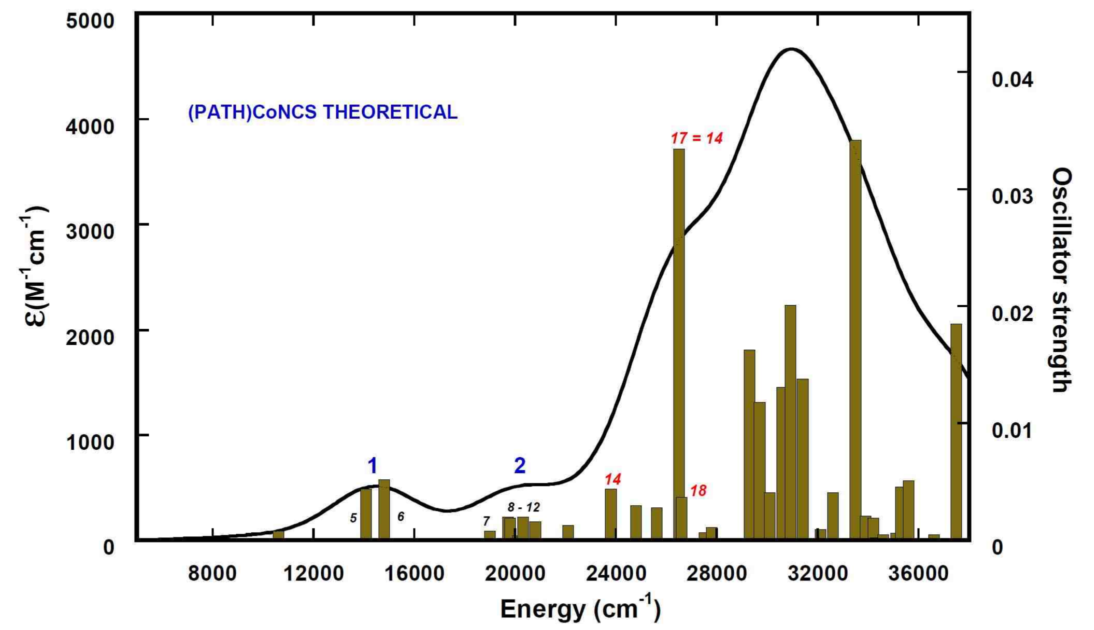

Figure 3.42: TD-DFT calculated absorption spectrum for (PATH)CoNCS from 40 excited states depicted by bars. Excited states 5 and 6 constitute band 1 whereas excited states 7 - 12 constitute band 2. All EDDMs for excited states 7 – 12 are almost identical displaying a LLCT. Excited states 14 and 18 are the two components of the pseudo A term in the MCD for S → Co charge transfer transitions. Excited state 17 also contains a one-electron transition for S → Co charge transfer but with a smaller molecular orbital coefficient than excited state 14.

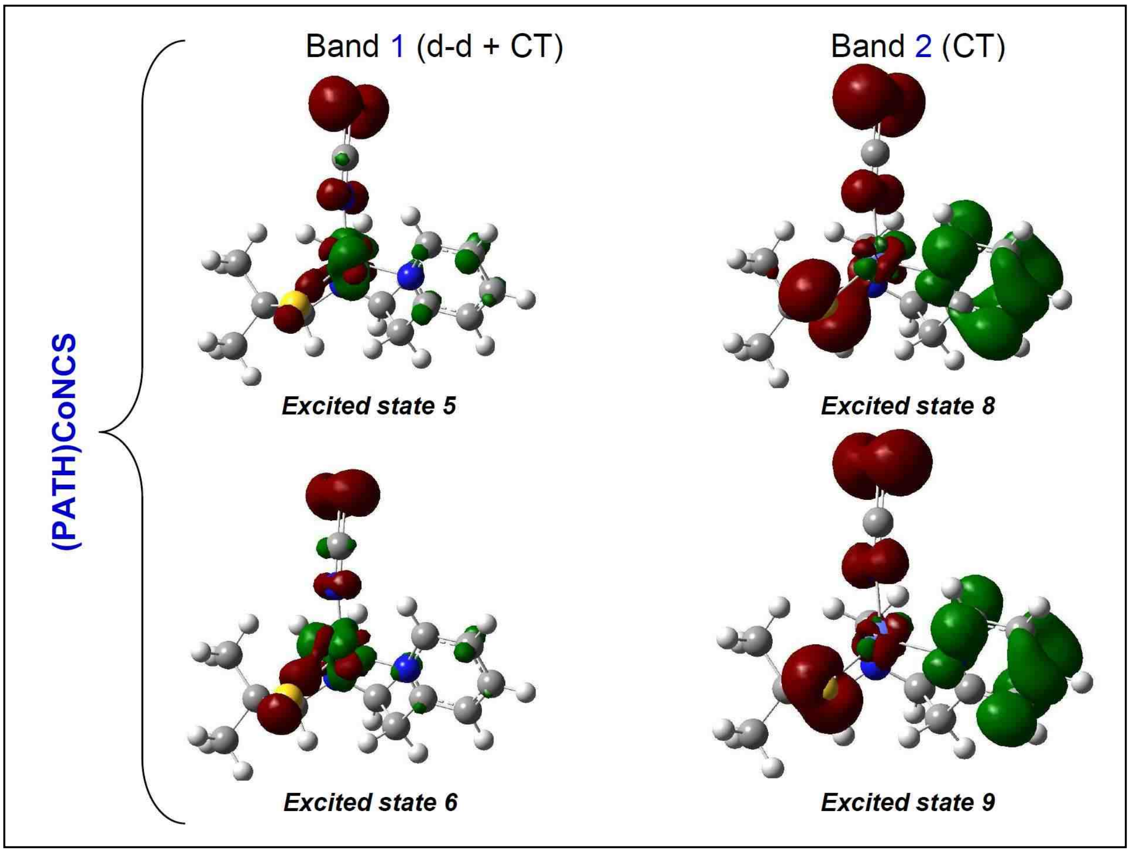
(PATH)CoNCS
Band 1 (d-d + CT)
Band 2 (CT)
Excited state 5
Excited state 8
Excited state 6
Excited state 9

Figure 3.43: Electron density difference maps (EDDMs) for (PATH)CoNCS where dark red represents a loss of electron density and green represents a gain of electron density in the transition.

The higher energy transitions which are observed as pseudo A terms at 25461 and 25500 cm^{-1} in MCD spectra for (PATH)CoBr and (PATH)CoNCS respectively (Figures 3.31 and 3.32) were calculated by TDDFT as transitions originating from S^V to d_{xy}/d_{xz} type orbitals of the metal. This S → Co charge transfer transition, also observed in wt luxS and the C84A and C84D mutants is important in providing information regarding the nature of first and second coordination sphere effects in luxS by monitoring key changes occurring in the Co-cysteine sulfur bonding as explained in the earlier discussion (section 3.6). Figures 3.44 and 3.45 depict the electronic transitions under the excited states 15, 18 for (PATH)CoBr shown previously in Figure 3.40, and electronic transitions under excited states 14, 18 for (PATH)CoNCS as shown in figure 3.42.

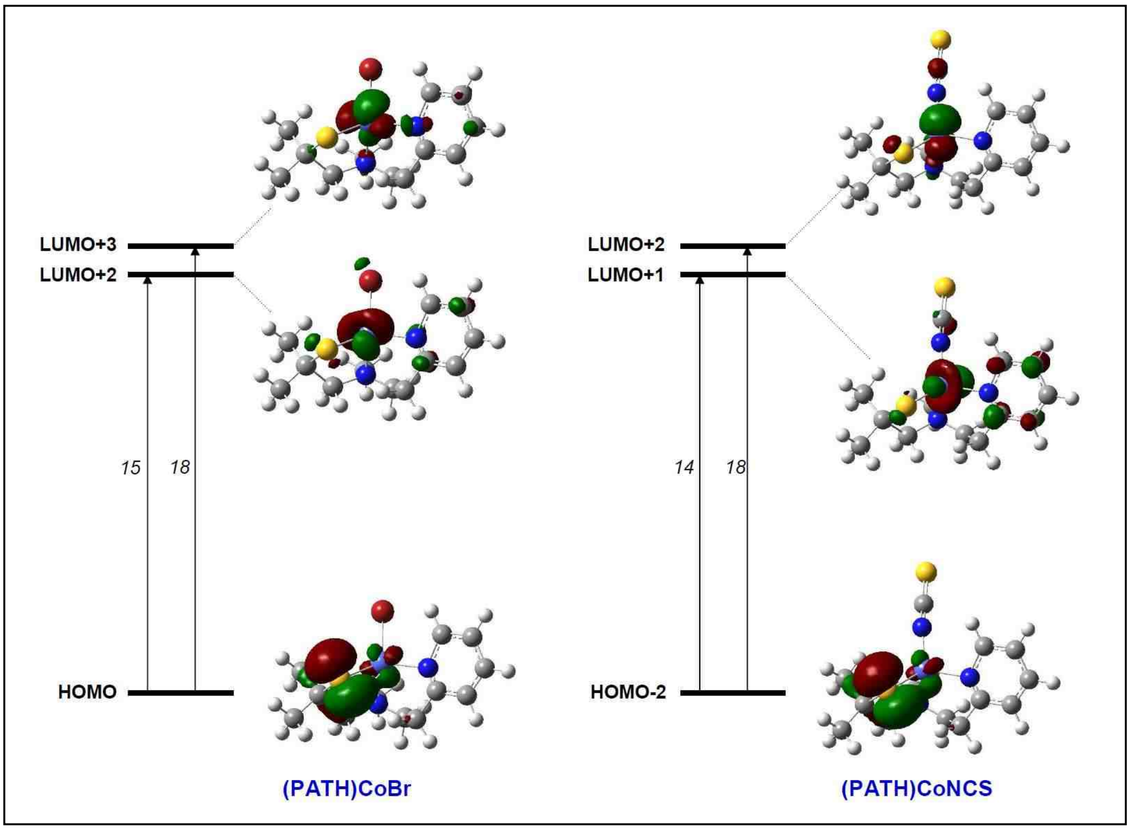

Figure 3.44: S → Co charge transfer transitions for (PATH)CoBr and (PATH)CoNCS. The two transitions for (PATH)CoBr occur at 26615 and 29030 cm^{-1} whereas transitions for (PATH)CoNCS occur at 23846 and 26563 cm^{-1}.

These transitions originate from a S^{v} (HOMO) orbital to the d_{xz} (LUMO+2) and d_{yz} (LUMO+3) type orbitals for (PATH)CoBr and from S^{v} (HOMO-2) orbital to d_{xz}

(LUMO+1) and d_{yz} (LUMO+2) type orbitals for (PATH)CoNCS. The EDDMs for these (PATH)CoBr and (PATH)CoNCS transitions are shown in Figure 3.45.

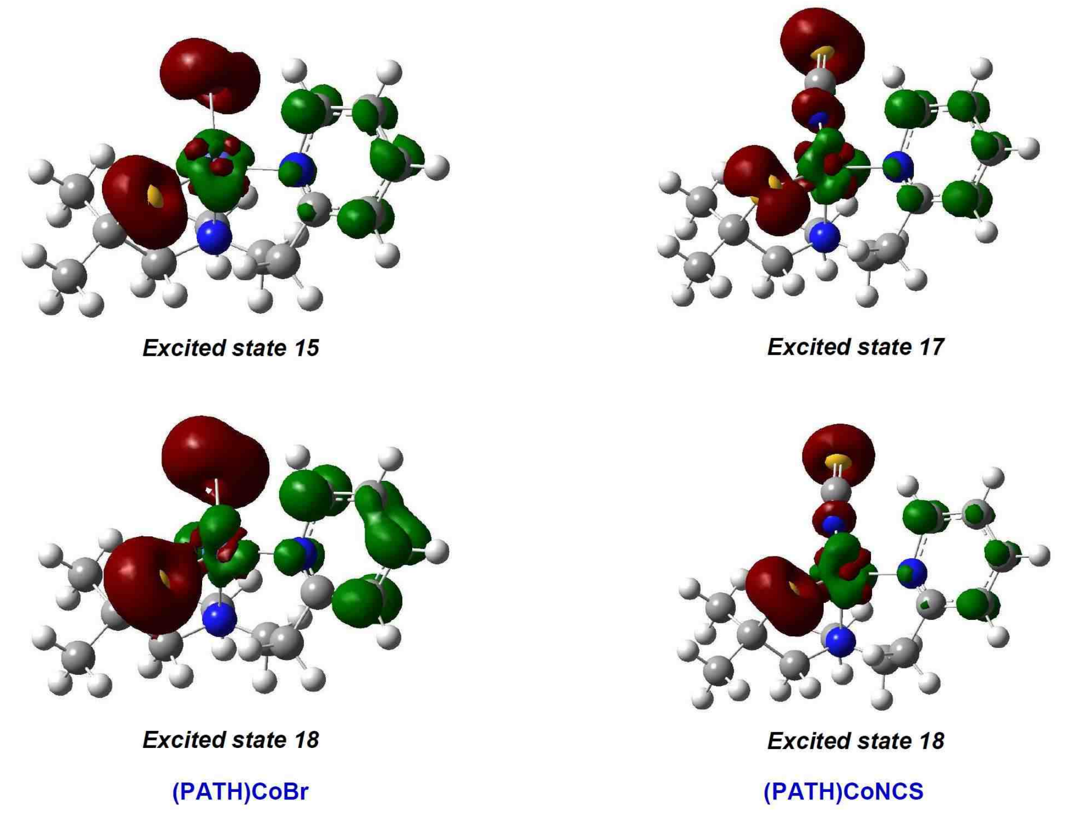

Excited state 15

Excited state 17

Excited state 18

Excited state 18

(PATH)CoBr

(PATH)CoNCS

Figure 3.45: Electron density difference maps (EDDMs) for S → Co charge transfer transitions of (PATH)CoBr and (PATH)CoNCS where dark red represents loss of electron density and green represents gain of electron density in the transition.

3.5.6.5 The Angular Overlap Model (AOM)

The input data comprised the cartesian coordinates for the metal center (Co), two nitrogens (N), one sulfur (S) and either a bromine (Br) for (PATH)CoBr or nitrogen (N) of the thiocyanate (SCN^-) for (PATH)CoNCS. The geometries were taken from the crystal structures reported by Chang and co-workers [141]. Figure 3.46 displays the adapted crystal structures for (PATH)CoBr and (PATH)CoNCS and the crucial bond angles and bond lengths selected for AOMX calculations.

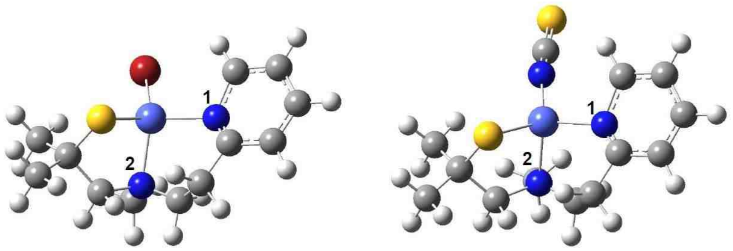

	(PATH)CoBr	(PATH)CoNCS
Co – Br/NCS	2.381	1.941
Co - S	2.233	2.231
Co – N1	2.036	2.008
Co – N2	2.090	2.084
Br/NCS – Co - S	122.94	123.13
Br/NCS – Co – N1	103.53	107.85
Br/NCS – Co – N2	116.36	111.00
N1 – Co – S	119.72	117.11
N2 – Co – S	91.86	93.39
N1 – Co – N2	100.24	100.81

Figure 3.46: Selected bond distances (Å) and bond angles (degrees) for (PATH)CoBr and (PATH)CoNCS adapted from Chang and co-workers.

As was the case for wt-luxS, C84A and C84D, the cartesian coordinates from the crystal structures for (PATH)CoBr and (PATH)CoNCS remained fixed throughout the calculations and the best fits to d-d transition energies were obtained by varying the Racah parameter (B), the spin orbit coupling constant (ξ), and eσ and eπ. Table 3.5 summarizes the AOMX best simulation results for (PATH)CoBr, (PATH)CoNCS and the AOMX parameters used to generate the the spin allowed transitions $^4A_2$ (F) → $^4T_2$ (F), $^4A_2$ (F) → $^4T_1$ (F) and $^4A_2$ (F) → $^4T_1$ (P).

Table 3.5: Observed vs. AOMX-calculated d-d transitions for (PATH)CoBr and (PATH)CoNCS

(PATH)CoBr		
$^4A_2 \rightarrow {}^4T_2$(F)	Not observed	4366 cm^{-1}
$^4A_2 \rightarrow {}^4T_1$(F)	6573 cm^{-1}	7055 cm^{-1}
$^4A_2 \rightarrow {}^4T_1$(F)	8442 cm^{-1}	8442 cm^{-1}
$^4A_2 \rightarrow {}^4T_1$(F)	11062 cm^{-1}	11027 cm^{-1}
$^4A_2 \rightarrow {}^4T_1$(P)	14877 cm^{-1}	14869 cm^{-1}
$^4A_2 \rightarrow {}^4T_1$(P)	15965 cm^{-1}	16287 cm^{-1}
$^4A_2 \rightarrow {}^4T_1$(P)	17895 cm^{-1}	17357 cm^{-1}
(PATH)CoNCS		
$^4A_2 \rightarrow {}^4T_2$(F)	Not observed	4430 cm^{-1}
$^4A_2 \rightarrow {}^4T_1$(F)	6817 cm^{-1}	7662 cm^{-1}
$^4A_2 \rightarrow {}^4T_1$(F)	8772 cm^{-1}	8706 cm^{-1}
$^4A_2 \rightarrow {}^4T_1$(F)	11521 cm^{-1}	11482 cm^{-1}
$^4A_2 \rightarrow {}^4T_1$(P)	14873 cm^{-1}	15189 cm^{-1}
$^4A_2 \rightarrow {}^4T_1$(P)	16737 cm^{-1}	16905 cm^{-1}
$^4A_2 \rightarrow {}^4T_1$(P)	18404 cm^{-1}	18418 cm^{-1}
AOMX PARAMETERS' FITTING VALUES		
Parameter	**(PATH)CoBr**	**(PATH)CoNCS**
N (N1 & N2); eσ	5340 cm^{-1}	5800 cm^{-1}

S; eσ, eπ	1750, 0 cm^{-1}	1700, 200 cm^{-1}
Br/NCS; eσ, eπ	3800, 120 cm^{-1}	4200, 100 cm^{-1}
B	630 cm^{-1}	630 cm^{-1}
Dq	436.6 cm^{-1}	443.0 cm^{-1}
ξ, |zfs = 2D|	500, 26.4 cm^{-1} (|D| = 13.2 vs. *-12 from VTVH*)	500, 17 cm^{-1} (|D| = 8.5 vs. *-12 from VTVH*)

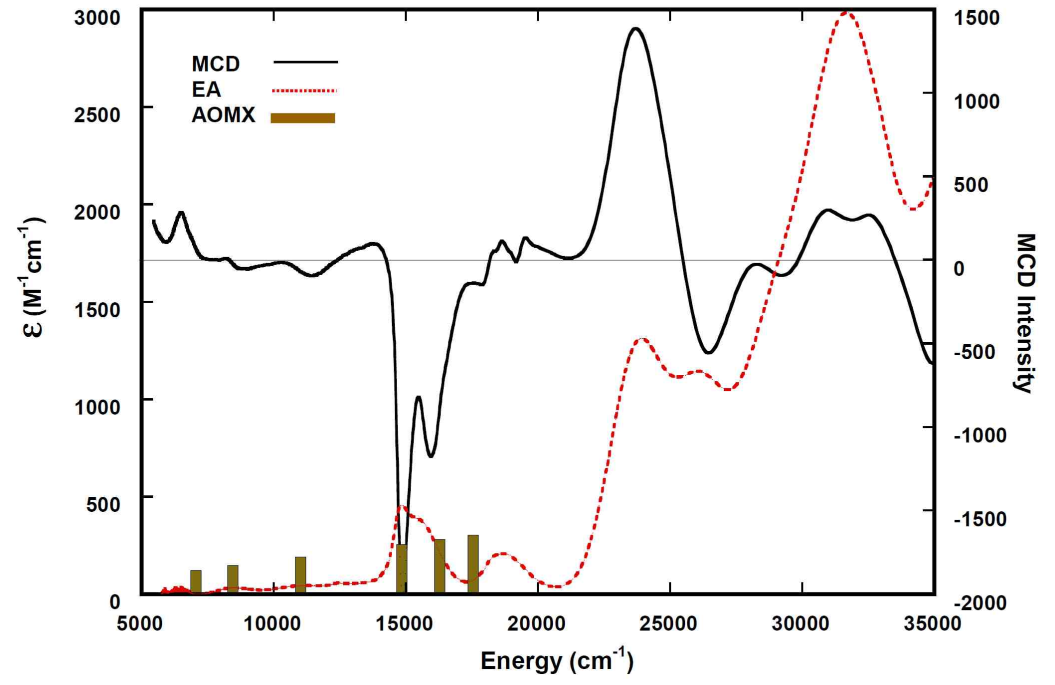

Figure 3.47: MCD, electronic absorption (EA) and AOMX overlays for (PATH)CoBr.

Figures 3.47 and 3.48 depict MCD and absorption spectral overlays and the positions of the d-d transitions calculated from AOMX for (PATH)CoBr and (PATH)CoNCS. The calculations for the ligand field strength (10Dq/B) gives 6.9 and 7.4 for (PATH)CoBr and (PATH)CoNCS, respectively. This indicates that the thiocyanate (SCN-) ligand is a stronger field ligand than bromine (Br) in these complexes. Summing all the results for the enzymes and model compounds in the order of the combined ligand field strength, we have (PATH)CoBr (Br, 10Dq/B = 6.9) < C84A (OH^-, 10Dq/B = 7.0) < wt-luxS (10Dq/B = 7.3) < (PATH)CoNCS (SCN^-, 10Dq/B = 7.4) < C84D (H_2O, 10Dq/B = 7.7)

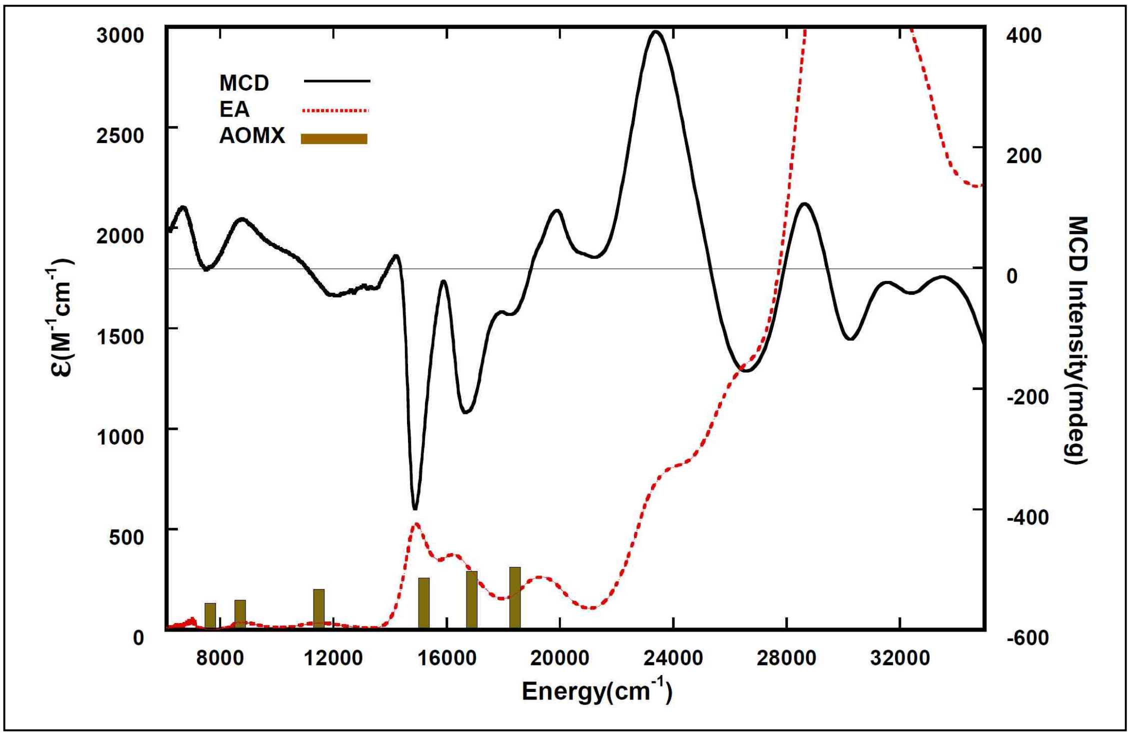

Figure 3.48: MCD, electronic absorption (EA) and AOMX overlays for (PATH)CoNCS.

3.6 Discussion and Conclusion

3.6.1 LuxS Active Site Geometry and Mechanistic Implications

The intensity, energy, and the splitting pattern of the $^4A_2(F) \rightarrow {}^4T_1(F)$ and $^4A_2(F) \rightarrow {}^4T_1(P)$ near infra-red and visible region LF transitions has provided new information about the active site geometry of luxS and mutants. Analysis of these transitions in wt enzyme, C84A and C84D mutants, and the model compounds ((PATH)CoBr and (PATH)CoNCS) have indicated deviations from tetrahedral symmetry (T_d) to either approximately C_{2V} symmetry where the ^4T states split into ^4A, ^4B and ^4B or C_{3V} where ^4T states split into ^4E and an ^4A states. Figure 3.49 shows two simple models (in boxes) which have C_{2V} ($Co(II)(NH_3)_2(OH)_2$) and C_{3V} ($Co(II)(NH_3)_3OH$) symmetries with their calculated spin density maps chosen to explain the approximate geometries for mutants and model compounds.

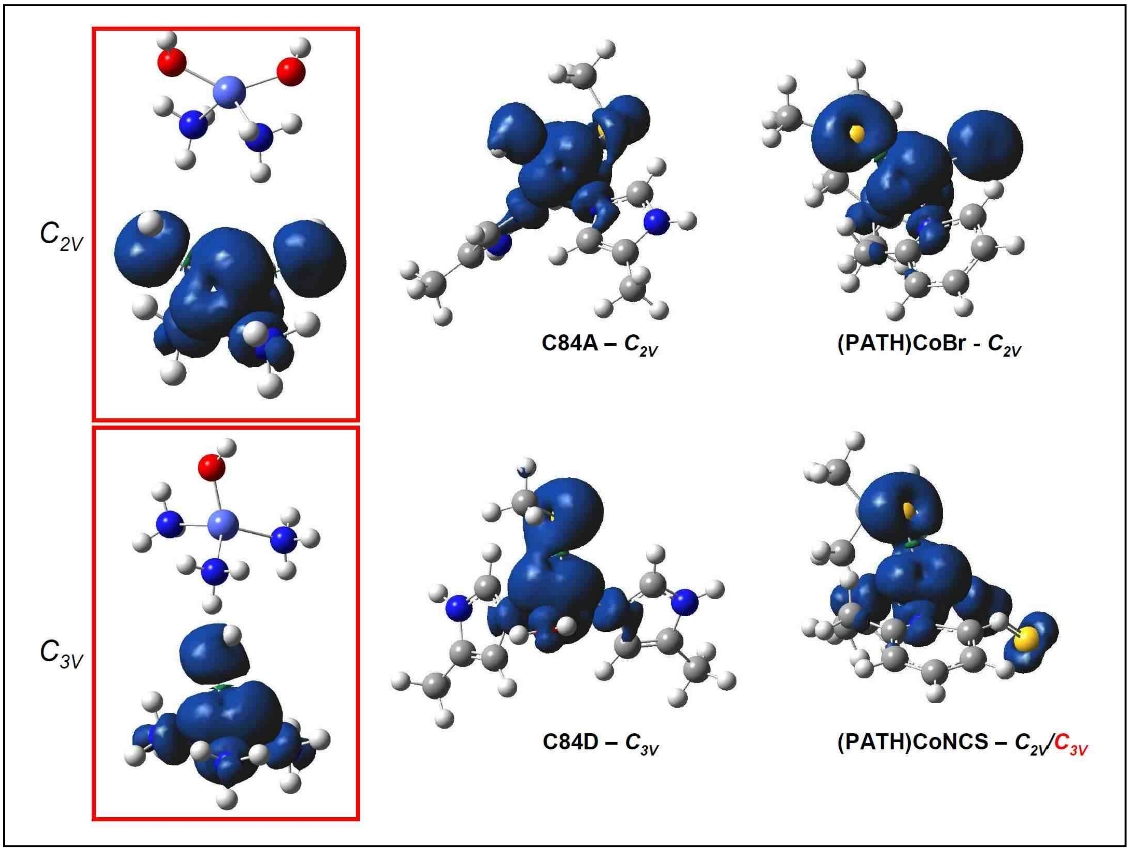

Figure 3.49: Spin density maps for C84A, C84D, and the model compounds ((PATH)CoBr and (PATH)CoNCS.

These spin density calculations have indicated a ligand field distortion from T_d symmetry to approximately C_{3V} for C84D and to C_{2V} for C84A and the model compounds ((PATH)CoBr and (PATH)CoNCS). Our experimental results, together with the computational results, strongly indicate a C_{2V} symmetry for the model compounds. On the other hand, MCD experimental results for wt-luxS and luxS mutants suggest the presence of both C_{3V}, based on the near infra-red transitions ($^4A_2(F) \rightarrow {}^4T_1(F)$), and C_{2V} based on the visible transitions ($^4A_2(F) \rightarrow {}^4T_1(P)$). However, computational results show a C_{2V} symmetry for C84A and C_{3V} symmetry for C84D. Faye and co-workers reported an absorption spectrum for Co(II)biquinolineCl_2 which is remarkably similar to C84A. Here, they proposed a distortion from tetrahedral geometry to C_{2V} symmetry [142]. Ferguson also reported absorption spectra of Co(II)X_2Y_2 type compounds in C_{2V} symmetry which are similar to the observed transitions in C84A and the (PATH)CoBr and (PATH)CoNCS model compounds[143]. On the other hand, Coleman and co-workers reported MCD and absorption spectra for Co(II) carbonic anhydrase (Co(II)$(His)_3$-H_2O) that is similar to C84D luxS [4,144]. Furthermore, Brader and co-workers also reported an MCD and electronic absorption of the Co(II) substituted insulin hexamer that consists of three dimeric units with a 3-fold symmetry axis [3]. The transitions associated with $^4A_2(F) \rightarrow {}^4T_1(P)$ state in these spectra indicated the presence of C_{3V} symmetry and are similar to the ones observed in C84D luxS. However, the splitting pattern of the $^4A_2(F) \rightarrow {}^4T_1(F)$ transition in the MCD spectra of wt-luxS and the mutants into ^4E (pseudo A) and ^4A (negative C) symmetry suggest the presence of approximately C_{3V} symmetry. This fits well for

C84D and agrees well with the reported and computational results. The absence of this splitting pattern in the $^4A_2(F) \rightarrow {}^4T_1(P)$ state MCD for C84D could be due to overlapping positive and negative C terms resulting from mixing of spin forbidden transitions originating from the doublet ^2G state. On the other hand, the splitting pattern of the $^4A_2(F) \rightarrow {}^4T_1(F)$ state for C84A can be described as a positive C-term and two negative C-terms consistent with C_{2V} symmetry and agrees well with the computational results. In the visible region, the $^4A_2(F) \rightarrow {}^4T_1(P)$ state for C84A shows splitting consistent with C_{2V} symmetry. Nonetheless, the comparison between the observed transition energies for $^4A_2(F) \rightarrow {}^4T_1(F)$ in MCD and electronic absorption for wt and mutants indicate a small perturbation of the ligand field parameter (10Dq). EPR and VTVH-MCD show remarkable differences in the electronic properties between C84A and C84D that are consistent with the computational results. VTVH-MCD and EPR spectroscopy are well known for their sensitivity in determining spin-Hamiltonian parameters that reflect variations in the metal environment. Furthermore, these techniques have the demonstrated capability of providing useful electronic and structural information about the metal coordination sphere in Co(II) complexes [5,8,14,145-148]. These findings suggest the presence of C_{3V} symmetry in C84D luxS and C_{2V} symmetry in C84A luxS and have indicated the potential role of C 84 in maintaining the catalytic geometry of luxS active site.

Another key feature that provides information regarding the changes taking place either in the first or second coordination sphere is the S → Co charge transfer transition. The first band for this transition occurs between 18000 and 20000 cm^{-1} and the second set between 25000 and 30000 cm^{-1}. The first S → Co charge transfer transition (band 2 in Figures 3.20 and 3.29) is characterized by large absorption intensity and very small MCD intensity that results in a very small C/D (MCD intensity over optical intensity) ratio characteristic of dipole allowed ligand to metal charge transfer (LMCT) bands [149-152]. This occurs at 18825 cm^{-1} for wt-luxS, 18956 cm^{-1} for C84D and 20000 cm^{-1} for C84A and these energies are comparable with similar S → Co/Cu charge transfer transitions observed in blue copper proteins (azurin, stellacyanin and plastocyanin) [7,9]. However, Faye and co-workers assigned this band as originating from a spin forbidden transition [142]. TDDFT calculations for C84A and C84D indicate that this transition originates from an S^{v} type orbital to the d_{xy} orbital of Co(II) ion, with calculated energies of 21600 cm^{-1} and 24500 cm^{-1} for C84D and C84A respectively. The second set of S → Co charge transfer transition occurs at 28697, 28816 and 29140 cm^{-1} for wt-luxS, C84D and C84A, respectively, and appears as pseudo A terms in the MCD spectra. These assignments are in excellent agreement with similar features observed in the 25000 to 30000 cm^{-1} range for Co(II) thiolate complexes [2]. TDDFT calculations for C84A and C84D indicate that this transition originates from either S^{v} or S^{σ} type orbitals to the d_{xz}/d_{yz} orbital set of the Co(II) ion with calculated energies of 29100 cm^{-1} and 31600 cm^{-1} for C84D and C84A respectively. However, the lowest energy S → Co charge transfer transition observed for wt-luxS, when compared to C84D and C84A, strongly suggests the presence of water at the active site and not hydroxide.

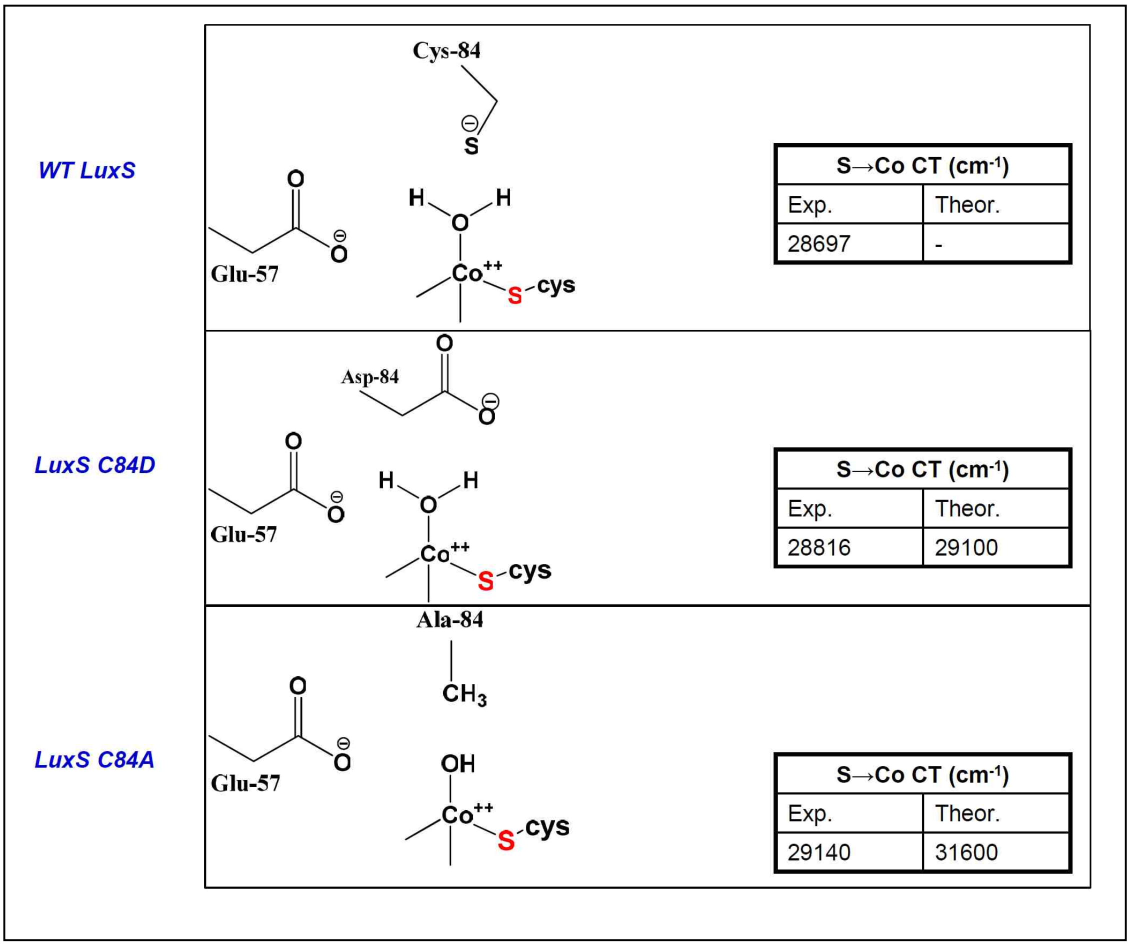

WT LuxS

S→Co CT (cm^{-1})	
Exp.	Theor.
28697	-

LuxS C84D

S→Co CT (cm^{-1})	
Exp.	Theor.
28816	29100

LuxS C84A

S→Co CT (cm^{-1})	
Exp.	Theor.
29140	31600

Figure 3.50: Electrostatic interactions at the active sites of wt-luxS, C84D, C84A and analysis of the S → Co charge transfer transition. Water is stabilized in wt-luxS and C84D whereas a hydroxide is stabilized in C84A.

However, the broadness of the wt-luxS could be originating from relaxation properties and a large spin orbit coupling. The model compounds have also produced very broad EPR spectra similar to wt-luxS. However, the differences in S → Co transition energies between wt-luxS and mutants (C84D and C84A) are a result of stabilization of either water (for wt and C84D) or a hydroxide (for C84A) resulting from electrostatic interactions between the amino acid residues (cysteine 84, aspartate 84 and alanine 84) and glutamate 57 in the secondary coordination sphere (Figure 3.50). The deprotonated cysteine 84 is a stronger base than the aspartate 84 [205]. However, there is a stronger electrostatic interaction between cysteine 84 and glutamate 57 for wt-luxS than there is for C84D. Consequently water is stabilized more in wt enzyme than in the C84D mutant (Figure 3.50). The reduced electrostatic interaction in C84D results in a stronger interaction between the water ligand and Co(II). This is potentially due to an increased sigma and pi donation to the Co(II) ion and consequently an observed higher energy S → Co charge transfer transition. In the presence of alanine 84, the electrostatic interaction is lost and as a result, the pKa of water is raised through hydrogen bonding with Glu 57. This, in turn, results in a deprotonation of water leading to the formation of a hydroxide coordinated to the Co(II) ion (Figure 3.50). However, the hydroxide ligand destabilizes both sigma and pi orbitals of Co(II) ion resulting in an observed S → Co charge transfer transition which occurs at highest energy compared to wt-luxS and C84D.

Figure 3.51 shows the energy level diagram for the molecular orbitals involved in ligand field and charge transfer transitions for wt-luxS, mutants and the model compounds. DFT calculations indicate that the S → Co charge transfer bands for C84A and the model compounds ((PATH)CoBr and (PATH)CoNCS) occur at relatively higher energy than in C84D (Figure 3.51), as expected. The lowest energy charge transfer bands for C84A and the model compounds are S →

imidazole and S/SCN⁻ → pyridine, respectively, whereas for C84D the lowest energy charge transfer band is calculated as S → Co (Figure 3.49).

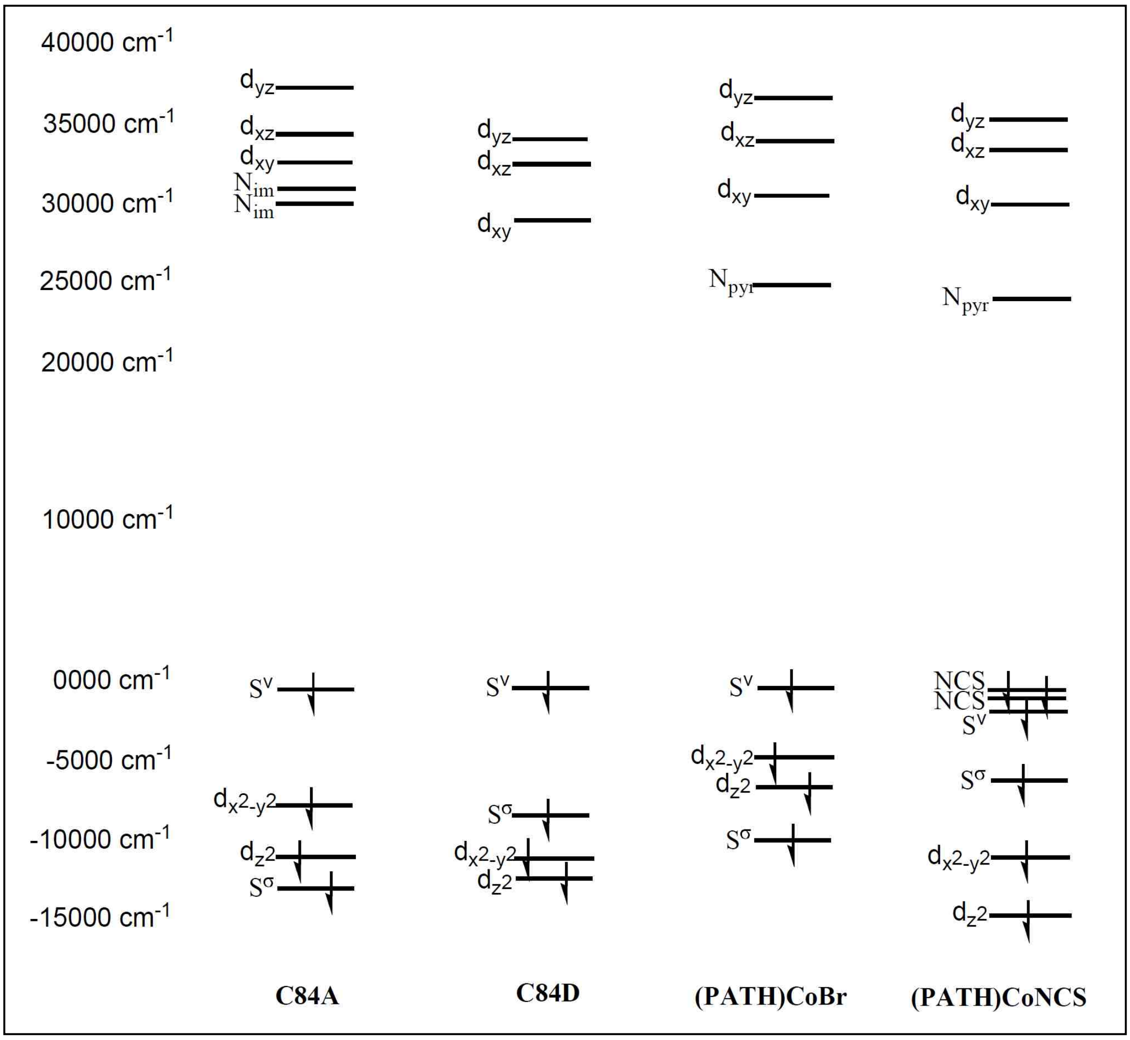
40000 cm-1
35000 cm-1
30000 cm-1
25000 cm-1
20000 cm-1
10000 cm-1
0000 cm-1
-5000 cm-1
-10000 cm-1
-15000 cm-1
dyz
dxz
dxy
Nim
Nim
Sv
dx2-y2
dz2
Sσ
NCS
NCS
Npyr
C84A
C84D
(PATH)CoBr
(PATH)CoNCS

Figure 3.51: Molecular orbital energy level diagram for mutants and model compounds.

However, the hydroxide ligand in C84A, the bromine (Br) in (PATH)CoBr and thiocyanate (⁻NCS) in (PATH)CoNCS are all grouped as sigma and pi donor ligands and are expected to give similar interactions with the Co(II) ion. C84D is likely coordinated to a water ligand which is a sigma donor only. Angular overlap model calculations (AOMX) strongly agree with these findings and $e\sigma$ and $e\pi$ parameters were used to obtain the best fit for C84A and model compounds, whereas only the $e\sigma$ parameter was used for the wt-luxS and C84D (Tables 3.3 and 3.4) spectral fits. The observed results coupled with computational results strongly indicate that the substrate S-rybosylhomocysteine (SRH) displaces metal bound water at the active site of wt-luxS at relatively minimum energy compared with C84D and this difference originates from electrostatic stabilizations caused by the basicity difference of deprotonated cysteine 84 in wt-luxS and aspartate 84 in C84D. This explains the huge reduction in catalytic efficiency for C84D [111]. The loss of electrostatic stabilization upon mutation of cysteine 84 to an alanine results in a coordinated hydroxide for C84A, which renders it completely inactive as observed by Zhu and co-workers [111,135]. However, deprotonated cysteine 84 plays the dual role of stabilizing metal bound water and abstracting a proton in the first step of catalysis in the proposed mechanism. These novel findings provide substantial support to the proposed catalytic mechanism of luxS.

Chapter 4

Mutations in the FMN Domain Modulate MCD Spectra of the Heme Site in the Oxygenase Domain of Inducible Nitric Oxide Synthase

4.1 Introduction

4.1.1 Nitric Oxide Synthase (NOS), Isoforms and Cofactors

The nitric oxide synthases (NOSs) are homodimeric flavocytochromes that contain the relatively tightly-bound cofactors (6*R*)-5,6,7,8-tetrahydrobiopterin (BH_4), FAD, FMN and iron protoporphyrin IX (heme) in each subunit of the dimer (Figure 4.1, 4.2, 4.3 and 4.4) [154-159].

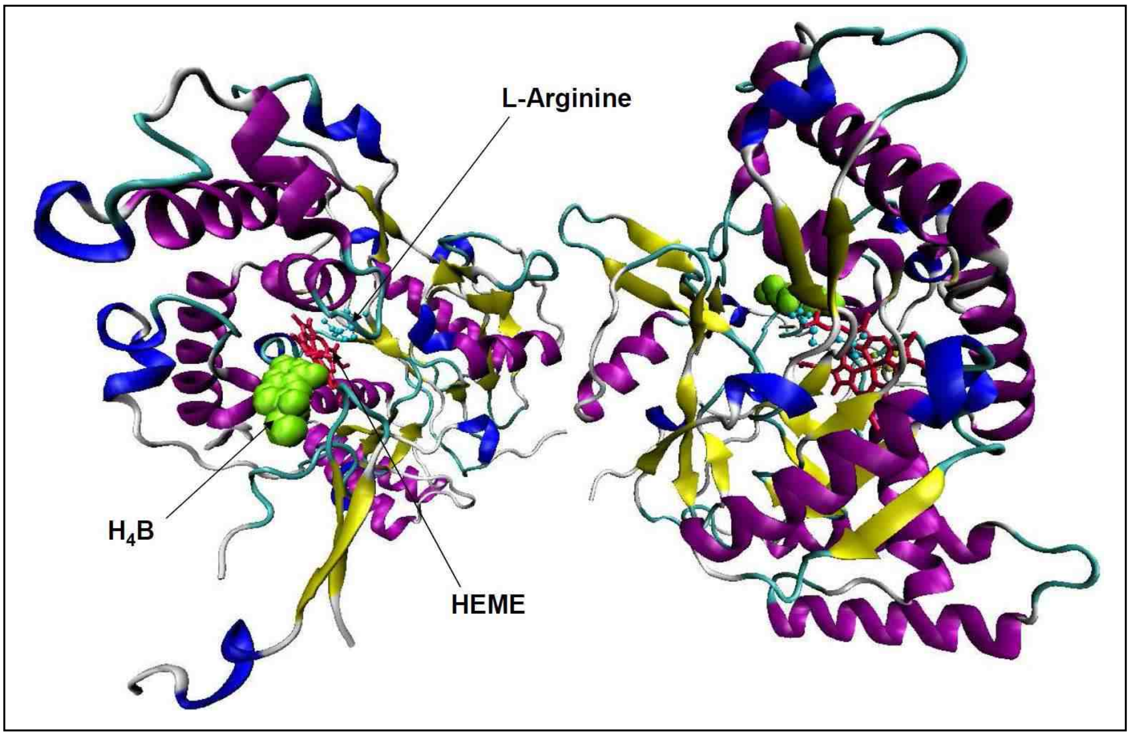

Figure 4.1: Stereoview of iNOS oxygenase dimer showing the heme domain (red) and tetrahydrobiopterin domain (green). L-arginine (cyan), the substrate is

shown to be bound close to the heme domain. The structure was downloaded from the protein data bank (PDB) 1NOD.

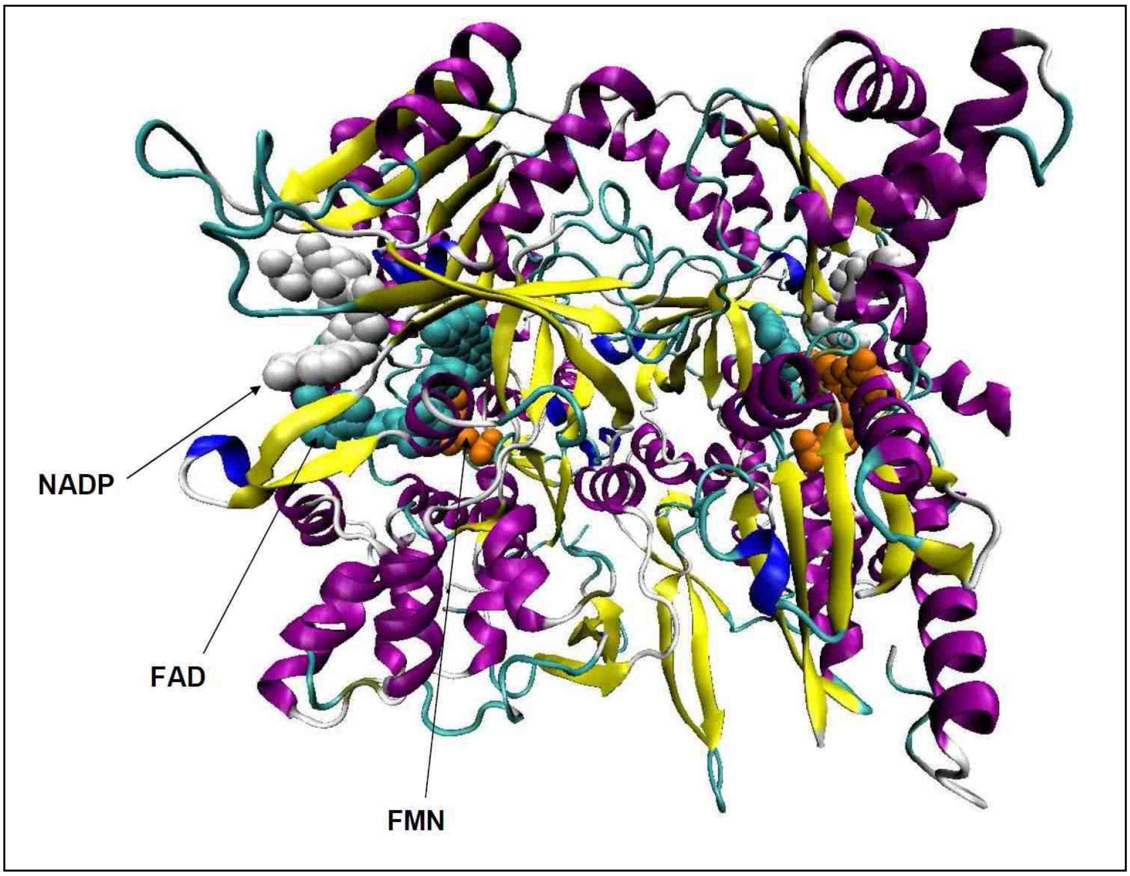

Figure 4.2: Stereoview of the nNOS reductase dimer showing different domains of iNOS reductase. These are the NADP domain (white), FAD domain (cyan) and FMN domain (orange). The structure was downloaded from teh protein data bank (PDB) 1TLL.

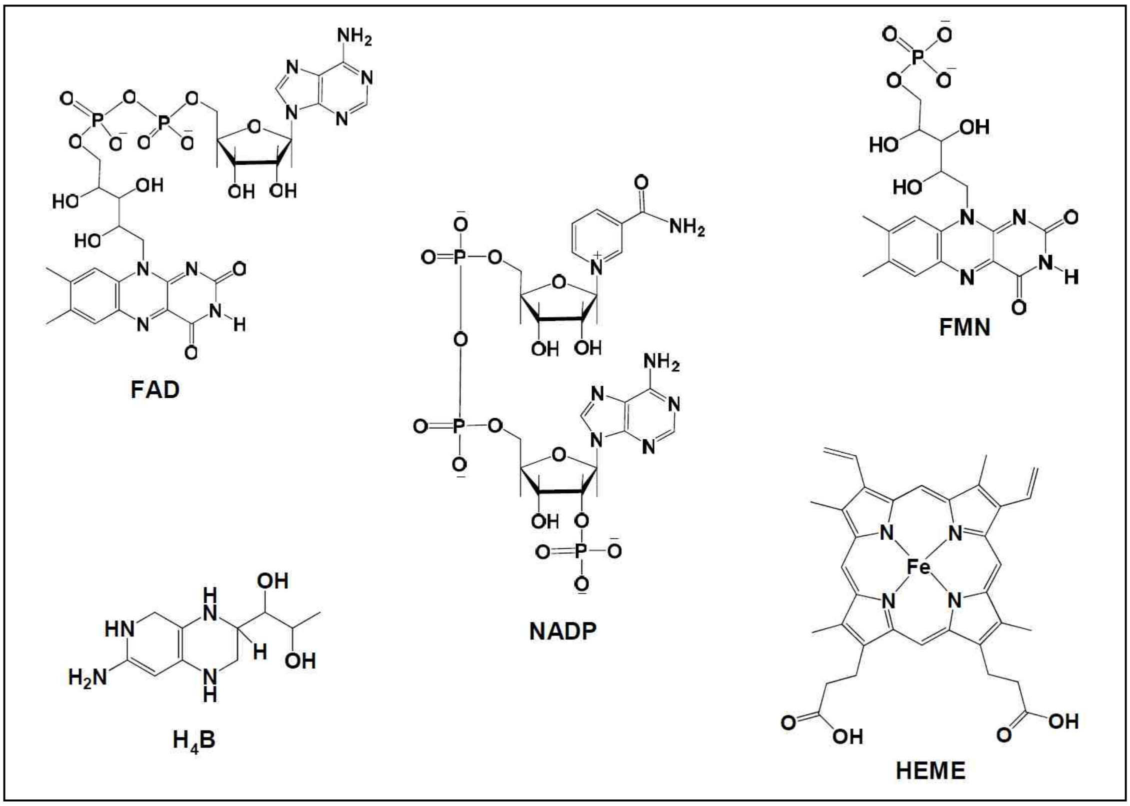

Figure 4.3: Redox cofactors in NOS enzymes. NADP, FAD and FMN constitute the reductase domain, whereas H_4B and heme constitute the oxygenase domain.

Each subunit contains a reductase domain that binds NADPH, FAD and FMN cofactors (Figure 4.2) and an oxygenase domain that binds the heme and tetrahydrobiopterin (Figure 4.1) [160-162]. Three distinct isoforms of NOS have been identified which include the constitutive isoforms, eNOS and nNOS regulated by the Ca^{2+}/CaM and a cytokine inducible isoform iNOS which is insensitive to Ca^{2+}/CaM binding [163] (Figure 4.4). These isoforms are distributed in both eukaryotic and prokaryotic organisms [164].

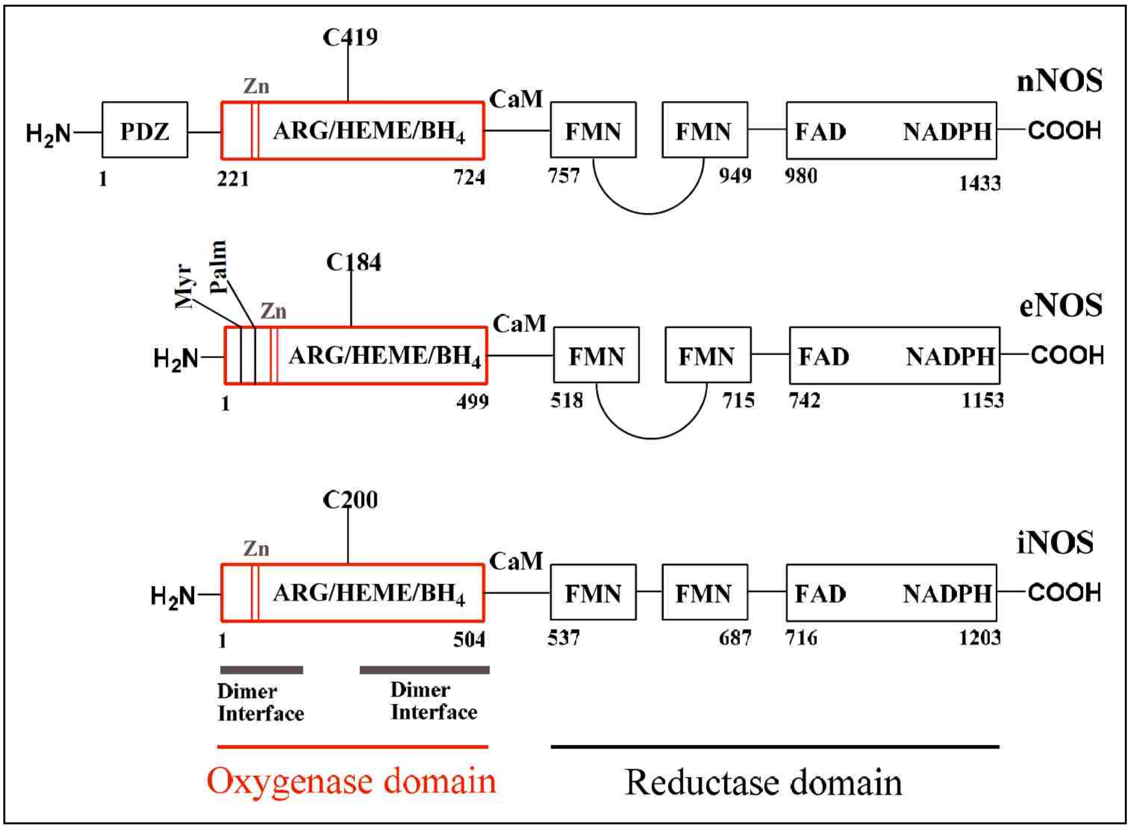
nNOS
H2N
PDZ
Zn
C419
ARG/HEME/BH4
CaM
FMN
FMN
FAD
NADPH
COOH
1
221
724
757
949
980
1433
eNOS
Myr
Palm
Zn
C184
ARG/HEME/BH4
CaM
FMN
FMN
FAD
NADPH
COOH
1
499
518
715
742
1153
iNOS
Zn
C200
ARG/HEME/BH4
CaM
FMN
FMN
FAD
NADPH
COOH
1
504
537
687
716
1203
Dimer Interface
Dimer Interface
Oxygenase domain
Reductase domain

Figure 4.4: Domain structure of human nNOS, eNOS and iNOS showing oxygenase, reductase and PDZ domains denoted by solid boxes and the amino acid residue number at the start/end in each isoform. The cysteine residue ligating the heme and the CaM-binding site is indicated for each isoform. Myristoylation (Myr) and palmitoylation (Palm) sites on eNOS are shown, together with the location of the zinc ligating cysteines. The autoinhibitory loop within the FMN regions of nNOS and eNOS are also shown. Grey bars indicate the dimer interface in the oxygenase domain.

The nNOS, eNOS and iNOS are products of different genes, with different localization, regulation, catalytic properties and inhibitor sensitivity. The human isoforms possess 51 – 57 % homology [165-168]. These are summarized in Table 4.1.

Table 4.1: NOS isoform homology

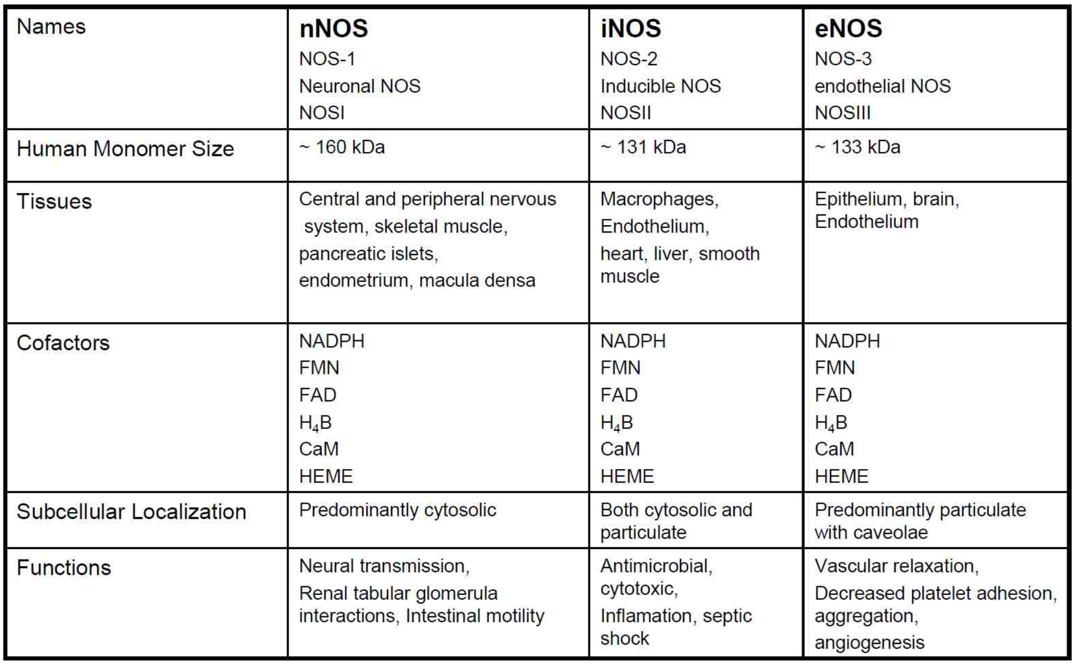

Names	**nNOS** NOS-1 Neuronal NOS NOSI	**iNOS** NOS-2 Inducible NOS NOSII	**eNOS** NOS-3 endothelial NOS NOSIII
Human Monomer Size	~ 160 kDa	~ 131 kDa	~ 133 kDa
Tissues	Central and peripheral nervous system, skeletal muscle, pancreatic islets, endometrium, macula densa	Macrophages, Endothelium, heart, liver, smooth muscle	Epithelium, brain, Endothelium
Cofactors	NADPH FMN FAD H_4B CaM HEME	NADPH FMN FAD H_4B CaM HEME	NADPH FMN FAD H_4B CaM HEME
Subcellular Localization	Predominantly cytosolic	Both cytosolic and particulate	Predominantly particulate with caveolae
Functions	Neural transmission, Renal tabular glomerula interactions, Intestinal motility	Antimicrobial, cytotoxic, Inflamation, septic shock	Vascular relaxation, Decreased platelet adhesion, aggregation, angiogenesis

4.1.2 Proposed Catalytic Mechanism

The NOS isoforms iNOS, eNOS, and nNOS, all achieve their key biological functions via an intriguing regulation of interdomain electron transfer (IET) processes [168,169]. Electrons are donated by NADPH to the reductase domain of the enzyme and proceed via FAD and FMN redox carriers to the oxygenase domain (active site) where they interact with the heme iron and BH_4 to catalyse the two steps reaction of oxygen with L arginine. This generates citrulline and NO as products (Scheme 4.1) [160,170-174].

Scheme 4.1

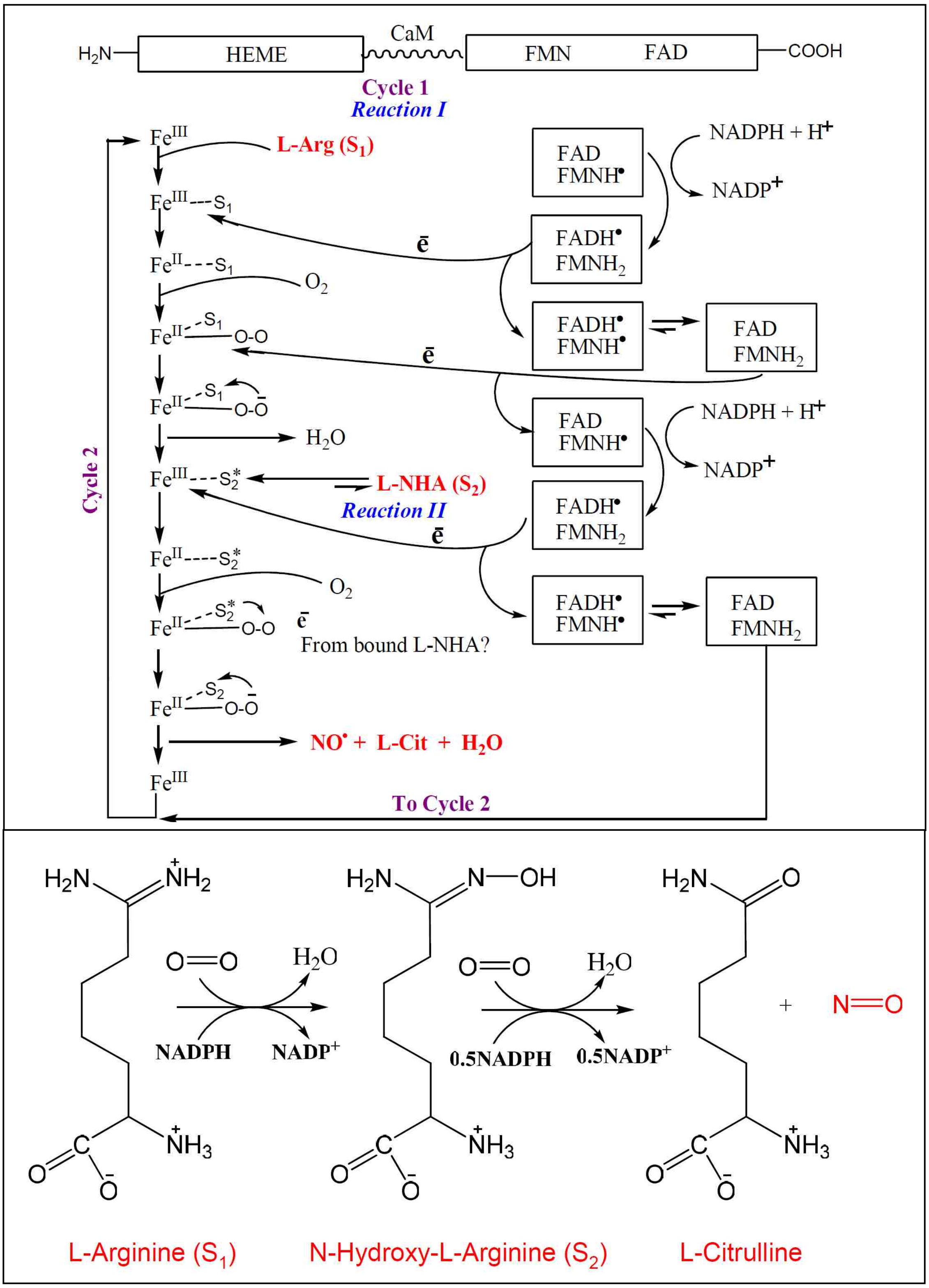
H2N
HEME
CaM
FMN
FAD
COOH
Cycle 1
Reaction I
Fe^III
L-Arg (S1)
Fe^III---S1
Fe^II---S1
O2
Fe^II ---S1 O-O
Fe^II ---S1 O-O^-
H2O
Fe^III---S2*
L-NHA (S2)
Reaction II
Fe^II----S2*
O2
Fe^II --S2* O-O
ē
From bound L-NHA?
Fe^II --S2 O-O^-
NO• + L-Cit + H2O
Fe^III
Cycle 2
To Cycle 2
FAD FMNH•
NADPH + H+
NADP+
FADH• FMNH2
ē
FADH• FMNH•
FAD FMNH2
ē
FAD FMNH•
NADPH + H+
NADP+
FADH• FMNH2
ē
FADH• FMNH•
FAD FMNH2
H2N
NH2+
O=O
H2O
NADPH
NADP+
NH3+
O
O-
H2N
N—OH
O=O
H2O
0.5NADPH
0.5NADP+
NH3+
H2N
O
+
N=O
NH3+
L-Arginine (S1)
N-Hydroxy-L-Arginine (S2)
L-Citrulline

$$\text{L-Arg} + 1.5\text{NADPH} + 1.5\text{H}^+ + 2\text{O}_2 \rightarrow 1.5\text{NADP} + \text{L-Cit} + \text{NO} + 1.5\text{H}_2\text{O}$$

The first step involves the formation of the intermediate hydroxylation product, N-hydroxyl-L-arginine (L-NHA) where one oxygen molecule and two electrons are consumed similar to P450 chemistry for N-hydroxylation [160,175]. The second step is not well understood and involves only one electron from NADPH to form iron (II) which then binds dioxygen [176]. It has been suggested that the iron (II) dioxo complex rearranges to superoxide iron(III) complex which must accept an electron and proton from L-NHA to promote O–O bond cleavage and hydroxylation of the carbon atom in L-NHA followed by NO and L-citrulline release.

The reductase and oxygenase domains in NOS proteins are linked by a polypeptide segment containing a CaM binding site [177]. CaM binding to NOS activates NO synthesis by triggering electron transfer from the FMN to the heme [178-180]. It also relieves repression of NOS flavoprotein electron transfer to external acceptors such as cytochrome c [181-183]. These processes are mostly unknown [184].

The hydroquinone form ($FMNH_2$) has been proposed to reduce the heme site as in the case of NADPH-cytochrome P450 reductase [185,186]. $^{18}O_2$ experiments determined that the source of the oxygen atoms for the formation of both $NO^{\bullet}$ and L-citrulline is molecular oxygen [187,188]. It was also observed that N-hydroxy-L-arginine is an intermediate in the biosynthesis of NO from L-arginine and that

1.5 and 0.5 mole of NADPH are consumed in the formation of NO_2^- and NO_3^- from L-arginine and L-NHA respectively [189,190].

The NO released by the constitutive isoforms function as a molecular signal (in neurotransmission and the regulation of blood flow/pressure (vasodilation)) whereas the larger amounts of NO produced by iNOS attacks proteins and DNA either directly or as peroxynitrite following combination with superoxide (cytotoxin) [180]. Aberrant NOS activity is implicated in cancer, stroke and hypertension [191].

The control mechanisms for the catalytically relevant IET processes between domains in the NOS holoenzymes are not well understood. The IET from FMN to heme is particularly essential in the delivery of electrons required for O_2 activation in the heme domain and the subsequent NO synthesis (Figure 4.5). This has been the major concern of this study. This interdomain FMN – heme IET is facilitated by the formation of the NOS output state, which is the electron donating state of the FMN domain. However, the structure and functional output state for NO production remains undetermined to date.

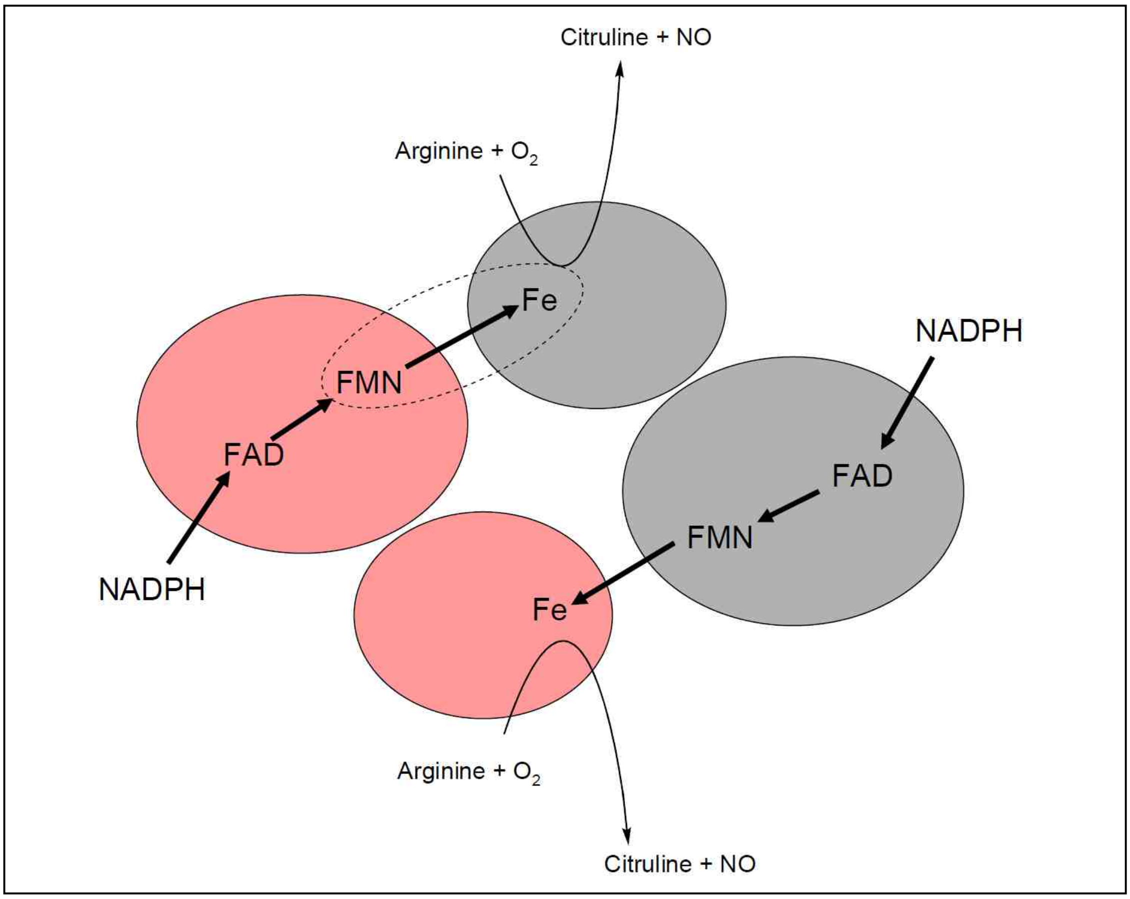
Citruline + NO
Arginine + O_2
Fe
FMN
FAD
NADPH
NADPH
FAD
FMN
Fe
Arginine + O_2
Citruline + NO

Figure 4.5: Electron flow in NOS enzymes. Here, electrons are delivered to the heme domain for NO production from the FMN domain by mechanisms that are not well understood.

Based on the crystallographic studies it has been proposed that the FMN domain acts as a tethered shuttle controlling important IET in NOS catalysis (Figure 4.6) [156,191,192]. It has also been suggested from recent evidence that facile IET requires a conformational change of the FMN domain from its original electron accepting conformation (input state) to a new electron donating state (output state) [163]. The putative NOS output state is defined as a complex between the

FMN-binding and oxygenase domains and facilitates IET between FMN hydroquinone and the oxygenase domain catalytic heme.

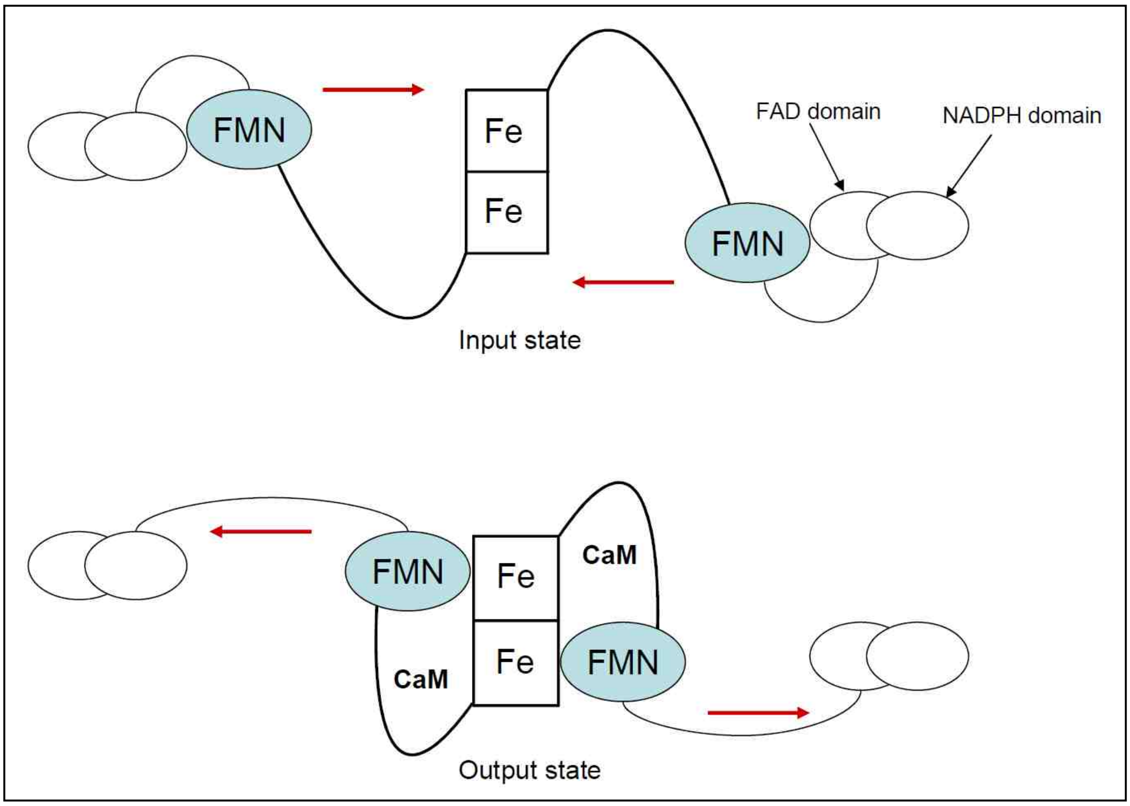
FMN
Fe
Fe
FAD domain
NADPH domain
FMN
Input state
FMN
Fe
CaM
Fe
FMN
CaM
Output state

Figure 4.6: Representation of a tethered shuttle model: FMN-binding domain shuttles between the FAD domain and heme containing oxygenase domain. Top: input state; bottom: putative output state. The two tethers correspond to the hinge region between the FMN and FAD domains, and the CaM binding linker between the FMN and oxygenase domains. CaM binding unlocks the input state, thereby enabling the FMN domain to shuttle between the two enzyme states.

We have investigated this crucial interdomain interaction on bidomain NOS oxyFMN constructs, in which only the oxygenase domain, the FMN domain, and the CaM binding regions are expressed. Low temperature magnetic circular dichroism (MCD) spectroscopy, variable temperature variable field magnetic circular dichroism (VTVH-MCD) spectroscopy and electron paramagnetic resonance spectroscopy (EPR) were used to probe how mutations in the adjacent FMN domain affect the heme center in a human iNOS oxyFMN construct. The wild type iNOS oxyFMN and the mutants (E546N-iNOS oxyFMN and E603N-iNOS oxyFMN), together with their corresponding cyano adducts, were spectroscopically analyzed with and without L-arginine treatment. E546 and E603 are charged surface residues that are conserved in all NOS isoforms and are located at the edge of the FMN domain in human iNOS. The iNOS oxygenase domain was used as a control. The results indicated by spectral perturbations of L-arginine on wt and mutants strongly suggested a role for the FMN domain in the IET and have provided the first direct paramagnetic spectroscopic evidence to indicate that the docked FMN domain affects the nature of interactions between the L-Arg substrate and the catalytic heme center located in an adjacent domain in iNOS [1]. This work strongly suggests that the FMN domain in the iNOS oxyFMN constructs has to align properly with the heme domain for the efficient production of NO.

4.2 Statement of the Research Problem

Mechanisms and regulation of NOS electron transfer in NOS proteins have been a subject of debate, as they are the only calcium binding (CaM) enzymes known to utilize the four redox cofactors of FAD, FMN, H_4B and heme. The presence of these four cofactors makes the study of interdomain electron transfer difficult. Particular interest has been focused on the FMN/heme interactions with bound CaM (output state). However, the important sites in the alignment of the FMN and the heme domains are still undetermined. It is not known whether the conserved FMN residues in NOS isoforms play any role in catalysis. Therefore, detailed spectroscopic studies of wild type iNOS oxyFMN co-expressed with CaM constructs and mutants will help identify important residues for the alignment of FMN and heme domains and determine the nature of interdomain FMN-heme interactions in facilitating the production of NO at the oxygenase domain.

4.3 Hypothesis

The conserved residues in the FMN domain (E546 and E603) of NOS proteins play key roles in the modulation of electron transfer by facilitating a productive alignment of the FMN and heme domains.

4.4 Materials and Methods

Protein samples. Purified iNOS samples and mutants were provided by our collaborator Changjian Feng and his research group from College of Pharmacy, MSC09 5360, 1 University of New Mexico, Albuquerque, NM 87131-0001.

MCD experiments. The iNOS oxyFMN proteins used for the MCD experiments have a A_{280}/A_{400} of 2.1-2.4. An optically transparent glass is required for low temperature MCD measurements. This was achieved by preparing the protein samples in 42% v/v ethylene glycol. The sample was centrifuged to remove any precipitate, if necessary. The final concentration of the NOS protein in the MCD sample cell was about 22 μM; buffer: 50 mM Tris-Cl, 200 mM NaCl, 1 mM DTT, 2 μM H_4B, pH 7.6. Low temperature MCD spectra were measured in an applied magnetic field of 7 T using a JASCO J-810 spectropolarimeter that is interfaced to a computer and an Oxford Instruments Spectromag 4000-7 split-coil superconducting magnet system.

EPR spectroscopy. EPR spectra of the frozen samples were recorded on a Bruker model EMX spectrometer operating at X-band (~9.4 GHz). A microwave power of 20 dB was used for all the iNOS experiments and spectra were collected at 4K for high spin heme proteins (S = 5/2) and 20 K for low spin heme proteins (S = ½) using a liquid helium flow cryostat. Computer simulations were accomplished using EasySpin software program [204].

4.5 Results and Analysis

4.5.1 Perturbations of MCD Spectra From Mutations in the FMN Domain (iNOSoxyFMN vs. E546N and E603N)

The variable temperature MCD (VT-MCD) spectra of the heme site in the as isolated iNOS oxyFMN construct and the mutants (E546N and E603N) were obtained at 5, 10, and 20K in a 7T applied magnetic field (Figures 4.7). Both wt and mutant constructs display temperature dependent MCD C-term bands allowing for analysis of saturation magnetization and/or EPR studies of both low (S = ½) and high spin (S = 5/2) forms of iNOS. MCD spectral overlays for the wt and mutant enzyme forms are presented in Figure 4.7(d). These spectra were collected at 5K and 7T and clearly show that there are differences between the wt and mutant forms. The Soret peak for E603N mutant is red shifted by about 240 cm^{-1} from the wt construct, whereas the Soret peak for E546N is red shifted by about 531 cm^{-1}.

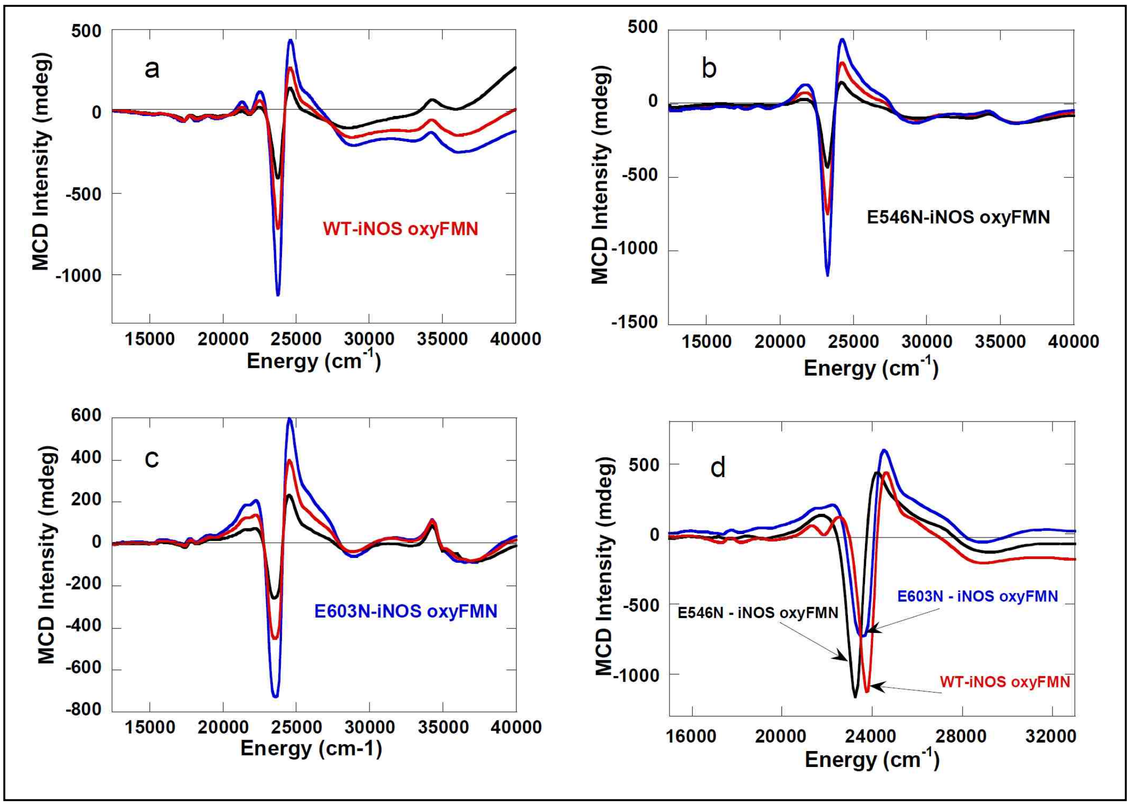

Figure 4.7: a, b and c are VT-MCD spectra recorded at 5, 10, 20K and 7T for the heme site in the as-isolated human iNOS oxyFMN construct whereas d represents an MCD overlay of wt-iNOS oxyFMN and mutants without L-arginine recorded at 5K and 7T.

These spectral shifts may be due to different distance dependences of amino acid residues around the heme site. In the crystal structure (Figure 4.23), E546 is closest to the heme domain, whereas E603 is farthest from the heme domain.

4.5.2 L-arginine Perturbations on the MCD Spectra of the iNOS oxyFMN, E564N, E603N and iNOS Oxygenase Domain

The variable temperature MCD (VT-MCD) spectra for wt-iNOS and the mutant (E546N and E603N) oxyFMN constructs with added L-arginine were collected at 5, 10, and 20K in a 7T applied magnetic field. These are presented in Figure 4.8.

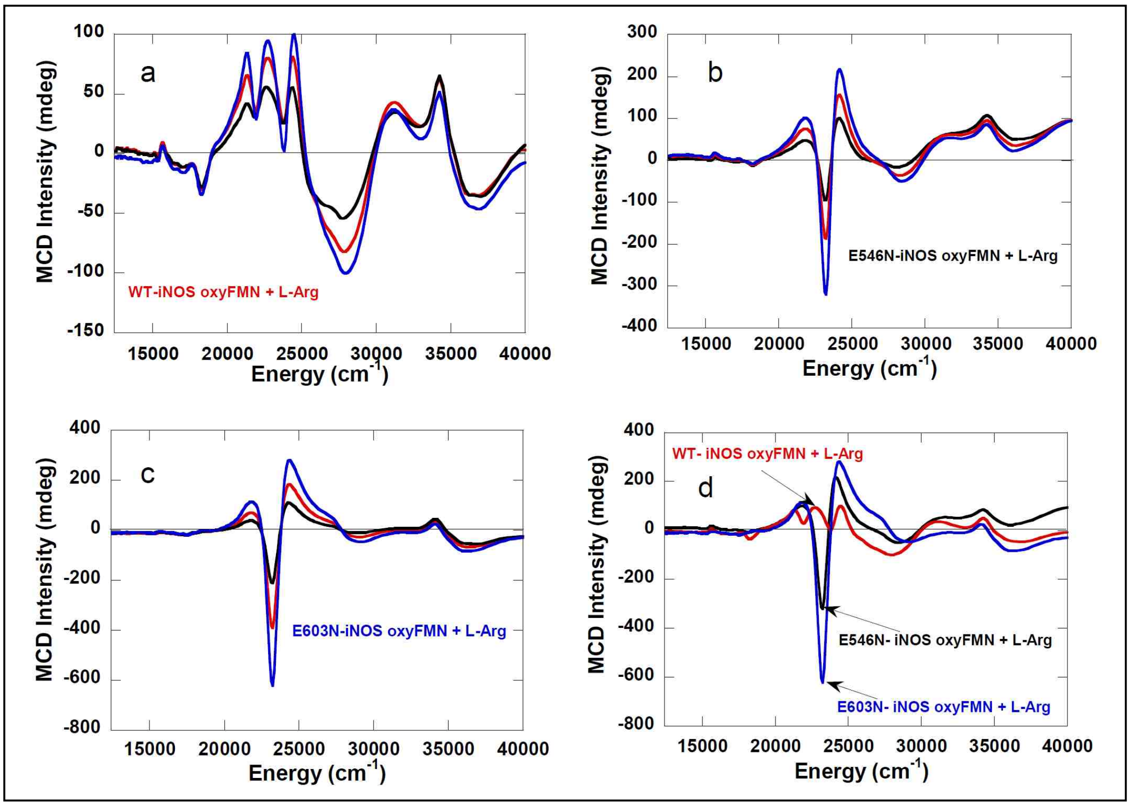

Figure 4.8: a, b and c are VT-MCD spectra recorded at 5, 10, 20K and 7T for the heme site in the as-isolated human iNOS oxyFMN construct with L-arginine

whereas d represents an MCD overlay of wt-iNOS oxyFMN and mutants with added L-arginine recorded at 5K and 7T.

The wt-oxyFMN also displayed different L-arginine binding effects at the heme domain compared to the mutants-oxyFMN and oxygenase domain only constructs.

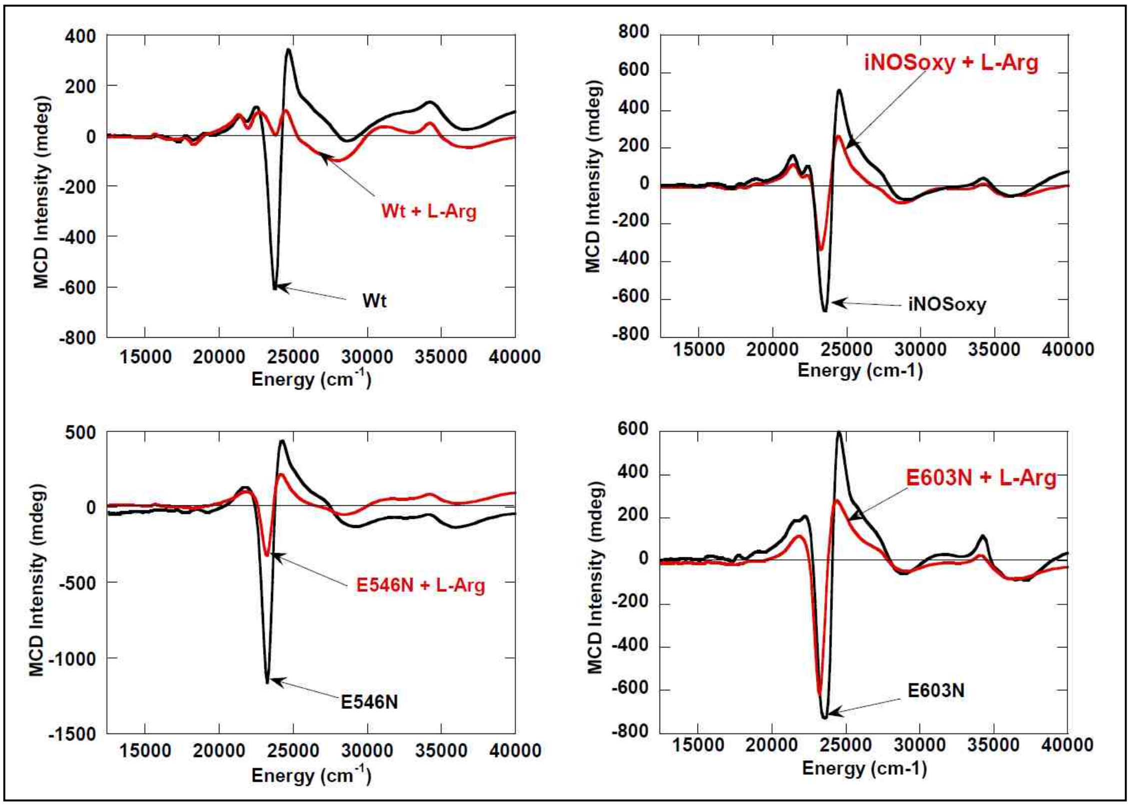

Figure 4.9: MCD overlays for wt-iNOS oxyFMN, wt-iNOS oxygenase and mutants without and with added L-arginine MCD spectra. The overlays were recorded at 5K and 7T.

The iNOS oxygenase domain has only the heme domain and not an FMN domain, so it's MCD spectrum was used as a control in the analysis of the FMN contributions to MCD spectral perturbations for oxyFMN constructs. Both wt and mutants oxyFMN constructs with added L-arginine showed temperature dependant MCD C-term behavior.

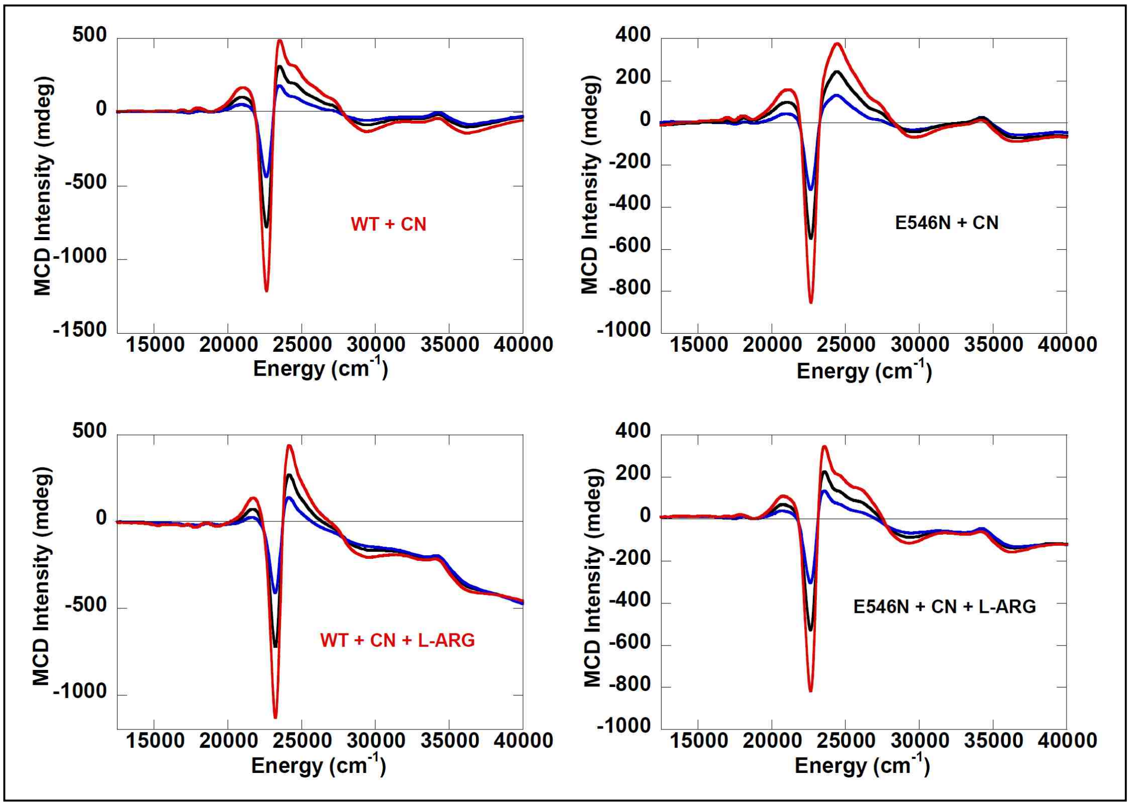

Figure 4.10: VT-MCD spectra recorded at 5, 10, 20K and 7T for the heme site of cyanide treated wt iNOS oxyFMN and mutant constructs with and without L-arginine.

However, it is noticed that the MCD spectrum of wt iNOS oxyFMN is highly perturbed upon incubation with the L-Arg substrate (Figure 4.8a) compared to the

MCD spectra for the E546N and E603N mutants (Figures 4.8b and c). The MCD overlay is presented in Figure 4.8d and clearly shows the markedly different spectra of the wt and mutant enzymes. The MCD spectrum of the iNOS oxygenase construct (only the heme domain, Figure 4.9; iNOSoxy + L-arg) indicated a small perturbation upon addition of L-arginine comparable to that of mutants. Figure 4.9 compares the MCD overlays for wt, mutants and oxygenase domains with and without L-arginine. Clearly, the spectral perturbation induced by L-Arg binding in the wt iNOS oxyFMN is completely absent in the iNOS oxygenase construct (possesses only a heme domain and no FMN) and the mutants (E546N and E603N).

MCD spectral perturbations induced by L-arginine were also studied by using the wt and mutant constructs of iNOS oxyFMN that have been treated with cyanide. Both cyanide treated wt and mutant oxyFMN constructs with and without added L-arginine displayed a temperature dependent MCD C-term features characteristic of only low spin heme (Figure 4.10). The MCD spectra also display no reduction in the magnitude of the Soret peak (~ 23,000 cm^{-1}) upon addition of L-arginine, indicating absence of conversion from low to high spin state for cyano adducts. EPR experiments confirmed that both cyano adducts with and without L-arginine are low spin hemes (Figures 4.20 and 4.21). Nonetheless, perturbations induced by L-arginine on the cyano adduct of wt iNOS oxyFMN construct resulted in a blue shift of its Soret peak (22615 to 23252 cm^{-1}) and this shift is not observed in the cyano adduct of the mutant with added L-arginine

(Figure 4.11). Taken together, these data strongly suggest a correlation between the L-Arg perturbation of the heme MCD spectrum and the existence of a properly aligned FMN domain in the FMN-heme complex of the wt iNOS protein.

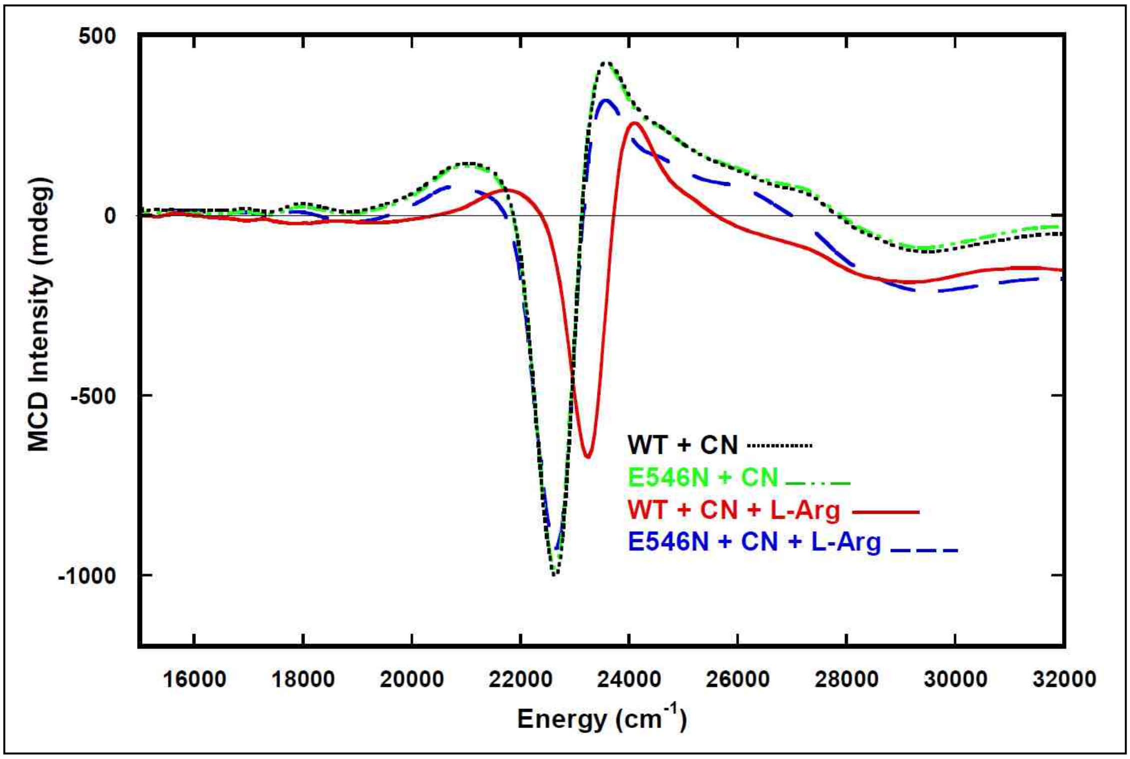

Figure 4.11: MCD overlays for wt-iNOS oxyFMN and E546N mutant cyano adducts without and with added L-arginine. MCD spectra overlays were recorded at 5K and 7T.

4.5.3 Perturbations of VTVH-MCD Spectra From Mutations in the FMN Domain (Wt-iNOS oxyFMN vs. E546N-iNOS oxyFMN)

The VTVH-MCD magnetization curves for the wt and as isolated mutant oxy FMN constructs were collected and compared in terms of the g values, zero field splitting parameters, and transition polarizations. The VTVH results were correlated with the spin Hamiltonian parameters obtained by EPR spectroscopy. However, the magnetization curve for the wt construct (Figure 4.10) shows nesting behavior indicative of a high spin ferric heme (S = 5/2), whereas the magnetization curve for the mutant (Figure 4.13) shows no nesting indicating the presence of predominantly low spin heme sites (S = ½). However, for the low spin Fe^{3+} heme (S = 1/2), there is no zero field splitting. The high spin Fe^{3+} heme has an 5/2 spin state and has the components Ms = ±1/2, ±3/2, ±5/2 which are degenerate (D = 0) at cubic symmetry. The degeneracy between these doublets is lifted when the ligand field is less than cubic and this results in a zero field splitting (D ≠ 0). For D > 0, the ±1/2 is lowest in energy and for D < 0 the ±5/2 is lowest in energy. Thus, VTVH spectral simulations for the high spin ferric heme (S = 5/2) resulted in a large zfs (D = 20 cm^{-1} with E/D = 0.08 cm^{-1}). EPR spectra (Figure 4.17) indicate that both wt and mutant are mixtures of high and low spin hemes. However, the heme center for the wt construct has a greater percentage of the high-spin form (Figure 4.12) than the low spin form, whereas the mutant E546N (Figure 4.13) has a greater percentage of low spin form than the high spin form. Thus VTVH-MCD spectral simulations for the as isolated wt and mutant forms were performed by considering 100% high spin heme for wt enzyme and

100% low spin Fe for the E546N mutant. Nonetheless, the spectral properties for the wt and mutant are different, indicating the role of E546 located in the FMN domain which facilitates FMN-heme interdomain electron transfer (IET) and the subsequent synthesis of NO.

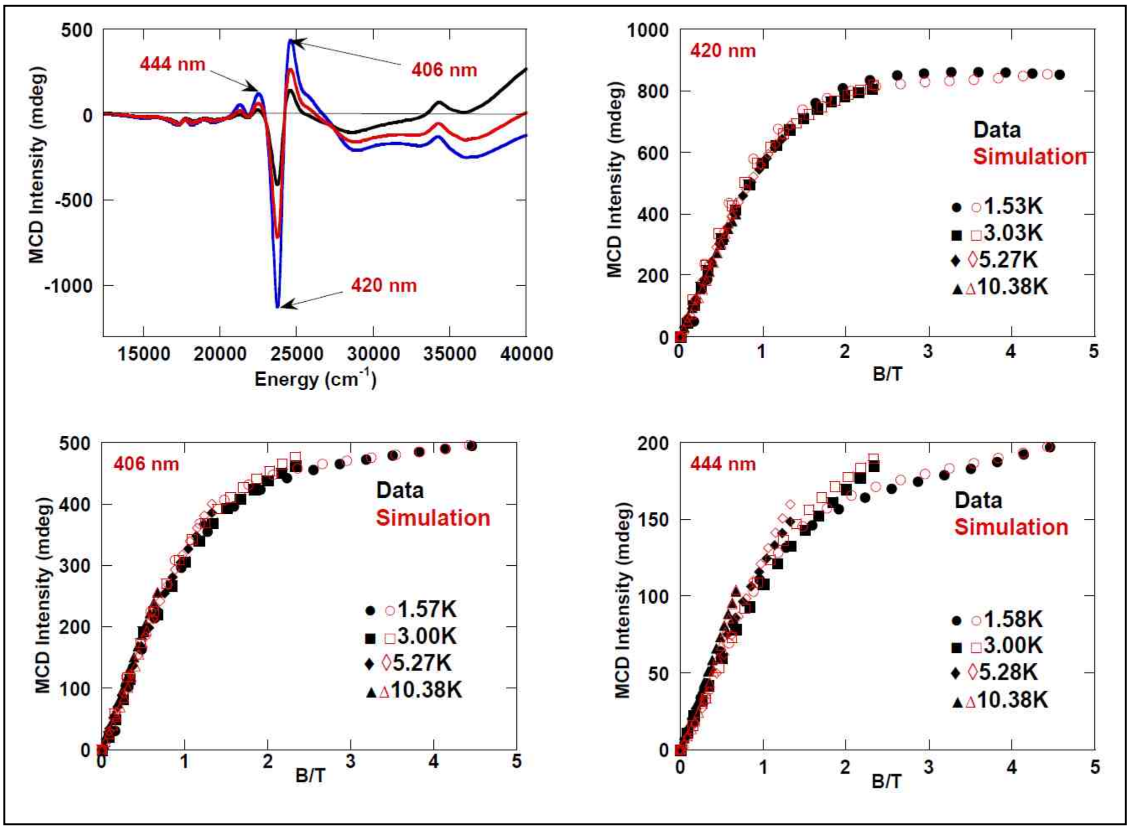

Figure 4.12: MCD magnetization curves for the as isolated wt human iNOS oxyFMN construct at 406, 420 and 444 nm without L-Arginine. Spectral simulation has been achieved with g_x = 2.003, g_y = 1.949, g_z = 2.015, S = 2.5, D=20 cm^{-1}, E/D = 0.08 cm^{-1}, Ax = Ay = Az = 0 cm^{-1}, Lx = 90, Ly = 40, Lz = 50; polarizations are: xy = 1.000, xz = 0.000, yz = -0.100 at 420 nm; xy = 1.000, xz = -0.010, yz = -0.08 at 406 nm, and xy = 1.000, xz = -0.030, yz = -0.040 at 444 nm.

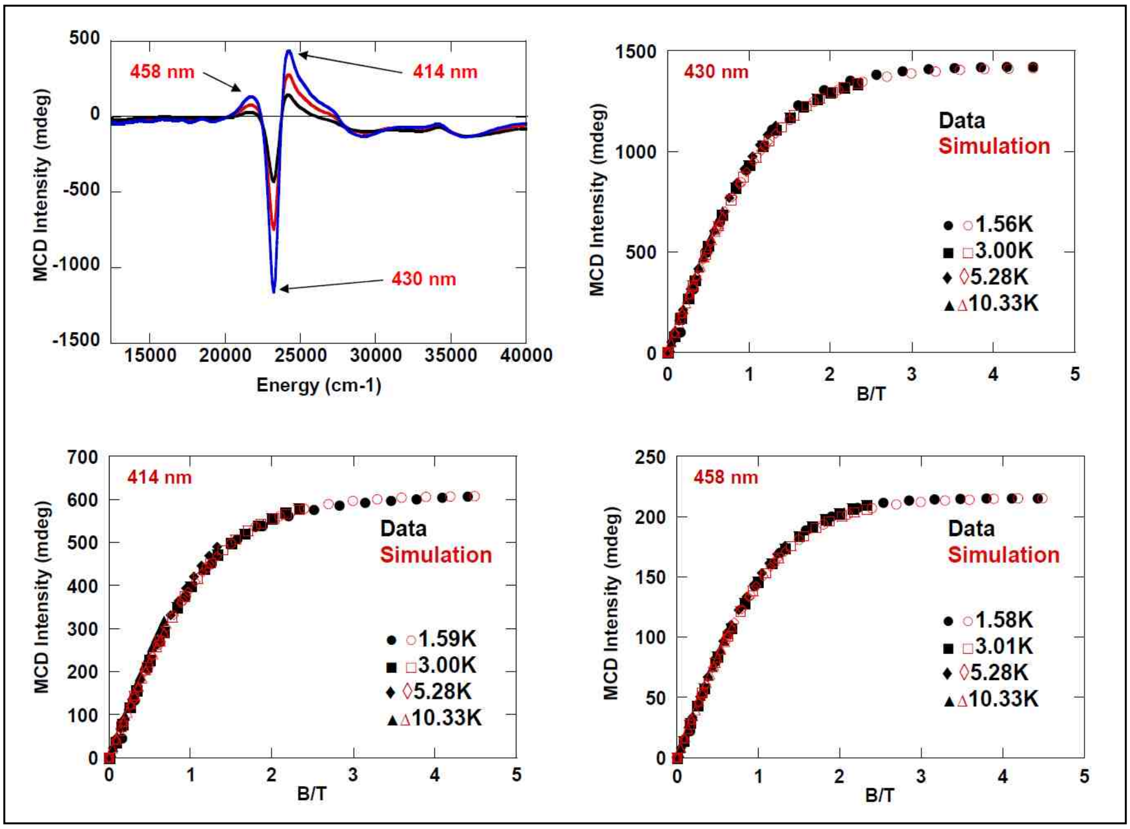

Figure 4.13: MCD magnetization curves for the as isolated E546N-iNOS oxyFMN construct at 414, 430 and 458 nm without L-Arginine. Spectral simulation has been achieved with $g_x = 2.6740$, $g_y = 2.3048$, $g_z = 1.8540$, S = 0.5, Ax = Ay = Az = 0 cm^{-1}, Lx = 60, Ly = 15, Lz = 110; polarizations are: xz at 430 nm; xz at 414 nm, and xy at 458 nm.

4.5.4 L-arginine Perturbations on the VTVH-MCD of iNOSoxyFMN, E564N, and E603N

The wt-iNOS oxyFMN with added L-arginine magnetization curves displayed different L-arginine binding effects as determined from thier g values, zero field splitting parameters, and transition polarizations when compared to mutant oxyFMN constructs with added L-arginine. Analysis of the EPR data indicated variations in spin composition of low and high spin states forms between wt and mutants (Figure 4.17 and 4.18). Here, the magnetization curve for the wt construct (Figure 4.14) shows a very small nesting and a large zero field splitting (zfs). I’ts corresponding EPR spectrum (Figure 4.18 and 4.19) indicates that the heme center is predominantly a high-spin form. On the other hand, the mutant (E546N) magnetization curve (Figure 4.15) shows a higher degree of nesting than the wt, indicating a relatively smaller zfs value and the greater presence of the high spin state form ($S = 5/2$) than the low spin state form ($S = ½$). The EPR spectrum for the mutant (Figure 4.16) still indicates the presence of a small percentage low spin state heme. VTVH spectral simulations were performed assuming 100% composition of high spin ferric heme for both wt and mutant. The VTVH simulations gave D of 20 cm^{-1} and an E/D of 0.08 cm^{-1} for the wt compared to a D of 18 cm^{-1} and an E/D value of 0.08 cm^{-1} for the mutant. VTVH-MCD simulations for the E603N mutant (Figure 4.16) gave a D value of 22 cm^{-1} and an E/D of 0.08 cm^{-1}. In general, this observation correlates directly with the observed MCD perturbations upon addition of L-arginine and the MCD spectral features are associated with conversion of low spin to high spin states. Thus, these results explain the key roles played by E546 and E603 in the productive FMN-heme interdomain interaction of iNOS.

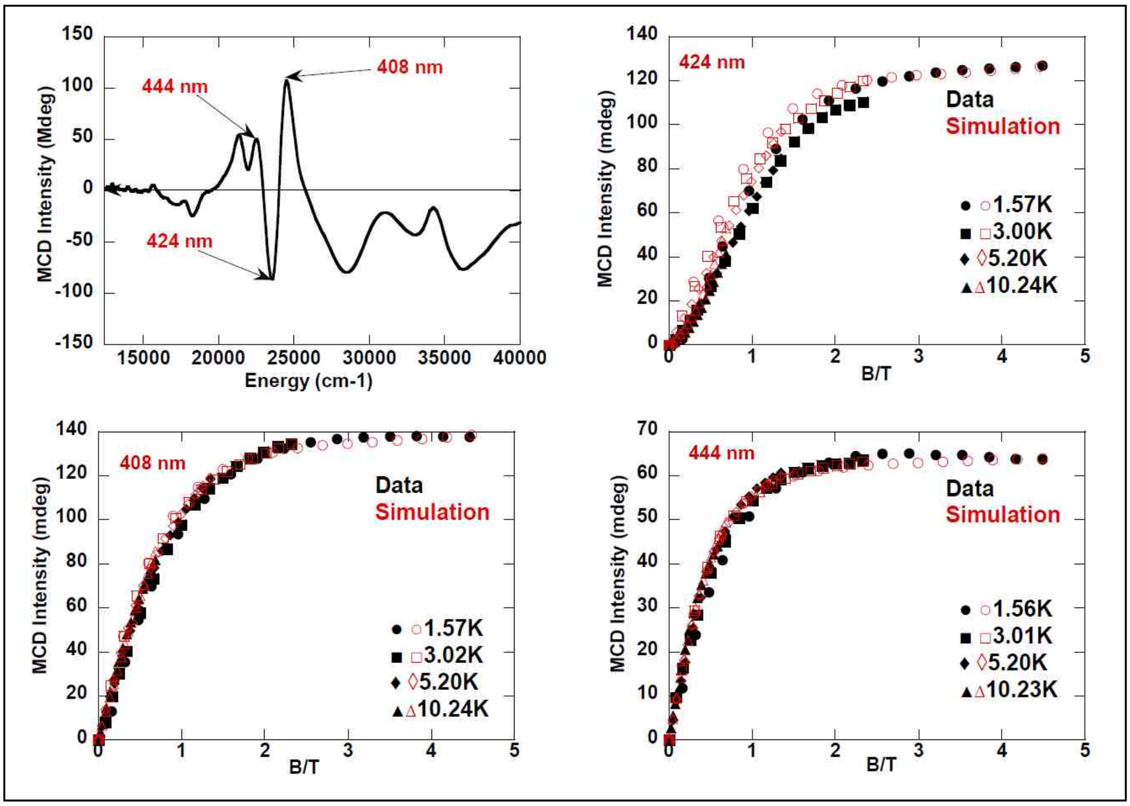

Figure 4.14: MCD magnetization curves of the as isolated wt human iNOS oxyFMN construct at 408, 424 and 444 nm with added L-Arginine. Spectral simulation has been achieved with $g_x = 2.020$, $g_y = 1.949$, $g_z = 2.024$, S = 2.5, D = 20 cm^{-1}, E/D = 0.08 cm^{-1}, Ax = Ay = Az = 0 cm^{-1}, Lx = 90, Ly = 40, Lz = 50; polarizations are: xy = 1.000, xz = -0.010, yz = -0.100 at 424 nm; xy = 1.000, xz = 0.019, yz = 0.100 at 408 nm, and xy = 1.000, xz = 0.140, yz = -0.130 at 444 nm.

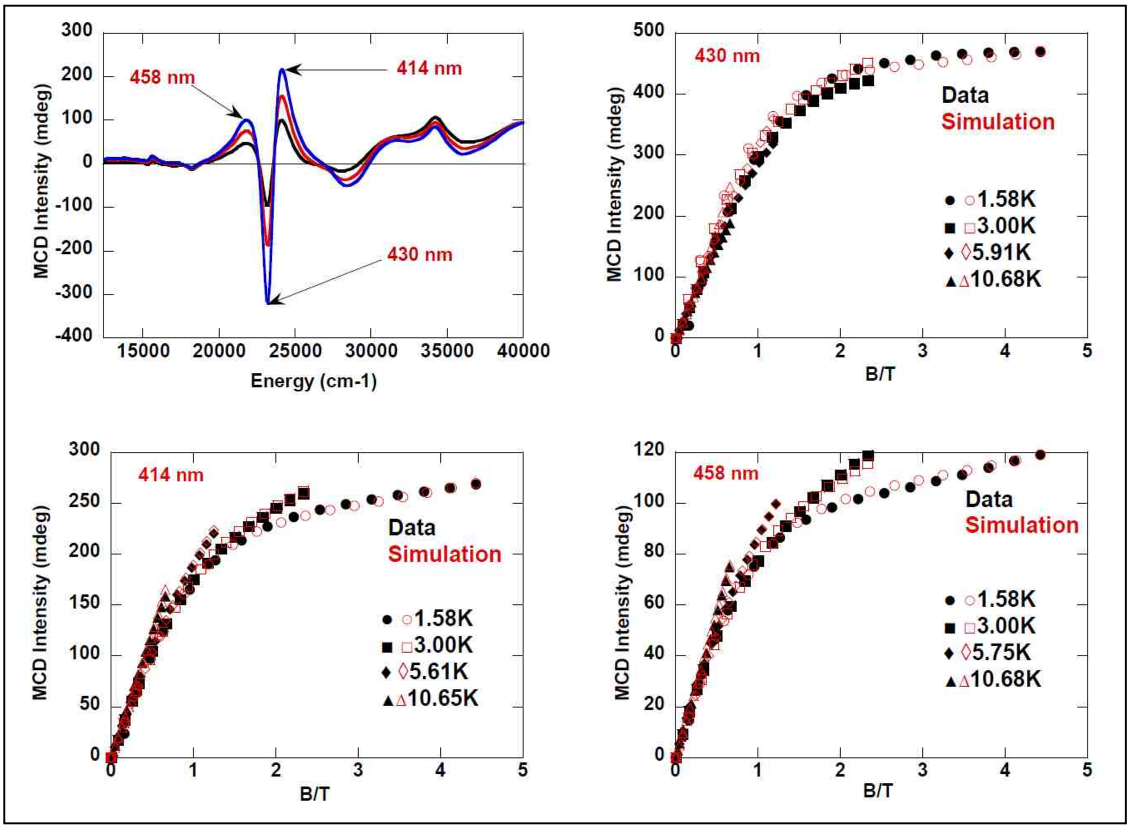

Figure 4.15: MCD magnetization curves of the as isolated E546N-iNOS oxyFMN construct at 414, 430 and 458 nm with added L-Arginine. Spectral simulation has been achieved with g_x = 2.030, g_y = 1.949, g_z = 2.030, S = 2.5, D = 18 cm^{-1}, E/D = 0.08 cm^{-1}, Ax = Ay = Az = 0 cm^{-1}, Lx = 90, Ly = 40, Lz = 50; polarizations are: xy = 1.000, xz = 0.000, yz = -0.100 at 430 nm, xy = 1.000, xz = -0.012, yz = -0.050 at 414 nm, and xy = 1.000, xz = -0.010, yz = -0.040 at 458 nm.

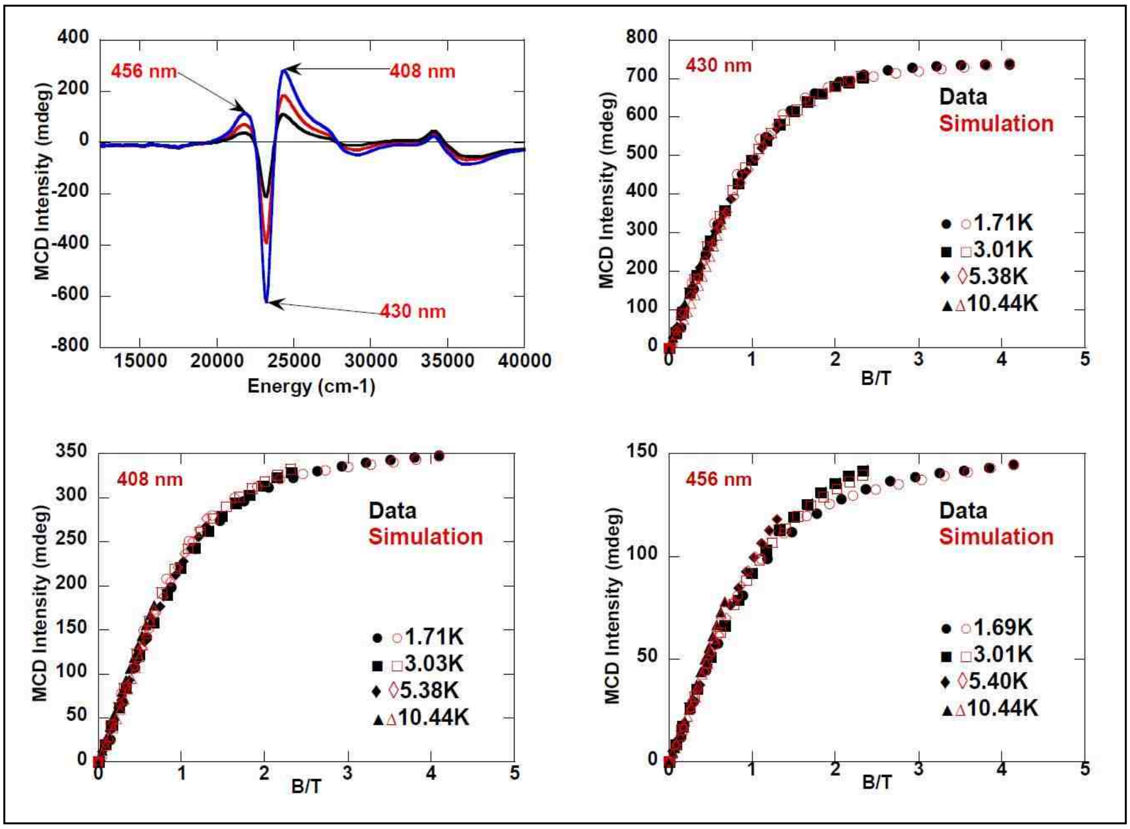

Figure 4.16: MCD magnetization curves of the as isolated E603N-iNOS oxyFMN construct at 408, 430 and 456 nm with added L-Arginine. Spectral simulation has been achieved with g_x = 2.0030, g_y = 1.9600, g_z = 2.0092, S = 2.5, D = 22 cm^{-1}, E/D = 0.08 cm^{-1}, Ax = Ay = Az = 0 cm^{-1}; polarizations are: xy = 1.000, xz = -0.008, yz = -0.090 at 430 nm; xy = 1.000, xz = -0.010, yz = -0.080 at 408 nm, and xy = 1.000, xz = -0.020, yz = -0.050 at 456 nm.

4.5.5 L-arginine Perturbations on the EPR Spectra of Wt-iNOSoxyFMN and the E564N Mutant

The final experimental analysis of iNOS heme spin states in wt and mutant oxyFMN constructs,as a function of L-arginine was probed using EPR spectroscopy in order to determine their spin Hamiltonian parameters. EPR is useful in providing information about heme symmetry, identifying heme ligands, and in understanding the electronic structure of the heme site. It possesses much higher sensitivity for determining heme symmetry than other spectroscopic methods, and this makes it a very useful tool in delineating the structural perturbations caused by the binding nature of axial ligands.

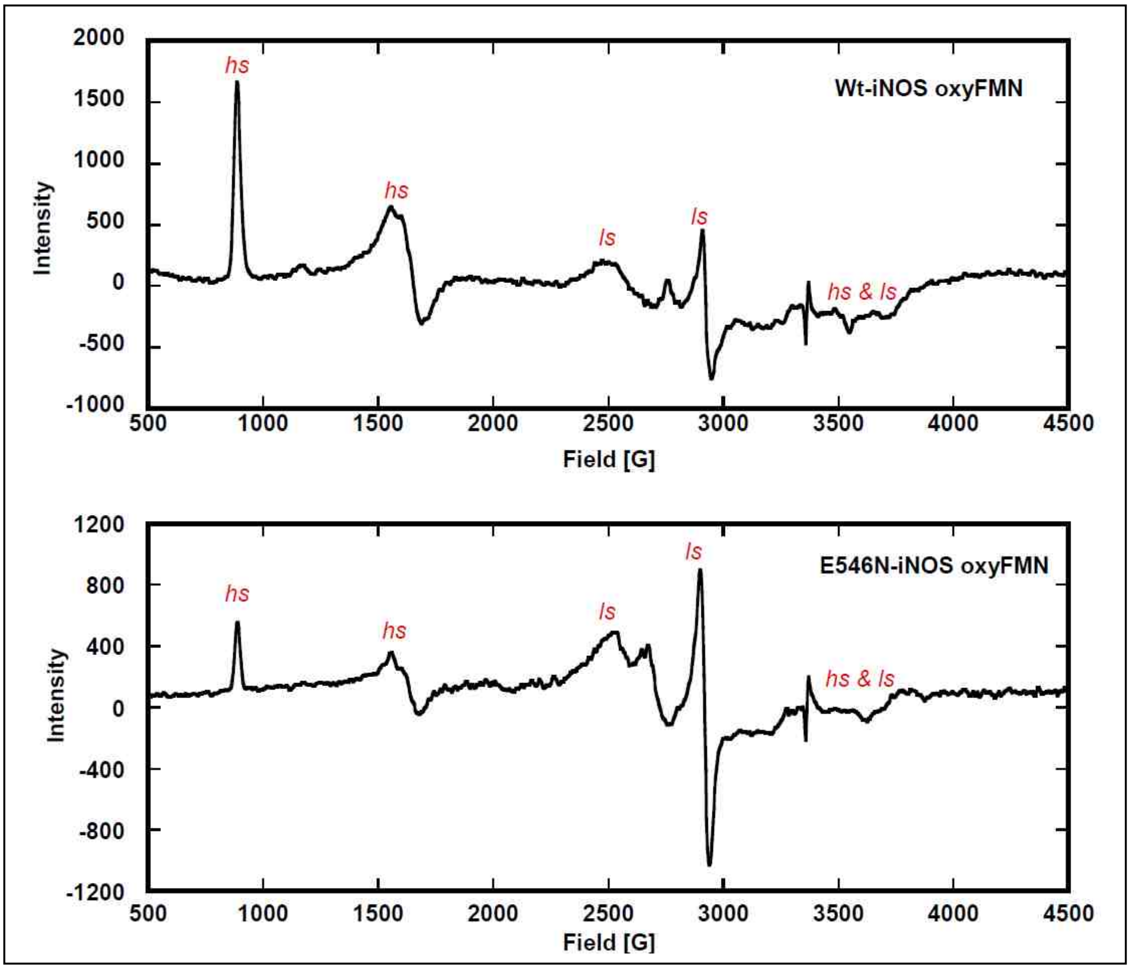

Figure 4.17: EPR spectra collected at 20K for wt-iNOS oxyFMN (top) and E546N mutant (bottom) without L-arginine showing a mixture of low and high spin states. Notice the relative ratios of low and high spin states for wt and mutant forms.

Both wt and mutant enzyme without L-arginine were shown to be mixtures of low and high spin states. The EPR spectrum for wt-iNOS oxyFMN taken at 20K indicates a greater percentage of the high spin state (S = 5/2) than the low spin state (S = ½), whereas the mutant (E546N-iNOS oxyFMN) EPR spectrum collected at the same temperature, contains a greater percentage of low spin state than high spin state (Figure 4.17).

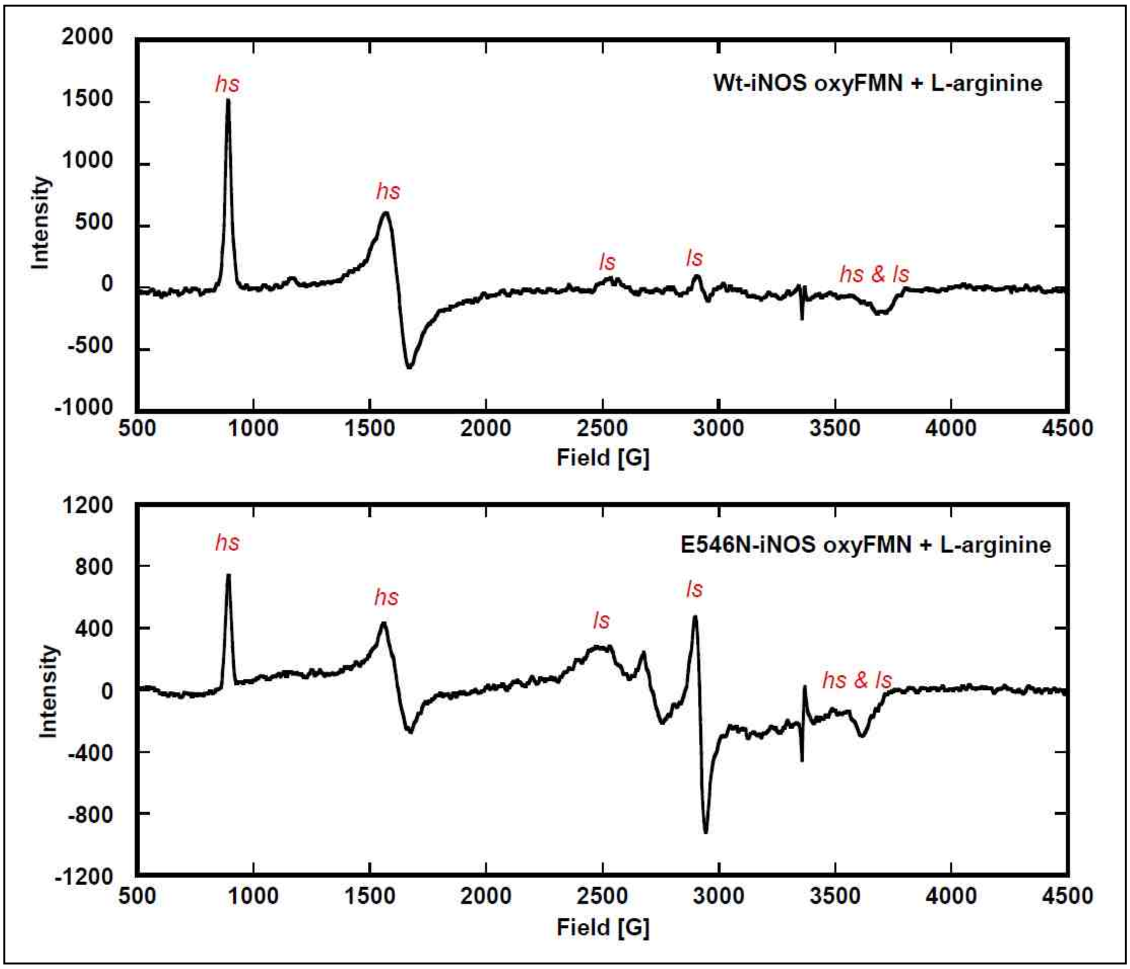

Figure 4.18: EPR spectra collected at 20K for wt-iNOS oxyFMN (top) and E546N mutant (bottom) with added L-arginine showing ratios of low and high spin states

present. Notice the wt is predominantly a high spin heme whereas the mutant still has both low and high spin states.

The EPR spectrum of wt-iNOS oxyFMN with added L-arginine indicates that binding of L-Arg near the wt construct heme center results in its conversion to a predominantly high-spin form (Figure 4.18). The EPR spectrum for the L-Arg-bound mutant (E546N) still indicates a low-spin (S = ½) heme is present.

These EPR results indicating the composition of low and high spin states for the wt and mutants with and without L-arginine directly correlates with observed spectral changes in the MCD and VTVH-MCD spectra presented in the previous sections. The relaxation behavior of the high and low spin heme EPR are different [193-195]. However, the high spin state becomes well resolved at 4K (Figure 4.19) whereas the low spin has its maximum intensity at 20K. Thus, the spin Hamiltonian parameters for the high and low spin states can best be analyzed at 4 and 20K respectively. The marked difference in relaxation behavior of the two species reflects the different mechanisms that dominate in each case. The low spin center relaxes via a Raman relaxation process and exhibits an approximate T^7 temperature dependence arising from the low frequency modulation of the orbital magnetism [193-195]. The relaxation of the high spin heme is dominated by coupling to nearby Kramer’s doublets, and this is an Orbach relaxation process [195,196,197]. Treatment of the wt and mutant constructs with cyanide converts the high spin state of the heme to exclusively low spin (Figure 4.20), and thus avoids these issues.

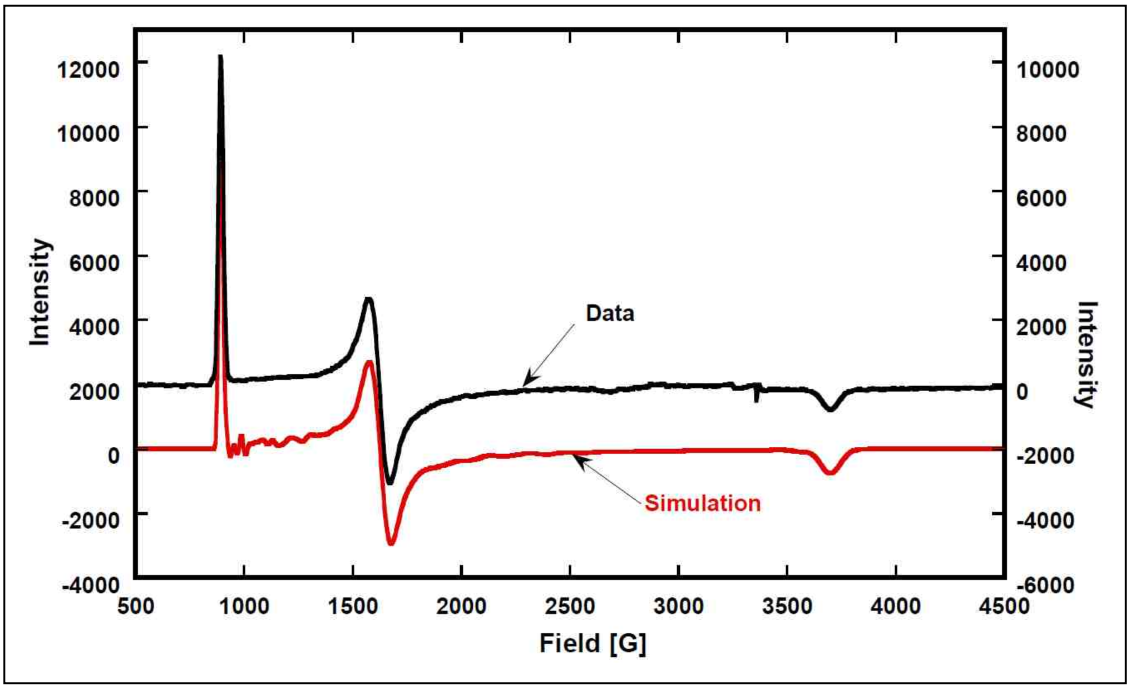

Figure 4.19: Data and simulation EPR spectra overlays for wt human iNOS oxyFMN construct with added L-Arginine. Spectral simulation has been achieved with g_x = 2.020, g_y = 1.949, g_z = 2.024, S = 2.5, D = 20 cm^{-1}, E/D = 0.08 cm^{-1}, Ax = Ay = Az = 0 cm^{-1}, Lx = 90, Ly = 40, Lz = 50. These values are the same ones used for the VTVH-MCD simulation for wt construct with added L-arginine (Figure 4.17).

Further analysis of the L-arginine perturbations on the EPR spectra of the cyano adducts of wt and mutant was performed. Since cyanide is a strong field ligand π

acceptor ligand, its treatment with the wt and mutant converts the heme sites to exclusively low spin states.

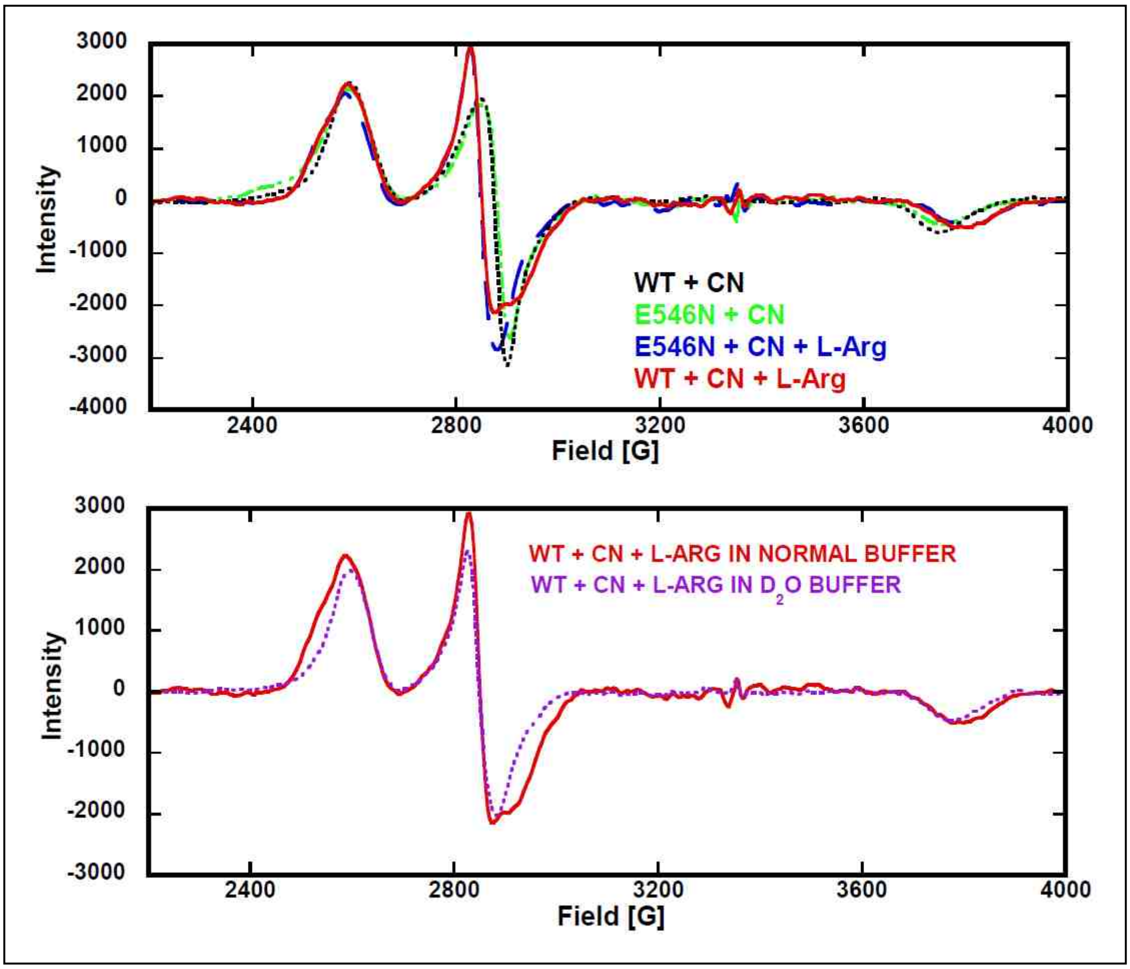

Figure 4.20: EPR spectra overlays for the cyanide treated wt human iNOS oxyFMN and E546N mutant construct with and without L-arginine (top). Bottom; EPR overlays between wt construct in normal buffer and in deuterated buffer. Notice, the asymmetrical splitting at g_2 position disappears in deuterated buffer.

Thus the cyano adducts with and without L-arginine both give characteristic low spin EPR and MCD spectra. The results also indicate similar shifts of g_2 and g_3

values for both wt and mutant with cyanide upon treatment with L-arginine (Figure 4.21).

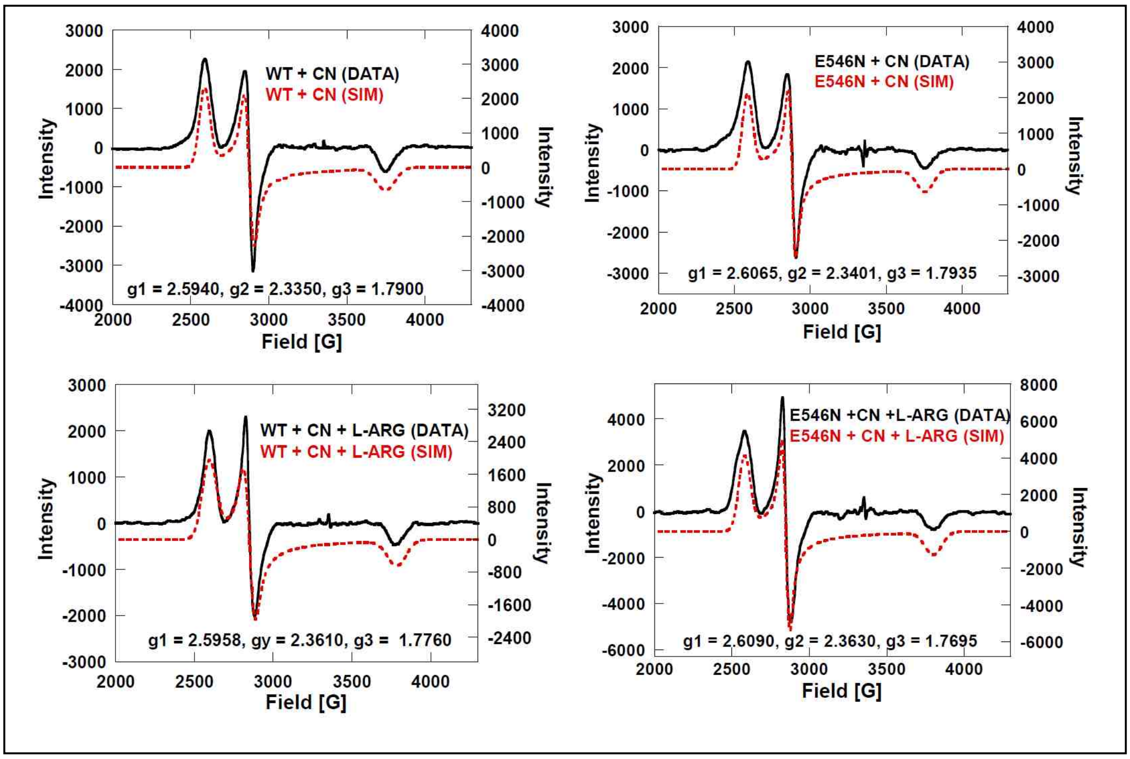

Figure 4.21: Data and simulation EPR spectra overlays for cyano-wt human iNOS oxyFMN construct and cyano- E546N mutant with and without added L-Arginine. Notice that the g values for the mutant are slightly higher than the wt construct.

The cyano adducts with added L-arginine are more rhombic than the cyano adducts without L-arginine as recognized by the larger separation between g_2 and g_3. Furthermore, all cyanide bound wt and mutant constructs with and without L-arginine have characteristic broad EPR resonances which have been implicated by binding of a water molecule at the active site. However, the wt construct possesses a more pronounced asymmetric splitting at the g_2 position than is observed in the mutant, which we associate it to a different mode of L-arginine binding at the wt heme site leading to a greater interaction with a water molecule. This splitting disappears when the reaction is carried out in deuterated buffer (Figure 4.20, bottom spectrum).

4.6 Discussion

4.6.1 L-arginine Perturbations on Wt-iNOS oxyFMN and E546N-iNOS oxyFMN

In this study, both as isolated wt and mutant forms are mixtures of low (S = ½) and high spin (S = 5/2) Fe^{3+} states. However, the ratio between the two spin states in the wt and mutants are different. The wt is dominatly high spin whereas the mutant is dominatly the low spin. EPR and MCD spectroscopic studies indicate that the substrate, L- arginine, converts the wt to an exclusively high spin state, whereas the mutant still possesses a greater percentage of low spin heme. Combination of the VTVH-MCD and EPR spectroscopic studies enabled the determination of the intrinsic values of the high spin heme spin Hamiltonian parameters by computer simulations. These values have not been reported previously. Tsai and co-workers reported characterization of the heme structure of eNOS by EPR spectroscopy on 16 heme complexes formed with different ligands including L-arginine. It was also observed that L-arginine converts the resting state of eNOS to an exclusively high spin state [198]. A similar observation was also reported by Salerno and co-workers using EPR [199]. Berka and co-workers observed similar a perturbation on the MCD spectrum of a heme complex formed with L-arginine for eNOS. The reduction in the amplitude of the Soret peak upon treatment with L-arginine indicates conversion from the low spin to the high spin state as confirmed by EPR spectroscopy [200]. The MCD spectra of as isolated iNOS oxyFMN and L-arginine-treated enzyme also closely resemble those reported for nNOS and those of 5-coordinate $P450_{cam}$ and chloroperoxidase [201]. The VTVH-MCD experiments in these investigations gave very large zero field splitting with $D = 20\ cm^{-1}$ for the wt with added L-arginine and $D = 18\ cm^{-1}$ for the mutant (E546N) with added L-arginine contrary to the $D = 5.7\ cm^{-1}$ for nNOS L-arginine complex reported by Galli and co-workers using EPR spectroscopy [202]. The zero-field splitting of the heme in nNOS with added L-arginine [202] was determined by measuring the integrated intensity of the heme iron g_x EPR transition as a function of temperature. We attribute the differences between the wt and the mutant zero field splitting parameters as being due to differences in the binding modes of L-arginine in the wt and mutant heme sites caused by disruption of the electrostatic interaction at the mutant heme site that facilitate inter-electron transfer between FMN and heme domains.

4.6.2 L-arginine Perturbations on Wt-iNOS oxyFMN and E546N-iNOS oxyFMN Cyanide Complexes

The catalytic conversion of L-arginine to nitric oxide (NO) and citrulline by NOS enzymes is a two-step mechanism (scheme 4.1) that requires binding of molecular oxygen to an Fe^{2+} heme complex obtained upon reduction of the heme from Fe^{3+} to Fe^{2+}. This oxygenated heme Fe^{2+} intermediate complex is similar to that of P450cam, hemoglobins, and myoglobins [203]. It has been proposed that the oxy-heme complex (Fe^{2+}-O=O) rearranges to a ferric superoxo complex (Fe^{3+}-O-O^{-}) to facilitate ligand binding followed by auto-oxidation to products, NO and L-citrulline. In P450cam, which has many of the same characteristics as NOS enzymes, cyanide has been reported to bind isosterically with oxygen and has a negative charge at the nitrogen atom. [203] Therefore, cyanide is a good oxygen mimic in the superoxide form when bound to the low spin Fe^{3+} heme. Figure 4.22 compares the ligand field splitting of β-orbitals obtained from spin unrestricted DFT calculations for L-arginine, CN^{-} and CN^{-}.L-arginine bound at the heme site. Input geometries were adapted from the crystal structures and the ligands positions in the complexes were frozen to mimic those observed in the crystal structures (PDB 3NOS for bound L-arginine in eNOS and PDB 1N2N for bound CN^{-} and L-arginine in iNOS oxy). Figures 4.23 and 4.24 show these geometries and the spin density maps respectively. Cyanide binds directly to the heme iron resulting in a low spin heme complex with the electron residing in a d_{yz} orbital, while L-arginine induces the formation of a high spin complex by indirectly perturbing the heme structure. For the high spin L-arginine bound heme, the electrons are residing in all five d-orbitals. Consequently, the ligand field splitting energy (the energy between the lowest (most stable) and the highest (least stable) d-orbitals) for L-arginine bound to the high spin heme is 12340 cm^{-1} which is much smaller than the ligand field splitting energies for CN^{-} and CN^{-}. L-arginine bound heme which are 50249 cm^{-1} and 52910 cm^{-1} respectively. Thus, analysis of the wild type iNOS oxyFMN and mutant cyanide complexes with and without L-arginine gave the expected characteristic low spin Fe^{3+} heme EPR spectra (Figure 4.17). The cyanide complex of iNOS- oxyFMN with added L-arginine and the cyanide complex of the mutant (E546N) with added L-arginine gave characteristic broad EPR spectra possessing asymmetric splitting at the g_2 position. We have associated this splitting with the nearby water molecule that couples to the Fe^{3+} low spin heme center but failed to account for its asymmetric splitting nature.

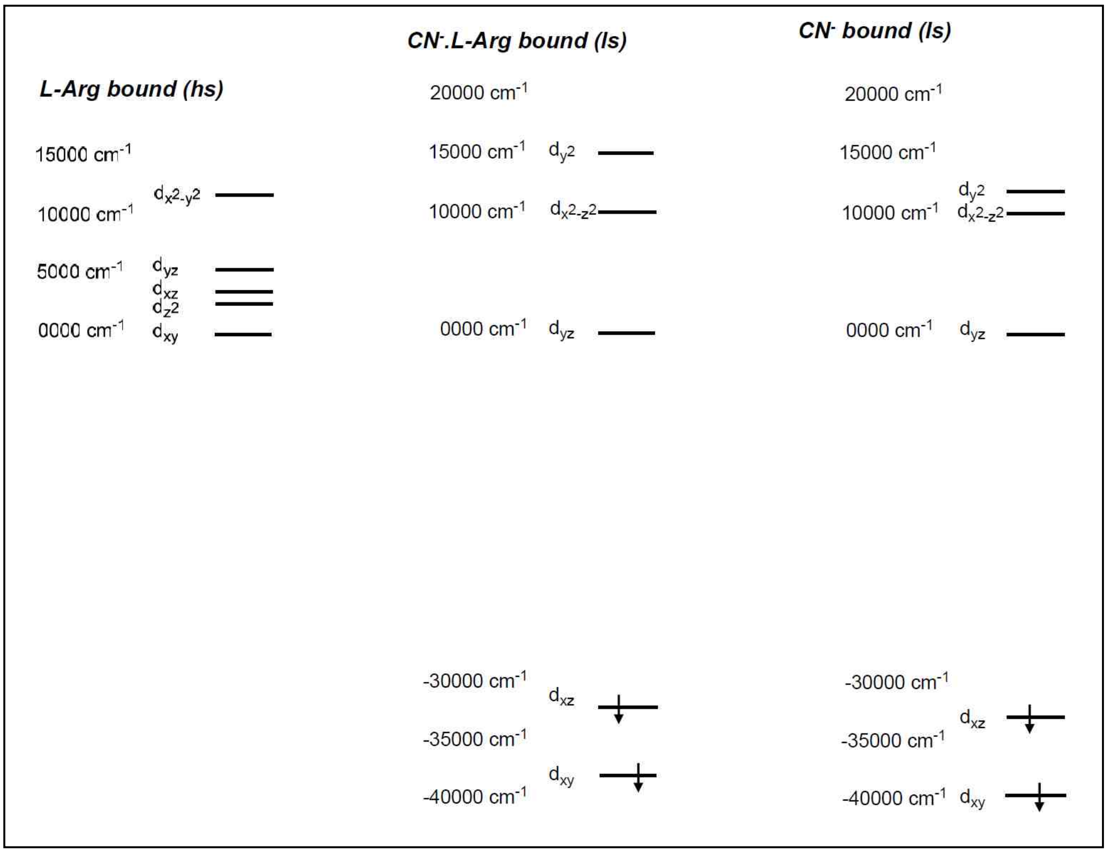
L-Arg bound (hs)
15000 cm-1
10000 cm-1
5000 cm-1
0000 cm-1
dx2-y2
dyz
dxz
dz2
dxy
CN-.L-Arg bound (ls)
20000 cm-1
15000 cm-1
10000 cm-1
0000 cm-1
-30000 cm-1
-35000 cm-1
-40000 cm-1
dy2
dx2-z2
dyz
dxz
dxy
CN- bound (ls)
20000 cm-1
15000 cm-1
10000 cm-1
0000 cm-1
-30000 cm-1
-35000 cm-1
-40000 cm-1
dy2
dx2-z2
dyz
dxz
dxy

Figure 4.22: Calculated molecular orbital energies for L-arginine, CN$^-$ and CN$^-$.L-arginine bound at the Fe^{3+} heme site for iNOS. The ligand field splitting energies are 12340 cm^{-1} for L-arginine, 50249 cm^{-1} for CN^{-1} and 52910 cm^{-1} CN$^-$.L-arginine. The molecular orbital energies have been normalized to LUMO+2 which is the first unoccupied metal orbital.

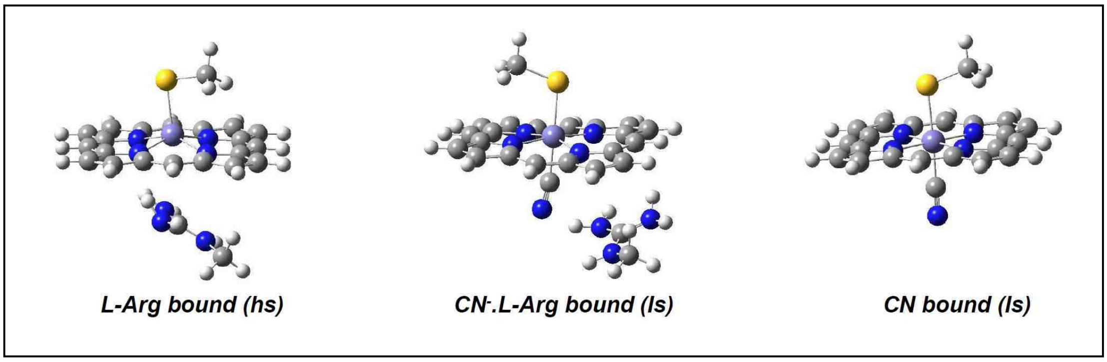
L-Arg bound (hs)
CN-.L-Arg bound (ls)
CN bound (ls)

Figure 4.23: Optimized geometries for computational model compounds of L-arginine (high spin), CN$^-$.L-arginine (low spin), CN$^-$ (low spin) and bound at the Fe^{3+} heme site. Note: L-arginine does not bind directly to the Fe^{3+} heme site.

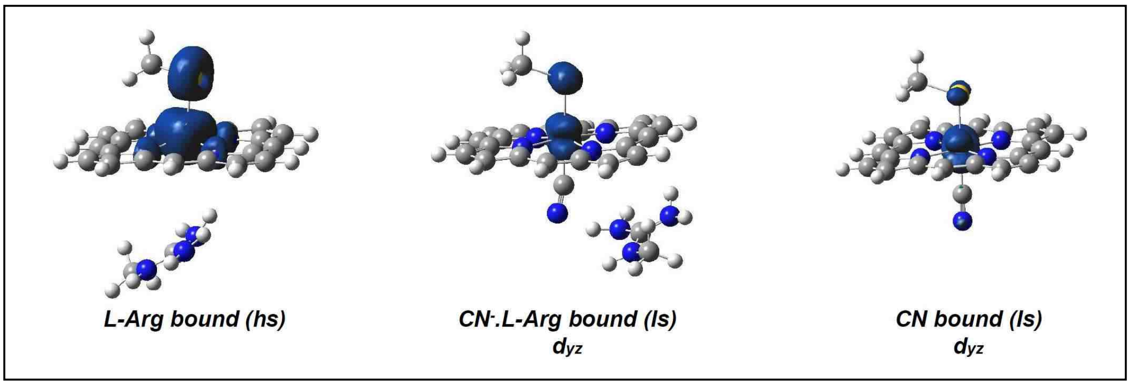
L-Arg bound (hs)
CN-.L-Arg bound (ls)
dyz
CN bound (ls)
dyz

Figure 4.24: Calculated spin densities for L-arginine (high spin), CN^-.L-arginine (low spin) and CN^- (low spin) and bound at the Fe^{3+} heme site. Notice: the spin density for low spin CN^- and CN^-.L-arginine bound is in the d_{yz} type orbital.

Fedorov and co-workers observed that the interaction of cyanide with L-arginine in the iNOS oxy construct induces the binding of a water molecule at the active site and is located 2.8Å from the nitrogen atom of the cyanide. Since the splitting of the wt iNOS oxyFMN construct is greater than the mutant, we attribute this effect as being due to a reduced L-arginine perturbation in the cyanide complex of the mutant caused by a disruption of electrostatic interactions between the heme and FMN domains.

4.6.3 Nature of Interdomain FMN - Heme Interactions with L-arginine Binding

The FMN cofactor of nitric-oxide synthase (NOS) plays a major role of transferring NADPH-derived electrons to the enzyme heme active site for use in oxygen activation and eventually NO synthesis from oxidation of L-arginine. This work provides considerable new spectroscopic information indicating how the docked FMN domain affects the nature of interactions between the L-Arg substrate and the catalytic heme center located in an adjacent domain in iNOS. These FMN domain and heme interaction studies are based on earlier work done by Panda et al., using a mutational and kinetics study that indicated the involvement of the equivalent FMN sites (E762, E819) in rat nNOS FMN/FAD alignment [184]. The crystal structure shows that the face of the FMN domain that interacts with heme is electronegative, whereas the complementary interacting surface is electropositive (Figure 4.25). This implies that charge interactions enable function. However, the output state is likely promoted and stabilized by electrostatic interactions between conserved, charged surface residues of the FMN and oxygenase domains (Figure 4.26) which are facilitated by CaM binding.

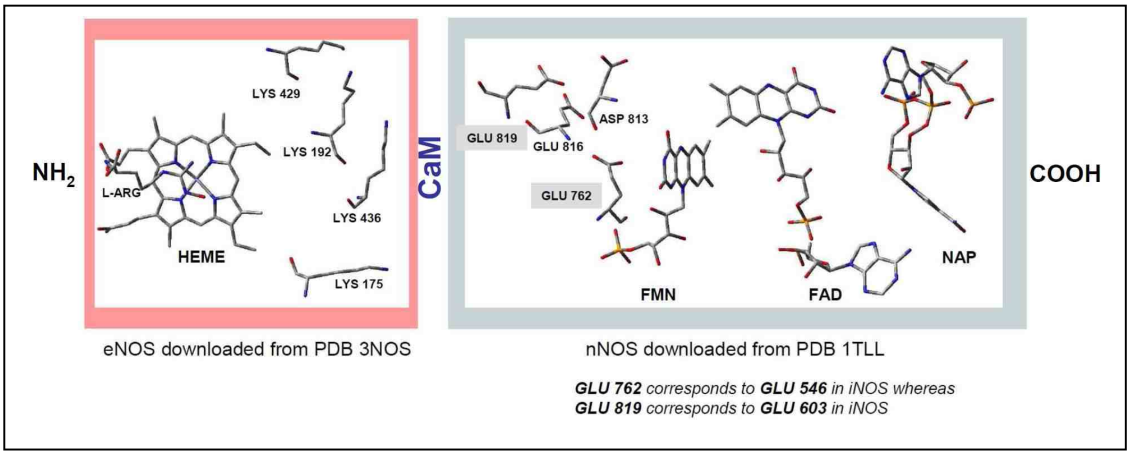

eNOS downloaded from PDB 3NOS

nNOS downloaded from PDB 1TLL

GLU 762 *corresponds to* ***GLU 546*** *in iNOS whereas*
GLU 819 *corresponds to* ***GLU 603*** *in iNOS*

Figure 4.25: Representations of selected positively charged surface residues at the back face of the heme in a human eNOS oxygenase domain (left, downloaded from PDB; 3NOS), and the negatively charged surface residues near the FMN edge in a rat nNOS reductase construct (downloaded from PDB; 1TLL). GLU 762 in nNOS corresponds to GLU 546 in iNOS whereas GLU 819 in nNOS corresponds to GLU 603. The charged surface residues are conserved in NOS isoforms.

Site-directed mutagenesis has been used to investigate the roles of six electronegative surface residues of the FMN domain in electron transfer and catalysis in neuronal NOS indicated that neutralizing or reversing the negative charge of each residue altered the NO synthesis. However, the largest effects occurred at the NOS-specific charged residue Glu762 [184] which is equivalent to Glu 546 in iNOS at the FMN domain.

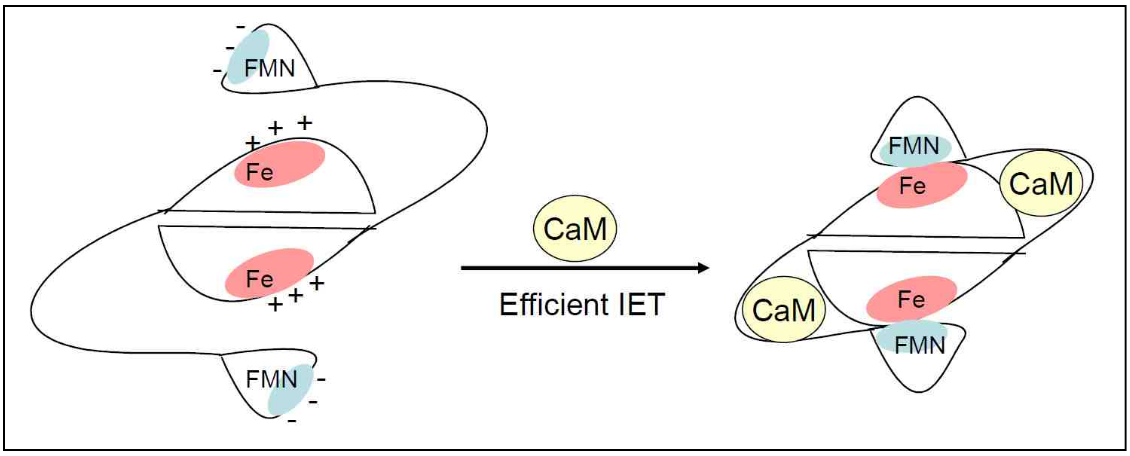

Figure 4.26: Electrostatic interactions between the FMN (blue, negative) and heme (red, positive) domains guide the CaM-induced docking, resulting in formation of the IET-competent FMN/heme complex (output state). The FAD and NADPH cofactors are omitted for clarity.

These investigations indicate that binding of L-arginine to the mutants induces less perturbation to the heme site than binding of L-arginine to the wild type construct. This large perturbation of the heme site in the wild type construct suggests the interaction of the heme domain to a properly docked FMN domain. It is therefore suggested from this work that charge neutralization of E546 and E603 sites disrupt complementary electrostatic interdomain FMN-heme interactions, disturb the FMN-heme complex, and thereby diminish the L-Arg perturbation [1] (Figure 4.27). This disruption should alter the NO synthesis in iNOS as observed by Panda and co-workers in their nNOS mutation studies.

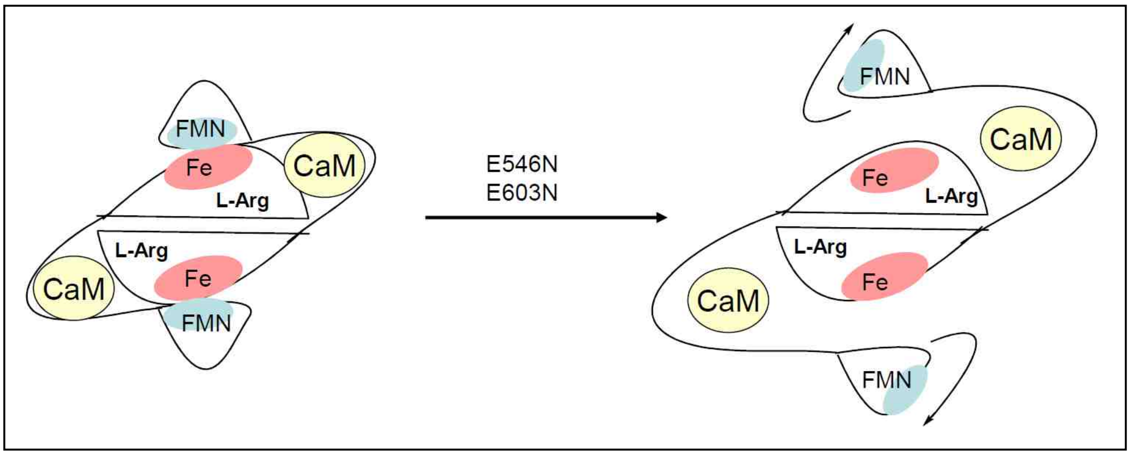

Figure 4.27: Schematic diagram of the truncated bidomain oxyFMN construct of human iNOS (left). Charge neutralization mutation at E546 or E603 of the FMN domain diminishes the L-Arg perturbation of the heme MCD spectrum, presumably by disrupting proper alignment of the FMN and heme domains (right).

4.7 Conclusion

This work highlights the joint application of EPR, low temperature MCD and VTVH MCD spectroscopic techniques as very sensitive probes of the heme and heme environment in NOS in terms of structural and domain-domain interactions. For the first time, we have observed effects of mutations at the FMN site on the electronic structure of heme center. Although L-arginine does not bind directly to the heme, it induces a significant spectroscopic change which is likely indicative of the productive FMN/heme alignment that allows change of spin state to a predominantly high spin heme. The use of cyanide as a stable oxygen analogue has allowed for a characterization of redox orbitals involved in both high and low spin states when L-arginine is bound at Fe^{3+} heme site. It also shows the involvement of a water molecule which can have stabilization or destabilization effect at the heme site upon CN^{-}.L-arginine binding and might be involved in a proton provision for NOS catalysis. In general, these techniques will continue to be key in the structural elucidation of heme sites and of interaction sites in the domains of NOS flavoproteins and other metalloenzymes involving interacting domains for catalysis.

References:

1. Sempombe J, Elmore BO, Sun X, Dupont A, Ghosh DK, Guillemette JG, Kirk ML, Feng C; Mutations in the FMN Domain Modulate MCD Spectra of the Heme Site in the Oxygenase Domain of Inducible Nitric Oxide Synthase. *Journal of the American Chemical Society* **2009**, *131*, 6940-6941.

2. Kirk M; Recent Applications of MCD Spectroscopy to Metalloenzymes: *Current Opinion in Chemical Biology*. **2003**, *7*, 220-227.

3. Brader ML, Kaarsholm NC, Harnung SE, Dunn MF; Ligand Perturbation Effects on a Pseudotetrahedral Co(II)(His)3-Ligand Site: A Magnetic Circular Dichroism Study of the Co(II)-Substituted Insulin Hexamer: *The Journal of Biological Chemistry*. **1997**, *272*, 1088-1094.

4. Crowder MW, Wang Z, Franklin SL, Zovinka EP, Benkovic SJ; Characterization of the Metal-Binding Sites of the Beta-Lactamase From *Bacteroides fragilis*. *Biochemistry* **1996**, *35*, 12126-12132.

5. Bubacco L, Magliozzo RS, Beltramini M, Salvato B, Peisach J; Preparation and Spectroscopic Characterization of a Coupled Binuclear Center in Cobalt(II)-Substituted Hemocyanin. *Biochemistry* **1992**, *31*, 9294-10303.

6. Larrabee JA, Alessi CM, Asiedu ET, Cook, JO, Hoerning, KR, Klingler, LJ, Okin, GS, Volkert, TL ; Magnetic Circular Dichroism Spectroscopy as a Probe of Geometric and Electronic Structure of Cobalt(II)-Substituted

Proteins: Ground-State Zero-Field Splitting as a Coordination Number Indicator. *Journal of the American Chemical Society* **1997**, *119*, 4182-4196.

7. Gewirth AA, Solomon EI; Electronic Structure of Plastocyanin: Excited State Spectral Features. *Journal of the American Chemical Society* **1988**, *110,* 3811-3819.

8. Krzystek J, Zvyagin SA, Ozarowski A, Fiedler AT, Brunold, TC, Telser, J; Definitive Spectroscopic Determination of Zero-Field Splitting in High-Spin Cobalt(II). *Journal of the American Chemical Society* **2004**, *126*, 2148-2155.

9. Solomon EI, Rawlings J, McMillin DR, Stephens PJ, Gray HB. Infrared and Visible Circular Dichroism and Magnetic Circular Dichroism Studies on Cobalt(II)-Substituted Blue Copper Proteins. *Journal of the American Chemical Society* **1976**, *98*, 8046-8048.

10. Jones RM, Inscore FE, Hille R, Kirk ML; Freeze-Quench Magnetic Circular Dichroism Spectroscopic Study of the "Very Rapid" Intermediate in Xanthine Oxidase. *Inorganic Chemistry* **1999**, *38*, 4963-4970.

11. Whittaker JW, Solomon EI; Spectroscopic Studies on Ferrous Non-Heme Iron Active Sites: Magnetic Circular Dichroism of Mononuclear Fe Sites in Superoxide Dismutase and Lipoxygenase. *Journal of American Chemical Society* **1988**, *110*, 5329-5339.

12. Basu P; Use of EPR Spectroscopy in Elucidating Electronic Structures of Paramagnetic Transition Metal Complexes. *Journal of Chemical Education* **2001**, *78*, 666-669.

13. Kim JH, Hille R; Reductive Half-Reaction of Xanthine Oxidase with Xanthine: Observation of a Spectral Intermediate Attributable to the Molybdenum Center in the Reaction of Enzyme with Xanthine. *The Journal of Biological Chemistry* **1993**, *268,* 44-51.

14. Cockle SA, Lindskog S, Grell E; Electron-Paramagnetic-Resonance Studies on Cobalt(II) Carbonic Anhydrase-Sulphonamide Complexes. *The Biochemical Journal* **1974**, *143,* 703-715.

15. George GN, Bray RC; Studies by Electron Paramagnetic Resonance Spectroscopy of Xanthine Oxidase Enriched with Molybdenum-95 and with Molybdenum-97. *Biochemistry* **1988**, *27*, 3603-3609.

16. Howes BD, Pinhal NM, Turner NA, Bray RC, Anger G, Ehrenberg A, Raynor, JB, Lowe, DJ; Proton Electron-Nuclear Double-Resonance Spectra of Molybdenum(V) in Different Reduced Forms of Xanthine Oxidase. *Biochemistry* **1990**, *29,* 6120-6127.

17. Hawkes TR, George GN, Bray RC; The Structure of the Inhibitory Complex of Alloxanthine (1H-pyrazolo[3,4-d]pyrimidine-4,6-diol) with the Molybdenum Centre of Xanthine Oxidase From Electron-Paramagnetic-Resonance Spectroscopy. *The Biochemical Journal* **1984**, *218,* 961-968.

18. Shanmugam M, Zhang B, McNaughton RL, Kinney RA, Hille R, Hoffman BM; The Structure of Formaldehyde-Inhibited Xanthine Oxidase Determined by 35 GHz 2H ENDOR Spectroscopy. *Journal of the American Chemical Society* **2010**, *132*, 14015-14017.

19. Greenwood RJ, Wilson GL, Pilbrow JR, Wedd AG; Molybdenum(V) Sites in Xanthine Oxidase and Relevant Analog Complexes: Comparison of Oxygen- 17 Hyperfine Coupling. *Journal of the American Chemical Society* **1993**, 115, 5385-5392.

20. Kemsley JN, Zaleski KL, Caradonna JP, Solomon EI; Circular Dichroism and Magnetic Circular Dichroism Spectroscopy of the Catalytically Competent Ferrous Active Site of Phenylalanine Hydroxylase and Its Interaction with Pterin Cofactor. *Bioinorganic Chemistry* **1999**, *2*, 1528-1536.

21. Pavlosky MA, Zhang Y, Westre TE, Gan QF, Pavel, EG, Campochiaro C, Hedman B, Hodgson KO, Solomon EI; Near-Infrared Circular Dichroism , Magnetic Circular Dichroism , and X-ray Absorption Spectral Comparison of the Non-Heme Ferrous Active Sites of Plant and Mammalian. *Journal of the American Chemical Society* **1995**, *117*, 4316-4327.

22. Loebj KE, Zaleski JM, Westre TE, Guajardo RJ, Mascharak PK, Hedman B, Hodgson KO, Solomon EI; Spectroscopic Definition of the Geometric and Electronic Structure of the Non-Heme Iron Active Site in Iron(II) Bleomycin: Correlation with Oxygen Reactivity. *Journal of the American Chemical Society* **1995**, *117*, 4545-4561.

23. Pavel EG, Zhou J, Busby RW, Gunsior M, Townsend CA, Solomon EI; Circular Dichroism and Magnetic Circular Dichroism Spectroscopic Studies of the Non-Heme Ferrous Active Site in Clavaminate Synthase and Its Interaction with R-Ketoglutarate Cosubstrate. *Journal of the American Chemical Society* **1998**, *120*, 743-753.

24. Que L Jr; *Physical Methods in Bioinorganic Chemistry: Spectroscopy and Magnetism*. University Science Books, Sausalito, California, **2000**.

25. Solomon EI, Lever ABP; *Inorganic Electronic Structure and Spectroscopy: Volume I, Methodology*. John Wileys and Sons, Inc, **2006**.

26. Drago RS; *Physical Methods for Chemists:* Second Edition. Surfside Scientific Publishers, **1992**.

27. Shriver DF, Atkins PW; *Inorganic Chemsitry*: Third Edition. Oxford University Press, **1999**.

28. Hens Z; Can the Oscillator Strength of the Quantum Dot Bandgap Transition Exceed Unity? *Chemical Physics Letters* **2008**, *463*, 391-395.

29. Malkina OL, Vaara J, Schimmelpfennig B, Munzarova, M, Malkin VG, Kaupp M; Density Functional Calculations of Electronic g -Tensors Using Spin−Orbit Pseudopotentials and Mean-Field All-Electron Spin−Orbit Operators. *Journal of the American Chemical Society* **2000**, *122*, 9206-9218.

30. William WJ; *Magnetic Atoms and Molecules*. Dover Publications, Inc, New York, **1983**.

31. Atherton NM; *Principles of Electron Spin Resonance*. Ellis Horwood New York, **1993**.

32. Mabbs FE, Collison D; *Electron Paramagnetic Resonance of d Transition Metal Compounds: Studies in Inorganic Chemsitry: Volume 16*. Elsevier Amsterdam, **1992**.

33. Wertz JE, Bolton JR; *Electron Spin Resonance: Elementary Theory and Practical Applications*. Chapman and Hall, New York, **1986**.

34. Abragam A, Bleaney B. *Paramagnetic Resonance of Transition Ions*. Dover Publications, Inc. New York, **1970**.

35. Weil JA, Bolton JR, Wertz JE; *Electron Paramagnetic Resonance: Elementary Theory and Practical Applications*. John Wiley & Sons, Inc, **1994**.

36. Oganesyan VS, George SJ, Cheesman MR, Thomson AJ; A Novel, General Method of Analyzing Magnetic Circular Dichroism Spectra and Magnetization Curves of High-Spin Metal Ions: Application to the Protein Oxidized Rebredoxin, *Desulfovibrio gigas*. *Journal of Chemical Physics* **1999**, *110*, 762-777.

37. Neese F, Solomon EI; MCD C-Term Signs, Saturation Behavior, and Determination of Band Polarizations in Randomly Oriented Systems with Spin $S \geq ½$: Applications to $S = 1/2$ and $S = 5/2$. *Inorganic Chemistry* **1999**, *38*, 1847-1865.

38. Maren TH; Carbonic Anhydrase Inhibition in Ophthalmology: Aqueous Humor Secretion and the Development of Sulfonamide Inhibitors. *Journal of Biological Chemistry* **2000**, *247*, 425-35.

39. Brader ML, Kaarsholm NC, Harnung SE, Dunn MF. Ligand Perturbation Effects on a Pseudotetrahedral Co(II)(His)3-Ligand Site. A Magnetic Circular Dichroism Study of the Co(II)-Substituted Insulin Hexamer. *Journal of Biological Chemistry* **1997**, *272*, 1088-1094.

40. Yang J, Rothery R, Sempombe J, Weiner JH, Kirk ML; Spectroscopic Characterization of YedY: The Role of Sulfur Coordination in a Mo(V) Sulfite Oxidase Family Enzyme Form. *Journal of the American Chemical Society* **2009**, *131*, 15612-15614.

41. Mack J, Stillman M, Kobayashi N; Application of MCD Spectroscopy to Porphyrinoids. *Coordination Chemistry Reviews* **2007**, *251*, 429-453.

42. Craft JL, Horng Y-C, Ragsdale SW, Brunold TC; Spectroscopic and Computational Characterization of the Nickel-Containing F430 Cofactor of Methyl-Coenzyme M Reductase. *Journal of Biological Inorganic Chemistry* **2004**, *9*, 77-89.

43. Mabrouk PA, Orville AM, Lipscomb JD, Solomon EI; Variable-Temperature Variable-Field Magnetic Circular Dichroism Studies of the Fe(II) Active Site in Metapyrocatechase: Implications for the Molecular Mechanism of Extradiol Dioxygenases. *Journal of the American Chemical Society* **1991**, *113*, 4053-4061.

44. Kirk ML; Magnetic Circular Dichroism Spectroscopy of Pyranopterin Molybdenum Enzymes. In: Telser J, ed. *Paramagnetic Resonance of Metallobiomolecules*. American Chemical Society, Washington, DC; **2003**, 340-357.

45. Hille R; The Mononuclear Molybdenum Enzymes. *Chemical Reviews* **1996**, *96*, 2757-2816.

46. Xia M, Dempski R, Hille R; The Reductive Half-Reaction of Xanthine Oxidase: Reaction with Aldehyde Substrates and Identification of the Catalytically Labile Oxygen. *Journal of Biological Chemistry* **1999**, *274*, 3323-3330.

47. Romão MJ; Molybdenum and Tungsten Enzymes: A Crystallographic and Mechanistic Overview. *Dalton Transactions* **2009**, 4053-4068.

48. Doonan CJ, Rubie ND, Peariso K, Harris HH, Knottenbelt SZ, George GN, Young CG, Kirk ML; Electronic Structure Description of the Cis-MoOS Unit

in Models for Molybdenum Hydroxylases. *Journal of the American Chemical Society* **2008**, *130*, 55-65.

49. Okamoto K, Matsumoto K, Hille R, Eger BT, Pai EF, Nishino T; The Crystal Structure of Xanthine Oxidoreductase During Catalysis: Implications for Reaction Mechanism and Enzyme Inhibition. *Proceedings of the National Academy of Sciences of the United States of America* **2004**, *101*, 7931-7936.

50. Hille R; Molybdenum Containing Hydroxylases. *Archives of Biochemistry and Biophysics* **2005**, 433, 107-116.

51. Garattini E, Mendel R, Romão MJ, Wright R, Terao M; Mammalian Molybdo-flavoenzymes, an Expanding Family of Proteins: Structure, Genetics, Regulation, Function and Pathophysiology. *The Biochemical Journal* **2003**, 372, 15-32.

52. Hille R; Microreview: Structure and Function of Xanthine Oxidoreductase. *Europian Journal of Inorganic Chemistry* **2006**, 1913-1926.

53. Yamaguchi Y, Matsumura T, Ichida K, Okamoto K, Nishino T; Human Xanthine Oxidase Changes its Substrate Specificity to Aldehyde Oxidase Type Upon Mutation of Amino Acid Residues in the Active Site: Roles of Active Site Residues in Binding and Activation of Purine Substrate. *Journal of Biochemistry* **2007**, *141*, 513-524.

54. Rooseboom M, Commandeur JNM, Vermeulen NPE. Enzyme-Catalyzed Activation of Anticancer Prodrugs. *Pharmacological Reviews* 2004, *56*, 53-102.

55. Rashidi MR, Smith JA, Clarke SE, Beedham C. In Vitro Oxidation of Famciclovir and 6-Deoxypenciclovir by Aldehyde Oxidase From Human , Guinea Pig , Rabbit , and Rat Liver. *Drug Metabolism and Disposition* **1997**, *25*, 805-813.

56. Hille R, Nishino T; Xanthine Oxidase and Xanthine Dehydrogenase. *Journal of the Federation of American Societies for Experimental* Biology **1995**, *9*, 995-1003.

57. Leimkuhler S, Stockert AL, Igarashi K, Nishino T, Hille R. The Role of Active Site Glutamate Residues in Catalysis of *Rhodobacter capsulatus* Xanthine Dehydrogenase. *Journal of Biological Chemistry* **2004**, *279*, 40437-40444.

58. Truglio JJ, Theis K, Rappa R, Rajagopalan KV, Kisker C; Crystal Structures of the Active and Alloxanthine-Inhibited Forms of Xanthine Dehydrogenase from *Rhodobacter capsulatus. Structure* **2002**, *10*, 115-125.

59. Dietzel U, Kuper J, Doebbler JA, Schulte A, Truglio JJ, Leimkuhler S, Kisker C ; Mechanism of Substrate and Inhibitor Binding of Rhodobacter capsulatus Xanthine Dehydrogenase. *The Journal of Biological Chemistry* **2009**, *284*, 8768-8776.

60. Leimkühler S, Stockert AL, Igarashi K, Nishino T, Hille R; The Role of Active Site Glutamate Residues in Catalysis of *Rhodobacter capsulatus* Xanthine Dehydrogenase. *Journal of Biological Chemistry* **2004**, *279*, 40437-40444.

61. Huber R, Hof P, Duarte RO, Moura JJG, Moura I, Liu MY, LeGall J, Hille R, Archer M, Romao MJ; A Structure-Based Catalytic Mechanism for the Xanthine Oxidase Family of Molybdenum Enzymes. *Proceedings of National Academy of Sciences of the United States of America* **1996**, *93*, 8846-8851.

62. Enroth C, Eger BT, Okamoto K, Nishino T, Pai EF; Crystal Structures of Bovine Milk Xanthine Dehydrogenase and Xanthine Oxidase: Structure-Based Mechanism of Conversion. *Proceedings of the National Academy of Sciences of the United States of America* **2000**, *97*, 10723-10728.

63. Dobbek H, Gremer L, Meyer O, Huber R; Crystal Structure and Mechanism of CO Dehydrogenase, A Molybdo Iron-Sulfur Flavoprotein Containing S-Selanylcysteine. *Proceedings of the National Academy of Sciences of the United States of America* **1999**, *96*, 8884-8889.

64. Dobbek H, Gremer L, Kiefersauer R, Huber R, Meyer O; Catalysis at a Dinuclear [CuSMo(==O)OH] Cluster in a CO Dehydrogenase Resolved at 1.1 Å Resolution. *Proceedings of the National Academy of Sciences of the United States of America* **2002**, *99*, 15971-15976.

65. Schwarz G, Mendel RR, Ribbe MW; Molybdenum Cofactors, Enzymes and Pathways. *Nature* **2009**, *460*, 839-847.

66. Pauff JM, Zhang J, Bell CE, Hille R; Substrate Orientation in Xanthine Oxidase. *Journal of Biological Chemistry* **2008**, *283*, 4818 -4824.

67. Kisker C, Schindelin H, Rees DC; Molybdenum Cofactor Containing Enzymes: Structure and Mechanism. *Annual Review of Biochemistry* **1997**, 66, 233–267.

68. Ilich P, Hille R; Mechanism of Formamide Hydroxylation Catalyzed by a Molybdenum−Dithiolene Complex: A Model for Xanthine Oxidase Reactivity. *The Journal of Physical Chemistry B*. **1999**, 103, 5406-5412.

69. Hemann C, Ilich P, Stockert AL, Choi E-Y, Hille R; Resonance Raman Studies of Xanthine Oxidase: The Reduced Enzyme-Product Complex with Violapterin. *The journal of physical chemistry B* **2005**, 109, 3023-3031.

70. Pick FM, McGartoll MA, Bray RC; Reaction of Formaldehyde and of Methanol with Xanthine Oxidase. *European Journal of Biochemistry* **1971**, *18*, 65-72.
71. Morpeth FF, George GN, Bray RC; Formamide as a Substrate of Xanthine Oxidase. *The Biochemical Journal* **1984**, *220*, 235-242.

72. Howes BD, Bennett B, Bray RC, Richards RL, Lowe DJ; ^{13}C-ENDOR Studies of the Inhibited Species of Xanthine Oxidase: The First Direct Evidence for a Molybdenum-Carbon Bond in a Biological System. *Journal of the American Chemical Society* **1994**, *116*, 11624-11625.

73. Howes BD, Bray RC, Richards RL, Tuner NA, Bennett B, Lowe DJ; Evidence Favoring Molybdenum-Carbon Bond Formation in Xanthine Oxidase Action: ^{17}O- and ^{13}C-ENDOR and Kinetic Studies. *Biochemistry* **1996**, *35*, 1432-1443.

74. Malthouse JPG, George GN, Lowet DJ, Bray RC; Coupling of [^{33}S]Sulphur to Molybdenum (V) in Different Reduced Forms of Xanthine Oxidase. *Biochemical Journal* **1981**, *199*, 629-637.

75. Morpeth FF, Bray RC; Inhibition of Xanthine Oxidase by Various Aldehydes. *Biochemistry* **1984**, *23*, 1332-1338.

76. Bray, M.R. and Deeth RJ; Computer Modelling of Electron Paramagnetic Resonance-Active Molybdenum(V) Species in Xanthine Oxidase. *Journal of Chemical Society Dalton Transactions* **1997**, 4005-4009.

77. Massey V, Brumby PE, Komai H; Studies on Milk Xanthine Oxidase: Some Spectral and Kinetic Properties. *The Journal of Biological Chemistry* **1969**, *244*, 1682-1691.

78. Neese F; Prediction of Electron Paramagnetic Resonance g-Values Using Coupled Perturbed Hartree–Fock and Kohn–Sham Theory. *Chemical Physics* **2001**, *115*, 11080-11096.

79. Neese F; Metal and Ligand Hyperfine Couplings in Transition Metal Complexes: The Effect of Spin–Orbit Coupling as Studied by Coupled Perturbed Kohn–Sham Theory. *Journal of Chemical Physics* **2003**, *118*, 3939-3948.

80. Lenthe EV, Baerends EJ, Snijders JG; Relativistic Regular Two-Component Hamiltonians. *Journal of Chemical Physics* **1993**, *99*, 4597-4610.

81. Lenthe EV, Baerends EJ, Snijders JG; Relativistic total energy using regular approximations. *Journal of Chemical Physics* **1994**, *101*, 9783-9792.

82. Karlin KD; *Progress in Inorganic Chemistry*. John Wiley & Sons, Inc, Hoboken, New Jersey, **2007**, 252-258.

83. Khudyakov IV, Serebrennikov YA, Turro NJ; Spin-Orbit Coupling in Free-Radical Reactions: On the Way to Heavy Elements. *Chemical Reviews* **1993**, *93*, 537-570.

84. Nipales NS, Westmoreland TD; Correlation of EPR Parameters with Electronic Structure in the Homologous Series of Low-Symmetry Complexes Tp*MoOX 2 (Tp* = Hydrotris(3,5-dimethylpyrazol-1-yl)borate; X = F, Cl, Br). *Inorganic Chemistry* **1997**, *36*, 756-757.

85. Drew SC, Hill JP, Lane I, Hanson GR, Gable RW, Young CG; Synthesis, Structural Characterization, and Multifrequency Electron Paramagnetic Resonance Studies of Mononuclear Thiomolybdenyl Complexes. *Inorganic Chemistry* **2007**, *46,* 2373-2387

86. Drew SC, Young CG, Hanson GR; A Density Functional Study of the Electronic Structure and Spin Hamiltonian Parameters of Mononuclear Thiomolybdenyl Complexes. *Inorganic Chemistry* **2007**, *46*, 2388-2397.

87. Bray RC, Gutteridget S; Numbers and Exchangeability with Water of Oxygen- 17 Atoms Coupled to Molybdenum (V) in Different Reduced Forms of Xanthine Oxidase. *Biochemistry* **1982**, *21*, 5992-5999.

88. Manikandan P, Choi EY, Hille R, Hoffman BM; 35-GHz ENDOR Characterization of the "Very Rapid" Signal of Xanthine Oxidase Reacted with 2-Hydroxy-6-methylpurine (^{13}C-8): Evidence Against Direct Mo-C8 Interaction. *Journal of the American Chemical Society* **2001**, *123*, 2658-2663.

89. Davis MD, Olson JS, Palmerll G; The Reaction of Xanthine Oxidase with Lumazine. *Journal of Biological Chemistry* **1984**, *259*, 3526-3533.

90. Pauff JM, Cao H, Hille R; Substrate Orientation and Catalysis at the Molybdenum Site in Xanthine Oxidase: Crystal Structures in Complex with Xanthine and Lumazine. *Journal of Biological Chemistry* **2009**, 284, 8760 - 8767.

91. Ryan MG, Ratnam K, Hille R; The Molybdenum Centers of Xanthine Oxidase and Xanthine Dehydrogenase. *The Journal of Biological Chemistry* **1995**, *270*, 19209-19212.

92. Stockert AL, Shinde SS, Anderson RF, Hille R; The Reaction Mechanism of Xanthine Oxidase: Evidence for Two-Electron Chemistry rather than Sequential One-Electron Steps. *Journal of the American Chemical Society* **2002**, *124*, 14554-14555.

93. Harrison R; Structure and Function of Xanthine Oxidoreductase : Where are We Now ? *Free Radical Biology and Medicine* **2002**, *33*, 774 -797.

94. Higashi M, Kato S; Theoretical Study on Electronic and Spin Structures of $[Fe_2S_2]^{(2+,+)}$ Cluster: Reference Interaction Site Model Self-Consistent Field (RISM-SCF) and Multireference Second-Order Møller-Plesset Perturbation Theory (MRMP) Approach. *The journal of physical chemistry A* **2005**, *109*, 9867-9874.

95. Mayerle JJ, Denmark SE, DePamphilis BV, Ibers JA, Holm RH; Synthetic Analogs of the Active Sites of Iron-Sulfur Proteins. XI: Synthesis and Properties of Complexes Containing the Fe_2S_2 Core and the Structures of Bis[*o*-xylyl-α,α'-dithiolato-μ-sulfido-ferrate(III)] and Bisl*p*-tolylthiolato-μ-sulfido-ferrate(III)] Dianions. *Journal of the American Chemical Society* **1975**, *97*, 1032-1045.

96. Holm, R H, Gillum WO; Synthetic Analogues of the Active Sites of Iron-Sulfur Proteins. *Chemical Reviews* **1976**, *104*, 527-559.

97. Beinert H; Iron-Sulfur Clusters: Nature's Modular, Multipurpose Structures. *Science* **1997**, *277*, 653-659.

98. Gutteridge S, Bray RC; Oxygen- 17 Splitting of the Very Rapid Molybdenum (V) EPR Signal from Xanthine Oxidase*.* *Biochemical Journal* **1980**, *189*, 615-623.

99. Malthouse JPG, Williams JW, Bray RC; Molybdenum(V) EPR Signals Obtained from Xanthine Oxidase on Reduction with Aldehyde Substrates and with 2-Amino-4-Hydroxy-6-Formylpteridine. *Biochemical Journal* **1981**, *197*,421-425.

100. Barber MJ, Bray RC, Lowe DJ, Coughlan MP; Studies by Electron Paramagnetic Resonance Spectroscopy and Stopped-Flow Spectrophotometry on the Mechanism of Action of Turkey Liver Xanthine Dehydrogenase. *Biochemical journal* **1976**, *153*, 297-307.

101. Leimkuhler S, Hodson R, George GN, Rajagopalan KV; Recombinant *Rhodobacter capsulatus* Xanthine Dehydrogenase, a Useful Model System for the Characterization of Protein Variants Leading to Xanthinuria I in Humans. *Journal of Biological Chemistry* **2003**, *278*, 20802-20811.

102. Bayse CA; Theoretical Characterization of the “Very Rapid” Mo(V) Species Generated in the Oxidation of Xanthine Oxidase. *Inorganic Chemistry* **2006**, *45*, 2199-2202.

103. Hille R, Kim JH, Hemann C; Reductive Half Reaction of Xanthine Oxidase: Mechanistic Role of the Species Giving Rise to the "Rapid Type" 1 Molybdenum (V) Electron Paramagnetic Resonance Signal. *Biochemistry* **1993**, *32*, 3973-3980.

104. Bruice PY; *Organic Chemistry*, Third Edition. Prentice Hall: Upper Saddle River, New Jersey, 2001.

105. Metz S, Wang D, Thiel W; Reductive Half-reaction of Aldehyde Oxidoreductase Toward Acetaldehyde: A Combined QM/MM Study. *Journal of the American Chemical Society* **2009**, *131*, 4628-4640.

106. Metz S, Thiel W; A Combined QM/MM Study on the Reductive Half-Reaction of Xanthine Oxidase: Substrate Orientation and Mechanism. *Journal of the American Chemical Society* **2009**, 131, 14885-14902.

107. Sempombe J, Stein B, Kirk ML. Spectroscopic and Electronic Structure Studies Probing Covalency Contributions to C-H Bond Activation and Transition State Stabilization in Xanthine Oxidase. *Manuscript in preparation* **2011**.

108. Lewis HA, Furlong EB, Laubert B, Eroshkina GA, Batiyenko Y, Adams JM, Bergseid MG, Marsh CD, Peat TS, Sanderson WE, Sauder JM, Buchanan SG; A Structural Genomics Approach to the Study of Quorum Sensing: Crystal Structures of Three LuxS Orthologs. *Structure* **2001**, *9*, 527-537.

109. Ruzheinikov SN, Das SK, Sedelnikova SE, Hartley A, Foster SJ, Horsburgh MJ, Cox AG, McCleod CW, Mekhalifia A, Blackburn GM, Rice DW, Baker PJ ; The 1.2 Å Structure of a Novel Quorum-sensing Protein, *Bacillus subtilis* LuxS. *Journal of Molecular Biology* **2001**, *313*, 111-122.

110. Hilgers MT, Ludwig ML; Crystal Structure of the Quorum-sensing Protein LuxS Reveals a Catalytic Metal Site. *Proceedings of the National Academy of Sciences of the United States of America* **2001**, *98*, 11169-11174.

111. Zhu J, Dizin E, Hu X, Wavreille AS, Park J, Pei D ; S-Ribosylhomocysteinase (LuxS) is a Mononuclear Iron Protein. *Biochemistry* **2003**, *42*, 4717-4726.

112. Zhu J, Hu X, Dizin E, Pei D; Catalytic Mechanism of S-ribosylhomocysteinase (LuxS): Direct Observation of Ketone Intermediates

by 13C NMR Spectroscopy. *Journal of the American Chemical Society* **2003**, *125*, 13379-13381.

113. Greenberg EP; Minireview: Quorum Sensing in Bacteria : The LuxR-LuxI Family of Cell Density-Responsive Transcriptional Regulatorst. *Journal of Bacteriology* **1994**, *176*, 269-275.
114. Miller MB, Bassler BL; Quorum Sensing in Bacteria. *Annual Review of Microbiology* **2001**, *55*, 165-199.

115. Lyon GJ, Muir TW; Chemical Signaling Among Bacteria and Its Inhibition. *Chemistry and Biology* **2003**, *10*, 1007-1021.

116. Lowery CA, Abe T, Park J, Eubanks LM, Sawada D, Kaufmann GF, Janda KD; Revisiting AI-2 Quorum Sensing Inhibitors: Direct Comparison of Alkyl-DPD Analogues and a Natural Product Fimbrolide. *Journal of the American Chemical Society* **2009**, *131*, 15584-15585.

117. Amara N, Mashiach R, Amar D, Krief P, Spieser SAH, Bottomley MJ, Aharoni A, Meijler MM; Covalent Inhibition of Bacterial Quorum Sensing. *Journal of the American Chemical Society* **2009**, *131*, 10610-10619.

118. Geske GD, Wezeman RJ, Siegel AP, Blackwell HE. Small Molecule Inhibitors of Bacterial Quorum Sensing and Biofilm Formation. *Journal of the American Chemical Society* **2005**, *127*, 12762-12763.

119. Kaufmann GF, Sartorio R, Lee S-H, Mee JM, Altobell LJ, Kujawa DP, Jeffries E, Clapham B, Meijler MM, Janda KD; Antibody Interference with N-Acyl Homoserine Lactone-Mediated Bacterial Quorum Sensing. *Journal of the American Chemical Society* **2006**, *128*, 2802-2803.

120. Hodgkinson JT, Welch M, Spring DR; Learning the Language of Bacteria. *American Chemical Society Chemical Biology* **2007**, *2*, 715-717.

121. Lowery CA, Salzameda NT, Sawada D, Kaufmann GF, Janda KD; Medicinal Chemistry as a Conduit for the Modulation of Quorum Sensing. *Journal of Medicinal Chemistry* **2010**, *53*, 7467-7489.

122. Zhou J, Loftus AL, Mulley G, Jenkins ATA; A Thin Film Detection/Response System for Pathogenic Bacteria. *Journal of the American Chemical Society* **2010**, *132*, 6566-6570.

123. McWhirter MJ, Bremer PJ, Lamont IL, McQuillan AJ. Siderophore-Mediated Covalent Bonding to Metal (Oxide) Surfaces during Biofilm Initiation by *Pseudomonas aeruginosa* Bacteria. *Langmuir* **2003**, *19*, 3575-3577.

124. Mattmann ME, Blackwell HE; Small Molecules that Modulate Quorum Sensing and Control Virulence in *Pseudomonas aeruginosa*. *The Journal of Organic Chemistry* **2010**, *75*, 6737-6746.

125. Rudrappa T, Bais HP; Curcumin, a Known Phenolic from *Curcuma longa*, Attenuates the Virulence of *Pseudomonas aeruginosa* PAO1 in Whole Plant and Animal Pathogenicity Models. *Journal of Agricultural and Food Chemistry* **2008**, *56*, 1955-1962.

126. Pierson T, Matrakas D, Taylor YU, Manyam G, Morozov VN, Zhou W, Hoek ML ; Proteomic Characterization and Functional Analysis of Outer Membrane Vesicles of *Francisella novicida* Suggests Possible Role in Virulence and Use as a Vaccine. *Journal of Proteome Research* **2010**.

127. Chan WC, Coyle BJ, Williams P; Virulence Regulation and Quorum Sensing in Staphylococcal Infections: Competitive AgrC Antagonists as Quorum Sensing Inhibitors. *Journal of Medicinal Chemistry* **2004**, *47*, 4633-4641.

128. Lowery CA, Park J, Kaufmann GF, Janda KD; An Unexpected Switch in the Modulation of AI-2-Based Quorum Sensing Discovered Through Synthetic 4,5-Dihydroxy-2,3-pentanedione Analogues. *Journal of the American Chemical Society* **2008**, *130*, 9200-9201.

129. Teplitski M, Mathesius U, Rumbaugh KP; Perception and Degradation of N-Acyl Homoserine Lactone Quorum Sensing Signals by Mammalian and Plant Cells. *Chemical Reviews* **2011**, *111*, 100-116.

130. Truchado P, Gil-Izquierdo A, Tomás-Barberán F, Allende A; Inhibition by Chestnut Honey of N-Acyl-L-homoserine Lactones and Biofilm Formation in *Erwinia carotovora*, *Yersinia enterocolitica*, and *Aeromonas hydrophila*. *Journal of Agricultural and Food Chemistry* **2009**, *57*, 11186-11193.

131. Destruction BS; Bacterial Signal Destruction. *American Chemical Society Chemical Biology* **2007**, *2*, 89-92.

132. Gopishetty B, Zhu J, Rajan R, Sobczak AJ, Wnuk SF, Bell CE, Pei D; Probing the Catalytic Mechanism of S-Ribosylhomocysteinase (LuxS) with Catalytic Intermediates and Substrate Analogues. *Journal of the American Chemical Society* **2009**, *131*, 1243-1250.

133. Xavier KB, Miller ST, Lu W, Kim JH, Rabinowitz J, Pelczer I, Semmelhack MF, Bassler BL; Phosphorylation and Processing of the Quorum-Sensing Molecule Autoinducer-2 in Enteric Bacteria. *American Chemical Society Chemical Biology* **2007**, *2*, 128-136.

134. Alfaro JF, Zhang T, Wynn DP, Karschner EL, Zhou ZS; Synthesis of LuxS Inhibitors Targeting Bacterial Cell-Cell Communication. *Organic letters* **2004**, *6*, 3043-3046.

135. Zhu J, Knottenbelt S, Kirk ML, Pei D; Articles Catalytic Mechanism of S-Ribosylhomocysteinase: Ionization State of Active-Site. *Biochemistry* **2006**, *45*, 12195-12203.
136. Zhu J, Patel R, Pei D; Catalytic Mechanism of S-Ribosylhomocysteinase (LuxS): Stereochemical Course and Kinetic Isotope Effect of Proton Transfer Reactions. *Biochemistry* **2004**, *43*, 10166-10172.

137. Rajan R, Zhu J, Hu X, Pei D, Bell CE ; Crystal Structure of S-Ribosylhomocysteinase (LuxS) in Complex with a Catalytic 2-Ketone Intermediate. *Biochemistry* **2005**, *44*, 3745-3753.

138. Larrabee JA, Leung CH, Moore RL, Thamrong-nawasawat T, Wessler BSH. Magnetic Circular Dichroism and Cobalt(II) Binding Equilibrium Studies of *Escherichia coli* Methionyl Aminopeptidase. *Journal of the American Chemical Society* **2004**, *126*, 12316-12324.

139. Larrabee JA, Alessi CM, Asiedu ET, Cook JO, Hoerning KR, Klinger LJ, Okin GS, Santee SG, Volkert TL ; Magnetic Circular Dichroism Spectroscopy as a Probe of Geometric and Electronic Structure of Cobalt (II)-Substituted Proteins: Ground-State Zero-Field Splitting as a Coordination Number Indicator. *Journal of the American Chemical Society* **1997**, *119*, 4182-4196.

140. Hoggard PE; Angular Overlap Model Parameters. *Structure and Bonding* **2004**, *106*, 37-57.

141. S, Karambelkar VV, Sommer RD, Rheingold AL, Goldberg DP; New Monomeric Cobalt(II) and zinc(II) Complexes of a Mixed N,S(Alkylthiolate) Ligand: Model Complexes of (His)(His)(Cys) Metalloprotein Active Sites. *Inorganic chemistry* **2002**, *41*, 239-248.

142. Faye GH, Horwood JI; Correlation of Absorption Spectra and Structure of Some Co(II)- and Ni(II)-2,2’-Biquinoline Complexes. *Canadian Journal of Chemistry* **1967**, *45*, 2335-2345.

143. Ferguson J; Crystal Spectra of Metal Coordination Compounds. I. Tetrahedral Cobalt(II). *The Journal of Chemical Physics* **1960**, *32*, 528-532.

144. Coleman J E, Coleman RV. Magnetic Circular Dichroism of Co(II) Carbonic Anhydrase. *The Journal of Biological Chemistry* **1972**, *247*, 4718-4728.

145. Banci L, Bencini A, Benelli C, Gatteschi D, Zanchini C; Spectral-Structural Correlations in High-Spin Cobalt(II) Complexes. *Structure and Bonding* **1982**, *52*, 37-86.

146. Martinelkt RA, Hartson GR, Thompson JS, Holmquist B, Pilbrow JR, Auld DS, Vallee BL. Characterization of the Inhibitor Complexes of Cobalt Carboxypeptidase A by Electron Paramagnetic Resonance Spectroscopy. *Biochemistry* **1989**, *28*, 2251-2258.

147. Boyd JM, Ensign SA; Evidence for a Metal-Thiolate Intermediate in Alkyl Group Transfer from Epoxypropane to Coenzyme M and Cooperative Metal Ion Binding in Epoxyalkane:CoM Transferase. *Biochemistry* **2005**, *44*, 13151-13162.

148. Boa R; Zero-Field Splitting in Metal Complexes. *Coordination Chemistry Reviews* **2004**, *248*, 757-815.

149. Ray K, Petrenko T, Wieghardt K, Neese F; Joint Spectroscopic and Theoretical Investigations of Transition Metal Complexes Involving Non-Innocent Ligands. *Dalton Transactions* **2007**, 1552-1566.

150. Balagopalakrishna C, Kimbrough JT, Westmoreland TD; Electronic Structural Contributions to g-Values and Molybdenum Hyperfine Coupling Constants in Oxyhalide Anions of Molybdenum(V). *Inorganic Chemistry* **1996**, *35*, 7758-7768.

151. Kapre R, Ray K, Sylvestre I, Weyhermuller T, George SD, Neese F, Wieghardt K; Molecular and Electronic Structures of Oxo-bis(benzene-1,2-dithiolato)chromate(V) Monoanions. A Combined Experimental and Density Functional Study. *Inorganic chemistry* **2006**, 45, 3499-3509.

152. Farrar JA, Grinter R, Neese F, Nelson J, Thomson AJ; The Electronic Structure of the Mixed-Valence Copper Dimer $[Cu_2\{N(CH_2CH_2N{=}CHCH{=}NCH_2CH_2)_3N\}]^{3+}$. *Journal of the Chemical Society, Dalton Transactions* **1997**, 4083-4088.

153. McMillin DR, Holwerda RA, Gray HB; Preparation and Spectroscopic Studies of Cobalt(II)-Stellacyanin. *Proceedings of the National Academy of Sciences of the United States of America* **1974**, *71*, 1339-1341.

154. Crane BR; Structure of Nitric Oxide Synthase Oxygenase Dimer with Pterin and Substrate. *Science* **1998**, *279*, 2121-2126.

155. Garcin ED, Bruns CM, Lloyd SJ, Hosfield DJ, Tiso M, Gachhui R, Stuehr DJ, Tainer JA, Getzoff ED; Structural Basis for Isozyme-Specific Regulation

of Electron Transfer in Nitric Oxide Synthase. *Journal of Biological Chemistry* **2004**, *279*, 37918-37927.

156. Feng C, Tollin G, Holliday MA, Thomas C, Salerno JC, Enemark JH, Ghosh DK; Intraprotein Electron Transfer in a Two-Domain Construct of Neuronal Nitric Oxide Synthase: The Output State in Nitric Oxide Formation. *Biochemistry* **2006**, *45*, 6354-6362.

157. Garnaud PE, Koetsier M, Ost TWB, Daff S; Redox Properties of the Isolated Flavin Mononucleotide- and Flavin Adenine Dinucleotide-Binding Domains of Neuronal Nitric Oxide Synthase. *Biochemistry* **2004**, *43*, 11035-11044.

158. Ilagan RP, Tejero J, Aulak KS, Ray SS, Hemann C, Wang ZQ, Gangoda M, Zweier JL, Stuehr DJ; Regulation of FMN Subdomain Interactions and Function in Neuronal Nitric Oxide Synthase. *Biochemistry* **2009**, *48*, 3864-3876.

159. Tiso M, Tejero J, Panda K, Aulak KS, Stuehr DJ; Versatile Regulation of Neuronal Nitric Oxide Synthase by Specific Regions of its C-Terminal Tail. *Biochemistry* **2007**, *46*, 14418-14428.

160. Alderton WK, Cooper CE, Knowles RG. Nitric Oxide Synthases: Structure, Function and Inhibition. *Biochemical Journal* **2001**, *357*, 593-615.

161. Masters BSS, McMillan K, Sheta EA, Nishimura JS, Roman LJ, Martasek P; Neuronal Nitric Oxide Synthase, a Modular Enzyme Formed by Convergent Evolution: Structure Studies of a Cysteine Thiolate-Liganded Heme Protein that Hydroxylates L-Arginine to Produce NO as a Cellular Signal. *Federation of American Societies for Experimental Biology* **1996**, *10*, 552-558.

162. Xie QW, Cho H, Kashiwabara Y, Baum M, Weidnert JR, Elliston K, Mumford R, Nathan C; Carboxyl Terminus of Inducible Nitric Oxide Synthase: Contribution to NADPH Binding and Enzymatic Activity. *The Journal of Biological Chemistry* **1994**, *269*, 28500-28505.

163. Ghosh DK, Holliday MA, Thomas C, Weinberg JB, Smith SME, Salerno JC; Nitric-Oxide Synthase Output State: Design and Properties of Nitric-oxide Synthase Oxygenase/FMN Domain Constructs. *The Journal of Biological Chemistry* **2006**, *281*, 14173-14183.

164. Song N-K, Jeong C-S, Choi H-S; Identification of Nitric Oxide Synthase in *Flammulina velutipes*. *Mycologia* **2000**, *92*, 1027-1032.

165. Ji H, Li H, Martásek P, Roman LJ, Poulos TL, Silverman RB; Discovery of Highly Potent and Selective Inhibitors of Neuronal Nitric Oxide Synthase by Fragment Hopping. *Journal of Medicinal Chemistry* **2009**, *52*, 779-797.

166. Ji H, Li H, Flinspach M, Poulos TL, Silverman RB; Computer Modeling of Selective Regions in the Active Site of Nitric Oxide Synthases: Implication for the Design of Isoform-Selective Inhibitors. *Journal of Medicinal Chemistry* **2003**, *46*, 5700-5711.

167. Huang H, Martásek P, Roman LJ, Silverman RB; Synthesis and Evaluation of Peptidomimetics as Selective Inhibitors and Active Site Probes of Nitric Oxide Synthases. *Journal of Medicinal Chemistry* **2000**, *43*, 2938-2945.

168. Roman LJ, Martásek P, Masters BSS; Intrinsic and Extrinsic Modulation of Nitric Oxide Synthase Activity. *Chemical Reviews* **2002**, *102*, 1179-1190.

169. Zemojtel T, Scheele JS, Martasek P, Masters BSS, Sharma VS, Magde D; Role of the Interdomain Linker Probed by Kinetics of CO Ligation to an Endothelial Nitric Oxide Synthase Mutant Lacking the Calmodulin Binding Peptide (Residues 503-517 in Bovine). *Biochemistry* **2003**, *42*, 6500-6506.

170. Bryk R, Wolff DJ; Mechanism of Inducible Nitric Oxide Synthase Inactivation by Aminoguanidine and L-N6-(1-Iminoethyl)lysine. *Biochemistry* **1998**, *37*, 4844-4852.

171. Cho K-B, Gauld JW; Quantum Chemical Calculations of the NHA Bound Nitric Oxide Synthase Active Site: O_2 Binding and Implications for the Catalytic Mechanism. *Journal of the American Chemical Society* **2004**, *126*, 10267-10270.

172. Grant SK, Green BG, Stiffey-Wilusz J, Durette PL, Shah SK, Kozarich JW; Structural Requirements for Human Inducible Nitric Oxide Synthase Substrates and Substrate Analogue Inhibitors. *Biochemistry* **1998**, *37*, 4174-4180.

173. Visser SP de, Tan LS; Is the Bound Substrate in Nitric Oxide Synthase Protonated or Neutral and What is the Active Oxidant that Performs Substrate Hydroxylation? *Journal of the American Chemical Society* **2008**, *130*, 12961-12974.

174. Zhu Y, Silverman RB; Revisiting Heme Mechanisms: A Perspective on the Mechanisms of Nitric Oxide Synthase (NOS), Heme Oxygenase (HO), and Cytochrome P450s (CYP450s). *Biochemistry* **2008**, *47*, 2231-2243.

175. Sono M, Roach MP, Coulter ED, Dawson JH; Heme-Containing Oxygenases. *Chemical Reviews*. **1996**, *96*, 2841-2888.

176. Huang H, Hah J-mi, Silverman RB; Mechanism of Nitric Oxide Synthase: Evidence that Direct Hydrogen Atom Abstraction from the O-H Bond of N^G-

Hydroxyarginine Is Not Relevant to the Mechanism. *Journal of the American Chemical Society* **2001**, *123*, 2674-2676.

177. Bredt DS, Snyder SH. Isolation of Nitric Oxide Synthetase, a Calmodulin-Requiring Enzyme. *Proceedings of the National Academy of Sciences of the United States of America* **1990**, *87*, 682-685.

178. Abu-Soud HM, Stuehr DJ; Nitric Oxide Synthases Reveal a Role for Calmodulin in Controlling Electron Transfer. *Proceedings of the National Academy of Sciences of the United States of America* **1993**, *90*, 10769-10772.

179. Matsuda H, Iyanagi T; Calmodulin Activates Intramolecular Electron Transfer Between the Two Flavins of Neuronal Nitric Oxide Synthase Flavin Domain. *Biochimica et Biophysica Acta* **1999**, *1473*, 345-355.

180. Daff S; Calmodulin-Dependent Regulation of Mammalian Nitric Oxide Synthase. *Biochemical Society Transactions* **2003**, *31*, 502-505.

181. Gachhui R, Presta a, Bentley DF, Abu-Soud HM, McArthur R, Brudvig G, Ghosh DK, Stuehr DJ; Characterization of the Reductase Domain of Rat Neuronal Nitric Oxide Synthase Generated in the Methylotrophic Yeast *Pichia pastoris*: Calmodulin Response is Complete within the Reductase Domain Itself. *The Journal of Biological Chemistry* **1996**, *271*, 20594-20602.

182. Klatt P, Heinzel B, John M, Kastner M, Bohme E, Mayer B. Ca^{2+}/Calmodulin-Dependent Cytochrome c Reductase Activity of Brain Nitric Oxide Synthase. *The Journal of Biological Chemistry* **1992**, *267*, 11374-11378.

183. Newman E, Spratt DE, Mosher J, Cheyne B, Montgomery HJ, Wilson DL, Weinberg JB, Smith SME, Salerno JC, Ghosh DK, Guillemette JG; Differential Activation of Nitric-Oxide Synthase Isozymes by Calmodulin-Troponin C Chimeras. *The Journal of Biological Chemistry* **2004**, *279*, 33547-33557.

184. Panda K, Haque MM, Garcin-Hosfield ED, durra D, Getzoff ED, Stuehr DJ; Surface Charge Interactions of the FMN Module Govern Catalysis by Nitric-Oxide Synthase. *The Journal of Biological Chemistry* **2006**, *281*, 36819-36827.

185. Masters BSS; Nitric Oxide Synthases: Why so Complex ? *Annual Review of Nutrition* **1994**, *14*, 131-145.

186. Carolina N; The Mechanism of I- and Z-Electron Transfers Catalyzed Reduced Triphosphopyridine Cytochrome c Reductase. *The Journal of Biological Chemistry* **1965**, *240*, 4081-4088.

187. Kwon S, Griffith W, Stuehre J, Nathan CF, Matthews E, Stuehr DJ; L-Citrulline Production from L-Arginine by Macrophage Nitric Oxide Synthase. *The Journal of Biological Chemistry* **1990**, *265*, 13442-13445.

188. Leone AM, Palmer RM, Knowles RG, Francis PL, Ashton DS, Moncada S; Constitutive and Inducible Nitric Oxide Synthases Incorporate Molecular Oxygen into Both Nitric Oxide and Citrulline. *The Journal of Biological Chemistry* **1991**, *266*, 23790-23795.

189. Stuehr DJ, Kwon NS, Nathan CF, Griffith OW; N^{ω}-Hydroxy-L-arginine is an Intermediate in the Biosynthesis of Nitric Oxide from L-Arginine. *The Journal of Biological Chemistry* **1991**, *266*, 6259-6263.

190. Pufahl RA, Nanjappan PG, Woodard RW, Marletta MA; Mechanistic Probes of N-Hydroxylation of L-Arginine by the Inducible Nitric Oxide Synthase from Murine Macrophages. *Biochemistry* **1992**, *31*, 6822-6828.

191. Astashkin AV, Elmore BO, Fan W, Gillemette JG, Feng C; Pulsed EPR Determination of the Distance between Heme Iron and FMN Centers in a Human Inducible Nitric Oxide Synthase. *Journal of the American Chemical Society* **2010**, *132*, 12059-12067.

192. Feng C, Tollin G, Hazzard JT, Nahm NJ, Guillemette JG, Salerno JC, Ghosh DK; Direct Measurement by Laser Flash Photolysis of Intraprotein Electron Transfer in a Rat Neuronal Nitric Oxide Synthase. *Journal of the American Chemical Society* **2007**, *129*, 5621-5629.

193. Herrick RC, Stapleton HJ. Anomalous T^7 Raman Spin-Lattice Relaxation Rate of Low Spin Cytochrome P-450 from *Pseudomonas putida*. *The Journal of Chemical Physics* **1976**, *65*, 4778-4785.

194. Kulik LV, Lubitz W, Messinger J; Electron Spin-Lattice Relaxation of the S_0 State of the Oxygen-Evolving Complex in Photosystem II and of Dinuclear Manganese Model Complexes. *Biochemistry* **2005**, *44*, 9368-9374.

195. Harbridge JR, Eaton SS, Eaton GR; Electron Spin-Lattice Relaxation Processes of Radicals in Irradiated Crystalline Organic Compounds. *The Journal of Physical Chemistry A* **2003**, *107*, 598-610.

196. Herrick RC, Stapleton HJ; Determination of the Zero-Field Splitting of Fe^{3+} in Cytochrome P-450cam from Electron Spin-Lattice Relaxation Rates. *The Journal of Chemical Physics* **1976**, *65*, 4786-4790.

197. Ishikawa N, Sugita M, Ishikawa T, Koshihara S-ya, Kaizu Y; Mononuclear Lanthanide Complexes with a Long Magnetization Relaxation Time at High Temperatures: A New Category of Magnets at the Single-Molecular Level. *The Journal of Physical Chemistry B* **2004**, *108*, 11265-11271.

198. Tsai a L, Berka V, Chen PF, Palmer G; Characterization of Endothelial Nitric-Oxide Synthase and its Reaction with Ligand by Electron Paramagnetic Resonance Spectroscopy. *The Journal of Biological Chemistry* **1996**, *271*, 32563-32571.

199. Salerno JC, Frey C, McMillan K, Williams RF, Masters BSS, Griffith OW; Characterization by Electron Paramagnetic Resonance of the Interactions of L-arginine and L-thiocitrulline with the Heme Cofactor Region of Nitric Oxide Synthase. *The Journal of Biological Chemistry* **1995**, *270*, 27423-27428.

200. Berka V, Palmer G, Chen PF, Tsai AL; Effects of Various Imidazole Ligands on Heme Conformation in Endothelial Nitric Oxide Synthase. *Biochemistry* **1998**, *37*, 6136-6144.

201. Sono Masanori, Stuehr Dennis J, Saito-Ikeda Masao ADJH; Identification of Nitric Oxide Synthase as a Thiolate-ligated Heme Protein Using Magnetic Circular Dichroism Spectroscopy. *The Journal of Biological Chemistry* **1995**, *270*, 19943-19948.

202. Galli C, MacArthur R, Abu-Soud HM, Clark P, Stuehr DJ, Brudvig GW; EPR Spectroscopic Characterization of Neuronal NO Synthase. *Biochemistry* **1996**, *35*, 2804-2810.

203. Fedorov R, Ghosh DK, Schlichting I; Crystal Structures of Cyanide Complexes of P450cam and the Oxygenase Domain of Inducible Nitric Oxide Synthase-Structural Models of the Short-Lived Oxygen Complexes. *Archives of Biochemistry and Biophysics* **2003**, *409*, 25-31.

204. Stoll S, Schweiger A. EasySpin; A Comprehensive Software Package for Spectral Simulation and Analysis in EPR. *Journal of Magnetic Resonance* **2006**, *178*, 42-55.

205. Henchoz Y, Schappler J, Geiser L, Prat J, Carrupt PA, Veuthey JL; Rapid Determination of pKa Values of 20 Amino Acids by CZE with UV and Capacitively Coupled Contactless Conductivity Detections. *Analytical and Bioanalytical Chemistry* **2007***, 389,* 1869-1878.

206. Rinkevicius Z, Tunell I, Sałek P, Vahtras O, Ågren H; Restricted Density Functional Theory of Linear Time-Dependent Properties in Open Shell Molecules. *Journal of Chemical Physics* **2003,** *119,* 34-46